Measurement of $D^{*\pm}$ meson production in deep-inelastic scattering at HERA

Dissertation
zur Erlangung des Doktorgrades
des Fachbereichs Physik
der Universität Hamburg

vorgelegt von
Olena Bachynska
aus Wolodarka (Ukraine)

Hamburg
2012

Gutachter/in der Dissertation:	Prof. Dr. Erika Garutti PD Dr. Achim Geiser
Gutachter/in der Disputation:	Prof. Dr. B. Foster PD Dr. Thomas Schörner-Sadenius
Datum der Disputation:	05.12.2012
Vorsitzender des Prüfungsausschusses:	Dr. Georg Steinbrück
Vorsitzender des Promotionsausschusses:	Prof. Dr. Peter Hauschildt
MIN-Dekan des Fachbereichs Physik:	Prof. Dr. Heinrich Graener

Abstract

Measurements of charm production in deep-inelastic scattering at HERA at a centre-of-mass energy of 318 GeV are reported in this thesis. The analysis was performed using the data collected with the ZEUS detector during the years 2004 to 2007, corresponding to an integrated luminosity of $363\,\text{pb}^{-1}$. The production of charm quarks was studied through the full kinematic reconstruction of $D^{*\pm}$ mesons in the decay channel $D^{*\pm} \rightarrow D^0/\bar{D}^0\,\pi^{\pm}$. The studies have been performed for virtualities of the exchanged photon of $5 < Q^2 < 1000\,\text{GeV}^2$ and inelasticities of $0.02 < y < 0.7$. The visible $D^{*\pm}$ kinematic phase space is defined by the transverse momentum range, $1.5 < p_T^{D^{*\pm}} < 20\,\text{GeV}$, and by the pseudorapidity region, $|\eta^{D^{*\pm}}| < 1.5$, of the produced $D^{*\pm}$ mesons. The total visible cross section for $D^{*\pm}$ production as well as single- and double-differential cross sections were measured and compared to the corresponding $D^{*\pm}$ measurements performed by the H1 collaboration in the same phase-space region. The measurements are well described by NLO QCD predictions. The double-differential cross sections were exploited to extract the charm contribution to the proton structure function, $F_2^{c\bar{c}}$, expressed in terms of the reduced charm-production cross sections, $\sigma_{\text{red}}^{c\bar{c}}$, and compared to the predictions from HERAPDF1.5 and to the recent measurements from the H1 and ZEUS collaborations.

Zusammenfassung

In dieser Arbeit wird eine Messung der Produktion von Charmquarks in tiefunelastischer Streuung mit einer Schwerpunktsenergie von 318 GeV bei HERA präsentiert. Die Analyse wurde mit Daten durchgeführt, die mit dem ZEUS-Detektor in den Jahren 2004 bis 2007 aufgenommen wurden und einer integrierten Luminosität von $363\,\mathrm{pb}^{-1}$ entsprechen. Die Produktion von Charmquarks wurde untersucht indem die Kinematik der $D^{*\pm}$ -Mesonen in der Zerfallskette $D^{*\pm} \rightarrow D^0/\bar{D}^0\,\pi^\pm$ vollständig rekonstruiert wurde. Die Untersuchung wurde dabei in einer Region des Phasenraumes durchgeführt, die durch Schnitte auf die Virtualität Q^2 des ausgetauschten Bosons von $5 < Q^2 < 1000\,\mathrm{GeV}^2$ und durch Schnitte auf die Inelastizität von $0.02 < y < 0.7$ gekennzeichnet ist. Der sichtbare kinematische Phasenraum der produzierten $D^{*\pm}$ -Mesonen wurde von ihrem Transversalimpuls von $1.5 < p_T^{D^{*\pm}} < 20\,\mathrm{GeV}$ und von ihrer Pseudorapidität von $|\eta^{D^{*\pm}}| < 1.5$ bestimmt. Der sichtbare vollständige Wirkungsquerschnitt sowie einfach- und doppelt-differentielle Wirkungsquerschnitte für die Produktion von $D^{*\pm}$ -Mesonen wurde gemessen und die Ergebnisse mit denen der H1-Kollaboration im gleichen Phasenraumbereich verglichen. Des Weiteren wurden theoretische QCD-Vorhersagen in nächst-führender Ordnung mit den hier präsentierten ZEUS-Ergebnissen verglichen. Die doppelt-differentiellen Wirkungsquerschnitte wurden verwendet um den Beitrag der Charmproduktion $F_2^{c\bar{c}}$ zur Strukturfunktion des Protons zu bestimmen, wobei diese Größe mit Hilfe des reduzierten Wirkungsquerschnittes $\sigma_{\mathrm{red}}^{c\bar{c}}$ beschrieben wurde. Zusätzlich wurde die in dieser Arbeit gemessene Strukturfunktion $F_2^{c\bar{c}}$ mit der Vorhersage von HERAPDF1.5 und mit neusten Messungen von H1 und ZEUS verglichen.

"Mr. Spock, the women on your planet are logical. That's the only planet in the galaxy that can make that claim." – Kirk (Elaan of Troyius)

Star Trek

Table of Contents

Introduction

Ever since the time began, people were eager to learn more about the microworld, the intricacies of matter not observable by the naked eye. Nowadays, the fundamental constituents of matter are the subject of the field of particle physics. The Standard Model of particle physics describes all known phenomena connected to visible matter. In its framework all visible matter consists of six types of quarks and six types of leptons. Quarks can only be observed confined in hadrons. The production of hadrons containing charm and beauty quarks is of particular interest, because of the presence of the hard scale coming from the quark mass. Such a hard scale ensures the applicability of perturbative calculations.

In order to study the properties of heavy quarks and the forces that bind them, hadrons are produced in high-energy collisions which are provided by particle accelerators. Particles are either accelerated and sent onto a fixed target or two beams are accelerated and brought to collision. There were many accelerators built over the last years, among them the Stanford Linear Collider (SLC) at SLAC, the Large Electron Positron collider (LEP) at CERN, TEVATRON at Fermilab, HERA at DESY and the Large Hadron Collider (LHC) at CERN. Among them, HERA was the only electron-proton collider in the world. At HERA electron and proton beams were collided at a centre-of-mass energy of $\sqrt{s} = 318\,\mathrm{GeV}$. The accelerator was in operation for 15 years, accumulating almost $0.5\,\mathrm{fb}^{-1}$ of integrated luminosity per experiment. The HERA-collider physics-program [1] was very rich, including many different processes accessible by probing the proton with electrons. It included deep-inelastic scattering, photoproduction and diffractive processes, widening the observable phase space to large photon virtualities up to $30\,000\,\mathrm{GeV}^2$ and small Bjorken x, down to 10^{-6}. Deep-inelastic scattering processes are especially interesting, as they allow measurements of the proton structure. The gluon content is accessible through heavy quark production as the dominating production process is boson gluon fusion. HERA events containing heavy quarks are characterised by the presence of multiple hard scales, which in case of the deep-inelastic processes are given by the photon virtuality, by the mass of the heavy quark and by the transverse momenta of the produced quarks. These competing scales are a challenge for the corresponding perturbative QCD calculations.

The work presented in this thesis is a study of the contribution of charm quark to the proton structure function, $F_2^{c\bar{c}}$. The charm quarks are tagged though their fragmentation to $D^{*\pm}$ mesons. The production of $D^{*\pm}$ mesons in deep-inelastic scattering at HERA was studied to extract $F_2^{c\bar{c}}$. For the reconstruction of $D^{*\pm}$ mesons, the so-called "golden" decay channel with three particles in the final state was chosen. The measurements were performed with the ZEUS detector and were based on data collected during the HERA II running period with an integrated luminosity of 363 pb^{-1}. This way of measuring open charm production has proven to be the most precise at HERA. The results presented here are significantly improved with respect to previous ZEUS measurements due to larger statistics, new signal extraction methods, and improved calibration of the ZEUS detector.

The thesis is arranged as follows. First, Chapters 1–3 contain a brief theoretical outline which is necessary to understand the conclusions derived from the studies. Chapter 4 and 5 are devoted to the basic description of the ZEUS detector and reconstruction of events, respectively. Chapter 6 contains a description of the Monte Carlo processes that were used to simulate *ep* collisions. Chapter 7 describes the presented analysis: the event selection, the method of the $D^{*\pm}$ signal extraction, corrections to the acceptance, systematic uncertainties and the result of the $D^{*\pm}$ production measurement. Chapter 8 contains the results on $F_2^{c\bar{c}}$. Chapter 9 summarises the work presented in this thesis.

The author was also involved in the detector development for the future Linear Collider within the PLUME project as the technical task. The results of these studies are presented in Appendix A.

Chapter 1

The Standard Model of particle physics

A brief overview of the theoretical framework is necessary to understand the discussions and results presented in this thesis.

The current understanding of particle physics strongly relies on the so-called Standard Model [2]. It is a quantum field theory that provides a description of the known phenomena of particle physics. The Standard Model (SM) consists of several elements that describe different forces which all rely on gauge and symmetry principles. Electromagnetic and weak interactions enter the Standard Model as the Glashow-Salam-Weinberg model of electroweak forces [3, 4] and the strong force is described by Quantum Chromodynamics [5]. The purely electromagnetic part of the electroweak force is well described by Quantum Electrodynamics (QED) which generalises the classical theory of electromagnetism by Maxwell to become a quantum field theory. QED describes the interaction between charged spin-1/2 particles and photons. An example of a QED process is electron-positron annihilation into two photons. QED is based on the Abelian symmetry group U(1), where the Lagrangian for a free fermion field is invariant under phase transformations. The weak interaction [6] is responsible e.g. for the β decay of a neutron, $n \rightarrow p\ e^- \tilde{\nu}_e$ and it is based on the more complex symmetry group SU(2).

The particle content of the Standard Model is presented by 12 fermions called quarks and leptons that are listed in Table 1.1. The forces are mediated by bosons: massless photons and gluons for the electromagnetic and strong interactions, respectively, and massive $W^\pm$, Z^0 bosons for the weak interaction. In this model, all fermions obtain their masses by interacting with the Higgs field [7]. The spontaneous symmetry breaking connected to the Higgs field is responsible for the mass of the $W^\pm$, Z^0 bosons. The SM is well tested experimentally and the only missing piece is the Higgs boson. Recently both the ATLAS and CMS collaborations published results on the observation of a new Higgs-like boson with a mass of $\sim 125\,\mathrm{GeV}$ [8, 9].

Lepton	Charge	Mass, (MeV)	Quark	Charge	Mass, (GeV)
e^-	-1	0.511	d	- 1/3 e	$0.0047^{+0.0007}_{-0.0003}$
ν_e	0	$< 2.3 \times 10^{-6}$	u	+2/3 e	$0.0023^{+0.0007}_{-0.0005}$
μ^-	-1	105.66	s	- 1/3 e	0.095 ± 0.005
ν_μ	0	$< 190 \times 10^{-3}$	c	+2/3 e	1.275 ± 0.025
τ^-	-1	1776.82 ± 0.16	b	- 1/3 e	4.18 ± 0.03
ν_τ	0	<18.2	t	+2/3 e	160^{+5}_{-4}
Boson	Charge	Mass, (GeV)	Spin	Force	Range, (m)
γ	0	0	1	electromagnetic	∞
$W^\pm$	± 1	80.4	1	weak	10^{-18}
Z^0	0	91.2	1	weak	
8 g	0	0	1	strong	10^{-15}

Table 1.1: Standard model particles and force mediators with their parameters of charge and mass taken from PDG2012 [10]. The d-, u-, s- quarks, the mass value represents the "current mass" and for the c-, b, t-quarks - "running mass". The limit of the flavour mass of m_{ν_e} is taken from [11], for m_{ν_μ} from [12] and m_{ν_τ} from [13].

The SM has so far done extremely well in all possible experimental tests. However, the discovery of non-zero neutrino masses made a modest extension necessary. Despite its great popularity the SM is not able to explain the presence of dark matter and does not take into account the gravitational force.

1.1 Theory of electroweak interactions

The theory of electroweak interactions (EW) is a gauge theory based on the symmetry group SU(2)xU(1). The SU(2) part is called the weak isospin group with a new quantum number denoted as I and the projection as I_3. The Gell-Mann-Nishijima relation reads $I_3 = Q - Y/2$, where Q is the electric charge of the particle (see Table 1.1) and Y is its weak hypercharge (see Table 1.2). The SU(2) symmetry transformations act differently on left- and right-handed fermion fields. The left-handed fields, I=1/2, form three generation of doublets:

$$\begin{pmatrix} \nu_e \\ e \end{pmatrix}, \begin{pmatrix} u \\ d \end{pmatrix}; \begin{pmatrix} \nu_\mu \\ \mu \end{pmatrix}, \begin{pmatrix} c \\ s \end{pmatrix}; \begin{pmatrix} \nu_\tau \\ \tau \end{pmatrix}, \begin{pmatrix} t \\ b \end{pmatrix}. \tag{1.1}$$

The right-handed fields are represented as singlets $[e_R, u_R, d_R]$; $[\mu_R, c_R, s_R]$; $[\tau_R, t_R, b_R]$. They have I=0. In the SM, there are no right-handed neutrinos.

Fermion	Y	I_3
ν_{eL}, $\nu_{\mu L}$, $\nu_{\tau L}$	-1	+1/2
e_L, μ_L, τ_L	-1	-1/2
d_L, s_L, b_L	+1/3	-1/2
u_L, c_L, t_L	+1/3	+1/2
e_R, μ_R, τ_R	-2	0
d_R, s_R, b_R	-2/3	0
u_R, c_R, t_R	+4/3	0

Table 1.2: The weak isospin projection I_3 and hypercharge Y for the left- and right-handed particles.

The full EW Lagrangian can be written as [14]

$$\mathcal{L}_{EW} = \mathcal{L}_{gauge} + \mathcal{L}_F + \mathcal{L}_H + \mathcal{L}_Y \ , \tag{1.2}$$

where:

- $\mathcal{L}_{gauge} = -\frac{1}{4}W^a_{\nu\mu}W^{\nu\mu a} - \frac{1}{4}B_{\nu\mu}B^{\nu\mu}$ is the gauge field Lagrangian. W^a_μ are the three vector fields associated with the generators of the SU(2) group and B_μ is one vector field associated with the hypercharge group U(1).
- $\mathcal{L}_F$ represents the kinetic part of the fermion Lagrangian and the interaction between fermions and gauge bosons.
- $\mathcal{L}_H$ stands for the coupling of the gauge field to the Higgs field. The Higgs Lagrangian term reads $\mathcal{L}_H = (D_\mu\phi)^\dagger(D^\mu\phi) - V(\phi)$, where $D_\mu = \partial_\mu - ig_2\frac{\sigma^a}{2}W^a_\mu + i\frac{g_1}{2}B_\mu$ is the covariant derivative of the isospin doublet scalar Higgs field, ϕ, and $g_{1,2}$ are the EW coupling constants. The potential $V(\phi) = -\mu^2\phi^\dagger\phi + \frac{\lambda}{4}(\phi^\dagger\phi)^2$ with the constants μ, λ represents a gauge-invariant interaction of the scalar field. For μ^2, $\lambda > 0$, the potential has a "Mexican hat" shape with it minimum at $\phi^\dagger\phi = 2\mu^2/\lambda$. This corresponds to the ground state vacuum.

  Through the mechanism of spontaneous symmetry breaking [7], the gauge fields W_μ, B_μ become the "physical" massive fields representing W^+ and W^- bosons as $W^\pm_\mu = \frac{1}{\sqrt{2}}\left(W^1_\mu \mp iW^2_\mu\right)$ and the massive field of the Z^0 boson, Z_μ, and the massless field of the photon, A_μ, are transformed as

  $$\begin{pmatrix} Z_\mu \\ A_\mu \end{pmatrix} = \begin{pmatrix} \cos\theta_W & \sin\theta_W \\ -\sin\theta_W & \cos\theta_W \end{pmatrix} \times \begin{pmatrix} W^3_\mu \\ B_\mu \end{pmatrix},$$

  where θ_W is the Weinberg angle, $\cos\theta_W = \frac{M_{W^\pm}}{M_{Z^0}}$, that rotates the original W^3_μ and B_μ vector boson plane, producing as a result the Z^0 boson, and the photon. It was measured to be $\sin^2\theta_W = 0.231$ [10].

- $\mathcal{L}_Y$ stands for the Yukawa gauge invariant interactions between the Higgs and fermions fields through which fermions acquire their masses [2, 15].

1.2 Quantum Chromodynamics

Quantum chromodynamics (QCD) [16] is a non-Abelian gauge theory based on the SU(3) symmetry group. It describes strong interactions of quarks. QCD operates with the quantum number of "colour". There are three colours: Red, Green and Blue (RGB). Unlike the EW theory, QCD remains unbroken and furthermore it acts on the quark fields only. Colour is exchanged through eight gluons which carry both colour and anti-colour and belong to the adjoint representation of the colour group SU(3). In addition to the colour charge, each quark also carries a flavour u, d, s, c, b and t. For each given quark flavour there are three possible colour charges and anti-charges. Thus the theory operates with triplets of fermion fields $q = (q_1, q_2, q_3)$. The Lagrangian of QCD can be written as:

$$\mathcal{L}_{QCD} = \Sigma_q \bar{q}(i\gamma_\mu D^\mu - m_q)q - \frac{1}{4} G^a_{\mu\nu} G^{a,\mu\nu}, \tag{1.3}$$

where the sum over q runs over the six quark flavours and $a = 1...8$ runs over the gluons. The gluon field strength reads as $G_{\mu\nu}$. The covariant derivative is defined as $D_\mu = \partial_\mu - ig_s \frac{\lambda^a}{2} G^a_\mu$, where the strong coupling constant is $\alpha_s \equiv g_s^2/4\pi$ and λ^a are the eight Gell-Mann matrices. In the Lagrangian (1.3) the first term represents the quark field and the second represents quark-gluon and gluon-gluon interactions. An example of quark-gluon and triple and quartic gluon-gluon selfinteration is represented in Figure 1.1. The quark masses, m_q, enter the Lagrangian as free parameters. Different approaches how to treat the quark masses will be discussed later.

The effective strong coupling constant α_s depends on the energy scale of the interaction. This is referred to as running of α_s, see Figure 1.2. At small scale the strong coupling constant becomes large, which is referred to as the confinement, while at large scale α_s becomes small, which is called asymptotic freedom [17]. The latter can be explained by the gluon self-coupling and allows perturbative techniques

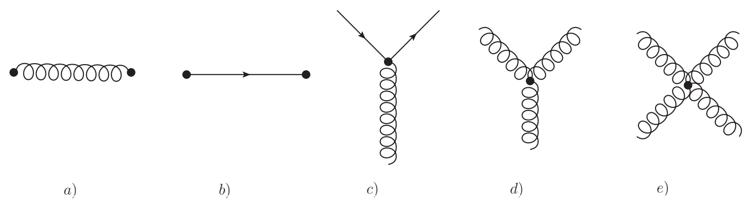

Figure 1.1: Feynman graph representation of a) gluon, b) quark, c) quark-gluon, d)-e) gluon-gluon parts of the QCD Lagrangian.

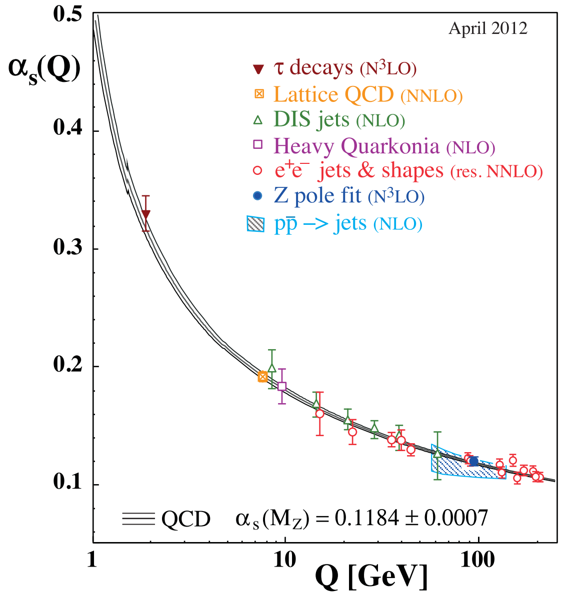

Figure 1.2: Summary of α_s measurements [10] as a function of the respective energy scale Q.

to be used in calculations at large energy scales. Confinement arises since the force between two colour charges grows with rising distance, producing new quark pairs before any of the existing ones can be separated. Therefore, only colourless objects, i.e. mesons ($q\bar{q}$ states) and baryons (3-quark states), are observed experimentally.

1.2.1 Perturbative QCD and renormalization scale

QCD can in general only be treated perturbatively. At high energies, the QCD Lagrangian can be evolved into a series with respect to α_s. In perturbative QCD (pQCD), any cross section, σ, is thus expressed as:

$$\sigma = \sum_{i=0}^{n} c_i \alpha_s^i, \tag{1.4}$$

where n is the order of the calculation and the coefficients c_i can be calculated from the relevant Feynman diagrams. The number of diagrams increases with rising order. Therefore, theoretical calculations are often made at small orders of α_s.

The lowest possible contribution is called leading order (LO, e.g. $n = 1$) and the one next to it is referred to as next-to-leading order (NLO, e.g. $n = 2$). Contributions from quark and gluon loops, Figure 1.3, start to play a role at higher orders. Integration over the phase space of the loops in Figure 1.3 will include infinite momenta of the virtual loop which leads to so-called ultraviolet divergencies. Another infinity comes from the collinear or soft gluon emission causing the

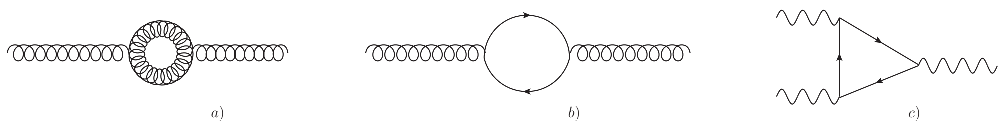

Figure 1.3: Feynman graph representation of examples of the loop corrections for a) gluon and b) quark loop corrections to the gluon propagator c) vertex between three gauge bosons.

infrared divergencies [16]. Those divergencies can be removed via changing the dimension of the space-time integration from four to $4-\epsilon$ in the trajectory integral: $\int d^4 \rightarrow \lim_{\epsilon\rightarrow 0}\int d^{4-\epsilon}$, called dimensional regularisation. The regularised divergencies can be removed by absorbing them in to the definition of α_s and mass. The prescription for this is referred to as renormalization scheme [18], that introduces a renormalization scale, μ_R. There are several prescriptions for the renormalization. The on-shell scheme [19] that can be used for the mass renormalization and the modified minimal subtraction, $\overline{MS}$, scheme [20, Chapter 9] that can serve either for quark mass or α_s renormalization. The choice of the renormalization scale, μ_R, is a priori not fixed. In theoretical calculations to all order, the value of μ_R does not affect the result for any physical observable, M, thus:

$$\mu_R^2 \frac{dM}{d\mu^2} = 0. \tag{1.5}$$

At n large enough, any changes in the calculation of M, due to introduction of μ_R, should be compensated through the re-normalised running coupling constant $\alpha_s(\mu_R^2)$ (or mass) under the renormalization group equation:

$$\mu_R^2 \frac{d\alpha_s}{d\ln\mu_R^2} = \beta(\alpha_s), \tag{1.6}$$

where $\beta(\alpha_s) = -\alpha_s^2 \sum_{i=0}^{n} b_i \alpha_s^i$ is the beta function of QCD. The b coefficients are calculable in QCD, e.g: $b_0 = \frac{33-2n_f}{12\pi}$ and $b_1 = \frac{153-19n_f}{24\pi^2}$ where n_f is the number of flavours that are considered in the calculation. At higher orders, the b_i coefficients depend explicitly on the renormalization scheme that is used. Numerically, the value of the strong coupling is usually given at the reference scale $\mu_R = M_{Z^0}$, from which it is possible to obtain its value at any other scale by solving Equation 1.6. At LO the solution is:

$$\alpha_s(\mu_R) = \frac{b_0^{-1}}{\ln(\frac{\mu_R^2}{\Lambda_{\mathrm{QCD}}^2})}, \tag{1.7}$$

where $\Lambda_{\mathrm{QCD}} \sim 200\,\mathrm{MeV}$ is called the QCD scale. The value of Λ_{QCD} corresponds to the scale where the perturbatively-defined strong coupling constant will diverge. The world average for the strong coupling constant is $\alpha_s(M_{Z^0}) = 0.1184 \pm 0.0007$ [10].

As it is not possible to calculate $\beta(\alpha_s)_{n\to\infty}$, renormalization scale dependencies are introduced, therefore the choice of μ_R is important.

1.2.2 Quark masses

After renormalization, the quark masses still remain as free parameters of the Lagrangian and have to be determined by comparing theoretical predictions with experimental data. There are two main approaches to treat quark masses, so-called "pole" and "running" quark masses.

The pole mass, m_q, is based on the concept of a "free" quark. In this case, the quark momentum p_q is substituted by the quark mass m_q, $p_q^2 = m_q^2$ at each quark pole in the propagator in the on-shell renormalization scheme. This definition introduces dependencies on $\frac{\Lambda_{\mathrm{QCD}}}{m_q}$ [21]. The pole mass cannot be used to arbitrarily high accuracy in pQCD because of non-perturbative infrared effects in QCD.

In the $\overline{MS}$ scheme, the mass depends on the scale μ_R and is referred to as a running mass [22, 23]. The relation between pole and running mass is:

$$m_q = \overline{m_q}(\mu_R)(1 + \alpha_s d^1 + \alpha_s^2 d^2 + \cdots), \tag{1.8}$$

where the coefficients d^i are known up to the third order [24].

For the light flavour quarks u, d and s, often a constituent quark mass is given. It basically denotes the mass of the quarks while surrounded by a cloud of gluons and virtual quark pairs. The constituent mass is used in non-relativistic quarks models at the scales of chiral symmetry breaking of $\approx 1\,\mathrm{GeV}$ [25, 10]. The constituent mass values are not directly related to the $\mathcal{L}_{QCD}$ mass parameters. They are only valid within the models that introduce them.

Chapter 2

Proton structure function

In this chapter, deep-inelastic scattering processes and their relation to proton structure functions are explained. Proton structure functions were introduced after measurements [26] revealed an internal structure. To study this internal structure, the proton has to be probed with energetic particles. A common approach is to use leptons (electrons, muons or neutrinos) as the probe. This can either be done by sending a lepton beam onto a nucleonic target [27] or by colliding electron and proton beams as done at HERA [1, 28].

2.1 Deep inelastic scattering

Deep-inelastic scattering (DIS) of leptons off a hadronic target are widely used in high energy particle experiments to study the internal structure of the nucleon and to test different theoretical approaches. The leading order Feynman diagram of this process is shown in Figure 2.1[1]. The incoming lepton interacts via boson exchange with the proton and the latter is being broken and a new hadronic final state is created. If the exchange occurs via one of the charged vector bosons, this is a *charge-current* (CC) interaction, and the scattered lepton becomes a neutrino of corresponding flavour. If the exchange occurs via a virtual photon or Z^0 boson, the process is called *neutral-current* (NC). Only NC processes will be considered from here on.

DIS can be characterised by the following kinematic variables, assuming that the momenta of the incoming particles are much higher than their masses, such that masses can be neglected. The centre-of-mass energy of the system, $\sqrt{s}$, is given by:

$$\sqrt{s} = \sqrt{(h+l)^2}, \tag{2.1}$$

[1]In the following the proton quark lines are skipped in all drawings of Feynman diagrams.

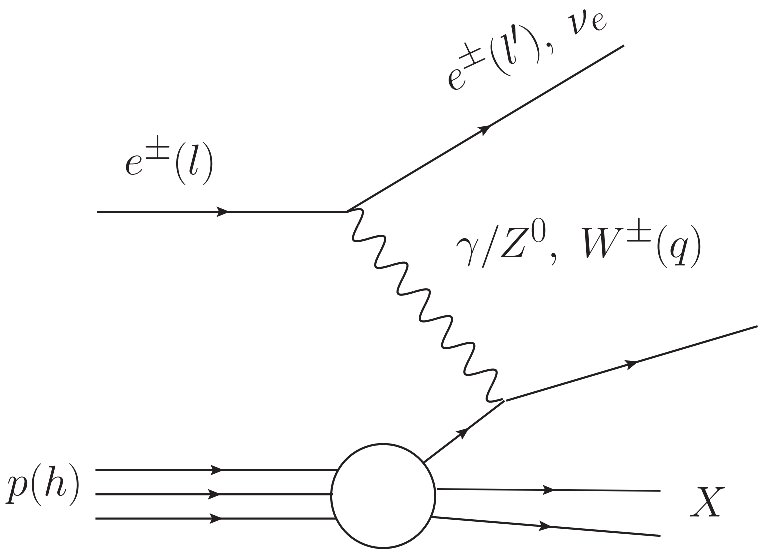

Figure 2.1: Feynman diagram of deep inelastic scattering in *ep* collisions. The incoming lepton is marked with $e^{\pm}$ and the scattered lepton $e^{\pm}$ or neutrino (depending on the type of the processes) is marked with e', ν_e. The proton and the hadronic system are marked with p and X correspondingly and the momenta are given in brackets.

where h and l are the 4-momentum of the incoming proton and the incoming lepton. The squared momentum of the exchanged boson is given by

$$Q^2 = -q^2 = -(l - l')^2, \tag{2.2}$$

where l' is the 4-momentum of the scattered lepton. Q^2 is referred to as the virtuality of the boson. The Bjorken scaling variable [29], x, can be written as:

$$x = \frac{Q^2}{2h \cdot (l - l')}. \tag{2.3}$$

It describes the fraction of the proton momentum carried by the struck quark within the Quark Parton Model (see Section 2.2). The inelasticity, y, of an event is:

$$y = \frac{h \cdot (l - l')}{h \cdot l}. \tag{2.4}$$

It denotes the fraction of the lepton momentum transferred to the proton. All these DIS variables are related through the equation $Q^2 = sxy$.

2.2 Quark Parton Model

The Quark Parton Model (QPM) was introduced by R. Feynman [30]. According to this model the proton consists of free point-like particles called partons. Each of

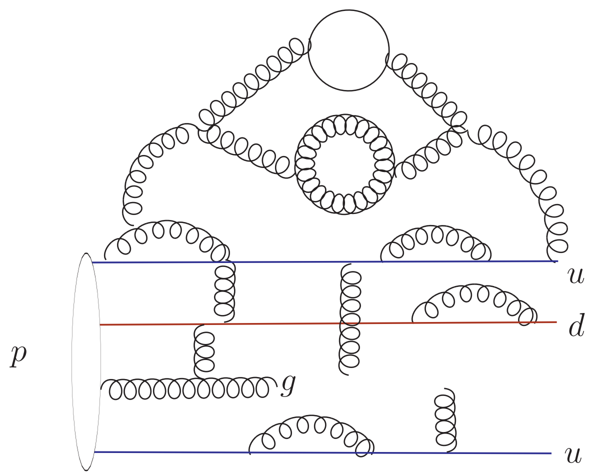

Figure 2.2: Illustration of the possible quantum fluctuations inside a proton.

those partons carries a fraction, ξ_i, of the proton momentum, p. Thus the parton momentum, p_i, can be written as: $p_i = \xi_i p$, where index i run over the constituent partons and $0 < \xi_i < 1$. In the infinite momentum frame with $\mathrm{p} \gg \mathrm{m_{proton}}$, like at the HERA collider (see Chapter 4), transverse momentum as well as masses of the partons can be neglected. Therefore the Bjorken scaling variable becomes $x = \xi_i$ for a struck massless parton i. The parton density of a parton i in the proton is described by parton distribution functions (PDF), $f_i(x)$. It denotes the density of partons that have momentum in the range of $\xi_i \pm d\xi_i$. At large Q^2 the static QPM can be re-formulated as follows. The proton is made up of valence quarks (udu) and virtual sea quark-anti-quark pairs, that are both treated as partons. The former define the flavour properties of the proton and the latter have no overall flavour. The anti-quark distributions within a nucleon belong to the sea distributions, while the quark distributions have both valence and sea components.

If the proton consisted of quarks only, the sum-rule would be

$$I = \int_0^1 x dx \sum_i f_i(x) = 1. \tag{2.5}$$

This sum-rule turned out not to be satisfied, as experimentally it was measured that $I \simeq 0.5$ [31], suggesting that approximately 50% of the nucleon momentum is carried by gluons. Thus, gluons inside the proton are also treated as constituent partons. The pure QPM model does not take into account interactions between the partons inside a nucleon. An example of such interactions can be seen in Figure 2.2. The fact that quarks are confined also needs to be considered. Therefore the naive QPM should be refined according to QCD.

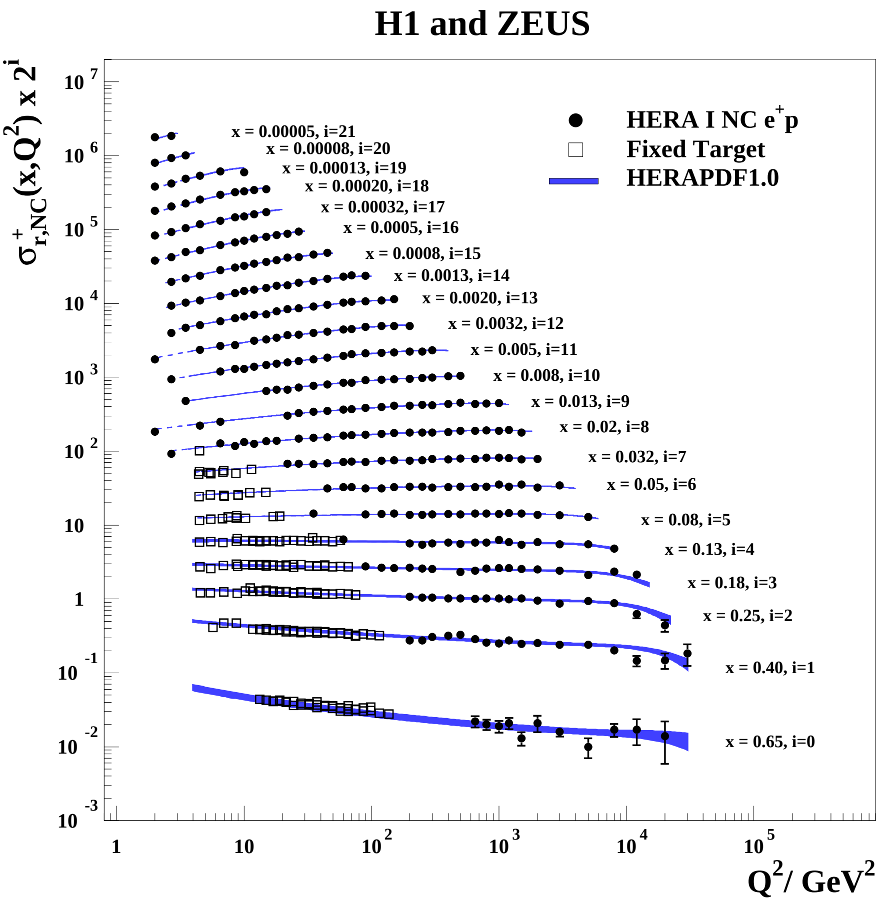

Figure 2.3: Combined HERA inclusive NC reduced cross sections (filled points) as function of Q^2 for different values of x and compared to the results from fixed target experiments (open squares) and to the theoretical predictions from HERAPDF 1.0 [28].

2.3 Proton structure functions

The differential cross section in Q^2 and x of the inclusive Neutral Current process (see Section 2.1) for electron proton collisions can be expressed in terms of the proton generalised structure functions, $\tilde{\mathrm{F}}_2$, $\tilde{\mathrm{F}}_3$ and $\tilde{\mathrm{F}}_L$, that are sensitive to the quark and gluon content of the proton [32]:

$$\frac{d^2\sigma^{e\pm p}_{\mathrm{NC}}}{dxdQ^2} = \frac{2\pi\alpha}{xQ^4}[Y_+\tilde{\mathrm{F}}_2(x,Q^2) \mp Y_-\tilde{\mathrm{F}}_3(x,Q^2) - y^2\tilde{\mathrm{F}}_L(x,Q^2)], \tag{2.6}$$

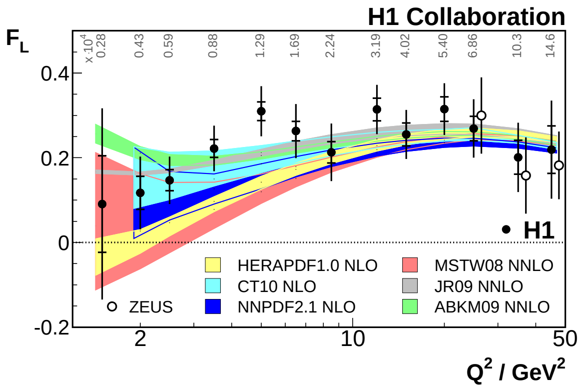

Figure 2.4: Longitudinal structure function measured by the H1 (filled points) and ZEUS (open points) collaborations compared to different theoretical predictions [33].

where $Y_{\pm} = 1 \pm (1-y)^2$ and α is the electromagnetic coupling constant. The generalised structure functions can be expressed as linear combination of contributions from pure photon, pure Z boson exchanges and Z-photon interference.

At HERA energies, $\tilde{F}_2$ component is the dominant one. It can be written in terms of the contributions arising from pure γ exchange, F_2^{γ}, (see Figure 2.1 for the Feynman diagram of the DIS process), γZ interference, $F^{\gamma Z}$, and pure Z exchange, F_2^Z [34, 35]:

$$\tilde{\mathrm{F}}_2 \equiv F_2 - v_e \frac{\kappa Q^2}{Q^2 + M_Z^2} F_2^{\gamma Z} + (v_e^2 + a_e^2) \left(\frac{\kappa Q^2}{Q^2 + M_Z^2} \right)^2 F_2^Z, \tag{2.7}$$

where

$$\kappa = \frac{1}{4 \sin^2 \theta_W \cos^2 \theta_W},$$

and a_e, v_e are the weak axial and vector couplings of the electron to the Z boson. In analogy to $\tilde{F}_2$, $x\tilde{F}_3$ can be written as:

$$x\tilde{F}_3 \equiv -a_e \frac{\kappa Q^2}{Q^2 + M_Z^2} xF_3^{\gamma Z} + 2 v_e a_e \left(\frac{\kappa Q^2}{Q^2 + M_Z^2} \right)^2 xF_3^Z. \tag{2.8}$$

F_2^Z is highly suppressed at HERA energies, because it only becomes important at $Q^2 \gtrsim M_Z^2$. $F_2^{\gamma Z}$ becomes important when Q^2 approaches M_Z^2. HERA data is dominated by F_2^{γ}.

$\tilde{\mathrm{F}}_L$ is called longitudinal structure function. In QPM, $F_L = 0$, that is called the Callan-Gross relation [36]. However, beyond leading order, F_L is non zero and it is relevant at high y. The measured $\tilde{F}_L$ [33] is shown in Figure 2.4.

Often, instead of structure functions reduced cross sections, $\tilde{\sigma}$, are discussed. By removing the kinetic term in front of $\tilde{\mathrm{F}}_2$, the reduced cross section is defined as

$$\tilde{\sigma}_{\mathrm{NC}} \equiv \frac{xQ^4}{1\pi\alpha^2}\frac{1}{Y_+}\frac{d^2\sigma}{dxdQ^2} = \tilde{\mathrm{F}}_2 \mp \frac{Y_-}{Y_+}x\tilde{\mathrm{F}}_3 - \frac{y^2}{Y_+}\tilde{\mathrm{F}}_L. \tag{2.9}$$

Figure 2.3 shows the measured reduced cross sections of the NC DIS process at HERA [28] over a wide kinematic range.

Bjorken predicted a scaling of the cross section such that it only dependent on x [29]. The data presented in Figure 2.3 show that such a scaling is only an approximation. There is a Q^2 dependence and it changes with x. This is described by QCD. Measurements of the proton structure functions serve as an input for the extraction of parton distribution functions that are universal for all processes.

2.4 Parton distributions and QCD dynamics

The higher the virtuality, Q^2, of the exchanged boson, i.e the smaller the wave length of the probe, the more detailed the interior of the proton can be studied, revealing the effects of the interactions between the partons. For example, the struck valence quark may radiate a gluon (see Figure 2.2) before the interaction with the vector boson. It can also happen that a gluon produces a $q\bar{q}$ pair of sea quarks and one of those becomes struck. Therefore PDFs can not be as simple as a number of partons of a certain type within a nucleon momentum fraction range. Thus, the quark momentum distribution inside a proton and the structure functions are also dependent on Q^2. This is referred to as Q^2 evolution.

One of the possible approaches to describe Q^2 evolution is the DGLAP formalism [37]. The quark distributions are described by:

$$\frac{dq_i(x,Q^2)}{d\ln Q^2} = \frac{\alpha_s(Q^2)}{2\pi}\int_x^1 \frac{d\xi}{\xi}\left[\sum_j q_j(\xi,Q^2)P_{q_iq_j}(\frac{x}{\xi}) + g(\xi,Q^2)P_{q_ig}(\frac{x}{\xi})\right], \tag{2.10}$$

where $q_i(\xi, Q^2)$ are the quark distributions for all momentum fractions $\xi \in [x...1]$ that contribute to gluon radiation and $g(\xi, Q^2)$ is the distribution of gluons producing quark-anti-quark pairs. The $P_{q_iq_j}(z)$ are called splitting functions. They give the probability of a parton p_j to emit a parton p_i with the momentum fraction $z = \frac{x}{\xi}$ of p_j. The gluon distribution, $g(x, Q^2)$, due to gluon radiation of quarks and gluons is described as:

$$\frac{dg(x,Q^2)}{d\ln Q^2} = \frac{\alpha_s(Q^2)}{2\pi}\int_x^1 \frac{d\xi}{\xi}\left[\sum_j q_j(\xi,Q^2)P_{gq_j}(\frac{x}{\xi}) + g(\xi,Q^2)P_{gg}(\frac{x}{\xi})\right]. \tag{2.11}$$

The analytical expressions for the splitting functions are known up to $\mathcal{O}(\alpha_s^2)$. They can be found in [32] together with more details about the PDFs.

Other approaches to QCD evolution like BFKL [38] are available. In the BFKL approach an evolution in x instead of Q^2 is performed on the gluon distribution only. Yet another approach is CCFM [39], where the parton evolution is treated in both x and Q^2 and relies on a different scheme of parton emission for quarks and gluons. So far, no convincing experimental evidence that BFKL or CCFM dynamics being better than DGLAP were shown.

2.5 Factorisation theorem

The PDFs themselves are not direct experimental observables. The factorisation theorem [40, 41] provides the connection between the measured cross sections of lepton-hadron DIS processes described by the structure functions and the PDFs, f_i. Accordingly, the proton structure function $F_2(x, Q^2)$ can be written as:

$$F_2(x, Q^2) = \sum_i \int_x^1 C_i(z, \frac{Q^2}{\mu_R^2}, \frac{\mu_F^2}{\mu_R^2}, \alpha_s(\mu_R)) f_i(z, \mu_F, \mu_R) \frac{dz}{z}, \tag{2.12}$$

where i runs over all partons, $q, \bar{q}, g$. Here C_i are the matrix elements of the hard parton-level process calculable in QCD. The μ_R is the renormalization scale (see Section 1.2.1) and μ_F is called factorisation scale. The PDFs, f_i, are also dependent on the scales μ_R and μ_R in this ansatz. The factorisation theorem presents the cross section of an *ep* process as a convolution of partially non-perturbative PDFs at long distances and perturbative partonic cross sections at short-distances.

The matrix elements (coefficient functions) C_i have expansions in powers of $\alpha_s(\mu_R)$ in the pQCD approach. The μ_F represents the scale at which the short and long distance processes can be separated. As in the case of renormalization, the measured cross sections should not depend on the choice of μ_F. That leads to the set of differential equations:

$$\frac{dC_i}{d \log \mu_F^2} = 0. \tag{2.13}$$

They can be solved iteratively. The solution for the C_1 is

$$C_1(\mu_R, \mu_F, \alpha_s) = C_1(1, \mu_R) + P_0 \int_x^1 C_0 \log \frac{Q^2}{\mu_F^2} f_i(z, \mu_F, \mu_R) \frac{dz}{z}, \tag{2.14}$$

where P_0 denotes the QCD evolution splitting function at leading order in α_s.

Due to the truncation of the perturbative chain the C_i will remain dependent on the factorisation scale. Therefore the choice of μ_F should be made carefully. Often, μ_F is set to be equal to μ_R, but the possibility of separating those two scales is also an option as they refer to different aspects of the calculation.

2.6 HERAPDF

While the Q^2 expansion is calculable through the DGLAP evolution, the x dependence of the PDFs must be measured. Different physics processes can constrain different parts of the PDFs at some reference scale. Thus, the inclusive DIS neutral- and charge-current cross sections [42, 43], are especially sensitive to the gluon content of the proton as measured at HERA. Also TEVATRON or LHC experiments perform $W^{\pm}$ asymmetry measurements [44] that can tighten up the uncertainties of the ratio of u to d quark content. Inclusive jet cross section data, also measured at HERA [45], allow to embed the strong coupling constant into the PDF determination.

There are several collaborations fitting the available data to extract PDFs: ABKM [46], CTEQ [47], MSTW [48], NNPDF [49]. The collaborations make different choices in the selection of data sets and in the way PDFs are treated within the theory. The details are beyond the scope of this discussion.

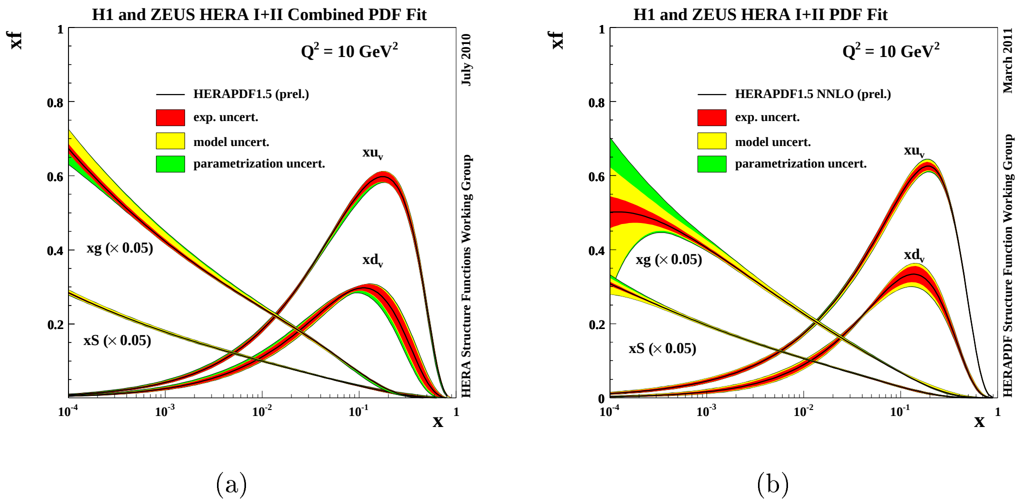

Figure 2.5: Parton distribution from HERAPDF 1.5 [50] as a function of x for given value of $Q^2 = 10\,\mathrm{GeV}^2$ at (a) NLO and b) NNLO. The sea and gluon PDFs are scaled by 0.05. Different contributions to the PDFs uncertainties are marked with colours.

The HERA experiments (see Chapter 4) provide their own set of PDFs called HERAPDF [50, 28]. These are based on HERA data only, obtained by the ZEUS and H1 collaborations. The PDFs are parametrised at the starting scale $Q_0^2 = 1.9$ GeV^2 chosen to be below the charm mass threshold as:

$$xg(x) = A_g x^{B_g}(1-x)^{C_g}, \tag{2.15}$$
$$xu_v(x) = A_{u_v} x^{B_{u_v}}(1-x)^{C_{u_v}}(1+E_{u_v}x^2), \tag{2.16}$$
$$xd_v(x) = A_{d_v} x^{B_{d_v}}(1-x)^{C_{d_v}}, \tag{2.17}$$
$$x\bar{U}(x) = A_{\bar{U}} x^{B_{\bar{U}}}(1-x)^{C_{\bar{U}}}, \tag{2.18}$$
$$x\bar{D}(x) = A_{\bar{D}} x^{B_{\bar{D}}}(1-x)^{C_{\bar{D}}}, \tag{2.19}$$

where $xg(x)$ represents the gluon distribution, $xu_v(x)$, $xd_v(x)$ are the valence up and down quark distributions, respectively, and $x\bar{U}(x)$, $x\bar{D}(x)$ correspond to the sea quark distributions. The A_{g,u_v,d_v} are the normalisation parameters constrained by the quark number and momentum sum-rules, the parameters B_{g,u_v,d_v} and C_{g,u_v,d_v} are set to be free. For the sea distribution only one parameter is set $B = B_{\bar{U}} = B_{\bar{D}}$. The contribution from strange sea quarks is set to be a fraction f_s of d_v-sea as: $x\bar{s} = f_s\bar{D}$. At $Q^2 > m_c^2$ and $Q^2 > m_b^2$ the sea distributions are $x\bar{U} = x\bar{u} + x\bar{c}$ and $x\bar{D} = x\bar{d} + x\bar{u}$ respectively taking into account heavy flavour contributions. The full sea parton distribution is denoted as $xS = 2x(\bar{U} + \bar{D})$. The strong coupling constant is set to $\alpha_s(M_{Z^0}) = 0.1176$ and the heavy flavour quark pole masses are set to $m_c = 1.4\,\mathrm{GeV}$ and $m_b = 4.75\,\mathrm{GeV}$.

During the fit PDFs are evolved using the DGLAP equations (2.11),(2.11) in the $\overline{MS}$ scheme setting $\mu_R = \mu_F = Q$. Figure 2.5 shows the obtained Parton Distributions in the framework of HERAPDF 1.5. There it is visible that the valence quarks are accessible at high values of x, while the gluon and the sea contributions are dominant at low x.

Chapter 3

Heavy flavour

This chapter contains the description of heavy flavour, c and b, production in ep collisions through neutral-current interactions. The main emphasis is placed on charm quark production, as it is the main subject of this thesis. The most relevant theoretical aspects of the heavy quark treatment in QCD are also covered.

3.1 Heavy flavour production in $e^{\pm}p$ collisions

In electron-proton collisions the charm and beauty quarks are mostly created by the boson-gluon fusion process (BGF), where the virtual exchange photon interacts with a gluon in the proton producing a heavy quark-anti-quark pair. Therefore charm production measurements are sensitive to the gluon content of the proton. The Feynman diagram of the BGF process is shown in Figure 3.1(a) with an example of $c\bar{c}$ production. The production of heavy flavour quarks, like c and b in BGF, is only possible when the centre-of-mass energy of the photon-gluon system, $\hat{s}$, exceeds the squared mass of the $q\bar{q}$ pair:

$$\hat{s} = (\gamma^* g)^2 > 4m_q^2. \tag{3.1}$$

At HERA collider energies, charm quark production is strongly favoured over beauty due to the large mass of the beauty quark, $m_b \approx 4.75\,\mathrm{GeV}$. In either case, m_q introduce a hard scale that allows perturbative techniques to be applied down to the production threshold. In DIS interactions, yet another hard scale is introduced by Q^2. That can lead to complications of the theoretical predictions due to $\log \frac{Q^2}{m_q^2}$ terms. This is referred to as the multiple hard scale problem. In this respect, the measurement of heavy flavour production provides a stress test for QCD. It was shown that the charm contribution to the inclusive structure function F_2 is sizeable, from 10 to 30 % [51], and therefore needs to be properly treated.

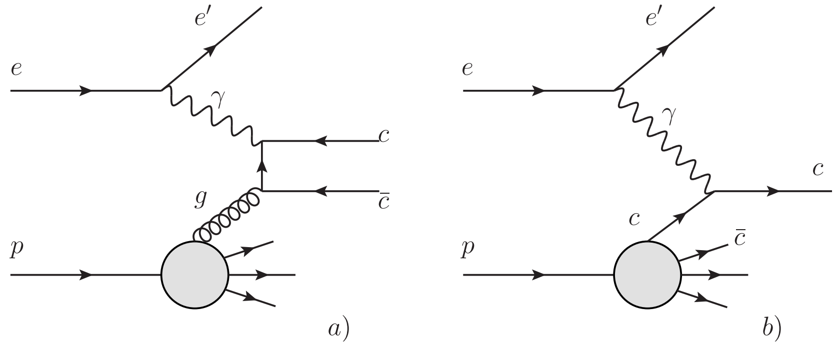

Figure 3.1: Feynman diagrams of charm production in *ep* collisions via a) boson-gluon fusion and b) via photon coupling to a sea-type charm quark in the proton.

Heavy flavour photoproduction. Processes are called photoproduction (PHP) when the virtuality of the exchanged photon is close to zero, $Q^2 \approx 0\,\mathrm{GeV}^2$. Then it is usually said that the exchange was done via a quasi-real photon, or photon-proton collisions took place. Typical diagrams for heavy quark production in such kind of interactions are shown in Figure 3.2. There are two components of PHP-like processes: direct photoproduction when the incoming photon has a point-like structure and resolved photoproduction when the photon itself shows an intrinsic hadronic structure via fluctuation into a quark-anti-quark pair and gluons.

The direct processes are calculable via the perturbative QCD approach, while the resolved component calculations are done via the convolution of non-perturbation photon PDFs [52] with matrix elements of the partonic cross sections.

Heavy flavour fragmentation. As quarks are confined, studies of heavy quarks are possible through the measurement of hadrons containing heavy flavours, like D

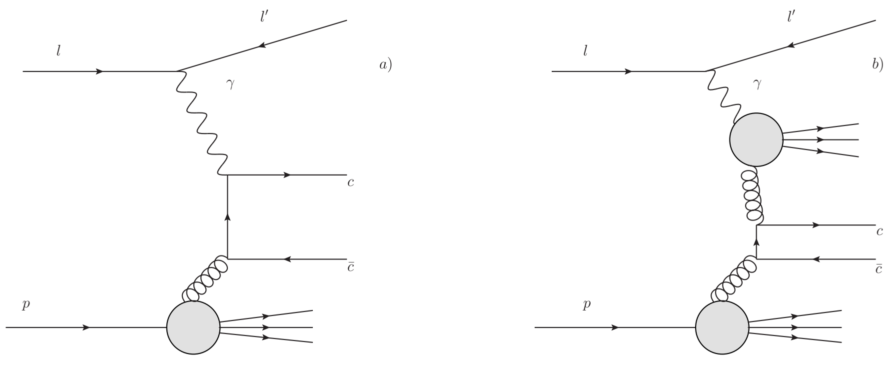

Figure 3.2: Feynman diagrams of the photoproduction processes: a) direct and b) resolved components.

or B mesons. The hadronisation process of the transition of a charm quark to a D meson is not calculable with pQCD and should be extracted from experiment [53]. In the hadronisation process two main notions are introduced. One is called fragmentation fraction, $f(c \to \mathrm{H})$, that characterises the probability of a quark to hadronise into a particular colourless object, H. The other is the fragmentation function or probability density distribution, $D(z)$, where z is the fraction of energy of the parent quark, q, transferred to the daughter hadron H. There are various models of fragmentation. The ones that often being used in the theoretical calculations of heavy flavour production cross sections are:

- Peterson fragmentation [54]:

$$D(z) \propto z(1 - \frac{1}{z} - \frac{\epsilon}{1-z})^{-2}, \tag{3.2}$$

  where ϵ is a measurable parameter.

- Bowler fragmentation [55]:

$$D(z) \propto \frac{1}{z^{1+r_q b m_q^2}}(1-z)^a e^{\frac{-bm_T^2}{z}}, \tag{3.3}$$

  where $m_T^2 = (p_T^{rel})^2 + m^2$ is the transverse mass of the hadron and p_T^{rel} is the transverse momentum of the hadron relative to the mother quark. Here a and b are the measurable parameters.

- Kartvelishvili fragmentation [56]:

$$D(z) \propto z^{\alpha}(1-z), \tag{3.4}$$

  with α being the measurable parameter.

3.2 Treatment of heavy flavour production in QCD

There are several ways to embed heavy flavour quark production into pQCD calculations. Among them:

- **Fixed Flavour Number Scheme** (FFNS) [57]. In this approach heavy quarks, c and b, are always treated as massive fermions. They are produced in the hard interaction process and the proton content is fixed by the light flavours and gluons. For the c-quark the light flavours are u, d, s, while for b-quark production, the c-quark can also be treated as light. For the perturbative series of the calculations in this approach complications arise from the presence of multiple hard scales. Thus at very high Q^2, in higher orders of the α_s

perturbative chain, terms proportional to $\log \frac{Q^2}{m_c^2}$ can become large. Therefore, this scheme is expected to be most precise at $Q^2 \approx m_{c,b}^2$. In practice, the scheme works in the whole HERA kinematic region.

- **Variable Flavour Number Scheme** (VFNS) [58] In this scheme, in order to sum part of these large logs, $\log \frac{Q^2}{m_{c,b}^2}$, the heavy quark is allowed to be a parton in the proton. Then the PDFs satisfy the renormalization group (DGLAP) equations in the same way as the light flavour partons.

- **Zero Mass Variable Flavour Number Scheme** (ZM-VFNS) [59]. This scheme treats the heavy flavours as infinitely massive partons below the threshold $m_{c,b}^2$, and totally massless above the threshold, $Q^2 > m_{c,b}^2$. It means that all coefficient functions, C_i (see Chapter 2) of the perturbative expansion are coupled directly to the charm quark, that is being "turned on" at the threshold. The evolution also begins at the threshold and the number of flavours in the C_i and the running coupling constant increases by one to $n_f + 1$ discontinuously at the threshold. Thus, the scheme works at large Q^2, while for the threshold regions has incorrect behaviour.

- **General Mass Variable Flavour Number Scheme** (GM-VFNS) [60]. This approach is an interpolation between the FFNS and ZM-VFNS. The formalism of FFNS is kept for low values of Q^2, while for high Q^2 the ZM-VFNS is used. According to this, the number of active flavours changes with Q^2 and therefore a careful treatment of the transition region is necessary, which introduces scheme dependent ambiguities.

3.3 D^* mesons

Heavy flavours can be studied through the reconstruction of heavy quark mesons. For the analysis of this thesis charm quarks were tagged by the reconstruction of $D^{*\pm}$ mesons with invariant mass of $2010.38 \pm 0.13\,\mathrm{MeV}$ [10]. There are three decay modes of $D^{*\pm}$ mesons:

$$D^{*+} \to D^0\pi^+ \qquad B = 67.7 \pm 0.5\,\% \tag{3.5}$$
$$D^{*+} \to D^+\pi^0 \qquad B = 30.7 \pm 0.5\,\% \tag{3.6}$$
$$D^{*+} \to D^+\gamma \qquad B = 1.6 \pm 0.4\,\%, \tag{3.7}$$

where B denotes the probability of a particular decay mode. For the presented studies the D^{*+} mesons and their charge conjugates were reconstructed from the decay channel (3.5) with a subsequent decay of $D^0 \to K^-\pi^+$. The probability of the latter decay is $(3.88 \pm 0.05)\,\%$. Thus, the branching ratio of the full decay chain

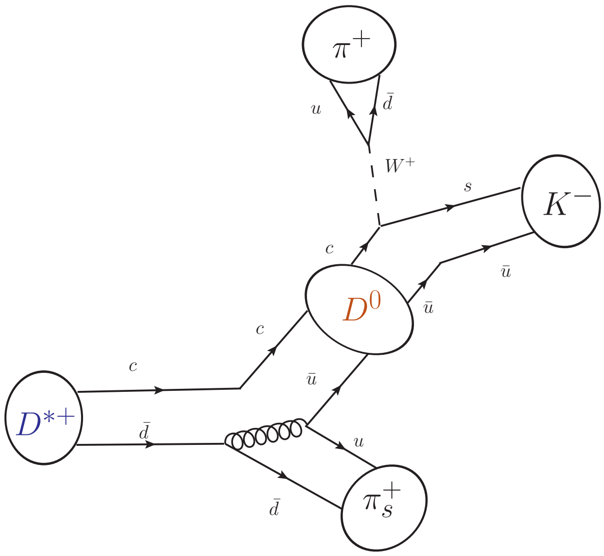

Figure 3.3: Quark level diagram of D^{*+} meson decay to D^0 and π^+ with a subsequent decay of D^0 to $K^-\pi^+$.

is $(2.627 \pm 0.053)\,\%$. The quark level diagram of the reconstructed decay channel is shown in Figure 3.3. The D^{*+} decays strongly into a D^0 and the latter decays to a Kaon and pion through the weak interaction. Thus the life time of D^* mesons is very short ($\sim 10^{-21}$ s), while the life time of D^0 is about 10^{-13}s. The decay of the D^{*-} can be deduced from the same diagram by replacing quarks by the corresponding anti-quarks. As the masses of D^* and D^0 mesons are very close, the pion of the D^* decay is often called the "slow" pion because the relative fraction of momentum carried by this particle is small.

There were several previous measurements of $D^{*\pm}$ production at HERA. Figure 3.4 shows the measured differential cross section of $D^{*\pm}$ meson production in deep-inelastic scattering at HERA from the previous ZEUS measurement [61], as a function of the exchanged photon virtuality, Q^2, Bjorken x, transverse momentum, $p_T^{D^*}$ pseudorapidity of D^*, η^{D^*}. The measurements were performed on HERA I data.

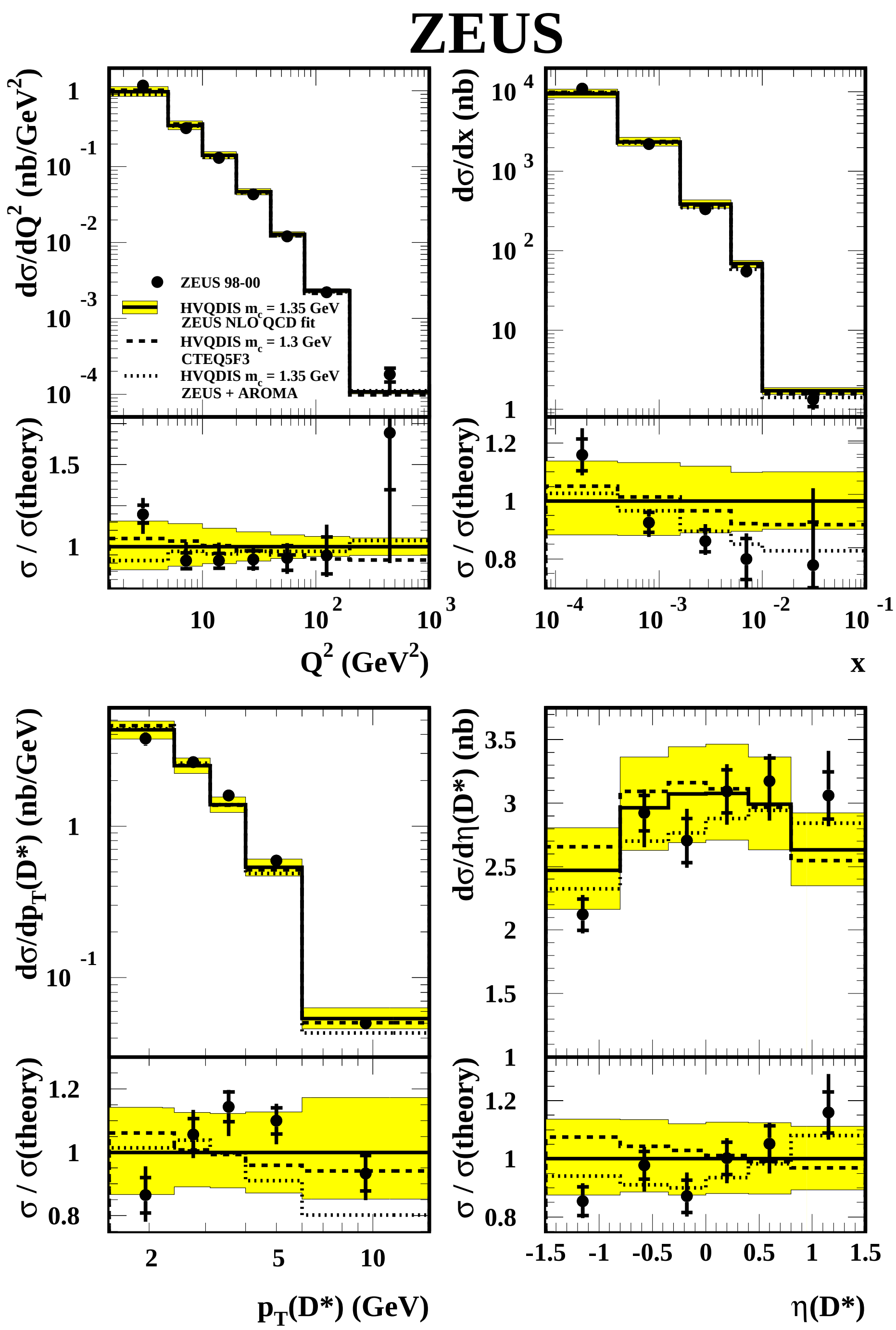

Figure 3.4: Differential cross sections of $D^{*\pm}$ meson production in DIS as a function of Q^2, x, $p_T^{D^*}$ and η^{D^*} (black points). The inner error bars show the statistical uncertainty and the outer error bars correspond to the statistical and systematic uncertainties added in quadratures. Predictions from NLO QCD are shown with the solid line. The colour band corresponds to the uncertainty of the predictions.

Chapter 4

Experimental setup

This chapter contains a brief description of the HERA accelerator and the ZEUS detector. Emphasis is placed on the most relevant components of the detector that were used for the measurements discussed in this thesis.

4.1 HERA collider

The Hadron Electron Ring Accelerator (HERA) [62] was so far the only electron-proton collider in the world. It was in operation from 1992 till 2007 and located in a tunnel 15 to 30 meters underground in Hamburg. The ring had a circumference

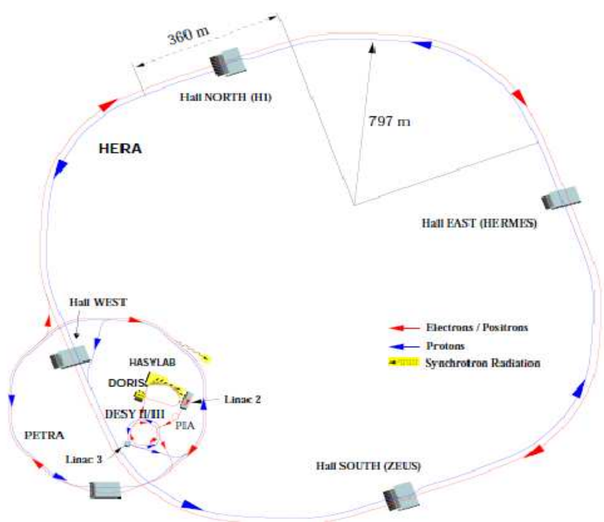

Figure 4.1: Schematic overview of the HERA accelerator facility at DESY.

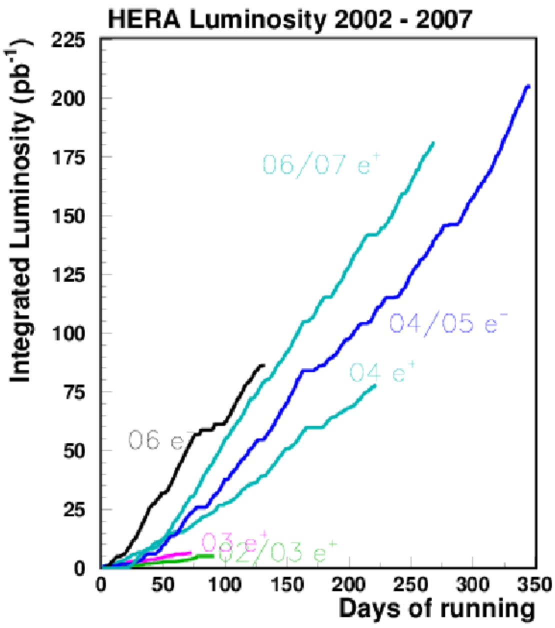

Figure 4.2: Integrated luminosity for different data taking periods for HERA II.

of 6.3 km. Electrons or positrons[1] with the energy of 27.5 GeV were collided with protons of the energy 920 GeV (820 GeV before 1998). Electrons, e, and protons, p, had separate storage rings and were injected into HERA from the pre-accelerator system at energies $E_e = 12$ GeV and $E_p = 40$ GeV, see Figure 4.1. Protons were held on the circular orbit using superconducting magnets [63] operating at a temperature of 4.4 K with a magnetic field strength of B=4.68 T. For the electron beam nominal conducting dipole magnets with B = 0.16 T were used. Colliding particles were grouped in bunches with a time distance between two bunches of 96 ns and a space distance of 30 m. During nominal operation around 220 bunches were circulating in the storage rings. Electrons and protons were collided at two experimental halls where the general purpose detectors H1 and ZEUS were installed. In addition, the HERMES experiment was taking data from collisions of the electron beam with a gas target to study the spin structure of the nucleons. Another experiment HERA-B directed the proton beam on a carbon, tungsten or titanium target with the goal to study heavy flavour physics.

There were two main data taking periods during the HERA operation: HERA I (1992-2000) [64] and HERA II (2002-2007). For the latter, detector upgrades were performed [65] and spin rotators for the electron beam were installed, introducing a longitudinal polarisation of 40 % on average. Figure 4.2 shows the integrated lumi-

[1] From here on, the lepton beam is referred to as electron, while both e^-p and e^+p collisions are meant.

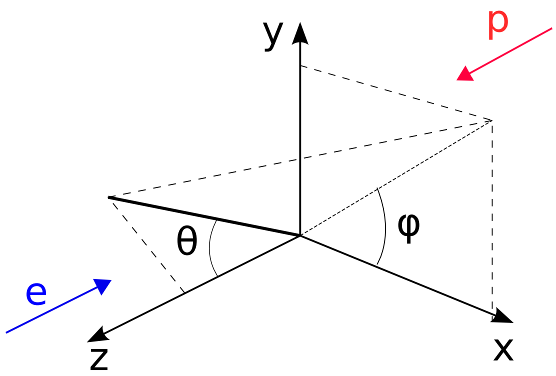

Figure 4.3: ZEUS coordinate system. Arrows from the left and from the right show the direction of electron and proton flight. The X axis is pointing to the centre of the HERA storage ring.

nosity HERA has delivered for different sub-periods at HERA II. Overall 0.5 fb^{-1} of integrated luminosity per experiment was recorded. During the last few months of operation, the proton beam energy was lowered to 575 GeV and 460 GeV (Medium and Low Energy Runs). During the years 2003–2004 and 2006–2007 a positron beam was used and the data sub-periods are called 0304p, 0607p, MER, LER, respectively. In the years 2005 and 2006 the electron beam was used with sub-period names 05e, 06e. The measurements presented in this work were done on the HERA II data.

4.2 ZEUS detector

The ZEUS detector [66] was located in the the south hall of the HERA tunnel. The ZEUS coordinate system, Figure 4.3, is a Cartesian right-handed system with the origin at the ep Interaction Point (IP). The x axis is pointing right to the centre of the accelerator ring, the y axis pointing upwards and the z axis is pointing in the proton beam direction. In spherical coordinates the radial distance is defined as usual. The azimuthal angle, ϕ, is the angle between the projection of a vector into the XY plain and the x axis. The polar angle, θ, is the angle between a vector and the z axis. The ZEUS detector has a full coverage of the azimuthal angle.

The differences between electron and proton beam energies resulted in a large boost of the centre-of-mass system in the direction of the proton beam and a large forward-backward asymmetry of the particle production. Therefore, the ZEUS detector had more sensitive material in the forward region. The terms forward (backward) region denote the positive (negative) z direction. At ZEUS the Lorentz-invariant kinematic variable of pseudo-rapidity is defined as $\eta = -\ln(\tan\frac{\theta}{2})$ and the transverse momentum is defined as $p_T = \sqrt{p_x^2 + p_y^2}$.

The ZEUS detector in the XY projection is depicted in Figure 4.4 and in the XZ

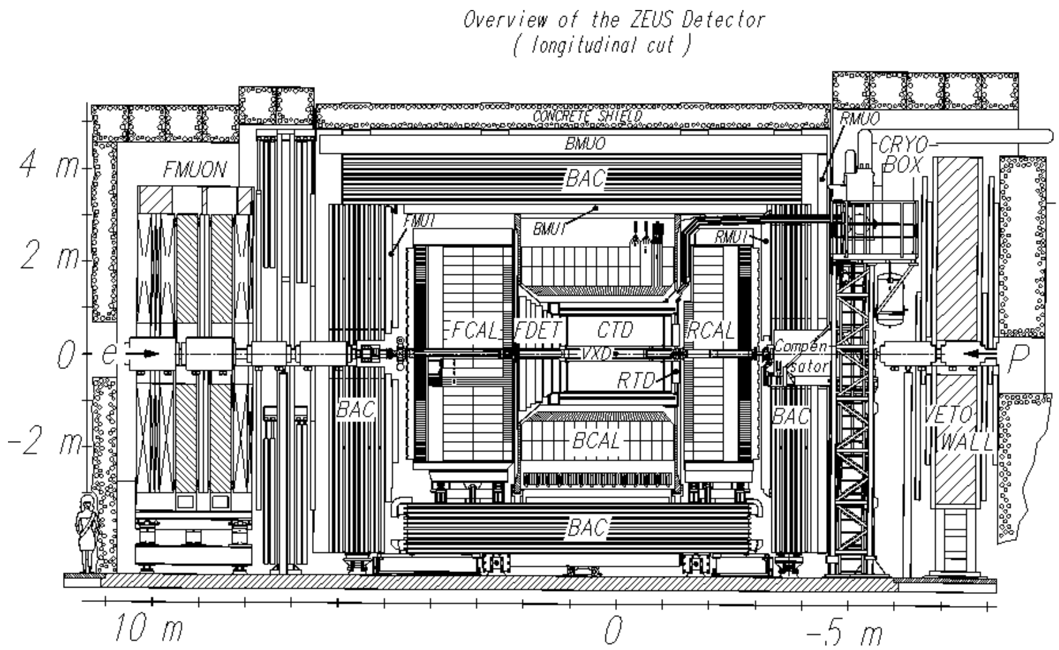

Figure 4.4: ZEUS detector projection to XZ plane.

projection in Figure 4.5[2]. The main components starting from the most inner part were:

- Micro-Vertex Detector (MVD), see Section 4.2.1.1. The silicon strip detector was mounted[3] during the luminosity upgrade shutdown in order to access the life-time information of the short-living particles and to improve the tracking resolution with respect to HERA I.

- Central Tracking Detector (CTD), see Section 4.2.1.2. A cylindrical drift chamber enclosing the MVD and serving for the measurement of charged tracks.

- Forward Tracking Detector (STT), see Section 4.2.1.3. A straw tube drift chamber was installed to measure tracks in the forward region not accessible by the CTD.

- Solenoid [67]. A magnet with the field strength of 1.43 T that was surrounding the trackers allowing track momentum measurements.

- The Uranium Calorimeter (CAL), see Section 4.2.2, that consisted of three different parts: Rear (RCAL), Barrel (BCAL) and Forward (FCAL) calorimeters with additional devices for a more precise reconstruction of the position

[2] The pictures show the ZEUS detector configuration for the HERA I data taking period.
[3] Instead of VXD in Figures 4.5 and 4.4.

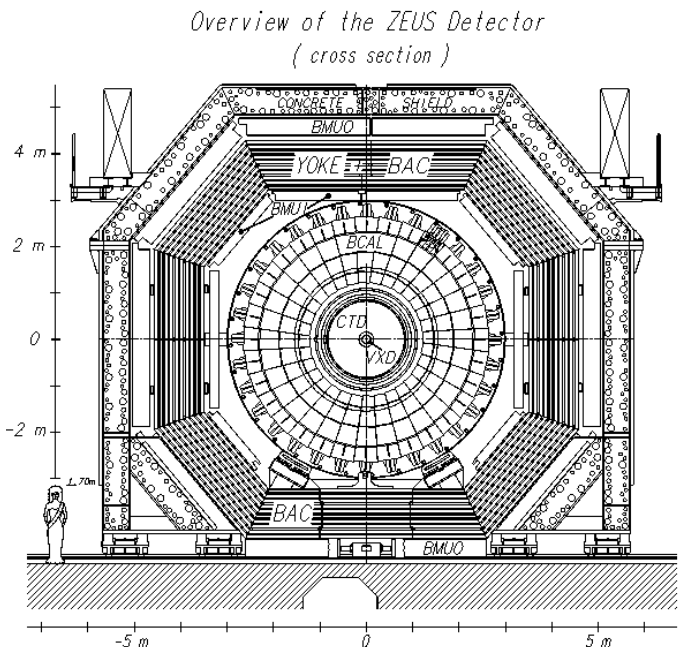

Figure 4.5: ZEUS detector projection to XY plane.

of the scattered electron Hadron Electron Separator and Strip Rear Tracking Detector.

- The iron yoke surrounded CAL and served as a return path for the magnetic field. The yoke was equipped with proportional counters, thus providing the possibility to measure the energies of particles not stopped in the CAL. This part of the detector is referred to as Backing Calorimeter (BAC).

- Muon chambers [68]. Specially dedicated detectors placed inside and outside the BAC.

- The VETO wall [69] was situated at $z = -7.5\,\mathrm{m}$. Its main purpose was to protect the central detector against particles from the beam halo accompanying the proton bunches by absorbing the background particles.

- The C5 counter [70, 71] was mounted at $z = 1.2\,\mathrm{m}$ and consisted of 2×2 scintillator layers interleaved with layers of tungsten. It was used to monitor beam-gas interactions from electron or proton beams, to measure bunch arriving times and to determine the interaction position.

- Luminosity monitors, see Section 4.2.3.

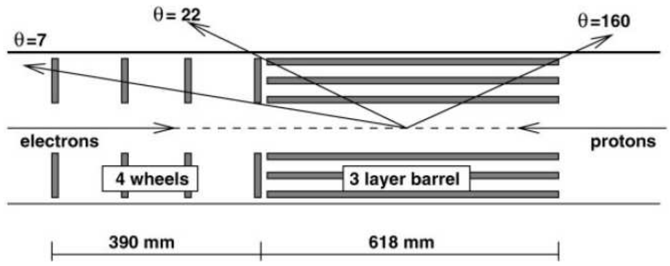

Figure 4.6: ZEUS Micro-vertex detector layout along the beam pipe.

4.2.1 Tracking system

4.2.1.1 MVD

The Micro-vertex detector [72] was installed during the upgrade shutdown in order to improve and extend the existing tracking system. Thus, making possible reconstruction of signatures from long-living particles with a life time $\tau \gtrsim 10^{-13}$ s. The position resolution was less than $20\,\mu$m. The MVD was composed of single-sided silicon strip sensors consisting of 320 μm of n-type material with $20\,\mu$m pitch p^+ strips implanted on top. More technical details can be found in [73].

When a charged particle passes through the sensitive area, electron-hole pairs are generated in the n-type bulk. The holes drift to the p-type strips which are maintained at a negative potential. Only every sixth strip was read out to minimise the number of readout channels.

The MVD consisted of a forward (FMVD, proton direction) and a barrel (BMVD, central) section (Figure 4.6). The barrel section was about 65 cm long and consisted of three layers of silicon strip sensors arranged in cylindrical planes surrounding the interaction point and in planar wheels in the forward region. The size of the MVD was dictated by the dimensions of the inner wall of the CTD that had a diameter of 32.4 cm. An example of a barrel module is depicted in Figure 4.7(b). It consisted of two (6.42×6.42) cm^2 sensors of silicon glued together side-by-side. The strips in one sensor were parallel to the beam line and those in the other were perpendicular. The BMVD modules were organised in 30 ladders and arranged in three cylindrical layers, see Figure 4.7(a) (most inner layers had fewer ladders due to the elliptical shape of the beam pipe). The barrel part had a polar angle coverage from 20 to 160 degrees. A wheel module was made of two layers of silicon of the same type as a barrel module but had a wedge shape. One layer had strips oriented parallel to one of the long sides of the wedge while the other layer had strips tilted by 13 degrees in the opposite direction [74, 75]. The 14 FMVD modules where arranged in a wheel making all together four wheels. The FMVD covered polar angles down to seven degrees.

In summary, the MVD had a single hit resolution of $\sim 20\,\mu$m with a capability of two track separation of $200\,\mu$m and an efficiency of track reconstruction of more than 95%. However, the MVD introduced additional material, thus increasing the probability of a particle to interact hadronically with material of the tracking system (see Chapter 7.5.2).

4.2.1.2 CTD

The Central Tracking Detector (CTD) [76] was the main tool to measure the position, direction, momentum and energy loss of tracks. It was a cylindrical multi-wire drift chamber filled with a gas mixture of Ar (83%), Ethane (14%) and CO_2 (3%) and water. The CTD active volume had an inner radius of 16.2 cm and an outer radius of 79.4 cm. The longitudinal size was 203 cm with the centre at the interaction point. The polar angle coverage was $15° < \theta < 164°$.

When an incident charged particle travels through the CTD volume it ionises the gas producing electron-ion pairs. The electrons drift towards the positively charged sense wires whereas the positive ions move to the negative anodes. Through the large electric field at the surface, electrons cause further showering, thus amplifying the signal that can be measured by the readout electronics. The high magnetic field produces large deviations from radial electron drift. The CTD was designed to operate with an angle between the electron drift velocity and the electric field (the Lorentz angle) of 45° [77]. The cell structure of the CTD was adapted for this accordingly.

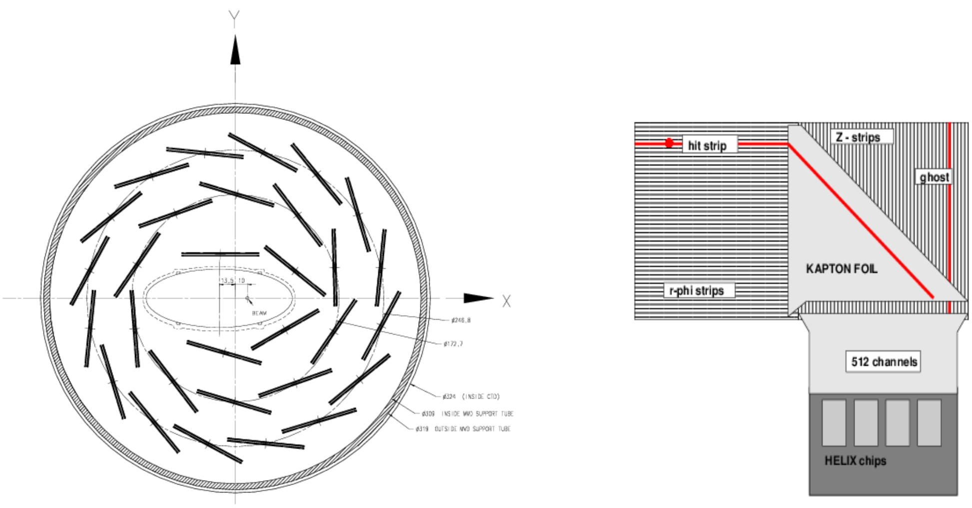

Figure 4.7: (a) Barrel part of the MVD projected to XY plane and (b) single MVD detector module.

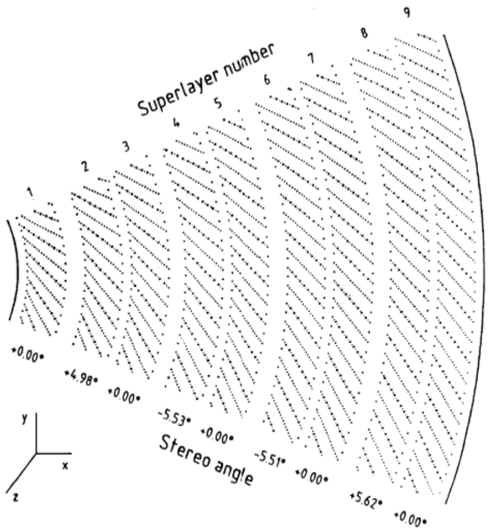

Figure 4.8: ZEUS Central Tracking detector octant.

The CTD wires were arranged into nine concentric super-layers (SL) numbered consecutively from the inside out. The odd-numbered SL have sense wires running parallel to the z axis (axial SL) while those in the even-numbered super-layers have a 5 °stereo angle inclination (stereo SL), see Figure 4.8. Three-dimensional information $(r,\ \phi,\ z)$ was extracted using these small angle stereo layers. In addition, super-layers 1, 3 and 5 were also instrumented with a z-by-timing system [78]. This determined the z position of a hit on one of the instrumented wires by measuring the difference in time between the arrival of the pulses at each end of the wire yielding a resolution of $\sim 4\,\text{cm}$. CTD based information was strongly used in many first level triggers where the main background rejection was done.

The combined tracking system, MVD+CTD, had a momentum resolution of

$$\frac{\sigma(p_T)}{p_T} = 0.0029 \cdot p_T \ \oplus\ 0.0081\ \oplus\ \frac{0.0012}{p_T}, \tag{4.1}$$

where the transverse momentum p_T is expressed in GeV. In Equation 4.1 the first term reflects the position resolution, whereas the second and third terms correspond to the multiple scattering effects before and after the CTD volume respectively. Details about the resolution parametrisation can be found in [79, 80].

4.2.1.3 STT

The ZEUS forward region was equipped with a gaseous drift chamber called Straw Tube Tracker (STT). The STT [81] covered the region of $5° < \theta < 25°$. The

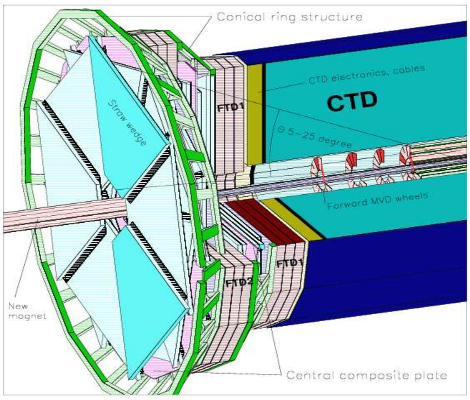

Figure 4.9: ZEUS Straw Tube Tracking detector together with CTD.

straws were approximately 7.5 mm in diameter with a length varying from 20 cm to 1 m and were arranged in wedges consisting of three layers rotated with respect to each other, to provide a three-dimensional reconstruction. Figure 4.9 shows the STT together with the other trackers. The operational gas mixture was Ar and CO_2 in the proportion 80 %:20 %. Due to the magnetic field configuration of the ZEUS solenoid, the STT delivered mainly the position information, whereas the momentum information was marginal.

4.2.2 Calorimetry system

Calorimeter [82, 83] in high energy physics is a tool to measure energies of charged and neutral particles. With a sufficient segmentation of the calorimeter some reconstruction of the position and direction of a particle can also be performed. When a particle travels through the absorbing material of a calorimeter it creates plenty of secondary particles which again provoke the creation of new particles, thus making a cascade called particle shower. This means that an incident particle leaves its energy in the detector that is converted to a measurable signal. A particle can undergo both electromagnetic (EM) and nuclear (hadronic) interactions. EM processes are more likely to occur at short passing distances, i.e. with small interaction length λ[4], whereas hadronic processes take place at larger λ. Thus, two types of particle showers are discerned.

The ZEUS calorimeter (CAL) [84] was a sampling and compensating calorimeter.

[4] The mean free path of a particle between interactions.

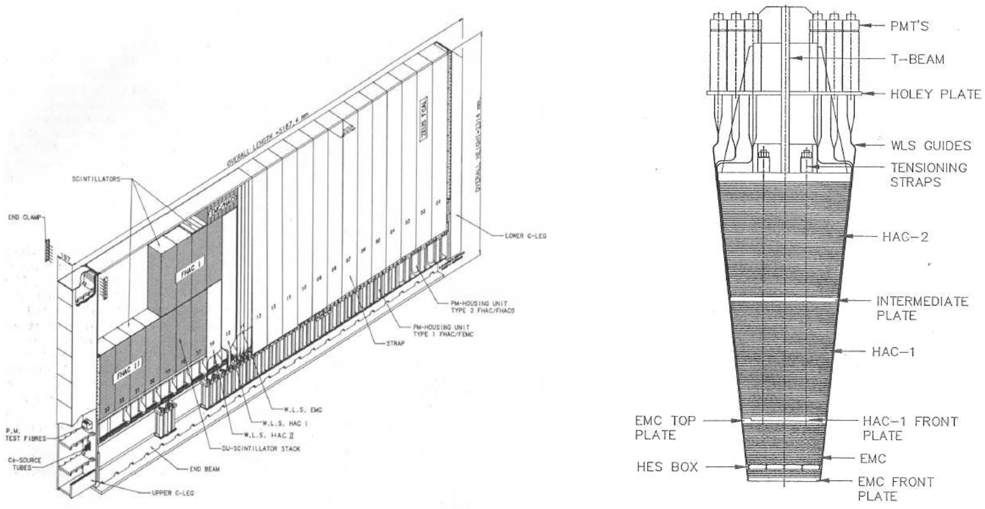

Figure 4.10: (a) Forward/Rear ZEUS calorimeter module and (b) Barrel ZEUS calorimeter module.

A single CAL module had a sandwich structure with a heavy but insensitive absorber of 3.3 mm thick depleted uranium[5], interleaved with lighter sensitive material made of an organic scintillator (SCSN-38 type) of 2.6 mm. Compensation refers to an equal response to EM and hadronic showers and was achieved by tuning the ratio of absorber to scintillator. Due to the presence of neutrinos, muons, slow neutrons or nuclear processes that did not result in a measurable signal, the ratio between measured and incident energies can be less than unity.

As was mentioned earlier in this chapter, the CAL was separated into three main parts (see Figure 4.4):

- **The FCAL** [85] with an angular coverage $2.2^\circ < \theta < 39.9^\circ$. Figure 4.10(a) shows a schematic drawing of a single FCAL module. The full FCAL consisted of 23 single modules placed vertically next to each other. One module had a width of 20 cm and a length of up to 4 m arranged in three units. The unit closest to the interaction point had a depth of $0.96\,\lambda$ and is referred as FEMC (forward electromagnetic calorimeter), with a cell size of $(10 \times 20)\,\mathrm{cm}^2$. The other two units were arranged consecutively with a depth of $3.06\,\lambda$ and referred to forward hadronic calorimeters FHAC1 and FHAC2. The FHAC had a cell size of $(20 \times 20)\,\mathrm{cm}^2$.

- **The BCAL** [86] was placed in the central region, $36.7^\circ < \theta < 129.1^\circ$, covered the full azimuthal angle and had 32 wedge-shape modules. One such

[5] 98.1% ^{238}U, 1.7% Nb, 0.2%^{235}U.

BCAL module is depicted in Figure 4.10(b). One single BCAL module had the azimuthal angle coverage of about 11° and a length of 3.3 m. The inner radius was 1.22 m and the outer 2.3 m. Like the FCAL this detector part had 3 sections. The electromagnetic unit had a depth of 0.85 λ (BEMC) and two hadronic units BHAC1 and BHAC2 had a depth of 2 λ each.

- **The RCAL** covered the region of $128.1° < \theta < 176.5°$. It had almost the same structure as FCAL with a difference in the size of the electromagnetic cell (REMC) that was $(5 \times 20)\,\mathrm{cm}^2$. The RCAL had only one hadronic unit called RHAC.

In order to improve the identification of electromagnetic objects a Hadron Electron Separator (HES) [87] was installed in the rear and forward calorimeter parts. It consisted of two layers of silicon pads with area $(3 \times 3)\,\mathrm{cm}^2$ providing a spatial resolution of about 0.9 cm for a single hit. A Small angle Rear Tracking Detector(SRTD) [88] was installed in the RCAL section covering the RCAL in the range of $162° < \theta < 176°$. The SRTD consisted of two layers of scintillator strips oriented perpendicular to each other.

Under test beam conditions, the ZEUS calorimeter had a resolution [85] of electromagnetic energy reconstruction of

$$\frac{\sigma_{el}}{E} = \frac{18\%}{\sqrt{E}}, \tag{4.2}$$

and for hadronic energy

$$\frac{\sigma_{had}}{E} = \frac{35\%}{\sqrt{E}}, \tag{4.3}$$

where E is the measured particle energy in GeV. The calorimeter was calibrated on a day-by-day basis during its operation using ^{228}U decays with an accuracy of 1 %.

4.2.3 Luminosity measurement

A precise knowledge of the luminosity is required for the precise determination of a cross section associated with any process. The value of the luminosity, L, gives the proportionality between the number of interaction per second, dR/dt, and the cross section σ:

$$dR/dt = L \times \sigma. \tag{4.4}$$

At collider experiments the luminosity needs to be monitored for each bunch crossing. At ZEUS the luminosity had been measured via investigation of the Bethe-Heitler(B-H) bremsstrahlung process [89]:

$$ep \rightarrow e'p\,\gamma. \tag{4.5}$$

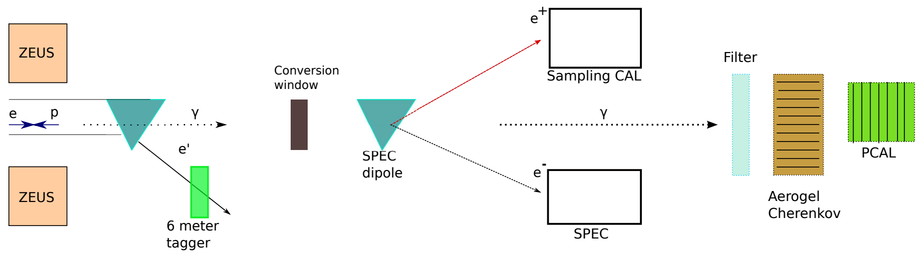

Figure 4.11: Schematic drawing of the ZEUS luminosity system at HERA II.

This process is well understood from QED, and has a high rate and an accurately calculable cross section. The luminosity was calculated as $L = R/\sigma_{\mathrm{B-H}}$, where R is the measured bremsstrahlung photon rate. During the HERA II data taking two luminosity measurement systems were in operation at ZEUS (Figure 4.11), the Luminosity Spectrometer (SPEC) [90] and the Photon Calorimeter (PCAL) [91].

The SPEC was located 100 m away from the interaction point[6] and consisted of two sampling calorimeters that were detecting electron-positron pairs from the photon conversion. The typical acceptance of the SPEC was 30 % and only 10 % of the photons were converted, therefore the detector operation was not always stable. The PCAL instead was measuring showers, rates and positions from non-converted photons. The two measurements were in agreement and by default the PCAL numbers were used for the luminosity and in the case that PCAL information was not available, the SPEC luminosity was taken instead.

4.2.4 Trigger system

The information from the ZEUS detector components was processed by a complicated data acquisition system (Figure 4.12). The main components were the trigger system [92], front-end electronics and data storage devices. Triggers played a very important role as they provided the decision on whether an event is selected to be recorded. At HERA beam collisions took place every 96 ns. The potential incoming data rate was thus 10^6 events/s. Not all of those events were produced by the physical processes scientists want to study. The main sources of background were beam-gas interactions, proton beam halo events, synchrotron radiation, cosmic-induced events etc.

The ZEUS trigger system consisted of three trigger levels. Events were analysed by a trigger level and if they passed certain trigger criteria they were passed on to the next level. With increasing level the precision as well as the complexity of the algorithms applied to the data increased. An event only was stored to disc if all

[6] Beam was already bent away at that point.

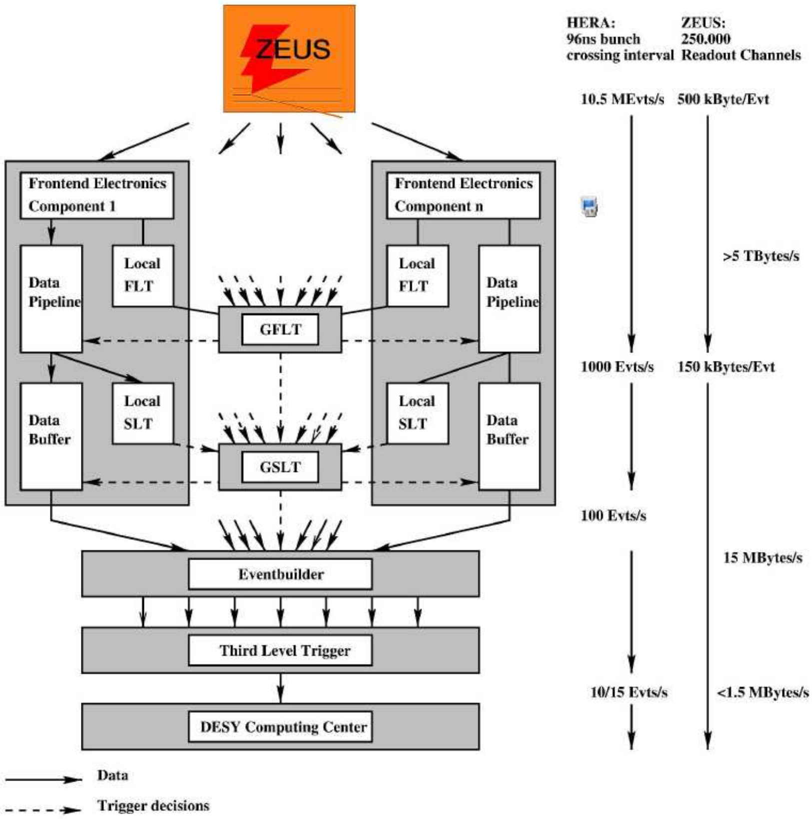

Figure 4.12: Schematic drawing of the ZEUS data acquisition system.

three levels accepted it as a candidate event of interest for physics analysis.

4.2.4.1 FLT

The First Level Trigger (FLT) [93] was a fully pipe-lined system implemented in hardware. The trigger logic and cuts were configured such that the rate of positive decisions was kept below the maximum input rate acceptable by the second level trigger, e.g. below 1 kHz. As it was not possible to take an immediate decision during the bunch crossing the data were put to a pipeline. Information from separate FLT components arrived within 2 μs after the bunch crossing and was passed to the Global FLT (GFLT), where a typical decision time was around 4 μs. The input to the FLT consisted of uncalibrated detector data only available in coarse gain resolution. Its algorithms were able to calculate only global event properties like:

- energy deposits in the EMC or HAC parts of the calorimeter cells with the specification of the position (BCAL, RCAL, FCAL);

- basic identification of clusters with energy deposits left by electrons or muons;
- track multiplicities with the implementation of different track qualities [94].

In addition, background rejection was done by using CTD z-by-timing, CAL timing and veto detector information. The first level trigger had 64 trigger slots (bits) devoted to different physical processes. The different slots had different calorimeter thresholds and tracking requirements.

4.2.4.2 SLT

The Second Level Trigger system (SLT) [95] was software-based with programmable algorithms that were running on-line on a massively parallel system of transputers. The SLT used partly calibrated detector information and simple track reconstruction algorithms. As in the case of the FLT single module, decisions were sent to the Global SLT (GSLT). The typical processing time was 7 μs. At this stage basic electron identification, track and vertex reconstruction as well as $E - p_z$ information was available. For fast tracking data processing the Global Tracking Trigger (GTT) was developed. It consisted of two parts: a "barrel algorithm" based on the track information from the CTD and MVD to obtain a global picture of the track topology in the barrel region and a "forward algorithm" that used information from forward MVD and STT. GTT improved the vertex resolution and the track finding efficiency at the ZEUS SLT level. The SLT lowered the event rate down to 100 Hz and passed data to the eventbuilder [96].

4.2.4.3 TLT

The Third Level Trigger system [97] was also purely software-based. At this stage of data processing, the full detector resolution and segmentation was reachable with complex reconstruction algorithms running on a dedicated computer farm. Plenty of trigger slots were developed to study particular physics processes, e.g. inclusive DIS, di-jet production and the production of different heavy-flavour mesons.

Chapter 5

General event reconstruction

The raw data from the detector contain an assembly of signals from the detector components. Before doing any physics analysis on the data those signals should be used to extract general characteristics of an event. In this section the basic concepts of general-purpose algorithms for the track, vertex and energy reconstruction are described. This chapter also contains the explanation of scattered electron identification that is relevant for the measurement of DIS processes.

5.1 Tracking

At ZEUS each track is parametrised [98] with five parameters, the covariance matrix and a point of reference (Figure 5.1). For the parametrisation function of the trajectory of a charged particle in a solenoidal magnetic field, a helix was chosen.

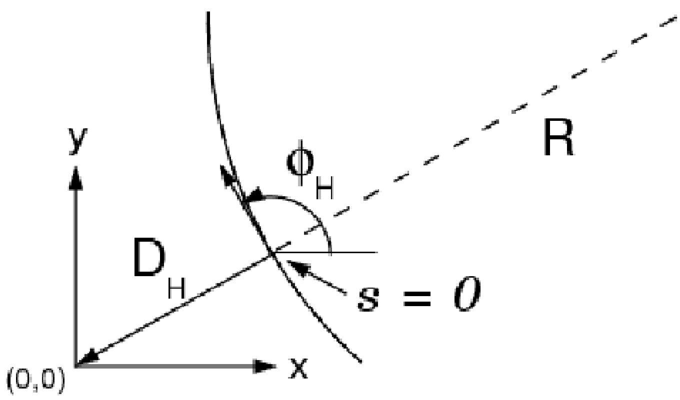

Figure 5.1: The projection of a track helix onto the XY plane.

Any point, $s(\phi)$, of this helix can be expressed as:

$$s(\phi) = -QR(\phi - \phi_H), \tag{5.1}$$

where ϕ is an outbound tangent angle in the XY plane, ϕ_H is the azimuthal angle of the direction vector of the helix at the point-of-closest approach. Q is the charge of a particle and R is the local radius. The full parametrisation consists of five parameters:

- ϕ_H,
- Q/R,
- $Q \cdot D_H$, where D_H connects the helix to the reference point $(x_{ref}, y_{ref}) = (0, 0)$,
- z_H, the z coordinate of the helix,
- $\cot(\theta) = \mathrm{tg}(\frac{\pi}{2} - \theta)$, the angle of the dip with respect to the XY plane.

The first three parameters specify a circle in the XY plane and the last two fix the location.

The track finding routine is based on the data from the three tracking detectors: STT, CTD and MVD. The procedure starts with hit reconstruction in each tracking detector separately. Then a pattern recognition is performed on the MVD+CTD+STT system, where groups of hits are combined to a seed starting from the most outer layer of CTD or STT[1]. The seed serves as a starting point. Its connection to the interaction point with the help of an approximate estimation of the momentum and charge of the track gives roughly the path and direction along which a search for further matching hits is performed. Thus, hits are continuously picked up until a road from the STT or CTD through the MVD to the interaction point is filled. Some tracks with multiply shared hits occasionally are removed. Tracks that have hits only from one of the tracking detectors are also stored and called CTD or MVD-only tracks.

As the next step, the so-called rigorous track fit [99] was performed. In this approach, inhomogeneities of the magnetic field, multiple scattering and the particle energy loss were considered. The fitting procedure was based on the Kalman filter [100] technique. Outlier hits were rejected during the track fit and hence the track quality was further improved.

After all tracks have been found, the primary and secondary[2] vertices can be reconstructed. As in the case of track reconstruction, vertex reconstruction has two

[1] For the forward region.

[2] Those that originated from the decay of long-lived particles or the interaction of particles with the detector material.

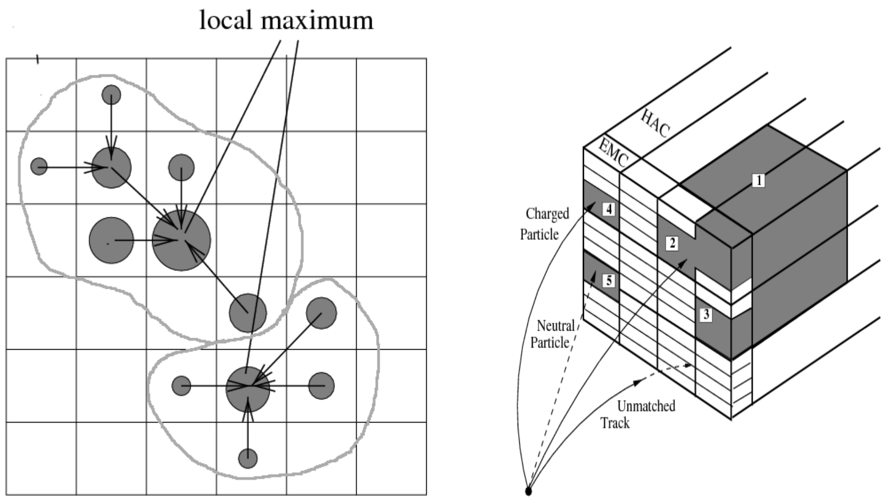

Figure 5.2: (a) Schematic drawing to illustrate the island determination procedure. Shaded circles represent the energy deposits in the calorimeter cell. The size of the circles represent the amount of energy deposit. The cell associations to the local maximum are shown with arrows. (b) Schematic drawing of EFO island with tracks matched to it.

stages: finding and fitting. Vertex finding involves the identification of the tracks belonging to the same decay vertex while the vertex fitting implies the estimation of the vertex position as well as the track parameters at the vertex. The primary vertex reconstruction initially assumes that a primary vertex lies along the proton beam-line[3]. Tracks with a common vertex are combined and a χ^2 fit is performed to determine the vertex position. The vertices with the best χ^2 are stored. After the primary vertex was found outliers are being removed and a search for secondary vertices is performed.

5.2 Energy Flow objects

In order to improve the reconstruction of the event kinematics, an algorithm that combines information from the tracking and calorimeter system was used to extract energy deposits caused by hadrons in the ZEUS detector. The method constructs Energy Flow Objects (EFOs) [101] in the following steps.

First, contiguous calorimeter cells from EMC, HAC1 and HAC2 are clustered into cell islands (Figure 5.2(a)) in order to improve the reconstruction of the CAL

[3] In addition, beam spot constraints can be used, where the beam spot is the centre of the elliptical intersection of the e and p beams determined every 2000 events.

angular information. This is performed by searching a seed cell with the highest energy deposit and then associating neighbouring cells to it to form an island.

Second, the cell islands undergo the cluster search in (θ, ϕ). This procedure starts from the most outer part of the CAL, moves inward to the beam pipe, and calculates the angular separation between the islands. As a result, 3D objects are built with the centre of the island, that is calculated by the logarithmic centre-of-gravity of the CAL shower. In the very forward FCAL region, sometimes only one island can be formed with the centre pointing along the beam pipe.

In the third step, tracks are matched to the islands. Charged tracks with a momentum $0.1 < p_T < 20\,\mathrm{GeV}$ that were fitted to a vertex and passed at least four CTD super-layers are extrapolated to the surface of the CAL taking the magnetic field into account. A match is found if the distance of the closest approach between the track and the position of the island is less than 20 cm. The track is also matched if it is located inside the island.

For the charged tracks associated to the island, CTD information was used for the energy assignment by the criteria of the best resolution. For non-matched tracks tracking information was used to derive the energy by assuming that the track comes from a charged pion particle. For the non-matched islands, only the CAL measurements are used, assuming that deposits were caused by a neutral particle. In the case that three or more tracks are matched to the island, only the CAL information is used. For the reconstruction of the energy of the scattered electron also the CAL information is used. More details can be found in [102].

In the measurements presented in this thesis EFOs were used for the reconstruction of hadronic energy.

5.3 Electron reconstruction

The measurement and identification of the scattered electron is essential for studies of Neutral-Current DIS processes. At ZEUS several software algorithms were developed to reconstruct scattered electrons called SINISTRA [103], EM and ELEC5 [104]. Each finder was optimised either for a particular phase space or for a particular process. For the current analysis electrons identified with the SINISTRA neural network finder were used.

A scattered electron passing through the calorimeter creates an electromagnetic shower. Most of its energy will be measured in the EMC cells with a small leakage fraction towards HAC cells. Identification starts from the search of the cell with maximum energy deposit to form a cell island with a similar approach as the one explained for EFOs in the previous section. Once islands are formed the information is passed to a neural network that performs a multi-variable analysis of the calorimeter showers and gives a probability, P, in the output. If $P = 0$ the shower was caused by hadrons and if $P = 1$ by electrons. The finder obtains a significantly smaller probability for electrons with low energy ($< 10\,\text{GeV}$) because it gets harder to disentangle electron energy deposits from hadronic ones like $\pi^{\pm}$. Also a contamination from photons misidentified as electrons can take place. The SINISTRA neural network was optimised for electron identification in RCAL and $Q^2 \leqslant 1000\,\text{GeV}^2$, but it can be used for the BCAL also. It was trained on NC low-Q^2 data and MC samples in 1995.

In order to obtain the scattering angle θ_e of an electron candidate, the x and y coordinates of an electron energy deposit, were reconstructed using the SRTD (if an electron was inside its geometrical cover) or HES detectors. If the electron track was measured by the CTD, this information was also used for additional constraints. In the case that none of the above information was available the geometrical centre of the CAL cell was taken for the x and y coordinates. More technical details can be obtained from [105].

5.4 Reconstruction of kinematic variables

There are several methods for the experimental reconstruction of the main kinematic variables for the DIS processes discussed in Section 2.1. After finding a candidate for the scattered electron and reconstruction of the hadronic system it is possible to deduce the variables Q^2, $x\,,y$. Different methods show different resolutions in different regions of the kinematic phase space. Therefore, it is important to figure out which of the methods is the best for this analysis.

- **The Electron method** is based on the measured electron information only and on energy and momentum conservation laws.

$$\begin{aligned} Q^2_{el} &= 2E_e E'_e(1+\cos\theta_e), \\ y_{el} &= 1 - \frac{E'_e}{2E_e}(1-\cos\theta_e), \\ x_{el} &= \frac{Q^2_{el}}{s \cdot y_{el}}. \end{aligned} \tag{5.2}$$

  Here E_e is the incoming electron(or positron) energy, E'_e and θ_e are the scattered electron energy and angle. This method relies strongly on the measurement of the electron energy and position (see Chapter 5.3) and because of the peculiarities of the ZEUS detector, those measurements are more precise in the rear region, therefore this method is optimal for low Q^2.

- **The Double-angle method** is based on the reconstruction of the angle of the scattered electron θ_{el} and the angle of the hadronic system γ_{had}. The variables are calculated as follows: the transverse momentum of the hadronic system is $P_{T,had} = \sqrt{{P_{x,had}}^2 + {P_{y,had}}^2}$ and $\delta_{had} = \sum_{had}(E_{had} - P_{z,had})$. The hadronic angle is defined as

$$\gamma_{had} = \arccos\left(\frac{P_{T,had}^2 - \delta_{had}^2}{P_{T,had}^2 + \delta_{had}^2}\right) \tag{5.3}$$

and the kinematic variables are:

$$\begin{aligned} Q^2_{DA} &= 4E_e^2 \frac{\sin\gamma_{had}\cdot(1+\cos\theta_e)}{\sin\gamma_{had}+\sin\theta_e-\sin(\gamma_{had}+\theta_e)}, \\ y_{DA} &= \frac{\sin\theta_e\cdot(1-\cos\gamma_{had})}{\sin\gamma_{had}+\sin\theta_e-\sin(\gamma_{had}+\theta_e)}, \\ x_{DA} &= \frac{E_e\cdot(\sin\gamma_{had}+\sin\theta_e+\sin(\gamma_{had}+\theta_e))}{E_p\cdot(\sin\gamma_{had}+\sin\theta_e-\sin(\gamma_{had}+\theta_e))}. \end{aligned} \tag{5.4}$$

This method has the advantage that it is not sensitive to the energy scales, but it relies on the determination of the angle of the hadronic system.

- **The Jaquet-Blondel method** is based purely on the information from the hadron system. The variables are defined as:

$$\begin{aligned} Q^2_{JB} &= \frac{P^2_{T,had}}{1-y_{JB}}, \\ y_{JB} &= \frac{\delta_{had}}{2E_e}, \\ x_{JB} &= \frac{Q^2_{JB}}{s\cdot y_{JB}}. \end{aligned} \tag{5.5}$$

This method has competitive resolution at low y, while having poor resolution for the Q^2 reconstruction. It is widely used in analyses where the scattered lepton is not detected like charged-current DIS processes or in photoproduction.

- **The Sigma method.** This method combines information from the electron and from the hadronic system:

$$\begin{aligned} Q^2_{\Sigma} &= \frac{{E'_e}^2\cdot\sin^2\theta_e}{1-y_\Sigma}, \\ y_\Sigma &= \frac{\delta_{had}}{\delta_{had}+E'_e\cdot(1-\cos\theta_e)}, \\ x_\Sigma &= \frac{{E'_e}^2\cdot\sin^2\theta_e}{s^2\cdot y_\Sigma\cdot(1-y_\Sigma)}. \end{aligned} \tag{5.6}$$

This method is a compromise in resolution and sensitivity between the electron and Jaquet-Blondel methods. One of the disadvantages is its high sensitivity to the electron energy scale.

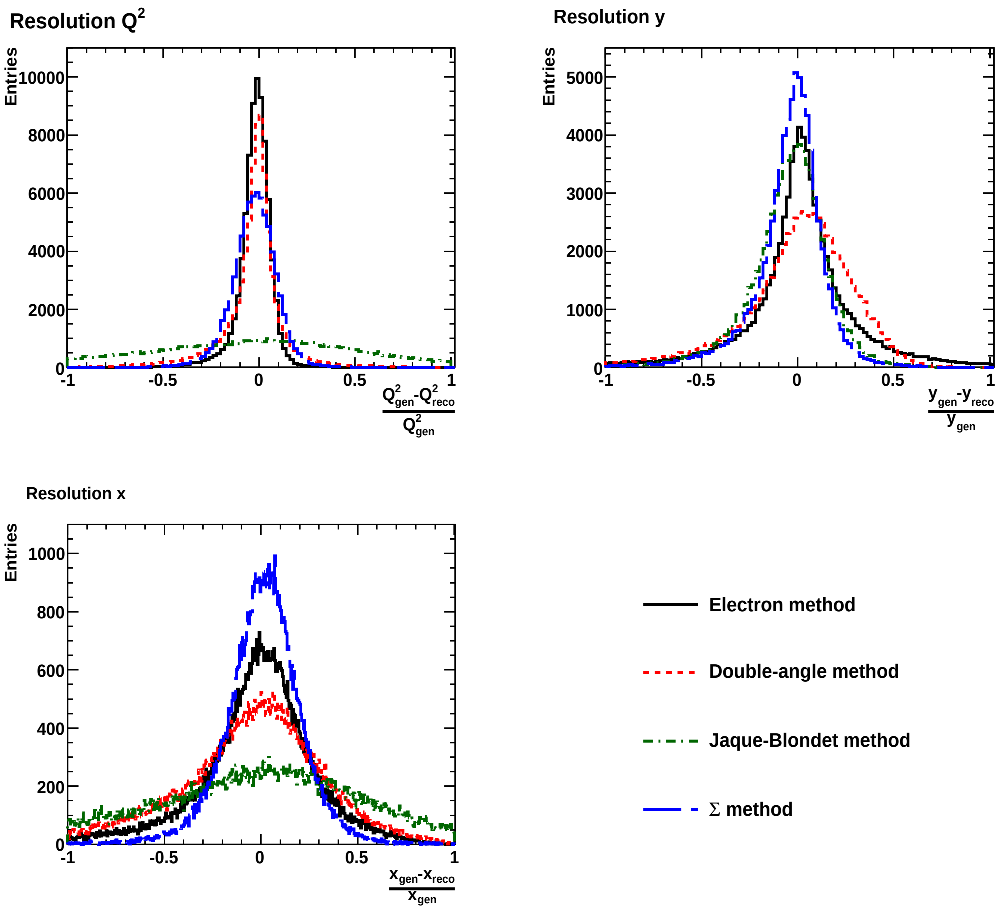

Figure 5.3: Resolutions for the DIS kinematic variables in the kinematic range of $5 < Q^2 < 1000\,\mathrm{GeV}^2$ and $0.02 < y < 0.7$ with different reconstruction methods. The black solid line represents the Electron method, the dashed red line corresponds to the Double-angle method, the green dotted-dashed line is for the Jaquet-Blondel method and the blue long-dashed line shows the Σ method.

The decision which method to take for this analysis was based on the best resolution criteria as obtained from MC studies. The resolution is defined as

$$\sigma_v = \frac{v_{gen} - v_{reco}}{v_{gen}}, \tag{5.7}$$

where v denotes one of the Q^2, x or y variables and v_{gen} stands for the original (generated) and v_{reco} for the detector level reconstructed quantities. The resolution plots for Q^2, y and x (Figure 5.3) were derived from the DIS signal MC generated with the RAPGAP program (see Chapter 6) in the kinematic region of $5 < Q^2 < 1000\,\mathrm{GeV}^2$ and $0.02 < y < 0.7$. The variable x is not a directly measurable quantity, it is calculated with the energy of centre-of-mass constraint, $Q^2 = sxy$. The x resolution then directly depends on the Q^2 and y resolutions. The width and the mean value of the resolution distribution both serve as an input for the choice of the method. The smaller the width and the smaller the shift of the mean value from zero, the better is the method.

The Σ method was found to give optimal performance for Q^2 and y according to the criteria described above and was used in this analysis.

Chapter 6

Monte Carlo simulations

In this chapter a review of the Monte Carlo (MC) generators that were used for the measurement presented in this thesis is given. MC simulations are widely used for different purposes like: description of the detector responses, optimisation of the event selection without experimental bias, predictions for various physical processes etc.

6.1 Detector simulation

Any measurement of the cross section with any experimental tool requires the knowledge of the fraction of event rate that this tool is able to detect. This quantity is called acceptance. For this purpose in high energy physics Monte Carlo [106] simulations are used.

The simulation involves several steps. First events from ep collisions[1] are generated according to some theoretical model. Then, generated events are passed through a virtual detector and data acquisition system in order to simulate the detector response. In the end the same physical analysis is performed on the Monte Carlo data as on real experimental data. The ZEUS detector with a full description of its sub-components was simulated with GEANT3.21 [107] software by a program called MOZART. Simulation of the ZEUS trigger system in MOZART are performed for all three trigger levels, but only for the slots related to the physics analysis. At the last stage generated events are passed through the reconstruction program ZEPHYR. For more details see [108] (Chapter 4).

Events generated with Monte Carlo methods and passed through the full simulation and reconstruction chain are used to extract the detector acceptance that enters directly into the cross section definition (see Chapter 7.8). It is important that the detector response and the physical processes of the simulation reflect those

[1] or any other process

of the experimental data.

The different stages of the basic event generation are depicted in Figure 6.1. At the first stage a calculation of the leading-order matrix elements of the hard scattering process is performed. At the second stage the production of parton emissions in the initial or final state is done through parton showering (PS) according to DGLAP backward (for the initial state) and forward (for the final state) evolution (see Chapter 2). PS stops when a predefined cut-off scale is reached. At this point parton density functions enter the generation processes. At the last stage all produced partons undergo the hadronisation procedure with the constraint that energy and momentum conservation laws are fulfilled. For the hadronisation Lund string model as it implemented in PYTHIA6.2 [109] was taken.

6.2 RAPGAP

The deep-inelastic scattering heavy flavour BGF creation, see Section 2.1, was simulated with RAPGAP 3.0 [110] using massive matrix elements. QED radiation processes were taken care of by the embedded HERACLES interface in RAPGAP. Besides the direct boson-gluon fusion process (Figure 6.1), where the exchanged photon is a point-like particle, resolved processes with the photon showing hadron structure (Figure 6.2 (a)) were also considered. Thus the RAPGAP simulation of

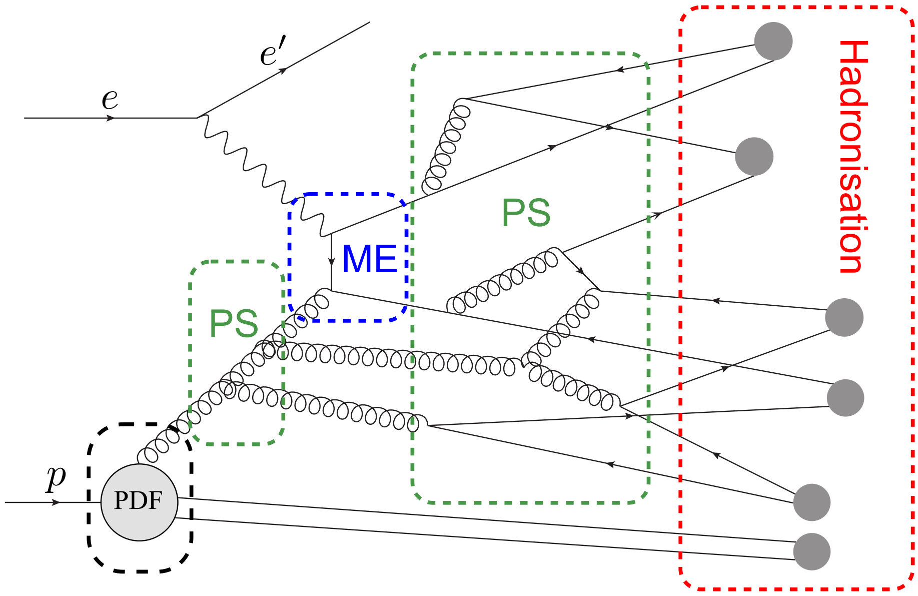

Figure 6.1: Illustration to the basic event generation stages in case of BGF in ep collisions. Different stages highlighted with dashed boxes. ME stands for matrix elements and PS for parton showering.

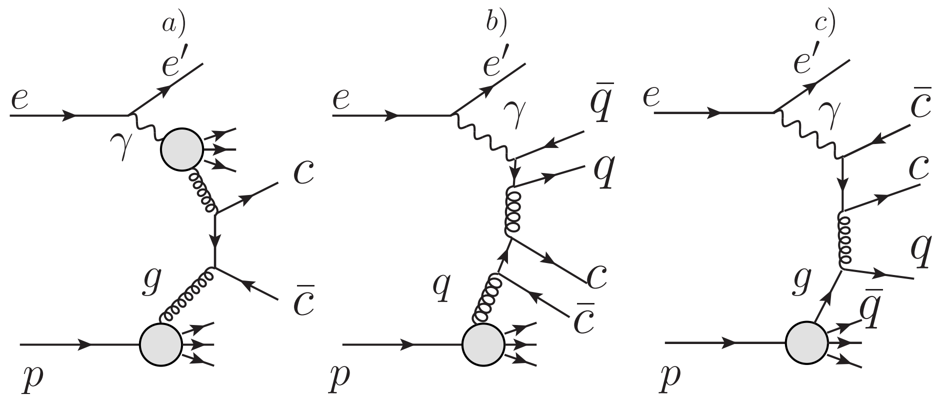

Figure 6.2: Feynman diagram of charm quark production in a) resolved, b) charm gluon excitation processes and c) charm photon excitation.

DIS processes consists of two components referred as direct and resolved. For the latter matrix elements are calculated with the massless approach. In the resolved component also heavy flavour photon and gluon excitation are included, see Figure 6.2 (b)-(c). Heavy flavour, charm and beauty, creation was simulated with quark mass parameter set to $m_c = 1.5\,\text{GeV}$ and $m_b = 4.5\,\text{GeV}$. For the proton and photon PDFs CTEQ5L [111] and GRV-G [112] were used respectively.

Diffractive open charm production was measured by ZEUS [113] and found to be $\sim 6\%$ of the total charm DIS events. Therefore for the correct description of the hadronic system the diffractive BGF processes need to be included. Diffraction itself was simulated using both Pomeron and Reggeon exchanges (Figure 6.3), that were parametrised using the H1 fit [114]. As in the case of inclusive DIS processes the resolved component was also added to the simulation. The beauty contribution to the diffractive heavy flavour creation was neglected due to small cross section. The Lund string model from Pythia6.2 [109] was used for the hadronisation of quarks to colourless objects (see Chapter 3). In this model the Bowler function was used to describe the heavy flavour quark's transverse momenta. For the light flavour quarks the Lund form of the Bowler function was used [115]. In the latter a string stretches between the oppositely coloured quark and anti-quark via gluon colour charges. Two gluons nearby in phase space act like a single gluon with equal total momentum, so the string model is infrared safe. The light flavour quarks are treated as massless.

6.3 PYTHIA

Photoproduction takes place at $Q^2 \approx 0\,\text{GeV}^2$. Due to detector resolution effects some PHP events may be reconstructed as DIS even though on the analysis side background rejection cuts were applied. For the photoproduction simulation the

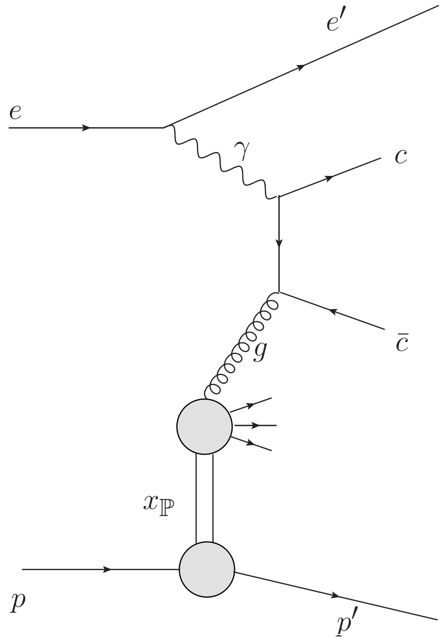

Figure 6.3: Feynman diagram of diffractive heavy flavour production in a BGF-like process via resolved Pomeron exchange.

Pythia 6.22 generator was taken. The simulation consists of the same sub-process as in the case of DIS. PHP events were generated complementary to DIS using a $Q^2 < 1.5\,\mathrm{GeV}^2$ cut.

6.4 ARIADNE

For some MC based studies like trigger efficiencies that were not related directly to the D meson reconstruction, an inclusive NC DIS sample generated with the ARIADNE [116] program was used. This generator is based on the colour dipole model [117]. In this model gluons emitted from $q\bar{q}$ pairs can be treated as radiation from the colour dipole formed between the q and $\bar{q}$. To a good approximation emission of a second softer gluon can be treated as radiation from the two independent dipoles, one formed between the q and g and one between the $\bar{q}$ and g. This process continues until all dipoles have reached a certain minimum of energy. This MC is disfavoured for the description of the heavy flavour signal because charm and beauty quarks are treated as massless. Nevertheless, ARIADNE satisfactorily describes general quantities of the event, e.g. $E - p_z$, and can be used for studies that do not require a fully correct charm signal component.

Chapter 7

Measurement of $D^{*\pm}$ meson production in DIS

This chapter covers the measurement of charm production in ep collisions at HERA in deep-inelastic processes using the $D^{*\pm}$ final state. This measurement serves as a test of pQCD due to the presence of the multiple hard scales like p_T, Q^2 and m_c. As was mentioned in Chapter 3, charm quarks are mainly produced via boson-gluon fusion.

The measurements is done via the full kinematic reconstruction of the $D^{*\pm}$ decay discussed in Chapter 3 are done. In the final state there are three charged particles, $K^{\mp}$, $\pi^{\pm}$ and $\pi_s^{\pm}$, which implies lower combinatorial background with respect to other channels. As the masses of D^* and D^0 mesons are very close, the pion of the D^* decay is often called the "slow" pion as the relative fraction of momentum carried by this particle is small. The limited phase space for "slow" pions translates into an advantage of the usage this channel as it reduces the combinatorial background. The reconstructed decay of channel is called "golden" decay channel. When the D^* is mentioned both charge states are considered.

7.1 Data and Monte Carlo samples

In this section a description of the data samples used for the measurement is given together with the final luminosity values and uncertainties. It also contains explanations of the normalization of each sub-sample and the description of the relevant MC samples.

7.1.0.4 Experimental data

Different data taking periods (see Chapter 4) had some differences in the experimental environment like the trigger setup etc. Table 7.1 contains the information

Year	$\int L$, pb^{-1}	N_{ev}, 10^6	C_L, %	δ_L, %
04p	32.4	47.5	+0.7	2.5
05e	132.9	132.2	+0.7	1.8
06e	55.1	44.2	+0.7	1.8
0607p	141.2	127.8	+1.0	1.8 (2.1[1])
04-07p	363	351.7	-	1.9

Table 7.1: Summary luminosity table of the experimental data for different periods used for the measurement of D^* meson production in DIS. The last row shows the sum after the application of the corrections listed in the 4^{th} column.

about the statistics collected during HERA II that was used in the current measurement expressed in terms of integrated luminosity (column 2). The total number of recorded events,N_{ev}, is also given. For the improvement of the luminosity values, a correction factor listed in the fourth column was applied on a sample-by-sample basis [118]. The uncertainty of the luminosity measurement (after the correction) is listed in the column number five. The full luminosity uncertainty of the data set 04-07p was calculated as a linear sum of the individual absolute uncertainties of the sub-samples, giving the resulting value of 1.9 %.

7.1.0.5 Monte Carlo samples

The MC samples used for the measurement of D^* meson production in DIS cover several processes: DIS and diffractive DIS heavy flavour creation, photoproduction heavy flavour creation. The MC was generated in such a way that it contains only signal events, thus the simulation of the light flavour contribution was not performed. Table 7.2 contains a summary of these MC samples. In order to speed up and simplify the analysis, only events containing certain heavy flavour hadrons were stored and only signal simulation was performed. D-mesons and their charge conjugates from eight decay channels were selected:

1. $D^{*+} \to D^0 (\to K^+, \pi^-)\ \pi^+$;
2. $D^{*+} \to D^0 (\to K^+, \pi^-, \pi^+, \pi^-)\ \pi^+$;
3. $D^{*+} \to D^0 (\to K_S, \pi^-, \pi^+)\ \pi^+$;
4. $D^0 \to K^+, \pi^-$;
5. $D_s^+ \to \phi^0 (\to K^+, K^-)\ \pi^+$;
6. $D^+ \to \phi^0 (\to K^+, K^-)\ \pi^+$;
7. $D^+ \to K^+, \pi^-, \pi^+$;

Process	Generator	$\int L$, pb^{-1}	Q^2, GeV^2
DIS direct $(c,\ b)$	RAPGAP 3.0	1373	$Q^2 > 1.5$
DIS resolved $(c,\ b)$	RAPGAP 3.0	1373	$Q^2 > 1.5$
Diffractive DIS direct $(c,\ b)$	RAPGAP 3.0	1640	$Q^2 > 1.5$
Diffractive DIS resolved $(c,\ b)$	RAPGAP 3.0	1640	$Q^2 > 1.5$
Photoproduction direct $(c,\ b)$	Pythia 6.22	1600	$Q^2 > 0$, full range
Photoproduction resolved $(c,\ b)$	Pythia 6.22	1600	$Q^2 > 0$, full range

Table 7.2: Summary table of MC samples used for the analysis.

8. $\Lambda_c^+ \to K^-, \pi^+, \pi^+$.

In addition, a selection of the so-called dangerous [119] backgrounds was performed. These are backgrounds which arise from other decay modes of the same D mesons and "similar" decay modes of other D mesons. The simulation of the full combinatorial background is not necessary for the present analysis, as the D^* signal extraction technique implies background subtraction. Additionally, an inclusive DIS MC sample generated with ARIADNE in the region $Q^2 > 4\,\mathrm{GeV}^2$ was used for the studies that were not related to the D meson reconstruction. The sample has approximately the same luminosity as the data.

7.2 DIS events selection

Deep-inelastic events were selected with the following requirements:

- Data collected after the run 48600 were selected. In earlier runs, the detector had very complicated and unstable trigger settings.
- At least one scattered electron identified with SINISTRA (see Section 5.3) with energy $E_e > 10\,\mathrm{GeV}$ and probability[2] $P_e > 0.9$. This ensures that the electron finder works well.
- $40 < E - p_z < 70\,\mathrm{GeV}$, where the sum $E - p_z = \sum(E_i - E_i \cdot \theta_i)$ runs over all EFO objects (see Section 5.2) and E_i is the energy deposit left in the EFO and p_z is the momentum projection on the z direction measured in the EFO. The lower boundary was selected to reject photoproduction events. The higher boundary ensures rejection of cosmic ray background events and overlapping interactions.
- The reconstructed scattered electron position is required to be inside a box of x and y of $(15 \times 15)\,\mathrm{cm}^2$. This removes the beam pipe region and some part

[2]The value of the probability is the output from the neural network finder SINISTRA.

of the inner RCAL region close to it. Additional fiducial cuts to the electron position due to the detector construction geometry are:

the Chimney cut, $\mathrm{y} > 80\,\mathrm{cm}$ and $\mathrm{x} > -10\,\mathrm{cm}$ and $\mathrm{x} < 10\,\mathrm{cm}$ and $\mathrm{z} < -150\,\mathrm{cm}$ removes a region of the top RCAL that was used for the cryogenics of the solenoid;

the Cracks cut, $\sqrt{\mathrm{x}^2 + \mathrm{y}^2} > 175\,\mathrm{cm}$ and $\mathrm{z} < -153\,\mathrm{cm}$ removes electrons detected in the region of RCAL that is partially shaded by the BCAL.

- The position of the primary vertex, $|Z_{vtx}| < 30\,\mathrm{cm}$, selects events in the nominal region of *ep* interactions, excluding so-called satellite events [120].

- Required trigger slots:

  – First-Level trigger slots. They are based on general background rejection criteria and a very preliminary scattered electron reconstruction. The FLT cuts are composed of calorimeter, CTD tracking and veto detector information. The last two FLT selection criteria can be found in [108] and only CAL-based cuts are described here as they are relevant for the data understanding improvements performed in this analysis.

    FLT 30 requires an electromagnetic energy (EMC) deposit in the RCAL outer region, $R_{emc} > 3.9\,\mathrm{GeV}$, or EMC energy inside the inner region of the RCAL to be $R^{th}_{emc} > 15\,\mathrm{GeV}$, where *th* denotes threshold. In addition, the requirement of an isolated EMC region (further denoted as ISOe, for details see Section 7.5) was present with AND logic. In order to have the correct acceptance calculation, events for which one of the FLT 30 threshold was set to infinity (mainly 0607p period) were excluded if they were triggered by FLT 30 only because this effect is not properly simulated by the MC;

    FLT 36 repeats the FLT 30 logic with the exception that $R^{th}_{emc} > 5\,\mathrm{GeV}$;

    FLT 44 requires an EMC deposit in the BCAL, $B_{emc} > 4.8\,\mathrm{GeV}$ or in the RCAL, $R_{emc} > 3.4\,\mathrm{GeV}$;

    FLT 46 takes events with $R_{emc} > 2\,\mathrm{GeV}$ or $R^{th}_{emc} > 3.7\,\mathrm{GeV}$ and ISOe;

  – Second-Level trigger slots. There was no particular SLT trigger chain selection that implies the OR logic of all SLT trigger slots that passed the FLT selection criteria and required by TLT.

  – Third-Level trigger slots:

    HFL02 (valid for all data taking periods) selects charmed hadrons in DIS with at least one TLT level reconstructed D-meson candidate. There were 17 dedicated D-meson reconstruction slots available and HFL02 uses all of them. As an example, the D^* TLT cuts were: at least 3 tracks with $p_T(K,\pi) > 0.35\,\mathrm{GeV}$ and $p_T(\pi_s) > 0.1\,\mathrm{GeV}$ and for the D^* itself $p_T > 1.35\,\mathrm{GeV}$ and $1.40 < M(K\pi) < 2.20\,\mathrm{GeV}$ and $M(K\pi\pi_s) - M(K\pi) < 0.171\,\mathrm{GeV}$.

SPP02 (valid only for 2004 and 2005) Low Q^2 DIS selection based on the information measured by calorimeter, $30 < E - p_z < 100\,\mathrm{GeV}$ and $E'_e > 4\,\mathrm{GeV}$. The position of the scattered electron candidate should lie outside a box of size $(12 \times 12)\,\mathrm{cm}^2$ in x, y;

SPP09 (valid since 2006) same as SPP02 but the box was increased to $(15 \times 15)\,\mathrm{cm}^2$;

HFL17 (valid since 2006) same as SPP02 with additional requirements of at least two TLT tracks measured in the CTD;

HPP31 (valid since 2006) $34 < E - p_z < 75\,\mathrm{GeV}$, $E'_e > 7\,\mathrm{GeV}$ and $Q^2 > 6\,\mathrm{GeV}^2$ (the value of Q^2 reconstructed online on the TLT level may differ from the one used in the final analysis) and at least one track in the CTD with $p_T > 0.2\,\mathrm{GeV}$ and $-60 < Z_{vtx} < 60\,\mathrm{cm}$ and the box cut used in SPP02.

- $5 < Q^2_\Sigma < 1000\,\mathrm{GeV}^2$. The lower cut is imposed by the box cut size of 15 cm and the upper one by the applicability of the SINISTRA electron finder. At higher Q^2 values the scattered electron is being detected in the FCAL region, where the SINISTRA finder does not work well. Another limitation comes from the available statistics.

- $y_{JB} > 0.02$ ensures that the hadronic system was measured precisely and $y_{el} < 0.7$ ensures that the scattered electron does not enter the FCAL region.

- For certain run ranges in the 06e and 0607p data periods, electron candidates reconstructed in the RCAL in the region $7.515 < \mathrm{x} < 31.845\,\mathrm{cm}$ and $7.90 < \mathrm{y} < 31.90\,\mathrm{cm}$ were not considered as the RCAL efficiency was not correctly reproduced [121] by MC for these candidates.

The corresponding control distributions of NC inclusive DIS ARIADNE MC compared to the data after the current DIS selection can be found in Appendix B. This MC sample was not used to measure the cross sections of the D^* production.

7.3 D^* meson selection

D^* mesons (see Chapter3) were identified using the so-called "golden" decay channel with three charged particles in the final state. D^* decays to D^0 and "slow" pion

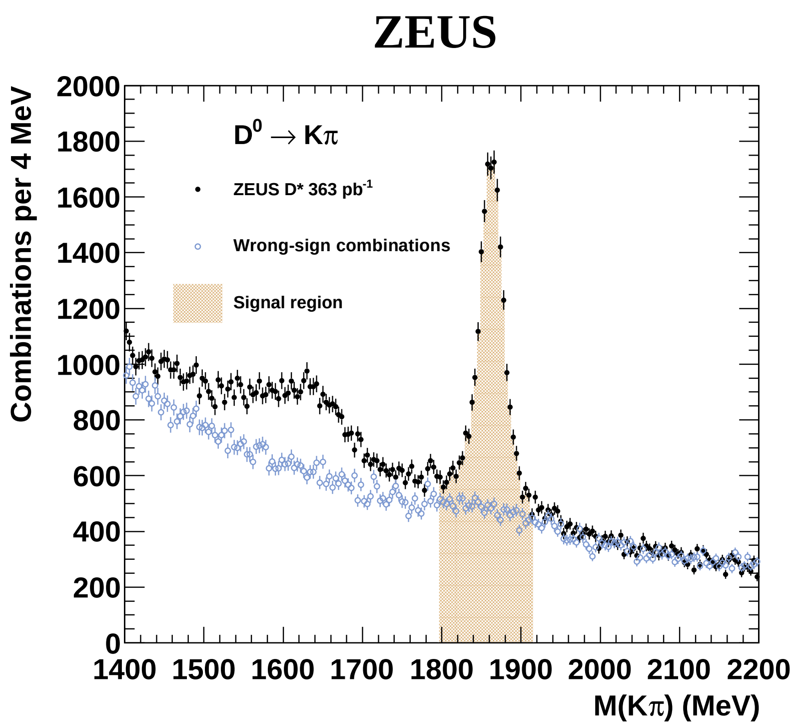

Figure 7.1: Mass spectrum of the reconstructed D^0 coming from D^* decays for ΔM selection window of $143.2 < M(K\pi\pi_s) - M(K\pi) < 147.7\,\mathrm{MeV}$. The correct sign combinations are marked with filled points, the wrong charge combinations are marked with open blue points. The D^0 selection window is highlighted as the shaded area.

with the subsequent decay of the D^0 to a Kaon and a pion:

$$\begin{aligned} D^{*\pm} &\to D^0\,\pi_s^{\pm} \\ &\quad\hookrightarrow K^{\mp}\,\pi^{\pm}. \end{aligned}$$

Due to the difference in mass between the D^* and the D^0 , which is just above the pion mass, only a small fraction of the D^* momentum is transferred to the pion in this decay, and therefore the designation “slow” is used.

The D^* search starts with combining two oppositely charged tracks into a D^0 candidate. Those tracks are required to have $p_T > 0.4\,\mathrm{GeV}$ and were alternately assigned the mass of K and π. Afterwards, the invariant mass of the D^0 , $M(K\pi)$, is calculated. The D^* candidates are formed from the two tracks from the D^0 decay and an additional charged track with π mass assignment and $p_T > 0.12\,\mathrm{GeV}$. All three tracks should originate from the same primary vertex as D^* decays strongly to D^0 (see Chapter 3). The life-time information from the MVD could also be used to reconstruct D^0 from secondary vertices in order to reduce background [122]. In the case of D^* mesons this introduces more systematic uncertainties than the statistical gain [123]. Therefore the life-time information was not used. In addition, all three tracks should pass at least three first CTD super-layers, which implies $|\eta^{K,\pi,\pi_s}| < 1.75$. After all these steps the invariant mass, $M(K\pi\pi_s)$, of the D^* is calculated.

After D^* candidates have been found, the following kinematic phase space selection criteria were applied:

- the transverse momentum of the D^*, $1.5 < p_T < 20$ GeV and $|\eta| < 1.5$;
- the mass window for the D^0 candidate, $1.8 < M(K\pi) < 1.92$ GeV;
- the D^* mass window of $143.2 < M(K\pi\pi_s) - M(K\pi) < 147.7$ MeV.

One of the advanced features of the D^* measurement is the possibility to estimate the combinatorial background by combining tracks with equal charges into "D^0" candidates and then form a "D^*" by adding another π_s. The charge of the π_s track corresponds to the opposite charge of the fake D^* meson candidate. Those background candidates are called Wrong-Sign (WS) combinations, while the signal candidates are referred as Correct-Sign (CS) combinations. The WS background usually describes the shape of the CS signal [124]. The mass spectrum of D^* meson is usually represented as the spectrum of $\Delta M = M(K\pi\pi_s) - M(K\pi)$ in order to improve the mass resolution. The D^* spectrum for all reconstructed D^* candidates is shown in Figure 7.2, showing a clear $D^{*\pm}$ peak.

The mass spectrum of the reconstructed D^0 from D^* decay is depicted in Figure 7.1. The WS distribution provides an estimate of combinatorial background. The excess of correct-sign candidates in the $M_{K\pi}$ distribution at lower masses than the D^0 peak is due to partly-reconstructed D^0 decay modes, mostly $D^0 \to K^-\pi^+\pi^0$ in which π^0 was not identified.

7.4 D^* signal extraction method

The procedure for the extraction of the D^* yields may differ from analysis to analysis [125]. It can be done by subtracting the WS spectrum with a proper normalisation, or by the approximation of the D^* candidate mass spectra with a function. In this analysis a hybrid technique was used. This technique combines both fitting and background subtraction. According to the method, the fit is performed in order to describe the background. The usage of both CS and WS distribution allows decreasing the statistical uncertainty because those are two independent data samples, and therefore the fit procedure is called a simultaneous fit. Thus the shape of the background fit function is derived from the WS and the normalisation from

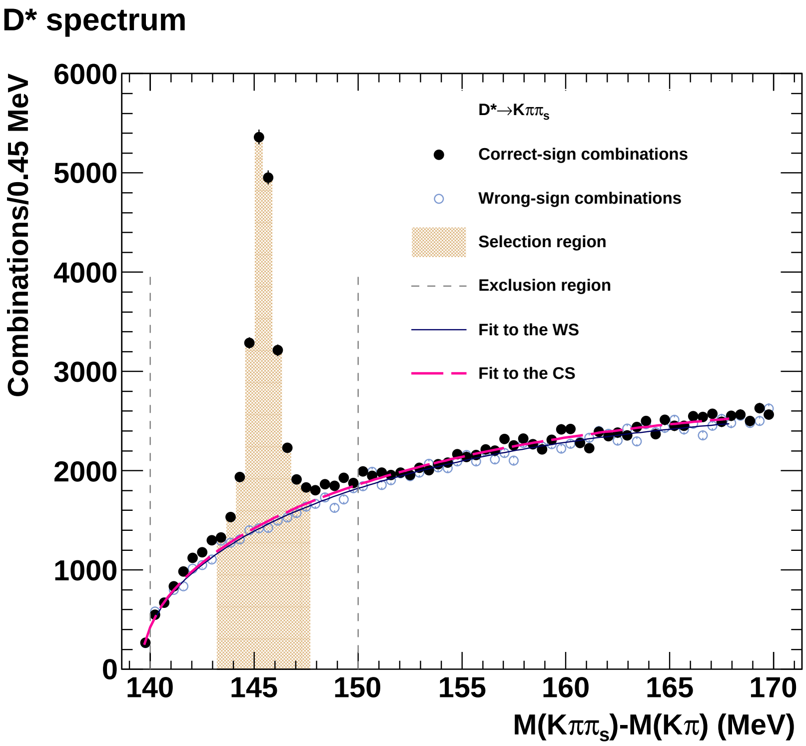

Figure 7.2: Illustration of the D^* selection and signal extraction methods on the D^* spectrum in the selected kinematic phase space. D^* ΔM spectrum is obtained for $1.8 < M(K\pi) < 1.92$ GeV. Correct-sign combinations are marked with filled points, wrong-sign combinations are marked with open blue points. The selection region for D^* is highlighted with the shaded area. For more details please refer to the text.

the CS combinations. The region of $140 < \Delta M < 150$ MeV was excluded from the CS mass spectrum when the fit was performed. This region is shown by the two vertical dashed lines in Figure 7.2. This was done in order not to bias the shape of the background with signal-like events. As the background fit function the Granet function:

$$G(x) = A \cdot x^B e^{C \cdot x}, \quad x = |\Delta M - m_\pi|, \tag{7.1}$$

was used for WS (long-dashed line in Figure 7.2). For the CS spectrum, a relative normalisation parameter D was used (solid line in Figure 7.2) for the same Granet function:

$$G'(x) = D \cdot G(x). \tag{7.2}$$

Here A, B, C, D are the free parameters of the fit that was performed in the range $139.6 < \Delta M < 168.0$ MeV. For the minimisation of the fit, the least χ^2-method was used, with an exception of some corners of phase space (low y, low Q^2), where the statistics of the events was small, e.g. less than 100 entries in the mass spectra. Then, a Poisson-Likelihood method was used.

After the fit, the integral of the fit function is calculated in the ΔM selection region and subtracted from the correct-sign combinations. The selection region was $143.2 < \Delta M < 147.7$ MeV (shaded area in Figure 7.2).

The possibility of fitting D^* peak was discarded, as in this case the fit[3] does not describe the peak tails which leads to a strong dependence on the choice of the fit function.

The usage of the hybrid method leads to a reduction of the statistical uncertainty with respect to the wrong-charge subtraction method. Thus, for the wrong charge subtraction method the relative uncertainty is 1.7 % and for the hybrid method it is 1.4 % [4]. The uncertainty is reduced because the background prediction uncertainty is reduced, becoming the one from the fit, and fluctuations are smoothed out. The total signal (Figure 7.2) in data is $N^{D^*} = 12893 \pm 185$.

More information about the D^* and D^0 spectra can be found in Appendix C.

7.5 Corrections applied to Monte Carlo simulations

Most of the the time for any detector simulation some simplifications are made, therefore not all detector features can be simulated with the full accuracy. This section describes the corrections applied to the simulated events in order to obtain a correct acceptance.

7.5.1 ISOe corrections

In the previous, Section 7.2, the FLT level selection was described. One of the criteria given there is an electron isolation, ISOe. The basic principle of this algorithm is illustrated in Figure 7.3. The ISOe algorithm analyses energy deposits in a block of 4×4 CAL cells (black quadrants in the picture). A 2×2 subsection of the section of the block is required to have EMC deposits greater than a given threshold. At the same time, the energy deposit left in the hadronic part of the CAL cells should be less then a certain HAC threshold. Both thresholds are given below. Towers marked with Q showed no activity, meaning that the energy deposits were less than some external threshold. When all these criteria are fulfilled, the

[3] Several different fit functions were tested and none of them gave a satisfactory description of the peak tails.

[4] The gain on the statistical uncertainty was larger for the signal extraction in a particular bin.

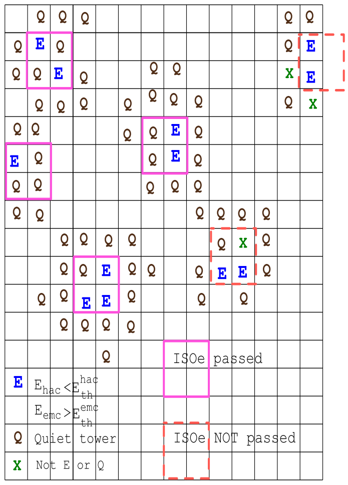

Figure 7.3: Illustration of the ISOe algorithm.

ISOe condition is satisfied. During the data taking, an inefficiency of the FLT slots using the ISOe requirement was found [126]. The detector simulation did not fully describe this inefficiency, thus introducing a bias to the acceptance calculations. Therefore, dedicated studies are necessary. The relevant efficiency is defined as

$$\epsilon = \frac{\text{FLT44 \& ISOe \& R}_{emc} > 3992}{\text{FLT44 \& R}_{emc} > 3992}, \tag{7.3}$$

where the numbers are given in MeV. FLT44 is the only trigger slot used in the current analysis that does not rely on the ISOe criteria. Thus, it was used as a

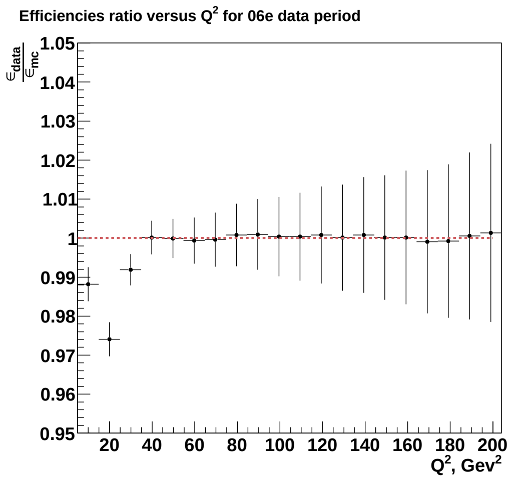

Figure 7.4: The ratio of data to MC ISOe efficiencies as a function of Q^2_Σ for the 06e data period. The high Q^2 region is out of the scope of the picture.

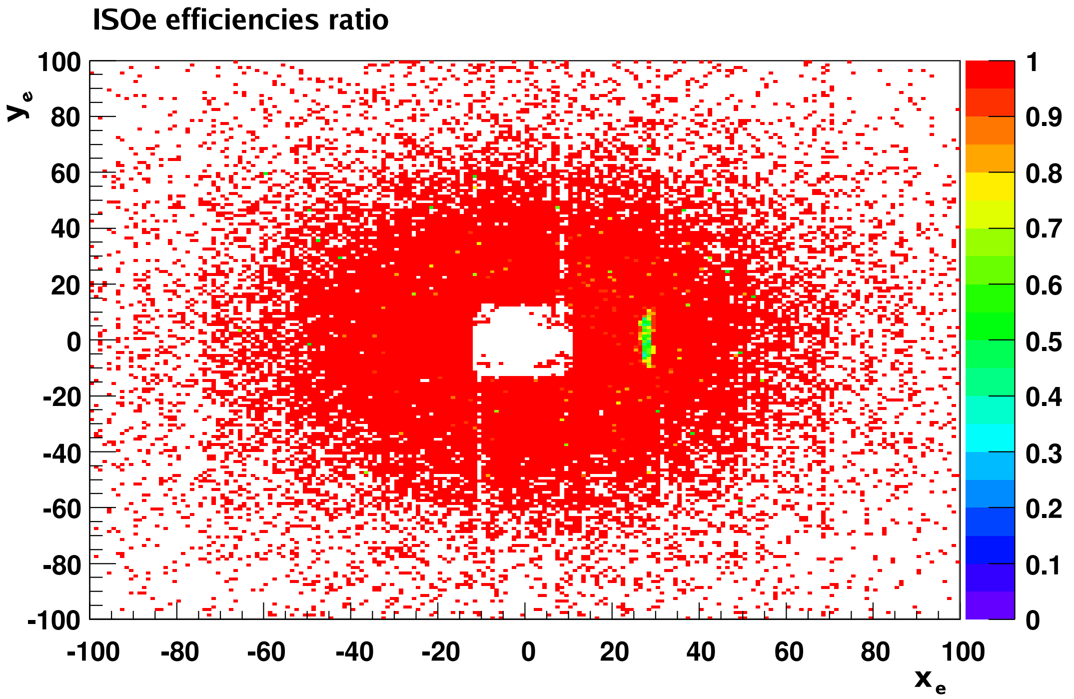

Figure 7.5: The same ratio as in Figure 7.4 as a function of the reconstructed electron position x_e and y_e for RunNr $<$ 60400 ($\sim$ 04p-06e data periods). The colour palette represents the ratio $\frac{\epsilon_{data}}{\epsilon_{mc}}$.

monitor trigger which is 100 % efficient with respect to ISOe. In Equation (7.3) an additional cut on the energy deposit in the outer part of the RCAL, R_{emc}, was used. This implies that event reconstruction relies on the outer part of the RCAL independently on what is happening in the inner part of the RCAL that has its own inefficiency.

The efficiency was calculated separately for the data and for the MC. The ratio of the two is the subject of interest, because it represents the relative inefficiency of the MC simulation with respect to the data. From Figure 7.5 it is seen that the simulation fails in the region $26.5 < x < 29.5$ cm and $|y| < 10$ cm which corresponds to the gap between two RCAL modules. This inefficiency affects mostly low Q^2 events. The inefficiency of the simulation as shown in Figure 7.4 is present only for the run range RunNr $<$ 60400 that corresponds to the data period from 04p to 06e and a small fraction of 06p.

The ratio was recalculated after removing the badly simulated region and the remaining inefficiency is shown in Figure 7.6 for the run range before and after run 60400. The final ISOe correction was implemented as follows. Events that were not triggered by FLT44 and had an electron reconstructed in the region of failure, $26.5 < x < 29.5$ cm, $|y| < 10$ cm, were removed from the analysis. After the exclusion

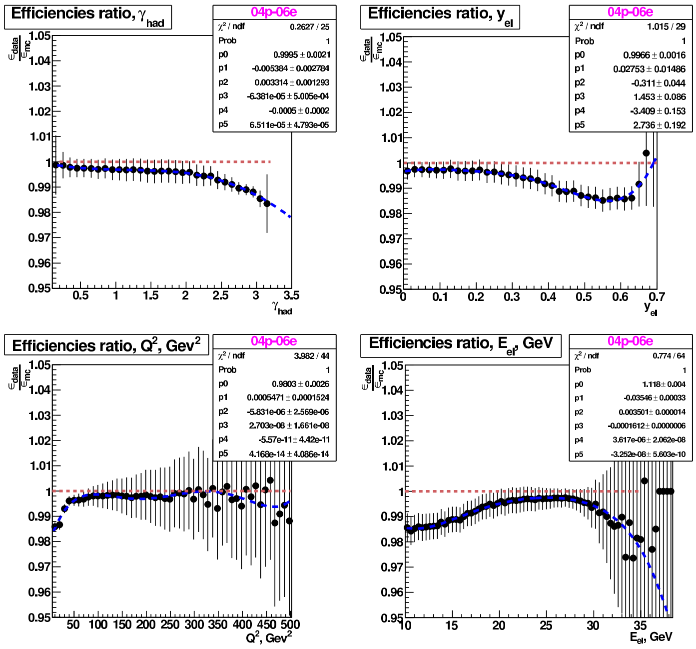

(a)

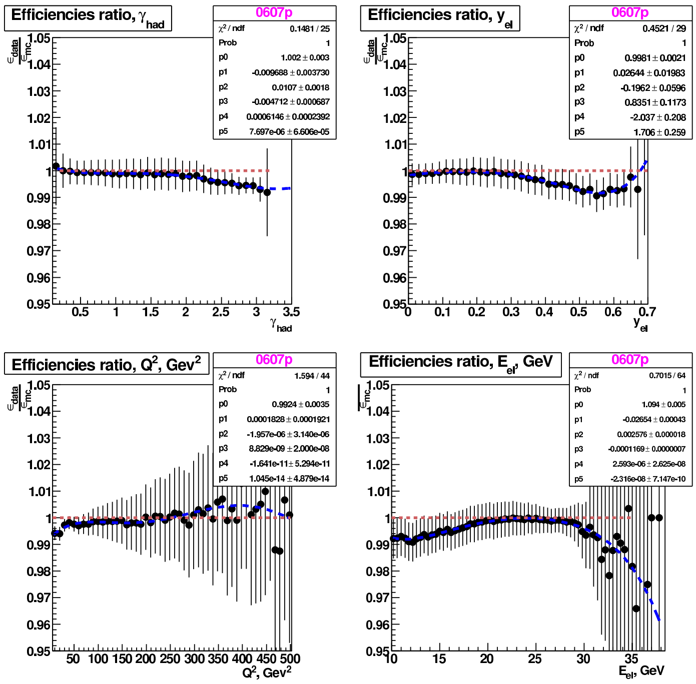

(b)

Figure 7.6: (a) Residual inefficiency of the ISOe simulation after cutting away the region of failure for the period RunNr < 60400 as a function (from left to the right) of γ_{had}, y_{el}, Q^2_Σ and E'_e. (b) Same as (a) for the period $RunNr >$ 60400. The blue solid line represents a fifth order polynomial approximation, the fit parameters are written in the box in each plot and listed in Appendix D.

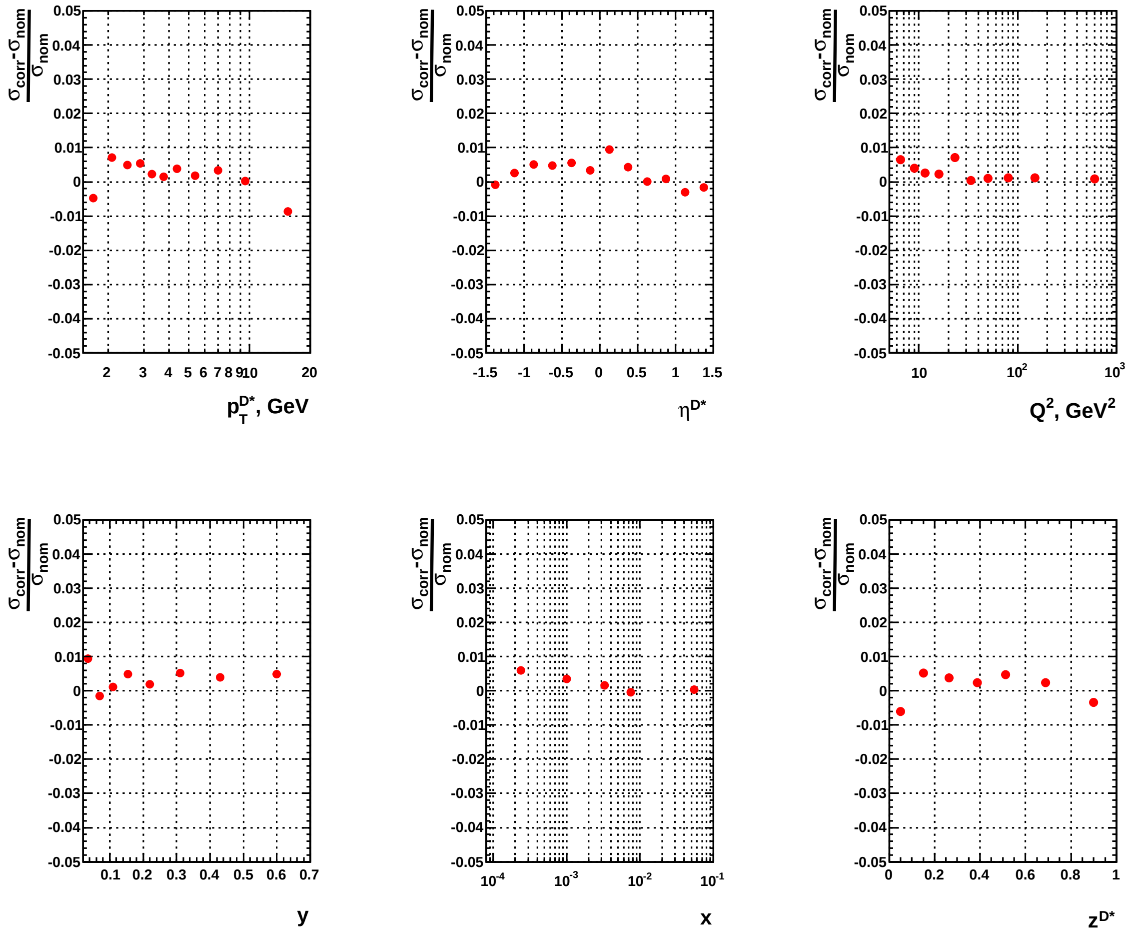

Figure 7.7: The effect of the ISOe correction, $\frac{\sigma_{\text{corr}}-\sigma_{\text{nom}}}{\sigma_{\text{nom}}}$, on the single differential cross sections for transverse momentum of D^* ($p_T^{D^*}$), pseudorapidity of D^* (η^{D^*}), virtuality of the exchanged photon (Q^2), event inelasticity (y), variable x and z^{D^*}.

of that region, the ratio of efficiencies did not become unity. Therefore, for the remaining events, a correction was applied to the MC as a function of the inelasticity of the event reconstructed with the Electron method, y_{el}, shown in Figure 7.6. The observable y_{el} was chosen, as it covers the effects of the scattered electron energy reconstruction and the reconstruction of Q^2, while e.g. the γ_{had} relies only on the hadronic angles. The effect of the correction on the single-differential cross section is shown in Figure 7.7. For the lowest Q^2 bins the correction shifts up the cross section by $\sim 1\%$ as shown. The definition of the cross section will be discussed later. More

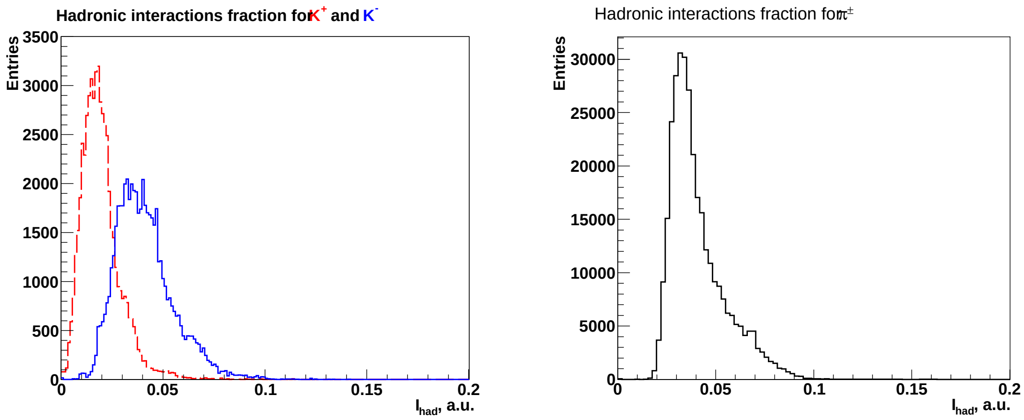

(a) (b)

Figure 7.8: Fraction of hadronic interactions, I_{had}, for (a) K^+ (red dashed line) and K^- (blue solid line), $I_{had} = I_K$, and for (b) pions, $I_{had} = I_\pi$, for an integrated particle momentum.

details and the effect of the correction on the double-differential cross sections are given in Appendix D.

First level triggers had also cuts based on tracking information. Thus, the FLT tracking efficiency were also studied. It was found that MC simulations describe the data well, therefore no correction is needed [127].

7.5.2 Tracking corrections

Another very important aspect of understanding the acceptance is the simulation of the tracking performance. There are a few sources that cause a tracking inefficiency like dead material, performance of the tracking detectors, trigger efficiency, track reconstruction software features. In [128], the relative track inefficiency in the data with respect to the MC for tracks with $p_T < 0.26$ GeV was estimated with K_S^0 decaying into two pions. The experimental technique of the calculation of the efficiency versus particle momentum is explained in [129]. The resulting correction was implemented as a weight to the MC detector level events as a function of the transverse momentum, for $p_T^{\pi_s} < 0.26$ GeV

$$f_p = 1 + 0.548 \cdot (p_T^{\pi_s} - 0.26), \tag{7.4}$$

where p_T is given in GeV. The function assumed to be unity for $p_T^{\pi_s} > 0.26$ GeV. The correction improved the MC description of the data for low-momentum D^*s with $p_T^{D*} < 2.5$ GeV.

Any tracking detector introduces additional material, where a particle can interact with a nucleus from the medium. This can cause imperfections in the detector simulation due to systematics of the model that is used to describe hadronic interactions. For the ZEUS tracking system the simulation shows an underestimation of the hadronic interactions by 40 % for tracks with $p_T < 1.5$ GeV estimated using exclusive ρ^0 decays [130], taking into account that the dead material distribution is reasonably described by the MC [131]. The transverse momentum threshold can be related to the GEANT3 GHEISHA hadronic shower package. It uses experimental data for pion and proton cross sections on nuclei for a particle momentum starting from 2 GeV. Below that some "reasonable" approximation is used [107]. Therefore, two possible thresholds can be considered, either for the tracks with $p_T < 1.5$ GeV or $p < 2$ GeV.

The value of the correction, W, should be calculated for each particle that is being considered in the analysis by convolving a probability of a particle to interact hadronically, I, with a fraction of hadronic interaction rate that is underestimated by the MC, ϵ. The value of I was estimated on the MC sample for the Kaon and pion hypothesis, separately for positive and negative charges, depending on the momentum, pseudo-rapidity and azimuthal angle of the track [132]. The correction should be applied to the detector-level MC events.

Thus, for the case of the D^* decay considered in this thesis, the correction was defined as

$$W_{had} = (1 - W_K) \cdot (1 - W_\pi) \cdot (1 - W_{\pi_s}), \tag{7.5}$$

where $W_K = \frac{\varepsilon \cdot I_K}{1 - I_K}$ is the correction for Kaons, $W_{\pi,\ \pi_s} = \frac{\varepsilon \cdot I_\pi}{1 - I_\pi}$ is the correction for pions and "slow" pions and $\varepsilon = 0.4$ stands for the 40 % that are missing. Figure 7.8 shows distribution of $I_{K,\pi}$ for Kaons and pions for the overall momentum and pseudorapidity range of the D^* analysis.

The effect on the cross section is shown in Figure 7.9. It is 3 % on average and rises up to 6 % for $p_T^{D^*} < 1.8$ GeV and for very rear and forward pseudorapidities, where there is more material and the interaction probability is larger. For the final results, the p_T threshold-like correction was applied.

7.5.3 Tails corrections

As was explained in Section 7.3, the D^* decay topology is characterised by the presence of a "slow" pion track with low momentum produced close to the threshold. In the ZEUS detector, tracks with momentum above 0.1 GeV can be reconstructed. The lower the momentum of a particle, the more sensitive it is to multiple scattering interactions, and therefore the reconstructed momentum will differ from the original. For the D^* measurement, a cut $p_T^{\pi_s} > 0.12$ GeV was used for the selection.

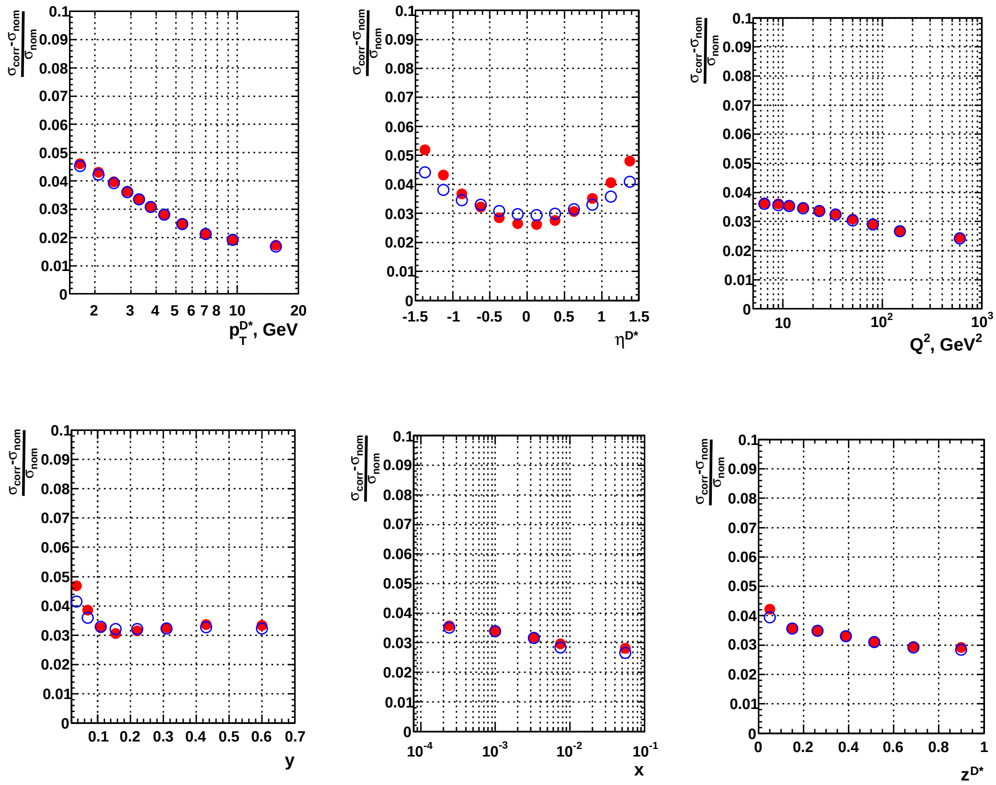

Figure 7.9: Effect of the tracking correction defined as $\frac{\sigma_{\mathrm{corr}}-\sigma_{\mathrm{nom}}}{\sigma_{\mathrm{nom}}}$ for the $p_T < 1.5\,\mathrm{GeV}$ (red filled points) and for the $p < 2\,\mathrm{GeV}$ thresholds (open blue points) on the differential cross sections in bins of $p_T^{D^*}$, η^{D^*}, Q^2, y, x, z^{D^*}.

Misreconstructed "slow" pions can cause a different mass assignment for the D^* reconstruction by enlarging the width of the ΔM spectrum, see Figure 7.10. This enlargement is called tail of the peak. It is important to check how well these effects are simulated by the MC.

For the ZEUS detector simulation the Mòliere approach [133] was used for the multiple scattering model. By comparing the tails in D^* ΔM spectra in the data and in the MC a sizeable difference was found. However, MC does not fully describe the size of the effect, an attempt to pin down the origin of the tails using the MC showed that they are caused by badly reconstructed D^*s, due to the "slow" pion and not because of the background [134].

For the discrimination variable of the tails, the fraction of missed events, κ, outside the selection region was defined under the assumption that any excess over

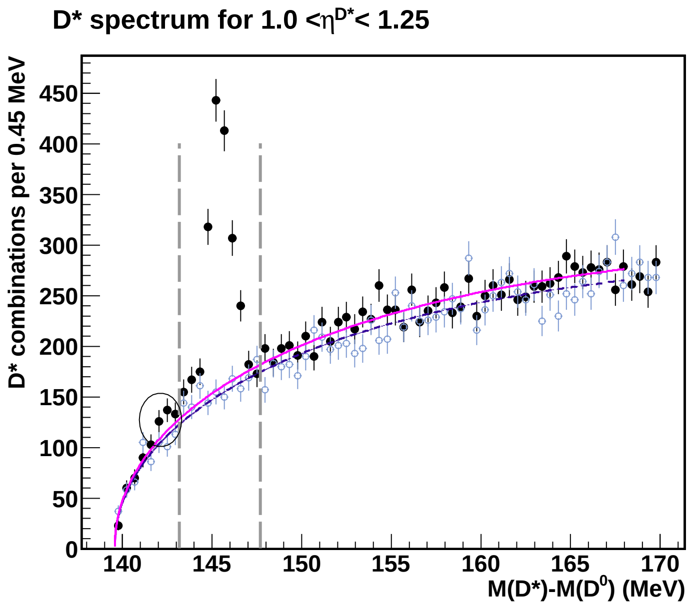

Figure 7.10: The $D^* \, \Delta M$ spectrum for the central region. The background fit to the CS combinations is shown with the solid line. The background fit the the WS combinations is shown with the dashed line. The circle to the left to the D^* peak demonstrates an example of the signal excess over the background that is referred as tail in the text. The signal region lies between the two vertical dashed lines.

the background in that region is due to signal events:

$$\kappa = \frac{N_\Sigma - N_{\sigma_i}}{N_\Sigma}. \tag{7.6}$$

Here, N_Σ is the number of D^*s extracted using the widest D^* selection region of $140 < \Delta M < 150$ MeV which corresponds to a 10σ width of the full D^* spectrum. Outside this region it is assumed that there is no D^* signal. The value of $\sigma = 0.46$ MeV is extracted from the fit with a Modified Gaussian, see Appendix C. N_{σ_i} is the number of D^*s extracted in the considered selection region. A scan of the tail contribution to the D^* peak in the data and in the MC was performed in steps of 1σ. Figure 7.11(a) demonstrates that the simulation underestimates the size of the tails. Therefore, a correction is needed. It can be defined as $\kappa_{data} - \kappa_{mc}$.

The presence of the tails is also relevant for the D^* reconstruction in photoproduction (PHP). The triggered rate of the D^* production in PHP is approximately three times higher than the one in DIS. Therefore the contribution to the D^* spectra tails was also extracted from the D^*s produced in the PHP processes. For more details about the D^* selection in PHP, see Appendix E and [135].

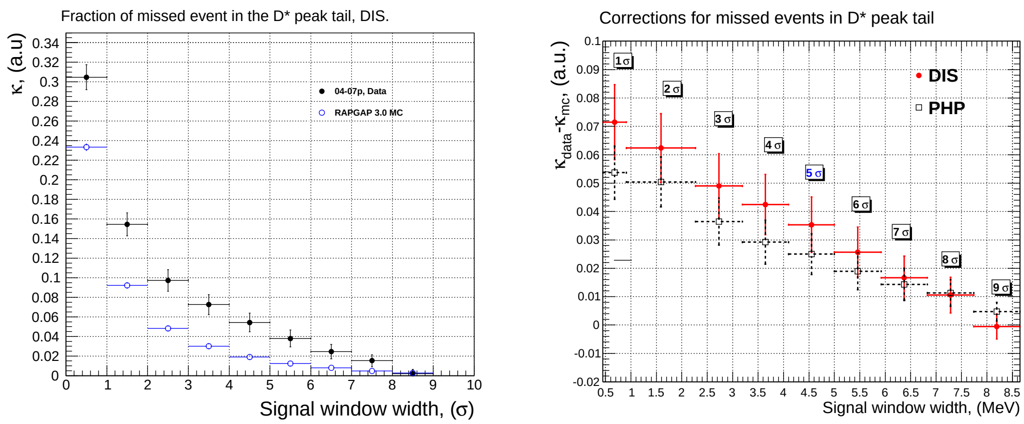

(a) (b)

Figure 7.11: (a) Data to MC comparison of the fraction of missed events outside the selection region, κ, as a function of the selection window width expressed in the number of σs. (b) DIS to PHP comparison of $\kappa_{data} - \kappa_{mc}$ with the selection window width expressed in MeV.

Figure 7.11(b) demonstrates the tails correction defined above for the DIS and PHP events. It can be seen that the corrections for these two samples are different.

One of the possible reasons of the difference is from trigger thresholds on D^* production that in the case of PHP were $p_T > 1.8\,\text{GeV}$ (due to larger backgrounds) and for DIS $p_T > 1.35\,\text{GeV}$. And the other reason could be the TLT tracking efficiency [123] which was based on information from the CTD only. It was observed that the tails strongly depend on the transverse momentum of the D^* (see Appendix G) and that is why the PHP sample can not be used to extract the correction for DIS events [5].

As the tails are caused by the "slow" pions, the correction was applied as function of $p_T^{\pi_s}$. Figure 7.12 shows the correction, $\kappa_{data} - \kappa_{mc}$, versus $p_T^{\pi_s}$ for the 5σ selection window of the ΔM spectrum of D^*. The correction itself was derived from the χ^2 fit of the $\kappa_{data} - \kappa_{mc}$ distribution in DIS shown in the figure. The fit was performed using a function

$$t(x) = a \cdot x^2 + b, \tag{7.7}$$

where x is the transverse momentum of the "slow" pion and $a = 0.0014 \pm 0.0006$ and $b = 0.0096 \pm 0.0113$ are the parameters from the fit. The correction was applied to the MC detector level events as a weight $(1 - t(x))$ under the assumption that $\kappa_{mc} \ll 1$ [136]. The effect of the correction on the single-differential cross sections is shown in Figure 7.13. The correction increases the cross section by $\sim 8\,\%$ in

[5] On some of the plots the correction for the PHP sample is shown, but it was not applied for DIS events.

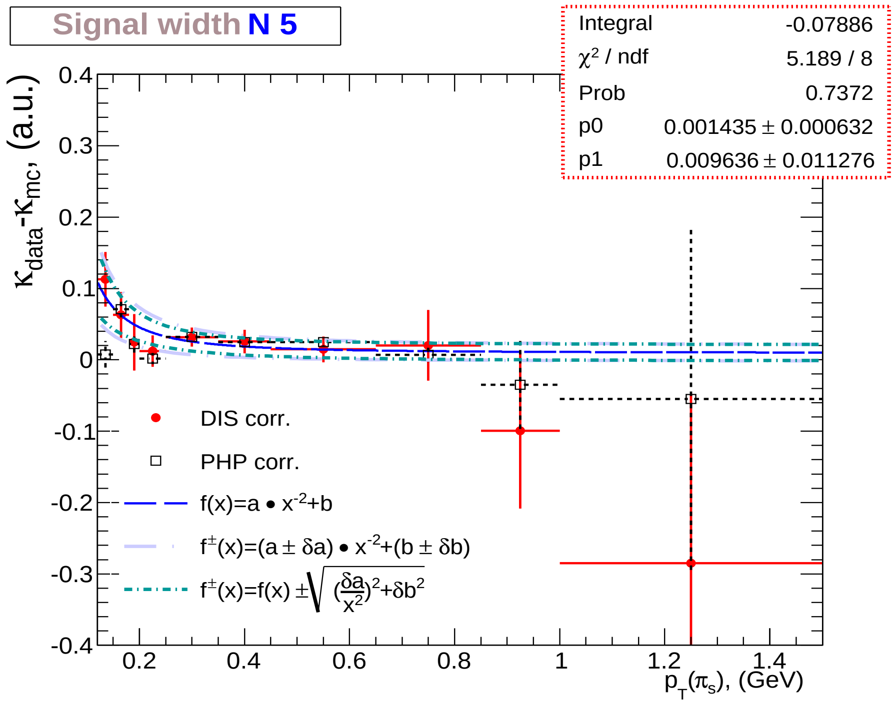

Figure 7.12: Tail correction as a function of $p_T^{\pi_s}$ for DIS (filled circles) and for PHP (open squares) for the selection region used in the current analysis. The parameters of the correction function and their uncertainties are given in the box. The correction function is marked with blue long-dashed line and its variation that was used as systematic uncertainty is marked with dotted-dashed green line.

the low $p_T^{D^*}$ bins and by $\sim 1\,\%$ for the high $p_T^{D^*}$ bins. The implementation of the correction significantly improved the understanding of the systematic effects related to the D^* reconstruction. The uncertainty of the correction will be discussed in Section 7.9.

The same studies were performed for the D^0 mass spectra after application of the tails correction for D^*. D^0 candidates were reconstructed in the D^* selection window $143.2 < \Delta M < 147.7\,\text{MeV}$, which is the one used in the current analysis. Figure 7.14 shows the tails in the data and in the MC, $\kappa_{data} - \kappa_{mc}$, versus the width of the D^0 selection window. The width is expressed in $\sigma = 12.75\,\text{MeV}$. The σ, as in the case of the D^* spectrum, was derived from the fit with a modified Gaussian (see Appendix C). The D^0 selection window corresponds to $N\sigma = 5$. For this window the MC describes the data within $2\,\%$ accuracy independently of the kinematic region. Therefore a correction for D^0 tails was not applied, but was treated as systematic uncertainty.

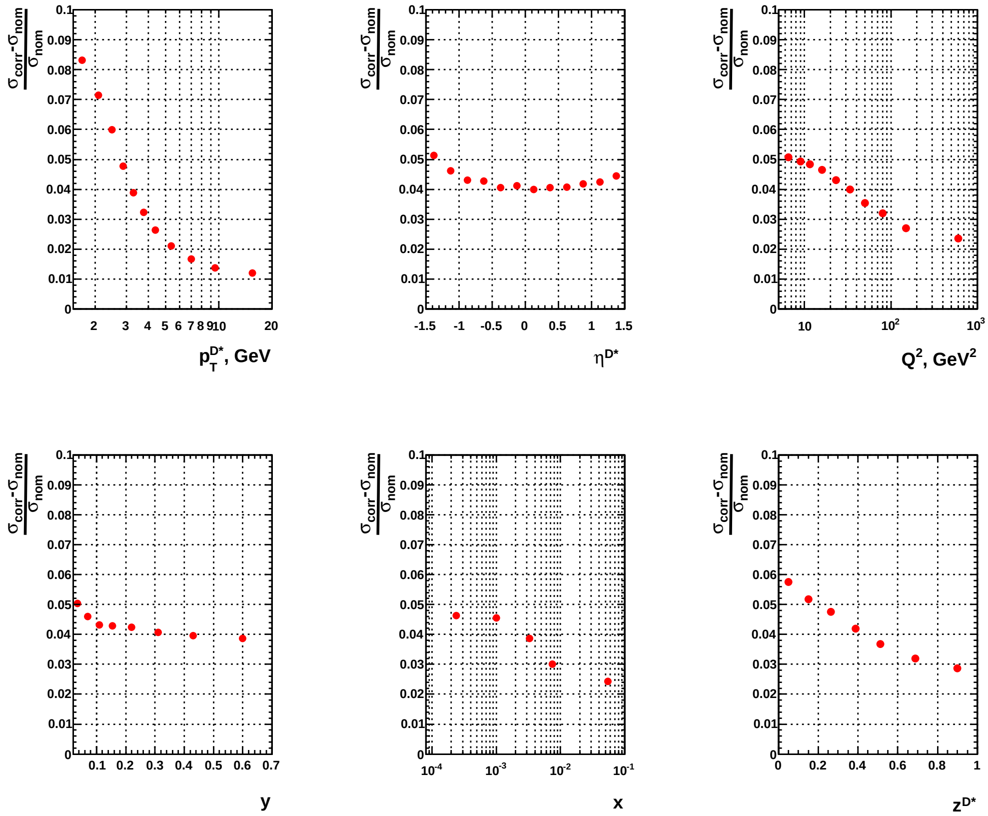

Figure 7.13: Effect of the tails correction on single-differential cross section as functions of $p_T^{D^*}$, η^{D^*}, Q^2, y, x, z^{D^*} expressed as a fraction of unity.

7.5.4 Monte Carlo reweighting

The RAPGAP Monte Carlo simulation does not fully describe the measured distributions of Q^2, $p_T^{D^*}$ and η^{D*} at ZEUS. It underestimates the low Q^2 part and overestimates the low $p_T^{D^*}$. The pseudorapidity spectrum is shifted to the rear region with respect to the data (Figure 7.15). Therefore, in order to have a correct evaluation of the acceptance the MC events were reweighted. The weighting factors were obtained from the ratio of rates, N_{data}/N_{MC}, after the application of the all correction discussed in the previous sections.

For the η reweighting, a smooth linear function was used:

$$w_\eta = 0.084 + 0.998 \cdot \eta^{D^*}. \tag{7.8}$$

The Q^2 and $p_T^{D^*}$ reweighting was done in a two-dimensional grid because the $p_T^{D^*}$ and Q^2 spectra are correlated. Therefore those two distributions were reweighted simultaneously using the grid as shown in Table 7.3.

$p_T^{D^*}$ \ Q^2	5-13	13-20	20-40	40-60	60-1000
1.5-2.6	0.993	0.816	0.903	0.77	0.694
2.6-3.5	1.178	1.122	1.140	0.636	0.772
3.5-4.5	1.188	1.134	1.078	0.853	0.678
4.5-20	1.335	1.110	1.135	1.191	0.933

Table 7.3: Weighting factors, w_{p_T,Q^2}, for the simultaneous Q^2, $p_T^{D^*}$ reweighting. The first row shows the Q^2 ranges in GeV^2 and the first column shows the $p_T^{D^*}$ ranges in GeV.

The result of the reweighting is shown in Figure 7.15 together with the ratio of data to MC rates before and after the reweightings. By construction, after the reweighting, the agreement between MC and data became significantly better.

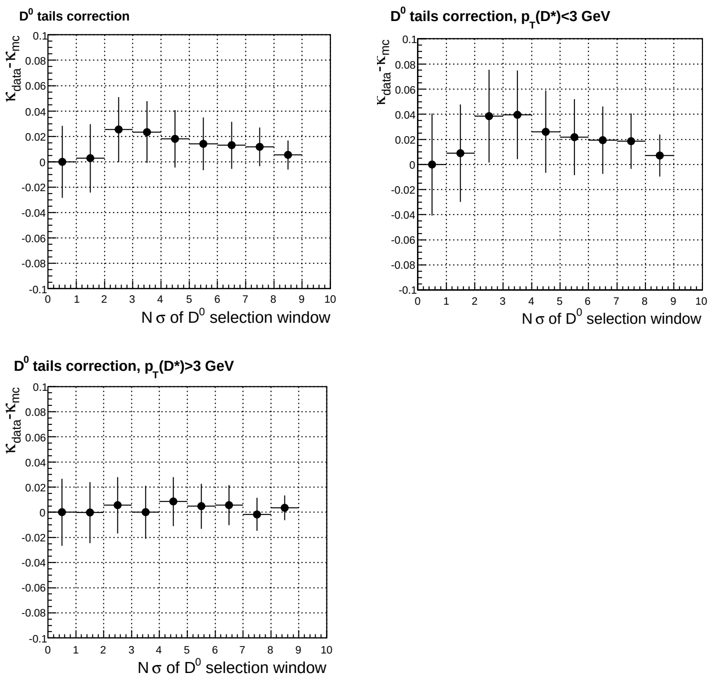

Figure 7.14: Difference in the fraction of events outside the selection window for the D^0 spectra versus the selection window width, σ, for the full, low and high p_T D^* kinematic regions.

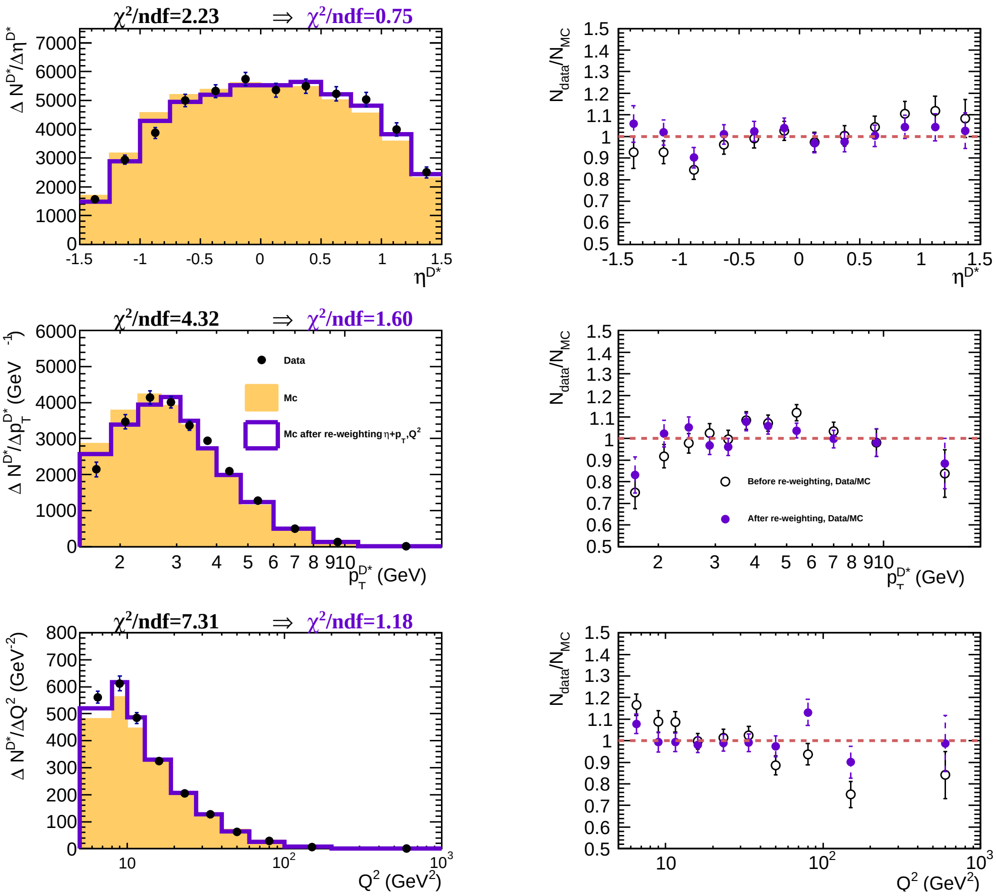

Figure 7.15: $\eta^{D^{*\pm}}$, $p_T^{D^{*\pm}}$ and Q^2 distributions (left) in data (black points) compared to the MC before (shaded area) and after reweightings were applied (solid line) together with the result of the χ^2 test. To the right the ratio of data to MC rates is displayed before reweightings (open points) and after (filled points). Dashed lines correspond to unity.

7.6 Control distributions

In this section the validation of the D^* signal description by the MC is shown. For the simulation, a mixture of sub-processes of charm and beauty RAPGAP DIS, charm RAPGAP Diffractive DIS and Pythia photoproduction in almost equal luminosities was used. The DIS part contained only direct photon BGF processes, see Section 7.1. The normalisation of the MC sub-processes was performed as follows:

- The beauty component, N_b, was normalised by a factor $k_F^b = 1.6$ consistently with the ZEUS measurements [137, 138, 139].
- Diffractive events, N_{diff}, were normalised with a factor $k_F^{diff} = 1.0$, i.e. the

normalisation as it comes from the RAPGAP generator. Often for the selection of the diffractive events the η_{max} observable is being used [140]. η_{max} is the rapidity of the most forward EFO with energy deposit larger than a threshold of 400 MeV. Figure 7.16 shows the distribution of η_{max} in the MC and in the data. The diffractive component of the DIS events dominates in the region of $\eta_{max} < 2$. In that region the RAPGAP MC underestimates the contribution from the diffractive processes. This was taken into account during the evaluation of systematic uncertainties.

- The hadron-like resolved photon processes in DIS were only included to evaluate a model systematic uncertainty.
- Photoproduction events, generated with Pythia, N_{php}, were normalised to the measured cross section of D^* mesons in photoproduction processes [141] with $k_F^{php} = 0.9$.
- The total charm contribution from non-diffractive and diffractive DIS, N_c, was normalised to data with k_F^c as

$$\begin{aligned} N_{data} &= N_c k_F^c + N_b k_F^b + N_{php} k_F^{php}, \\ N_c k_F^c &= N_c^{DIS} k_F^{bgf} + N^{diff} k_F^{diff}, \end{aligned} \tag{7.9}$$

where $k_F^{bgf} = 1.0$.

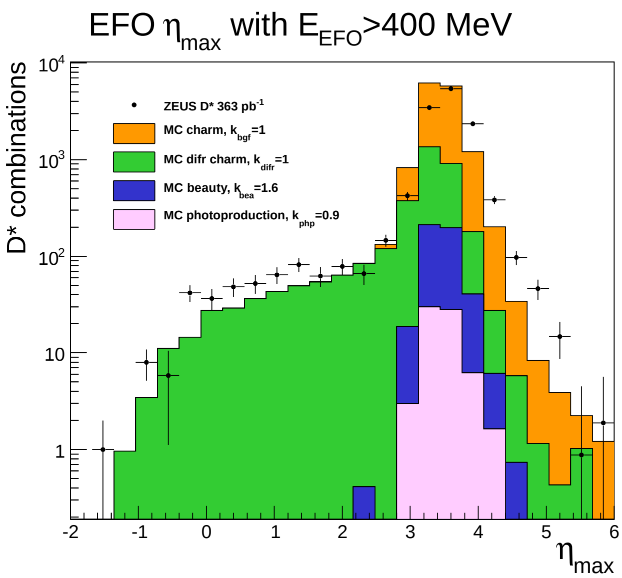

Figure 7.16: Distribution of η_{max} for the D^* signal, for the most forward EFO with E > 400 MeV in the MC composition (shaded areas) with respect to the data (filled points). Different MC samples are marked with different colours.

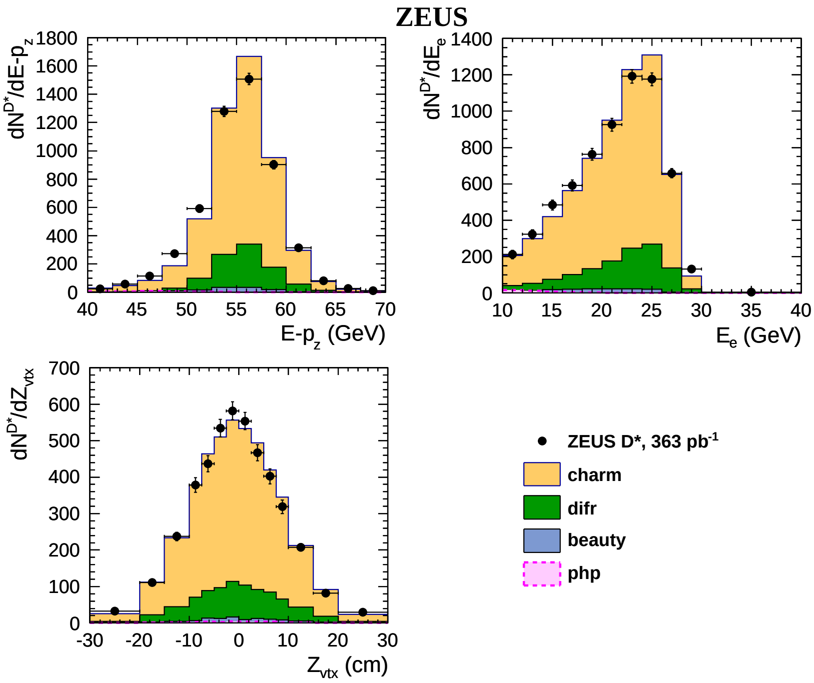

Figure 7.17: Distribution of $E - p_z$, Z_{vtx} of the event and the reconstructed energy of the scattered electron, E_e, in the MC composition (shaded areas) with respect to the data (filled points). Different MC samples are marked with different colours.

In addition, diffractive and photoproduction MC events were normalised to the luminosity of the charm BGF sample. The corrections and reweightings discussed before were applied.

Figure 7.17 shows the comparison of the distribution of the general observables $E - p_z$, the z coordinate of the primary vertex Z_{vtx}, and the energy of the scattered election, E_e, in the MC and in the data. Each bin in the given distributions corresponds to a separate extraction of the D^* signal from the corresponding δM peak as described in Section 7.4. Figure 7.18(a) shows the comparison of the DIS kinematic variables, Q^2, x and y distributions in the MC and in the data in the same binning as was used for the cross section extraction.

Figure 7.18(b) shows comparison of the D^*-related observables, $p_T^{D^*}$, η^{D^*} and z^{D^*}. The latter variable denotes the fraction of the full hadronic momentum carried by the D^* meson and was reconstructed as

$$z^{D^*} = \frac{(E - p_z)^{D^{*\pm}}}{(E - p_z)^{\text{had}}}.$$

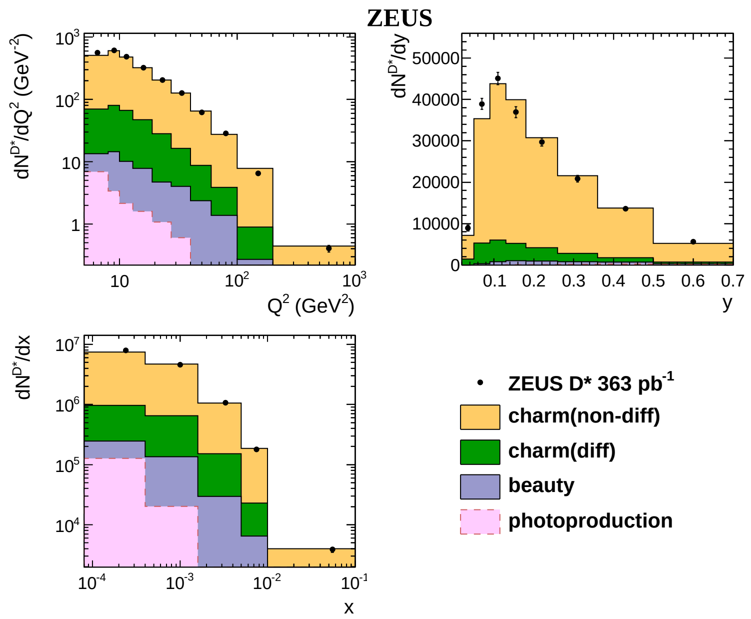

(a)

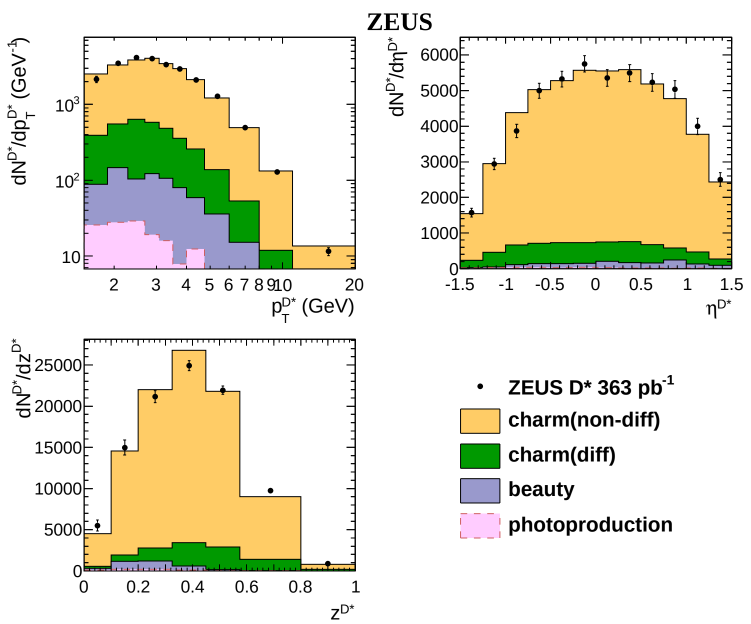

(b)

Figure 7.18: Comparison of the MC (filled histogram) D^* yields, $\Delta N/\Delta\zeta$, to the data (black points) for the (a) main DIS kinematic variables and (b) for the D^* variables. The different MC components are highlighted with different colours.

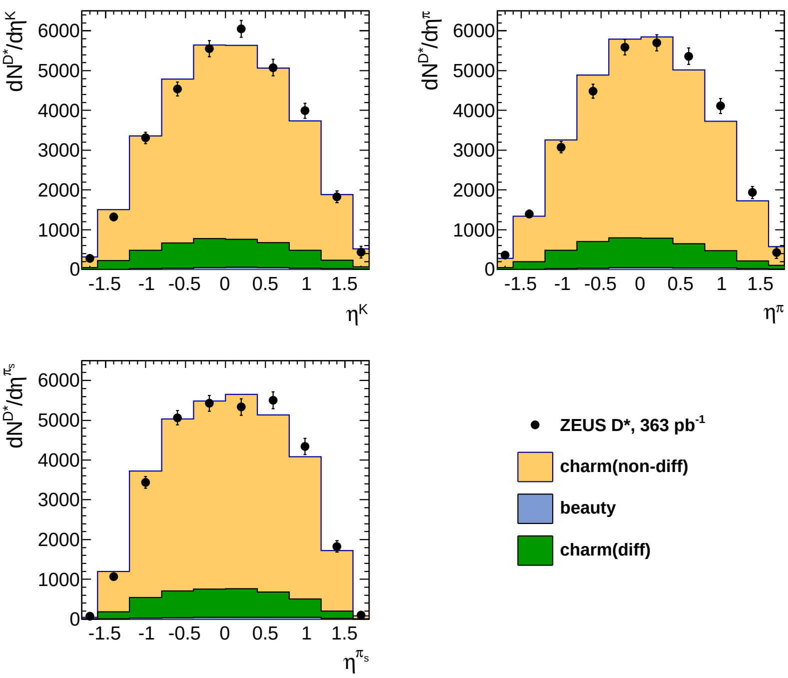

(a)

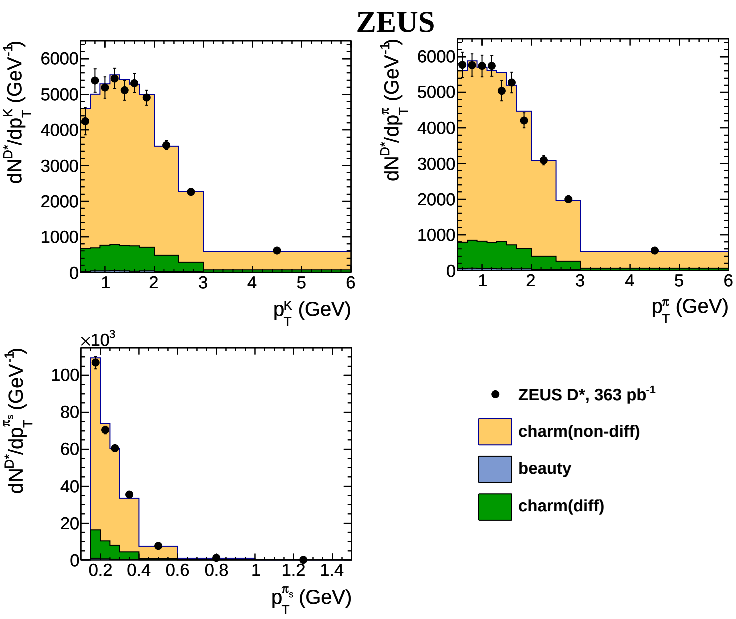

(b)

Figure 7.19: (a) Comparison of the MC D^* yields, $\Delta N/\Delta\zeta$, in bins of the pseudorapidity of the D^* decay products, K, π, π_s, with respect to the ZEUS data. (b) Comparison of the MC D^* yields in bins of the transverse momentum of the D^* decay products, K, π, π_s, with respect to the ZEUS data.

Figures 7.19(a) and 7.19(b) show the distributions of the transverse momentum and pseudorapidity for the D^* decay products: $K^\pm$, $\pi^\pm$ and $\pi_s^\pm$. The control distributions of the D^* production in bins of Q^2 and y can be found in Appendix F.

Overall the MC describes the data well, such that the acceptance can be reliably calculated.

7.7 Acceptance, purity, efficiency

Another important aspect of the analysis related to the MC simulation is the estimation of migrations. Due to resolution effects, the reconstructed value of physical observable may not be exactly the same as the one generated. Thus, e.g. an event instead of being reconstructed in the region ς ends up in the region $\varsigma + \delta\varsigma$ introducing the so-called migration. The lower the migrations effects the higher is the purity of the reconstructed signal.

Acceptance is defined as

$$\mathrm{A} = \frac{N_{reco}^{D^*}}{N_{gen}^{D^*}}, \tag{7.10}$$

where $N_{gen}^{D^*}$ is the generated number of D^*s, decaying to $K^\mp\pi^\pm\pi_s^\pm$ (before passing the detector simulation) and $N_{reco}^{D^*}$ is the number of reconstructed D^*s (at the detector level) in a given kinematic bin.

Purity reads as

$$\mathrm{P} = \frac{N_{reco}^{D^*\mathrm{M}}}{N_{reco}^{D^*}}, \tag{7.11}$$

where $N_{reco}^{D^*\mathrm{M}}$ is the number of D^*s that were generated and reconstructed in the same bins according to the matching criteria. The matching was done via angles according to $\Delta R = \sqrt{(\phi_{gen} - \phi_{reco})^2 + (|\eta_{gen}| - |\eta_{reco}|)^2}$, where ϕ_{reco}, η_{reco} are the azimuthal angle and pseudorapidity of the reconstructed D^* and ϕ_{gen}, η_{gen} of the generated one. The matching succeeded if $\Delta R < 0.025$. The higher is the purity, the lower are the migrations.

Efficiency is defined as $\mathrm{E} = \mathrm{A} \cdot \mathrm{P}$. It is a fraction of generated events that were reconstructed out of the total generated events.

Figure 7.20 shows the values of purity, acceptance and efficiency for every bin of $p_T^{D^{*\pm}}$, $\eta^{D^{*\pm}}$, $z^{D^{*\pm}}$, Q^2, y and x, in which the current analysis has been performed. The values of P, A and E were estimated on the MC after all the corrections and reweightings discussed earlier in the text. The values of purity are found to be satisfactory for the measurement of D^* production in DIS. The overall acceptance of the detector is 25 %, while it goes down to 15 % at low $p_T^{D^{*\pm}}$ and rises up to 40 % at high $p_T^{D^{*\pm}}$. The inefficiencies are mainly caused by the transverse momentum and pseudorapidity cuts on the decay products.

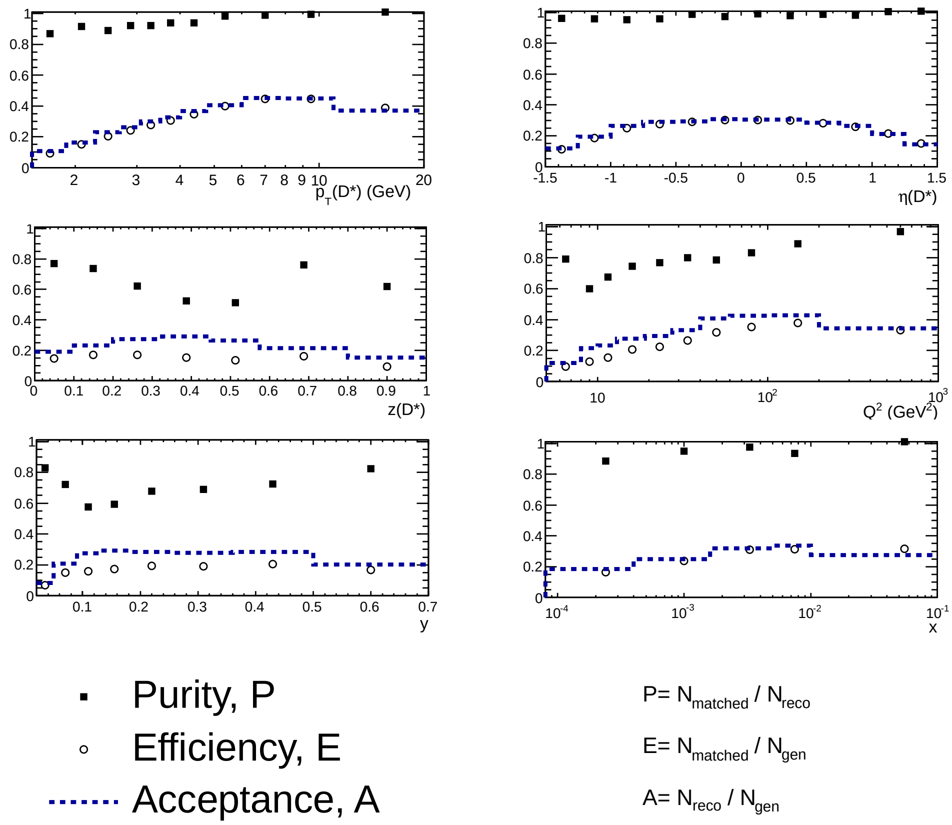

Figure 7.20: Purity (filled squares), efficiency (open points) and acceptance (dashed line) in bins of $p_T^{D^{*\pm}}$, $\eta^{D^{*\pm}}$, $z^{D^{*\pm}}$, Q^2, y and x.

7.8 Cross section definition

In this section the definition of measured D^* production cross sections is described. The kinematic region of the measured cross sections is:

$$\begin{aligned} &5 < Q^2 < 1000\ \mathrm{GeV}^2,\\ &0.02 < y < 0.7,\\ &|\eta^{D^*}| < 1.5,\\ &1.5 < p_T^{D^*} < 20\ \mathrm{GeV}. \end{aligned}$$

The differential cross section of the D^* production in a given bin of the measured observable ζ, corrected to the Born level, is given by:

$$\frac{d\sigma}{d\zeta} = \frac{N_{\mathrm{data}}^{D^*} - N_{\mathrm{php}}^{D^*}}{L \cdot BR \cdot \varepsilon \cdot \Delta\zeta} \cdot C_{\mathrm{QED}}, \tag{7.12}$$

where:

N^{D^*} is the number of D^*, measured at ZEUS in the given bin of ζ;

$N_{\mathrm{php}}^{D^*}$ is the D^* rate of the photoproduction background estimated with the Pythia MC and normalised as discussed in Section 7.6;

L is the integrated luminosity of the data collected by ZEUS, see Section 7.1;

$\Delta\zeta$ is the bin width of the measured observable ζ;

ε is the acceptance of the detector in the given bin of ζ, extracted from the MC and defined as in Section 7.7. The contribution from B-hadrons to D^* meson production is included in the acceptance;

C_{QED} is the correction to the QED Born level cross section. The incoming or scattered electron (positron) can undergo QED processes emitting a photon, thus introducing a bias to its initial or final energy. The correction is defined as

$$C_{\mathrm{QED}} = \frac{\sigma_{vis}^{Born}}{\sigma_{vis}^{Rad}}, \tag{7.13}$$

where σ_{vis}^{Born} is the RAPGAP cross section is the selected kinematic region without including QED radiation, but keeping the fine structure constant, α_{EM}, running and σ_{vis}^{Rad} is the RAPGAP cross section with QED radiation turned on [108, 121]. Typically, the QED correction ranges from 1 to 2 % ;

BR is the D^* branching ratio of the considered decay channel $\mathrm{BR}(D^{*+} \to D^0\pi^+) \times \mathrm{BR}(D^0 \to K^+\pi^-) = 2.627 \pm 0.053\%$ [10].

The single- and double-differential cross sections were measured in the common binning of the two experiments ZEUS and H1, which simplifies the combination and comparison and later combination of the measurements.

7.9 Systematic uncertainties

In this section a description of the systematic uncertainties of the measured cross section is given. The uncertainties themselves were calculated as $\delta = \frac{\sigma_{syst} - \sigma_{nom}}{\sigma_{nom}}$, where σ_{nom} is the nominal cross section and σ_{syst} is the cross section after the modification of the selection, extraction procedures etc. on a bin-by-bin basis. The final systematic uncertainty was calculated by summing up in quadratures the individual uncertainties. In the following, the considered sources of the systematic uncertainties are listed. The effect on the full visible cross section is given in brackets.

- Experimental apparatus:

  1. δ_1, energy scale of measured hadrons. To account for the differences of the hadron energy reconstruction in the detector with respect to the Monte Carlo simulation, the $E - p_z$ of the hadron system was shifted by $\pm$ 2% in the Monte Carlo according to the prescription [142] (± 0.5 %);
  2. δ_2, energy scale of the reconstructed electron. E'_e was shifted by $\pm$ 1% to account for the differences of the reconstructed electron energy in the detector with respect to the MC simulation for $E'_e > 10$ GeV according to [143] (± 1.1 %);
  3. δ_3, electron position. The alignment of the SRTD detector is known up to 2 mm. Therefore, to account for possible differences in the SRTD position in the simulation, the box cut was changed by applying shifts to the x and y coordinates of the box cut position by ± 2 mm [120, 143] (± 0.4 %);
  4. δ_4, reconstruction of DIS events. The size of the box cut of (15×15) cm^2 was varied in order to account for the non-homogeneity of the CAL response in regions that are not simulated in full detail by the MC. The variation was done in the data and in the MC by enlarging and squeezing the box cut by 1 cm. The upper variation, enlarging by 1 cm, cuts away a significant amount of statistics in the low y, low Q^2 bins. This makes this systematic uncertainty statistics dependent. Therefore only the down variation, reducing by 1 cm, was considered and the effect was symmetrised (± 0.3 %);
  5. δ_5, the tracking efficiency correction. The correction due to hadronic interaction described in Section 7.5.2 was varied by ± 50% (± 3 %);

6. δ_6, luminosity measurement. The luminosity uncertainty is 1.9%, see Section 7.1. This uncertainty is fully correlated, therefore it is listed separately. It was not included in the final numbers and is not shown in the cross section plots.

- Model uncertainties:

1. δ_7, the beauty quark contribution to the D^* cross section. The normalisation k_F^b was varied by $\pm 50\,\%$ to cover all beauty measurements by ZEUS ($\pm 0.1\,\%$);
2. δ_8, the photoproduction contribution. The normalisation factor k_F^{php} was varied by $\pm 100\,\%$ ($\pm 0.2\,\%$);
3. δ_9, the diffractive contribution. The normalisation factor k_F^{diff} for the diffractive events was varied by $\pm 50\,\%$ in order to cover previous ZEUS measurements [113] and to cover the tendency preferred by the ZEUS data, see Section 7.6 ($\pm 0.5\,\%$);
4. δ_{10}, the resolved contribution. Processes where the incoming photon has non point-like structure were included into the acceptance calculations. The MC reweighting function for η and factors for $p_T^{D^*}, Q^2$ were recalculated in order to make the MC describe the data ($\pm 1\,\%$);
5. δ_{11}, the $p_T^{D^*}, Q^2$ distribution reweighting. Reweighting factors were varied by $\pm 0.5 \cdot w_{p_T,Q^2}$ to account for possible shape differences of the distributions, see Section 7.5.4 ($\pm 0.8\,\%$);
6. δ_{12}, the η^{D^*} distribution reweighting. Reweighting factors were varied by $\pm 0.5 \cdot w_\eta$ to account for possible shape differences in the distributions ($< \pm 0.1\,\%$);
7. δ_{13}, the reweighting of the inelasticity distribution. RAPGAP has a tendency to underestimate D^* production in low y region. Thus, the reweighting of y distribution was performed on a bin-by-bin basis instead of the η reweighting as those two distributions are correlated. In the final uncertainty only δ_{13} was used instead of δ_{12} as it gave bigger effect ($\pm 0.7\,\%$).

- D^* signal extraction procedure:

1. δ_{14}, fit uncertainty. The Granet background function, see Section 7.4, was replaced by the function $f'(x) = A \cdot x^{\frac{3}{2}} + B \cdot x + C \cdot x^{\frac{1}{2}} + D$, where $x = \Delta M - m_{\pi^\pm}$. This function describes the WS and gives a reasonable quality of the fit ($\pm 0.2\,\%$);
2. δ_{15}, another fit uncertainty. The upper edge of the fit range was changed from 168.0 to 165.0 MeV ($< \pm 0.1\,\%$);

3. δ_{16}, D^* uncertainty of the correction for missed events outside the selection region, tails correction. The correction function, see Section 7.5.3, Equation 7.7, $t(x)$ was varied by $\pm\sqrt{\left(\frac{\delta a^2}{x}\right)^2 + \delta b^2}$, where δa and δb are the corresponding parameter uncertainties taken from the fit used to determine $t(x)$ ($\pm 4\,\%$);
4. δ_{17}, D^0 selection. The single-sided uncertainty of $+2\,\%$ was applied in each bin of the cross section to account for the D^0 tails, see Section 7.5.3.

- Acceptance correction uncertainty:

1. δ_{18}, statistical uncertainty of MC sample, used for the calculation of the acceptance, calculated with the binomial statistics approach as described in [144] ($\pm 1\,\%$);
2. δ_{19}, statistical uncertainty of the QED correction factors, calculated with the binomial statistics approach based on the additional RAPGAP MC samples used to determine the QED correction ($<\pm 0.1\,\%$).

- δ_{20}, branching ratio uncertainty from the PDG is 1.5%. As in the case for the luminosity measurement, it is listed separately.

The uncertainties of the ISOe correction and absolute tracking efficiency correction are found to be negligible ($<$0.5%) and thus were not considered. The full breakdown of the systematic uncertainties for each bin is given in Appendix H.

7.10 Theoretical predictions

The D^* production in DIS was calculated at next-to-leading order (NLO), $O(\alpha_s^2)$, in the fixed-flavour-number scheme (FFNS) (see Chapter 3). Both the single and double differential D^* production cross sections were calculated with the HVQDIS program [145].

The input parameters of the HVQDIS program were taken from the prescription of the HERA combination group [146]:

- the pole charm quark mass was set to $m_c = 1.50\,\mathrm{GeV}$;
- the renormalization and factorisation scales were set to be equal, $\mu_R = \mu_F = \sqrt{Q^2 + 4m_c^2}$;
- the strong coupling constant in the three-flavour FFNS was set to $\alpha_s^{\mathrm{nf}=3}(M_Z) = 0.105 \pm 0.002$;

- The PDFs were taken from a set of FFNS variants of the HERAPDF1.0 fit [147], obtained with the same m_c, μ_R, μ_F and α_s as used in the HVQDIS program;

- The HVQDIS program provides differential cross sections for c quark production. Therefore a fragmentation model [146] was implemented to allow a comparison to the measured D^* cross sections.

  The longitudinal fragmentation was performed in the $\gamma^* p$ centre of mass frame using the fragmentation function of Kartvelishvili, see Chapter 3, which is controlled by a single parameter, α_K. Different values of α_K are used in three different regions of the γ^*-parton centre-of-mass energy squared, $\hat{s}$. The parameters of the fragmentation function are reported in Table 7.4. More details about the fragmentation procedure can be found in [146];

- Transverse fragmentation was implemented assigning to the hadron a transverse momentum, k_T, with respect to the charm quark direction according to $f(k_T) = k_T \exp(-2k_T/\langle k_T \rangle)$, with $\langle k_T \rangle = 0.35 \pm 0.15$ GeV;

- The fraction of charm quarks hadronising into D^{*+} mesons was set to $f(c \to D^{*+}) = 0.2287 \pm 0.0056$ [148];

- The B-meson contribution to the $D^{*\pm}$ production was extracted from RAPGAP BGF MC processes and was added to the predictions by HVQDIS, as the beauty quark contribution is a part of the cross section definition.

$\hat{s}$ range (GeV^2)	α_K
$\hat{s} < \hat{s_1}$	6.1 ± 0.9
$\hat{s_1} < \hat{s} < 324$	3.3 ± 0.4
$\hat{s} > 324$	2.67 ± 0.31

Table 7.4: The parameters of the fragmentation function used for the calculation of $D^{*\pm}$ meson production. The first column shows the $\hat{s}$ range, with $\hat{s_1} = 70 \pm 40\,\mathrm{GeV}^2$. The particular value of α_K for each $\hat{s}$ range is given in the second column.

The uncertainties of the theoretical calculations were estimated by varying the setup parameters of the HVQDIS program, the effect on the total visible cross section is given in brackets:

- The fragmentation scale was varied by a factor two up and down ($^{+11}_{-16}$ %);

- The renormalization scale was varied by a factor two up and down independently of the fragmentation scale ($^{+12}_{-10}$ %);

- The charm quark mass was varied by $\pm 0.15\,\mathrm{GeV}$ ($^{+10}_{-9}\,\%$);
- The parameters of the fragmentation function $\hat{s}$ range and α_K were varied as given in Table 7.4 ($^{+3}_{-2}\%$) ;
- Variation of strong coupling constant by ± 0.002 ($< \pm 1\,\%$);
- The PDF uncertainties were calculated according to the HERAPDF1.0 prescription [147] and found to be negligible.

The total systematic uncertainty of the prediction was obtained by summing up all listed effects in quadratures.

7.11 Results

7.11.1 Total D^* cross section

The cross section of $D^{*\pm}$ meson production in DIS was measured for the visible kinematic phase space listed in Section 7.8, corrected to the Born level, as

$$\sigma^{vis}(D^{*\pm}) = \left[5.31\ \pm\ 0.08\,(\mathrm{stat.})\ \ ^{+0.27}_{-0.22}(\mathrm{syst.})\right]\ \mathrm{nb}\ \ \pm 1.9\%(\mathrm{L})\ \ \pm 1.5\%(\mathrm{BR}). \tag{7.14}$$

From the next-to-leading order QCD predictions by HVQDIS program with the settings parameters listed in the previous section, the total visible cross section is found to be

$$\sigma^{vis}(D^*)_{\mathrm{HVQDIS}} = \left[5.1\ \ ^{+1.0}_{-1.1}\ (\text{theory unc.})\right]\ \mathrm{nb}. \tag{7.15}$$

The theoretical predictions describe the measured visible cross section of the $D^{*\pm}$ production in DIS within the quoted theoretical and experimental uncertainties.

7.11.2 Single- and double-differential D^* cross sections

Single- and double-differential cross sections of the $D^{*\pm}$ production in deep-inelastic scattering were measured in the common phase space agreed by the two collaborations H1 and ZEUS [149]. The measurement is based on the full available statistics from HERA II with an integrated luminosity of 363 pb^{-1}. The phase space of the measurement is defined in Section 7.8.

Figure 7.21 shows the single-differential cross sections as functions of D^* observables: $p_T^{D^{*\pm}}$, $\eta^{D^{*\pm}}$ and $z^{D^{*\pm}}$. The cross sections fall with rising $p_T^{D^{*\pm}}$, while they remain almost flat with $\eta^{D^{*\pm}}$. The theoretical QCD predictions in next-to-leading order, as described in Section 7.10, are compared to the measured cross sections and found to be in good agreement within the quoted uncertainties. The predictions do not fully describe the measured cross sections in all $z^{D^{*\pm}}$ bins. This may suggest that the fragmentation treatment may require further investigations from the theoretical point of view. The Monte Carlo predictions for the BGF process from RAPGAP are also shown in Figure 7.21. The RAPGAP predictions are only LO, therefore they were scaled up by 10 % for the charm part in order to agree with the full visible cross section, see Section 7.11.1. The beauty component was scaled by a factor of 1.6 as discussed in Section 7.6. The MC predictions follow the measured data in shape.

Figure 7.22 shows the single-differential cross sections as a function of Q^2, y and x. The cross section falls with rising Q^2 by three orders of magnitude. A similar behaviour is seen with respect to x. As in the case of the D^* observables the NLO QCD predictions describe the measured cross sections within the quoted uncertainties.

The values of the cross sections as well as the uncertainties are reported in Tables 7.5 and 7.6.

Figure 7.23 shows the double-differential cross section of $D^{*\pm}$ production in deep-inelastic scattering in Q^2 and y for $Q^2 < 100\,\text{GeV}^2$. The previous measurement performed in the same "common" phase space by the H1 collaboration at low Q^2 [150] are compared to the current results. The H1 results are the most precise single measurement of $D^{*\pm}$ production in DIS so far. The two data sets are in a good agreement and have similar precision. As in the case of single-differential cross sections, the NLO calculations describe the data reasonably well.

Figure 7.24 shows the double-differential cross section of $D^{*\pm}$ production in deep-inelastic scattering in Q^2 and y for the region $100 < Q^2 < 1000\,\text{GeV}^2$. As in the low Q^2 case, the NLO theoretical predictions describe the data well. Previous H1 measurements in the high Q^2 region [151] are compared to the presented ZEUS measurements and found to agree within statistical uncertainties.

The measured double-differential cross section values are reported in Table 7.7.

A direct comparison of the $D^{*\pm}$ production cross sections to the HERA I measurements [61] is not possible since the previous measurements were performed in a different phase space and binning.

7.11.3 e^+/e^-p asymmetry

Previously the ZEUS collaboration measured the ratio of D^* production in e^-p and e^+p collisions [61]. The measurement was done on HERA I data with a luminosity of $79\,\text{pb}^{-1}$. According to this measurement some deviation of the ratio of $\sigma^{e^-p}/\sigma^{e^+p}$ from unity was observed in the region of $Q^2\!>\!40\,\text{GeV}^2$. There are no known physical processes that could explain this difference. The result was inter-

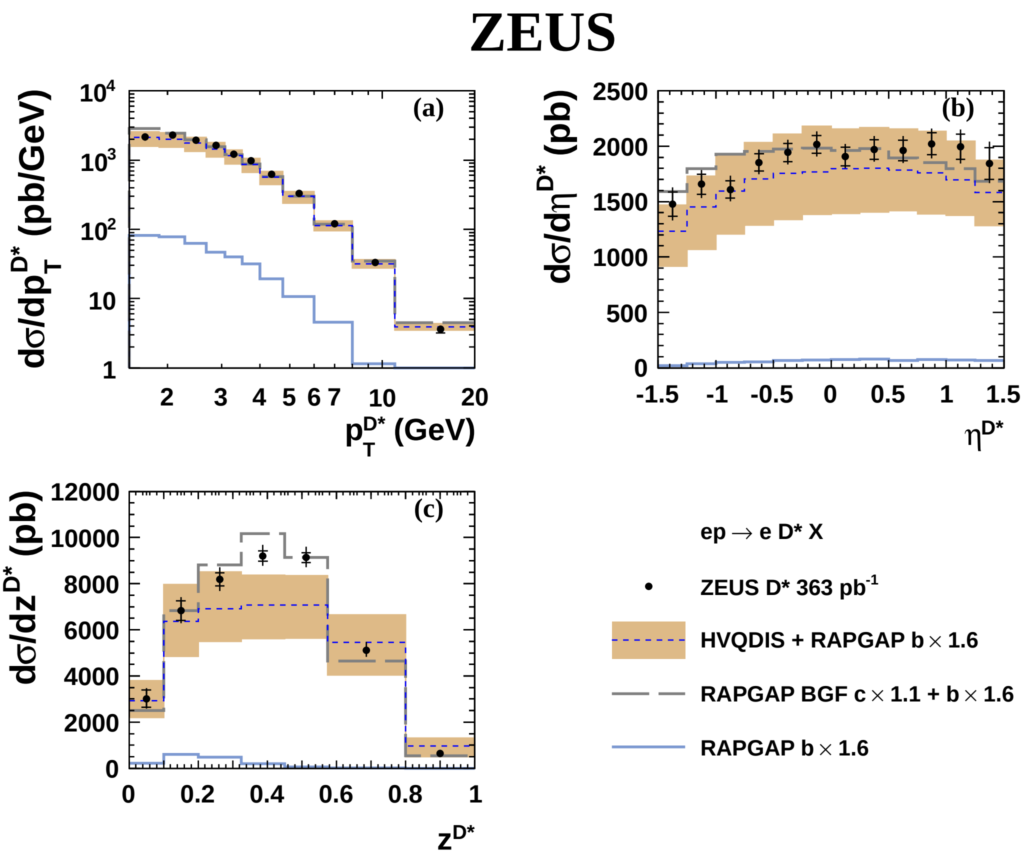

Figure 7.21: Single-differential cross section of the $D^{*\pm}$ production, marked with filled points, as functions of a) $p_T^{D^{*\pm}}$, b) $\eta^{D^{*\pm}}$ and c) z^{D^*}. The inner error bars represent the statistical uncertainty and the outer bar represents the statistical and systematic uncertainties added in quadratures. The NLO QCD theoretical predictions from HVQDIS are shown as a dashed line with theoretical uncertainties indicated by the band. The RAPGAP MC (long-dashed line) predictions are also shown. The beauty contribution from RAPGAP is shown as a separate blue solid line. The total prediction is the sum of the HVQDIS charm and scaled RAPGAP beauty predictions.

$p_T^{D^*}$ (GeV)	$d\sigma/dp_T^{D^*}$ (pb/GeV)	$\delta_{stat}(\%)$	$\delta_{syst}(\%)$	C_r
1.50 : 1.88	2160	9.9	$^{+7.0}_{-5.5}$	1.03
1.88 : 2.28	2300	5.8	$^{+5.4}_{-5.8}$	1.04
2.28 : 2.68	1950	4.4	$^{+5.0}_{-4.4}$	1.03
2.68 : 3.08	1630	4.0	$^{+4.7}_{-4.0}$	1.03
3.08 : 3.50	1220	3.8	$^{+4.9}_{-4.2}$	1.04
3.50 : 4.00	970	3.4	$^{+4.4}_{-3.7}$	1.03
4.00 : 4.75	630	3.2	$^{+4.2}_{-3.5}$	1.05
4.75 : 6.00	330	3.0	$^{+4.3}_{-3.7}$	1.01
6 : 8	120	3.8	$^{+4.1}_{-3.8}$	1.06
8 : 11	33	6.0	$^{+4.4}_{-3.7}$	1.11
11 : 20	3.6	12.3	$^{+5.3}_{-6.1}$	1.11
η^{D^*}	$d\sigma/d\eta^{D^*}$ (pb)	$\delta_{stat}(\%)$	$\delta_{syst}(\%)$	C_r
-1.50 : -1.25	1480.	7.5	$^{+6.8}_{-6.7}$	1.06
-1.25 : -1.00	1660	5.4	$^{+5.6}_{-5.3}$	1.05
-1.00 : -0.75	1610	4.9	$^{+6.1}_{-4.4}$	1.05
-0.75 : -0.5	1850	4.2	$^{+4.6}_{-3.8}$	1.03
-0.5 : -0.25	1940	4.2	$^{+4.3}_{-3.5}$	1.03
-0.25 : 0.00	2020	4.0	$^{+4.3}_{-3.7}$	1.04
0.00 : 0.25	1900	4.4	$^{+4.2}_{-3.4}$	1.04
0.25 : 0.50	1970	4.4	$^{+4.3}_{-3.3}$	1.05
0.50 : 0.75	1960	4.7	$^{+4.5}_{-3.6}$	1.03
0.75 : 1.00	2000	4.9	$^{+4.8}_{-4.2}$	1.02
1.00 : 1.25	2000	5.8	$^{+5.3}_{-5.1}$	1.01
1.25 : 1.50	1840	7.7	$^{+7.4}_{-5.6}$	1.01
z^{D^*}	$d\sigma/dz^{D^*}$ (pb)	$\delta_{stat}(\%)$	$\delta_{syst}(\%)$	C_r
0 : 0.1	3000	12.3	$^{+8.6}_{-7.1}$	1.00
0.1 : 0.2	6800	6.1	$^{+6.1}_{-5.0}$	1.01
0.2 : 0.325	8180	3.5	$^{+5.5}_{-4.9}$	1.02
0.325 : 0.45	9100	2.5	$^{+4.6}_{-3.8}$	1.03
0.45 : 0.575	9140	2.3	$^{+4.6}_{-4.0}$	1.05
0.575 : 0.8	5120	2.4	$^{+6.5}_{-5.1}$	1.07
0.8 : 1	630	9.1	$^{+9.9}_{-8.5}$	1.07

Table 7.5: Differential cross section of the $D^{*\pm}$ production in $p_T^{D^{*\pm}}$, $\eta^{D^{*\pm}}$ and $z^{D^{*\pm}}$ in the kinematic range $5 < Q^2 < 1000$ GeV^2, $0.02 < y < 0.7$, $1.5 < p_T^{D^{*\pm}} < 20$ GeV, $|\eta^{D^{*\pm}}| < 1.5$. The columns show the bin range, the bin-averaged differential cross section, the statistical and systematic uncertainties in percent and the QED correction factors, respectively. The overall normalization uncertainties from luminosity (1.9 %) and branching ratio (1.5 %) are not included.

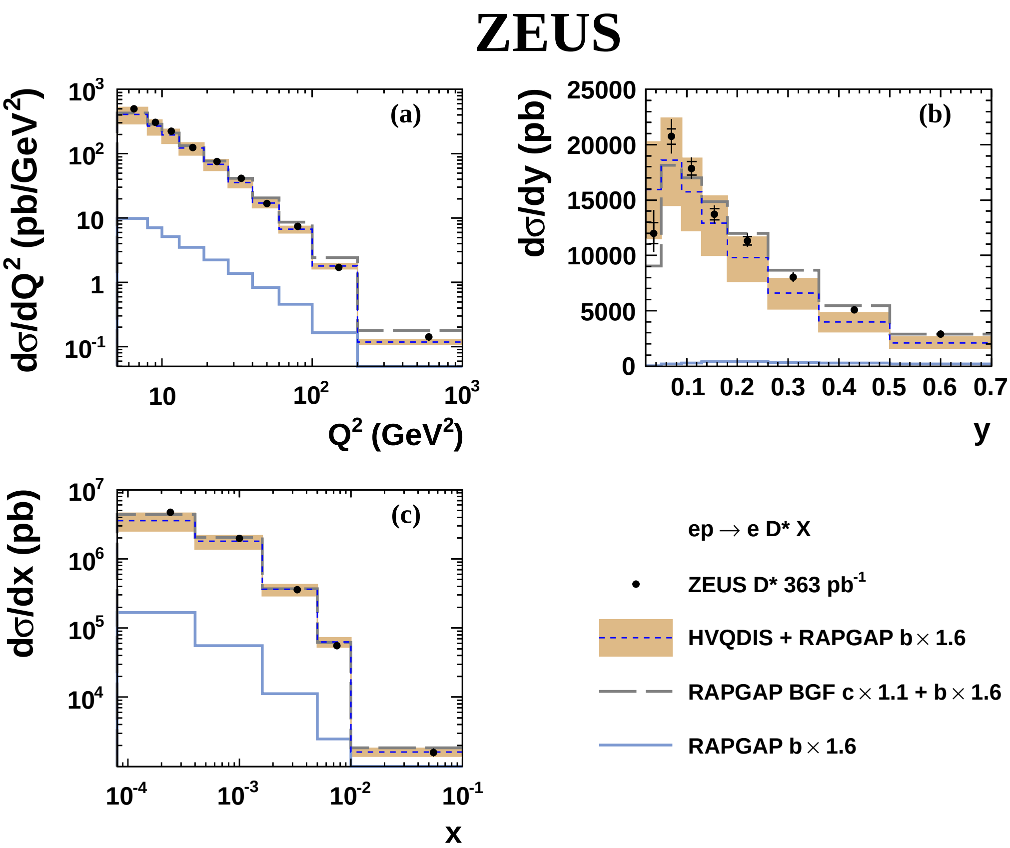

Figure 7.22: Single-differential cross section of the $D^{*\pm}$ production marked with filled points as a function of a) Q^2, b) y and c) x. The inner error bars represent the statistical uncertainties and the outer error bars represent the statistical and systematic uncertainties added in quadratures. The central values of the NLO QCD theoretical predictions from HVQDIS are shown as a dashed line with theoretical uncertainties indicated by the band. The scaled RAPGAP MC predictions (long-dashed line) are also shown. The scaled beauty contribution predicted by RAPGAP is shown as a separate blue solid line.

Q^2 (GeV^2)	$d\sigma/dQ^2$ (pb/GeV^2)	$\delta_{stat}(\%)$	$\delta_{syst}(\%)$	C_r
5 : 8	500	3.9	$^{+6.7}_{-6.1}$	1.03
8 : 10	310	4.3	$^{+6.0}_{-5.2}$	1.03
10 : 13	222	4.0	$^{+4.9}_{-4.1}$	1.02
13 : 19	125	3.5	$^{+5.6}_{-5.0}$	1.03
19 : 27.5	75	3.7	$^{+4.9}_{-4.0}$	1.04
27.5 : 40	41.5	3.9	$^{+4.8}_{-3.8}$	1.04
40 : 60	16.9	4.7	$^{+5.6}_{-5.6}$	1.05
60 : 100	7.5	5.0	$^{+7.1}_{-5.1}$	1.06
100 : 200	1.71	7.8	$^{+6.6}_{-4.4}$	1.07
200 : 1000	0.14	12.5	$^{+6.1}_{-5.2}$	1.14
y	$d\sigma/dy$ (pb)	$\delta_{stat}(\%)$	$\delta_{syst}(\%)$	C_r
0.02 : 0.05	12000	7.9	$^{+15.6}_{-11.8}$	1.07
0.05 : 0.09	20700	3.4	$^{+6.7}_{-6.5}$	1.05
0.09 : 0.13	17900	3.4	$^{+4.5}_{-4.0}$	1.04
0.13 : 0.18	13700	3.6	$^{+4.6}_{-4.8}$	1.04
0.18 : 0.26	11300	3.3	$^{+4.8}_{-3.7}$	1.04
0.26 : 0.36	8000	3.7	$^{+4.8}_{-4.0}$	1.03
0.36 : 0.50	5090	4.2	$^{+5.2}_{-4.5}$	1.02
0.50 : 0.70	2900	6.0	$^{+9.3}_{-7.1}$	1.01
x	$d\sigma/dx$ (pb)	$\delta_{stat}(\%)$	$\delta_{syst}(\%)$	C_r
$8 \cdot 10^{-5}$: 0.0004	$4750 \cdot 10^3$	3.5	$^{+6.0}_{-5.3}$	1.06
0.0004 : 0.0016	$1980 \cdot 10^3$	2.1	$^{+4.8}_{-3.9}$	1.03
0.0016 : 0.005	$357 \cdot 10^3$	2.6	$^{+4.9}_{-3.9}$	1.02
0.005 : 0.01	$55 \cdot 10^3$	5.7	$^{+6.3}_{-5.1}$	0.99
0.01 : 0.1	$1.59 \cdot 10^3$	10.7	$^{+9.2}_{-8.4}$	1.08

Table 7.6: Differential cross section of the $D^{*\pm}$ production in Q^2, y and x bins. See Table 7.5 for details.

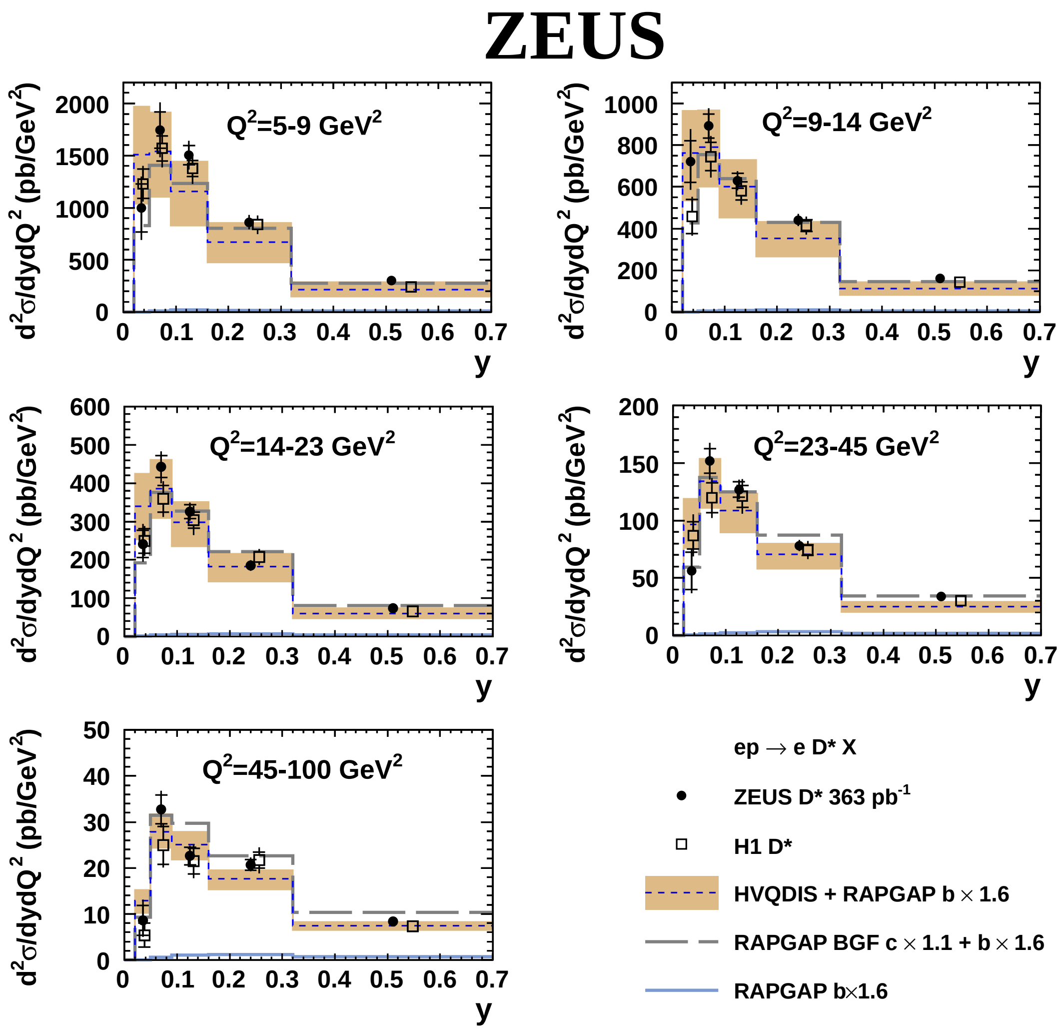

Figure 7.23: Double-differential cross section of the $D^{*\pm}$ production in bins of Q^2 and y for the region of $Q^2 < 100$ GeV^2. The results of this thesis are marked with filled black points. Measurements by the H1 collaboration are shown as open squares. In both, the inner error bars represent the statistical uncertainties and the outer eeror bars represent the statistical and systematic uncertainties added in quadratures. The NLO QCD theoretical predictions from HVQDIS as well as the scaled RAPGAP MC predictions (long-dashed line) are also shown. The scaled beauty contribution from RAPGAP is shown as a separate blue solid line.

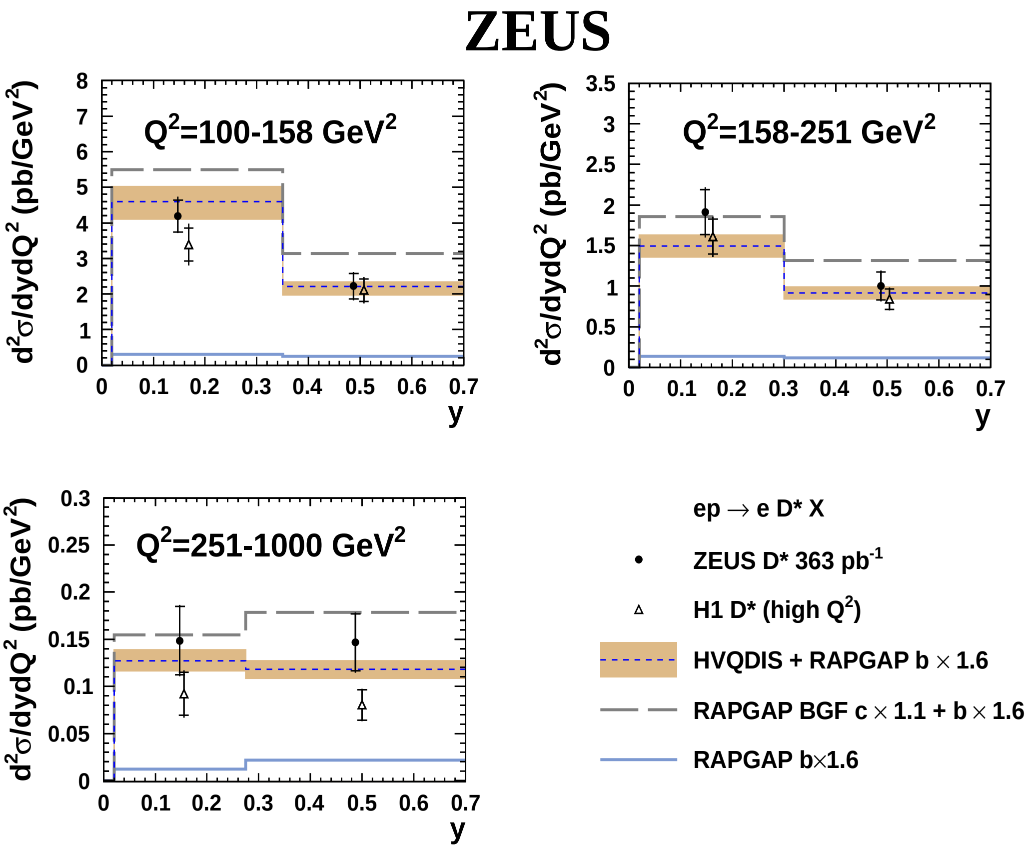

Figure 7.24: Double-differential cross section of the $D^{*\pm}$ production in bins of Q^2 and y for the region of $100 < Q^2 < 1000\,\mathrm{GeV}^2$. The results of this thesis are marked with filled black points. Measurements by the H1 collaboration are shown as open triangles. In both, the inner error bars represent the statistical uncertainties and the outer error bars represent the statistical and systematic uncertainties added in quadratures. The NLO QCD theoretical predictions from HVQDIS as well as the scaled RAPGAP MC predictions (long-dashed line) are also shown. The scaled beauty contribution from RAPGAP is shown as a separate blue solid line.

Q^2 (GeV^2)	y	σ_{vis} (pb)	$\delta_{stat}(\%)$	$\delta_{syst}(\%)$	$\sigma_{\mathrm{vis}}^{\mathrm{beauty}}$ (pb)	C_r
5 : 9	0.020 : 0.050	120	23.1	$^{+19.2}_{-20.1}$	0.0	1.04
	0.050 : 0.090	279	10.0	$^{+11.4}_{-11.1}$	1.5	1.04
	0.090 : 0.160	420	6.0	$^{+6.8}_{-7.0}$	5.2	1.04
	0.160 : 0.320	550	5.3	$^{+6.5}_{-5.8}$	11.0	1.03
	0.320 : 0.700	460	6.8	$^{+6.3}_{-5.5}$	18.2	1.02
9 : 14	0.020 : 0.050	108	13.9	$^{+16.5}_{-12.3}$	0.1	1.05
	0.050 : 0.090	178	6.5	$^{+7.0}_{-6.0}$	1.2	1.04
	0.090 : 0.160	220	5.8	$^{+4.7}_{-4.6}$	2.9	1.03
	0.160 : 0.320	352	5.1	$^{+4.5}_{-3.7}$	8.1	1.02
	0.320 : 0.700	307	7.2	$^{+6.6}_{-5.0}$	12.5	1.00
14 : 23	0.020 : 0.050	70	14.9	$^{+16.0}_{-12.1}$	0.2	1.07
	0.050 : 0.090	160	6.4	$^{+6.2}_{-7.2}$	1.2	1.04
	0.090 : 0.160	205	5.6	$^{+4.7}_{-4.7}$	3.1	1.03
	0.160 : 0.320	267	5.9	$^{+4.9}_{-4.4}$	9.0	1.03
	0.320 : 0.700	250	7.4	$^{+5.7}_{-6.7}$	13.5	1.01
23 : 45	0.020 : 0.050	37	29.1	$^{+17.6}_{-18.4}$	0.1	1.08
	0.050 : 0.090	134	7.0	$^{+7.5}_{-7.8}$	0.9	1.06
	0.090 : 0.160	196	5.3	$^{+4.4}_{-4.3}$	3.6	1.05
	0.160 : 0.320	275	5.1	$^{+4.1}_{-3.4}$	10.2	1.03
	0.320 : 0.700	284	6.1	$^{+6.4}_{-4.5}$	14.7	1.02
45 : 100	0.020 : 0.050	14	37.9	$^{+35.4}_{-17.8}$	0.0	1.25
	0.050 : 0.090	72	9.6	$^{+8.0}_{-7.2}$	1.2	1.07
	0.090 : 0.160	87	8.4	$^{+4.9}_{-4.6}$	3.9	1.04
	0.160 : 0.320	180	5.7	$^{+5.3}_{-3.9}$	9.4	1.04
	0.320 : 0.700	175	7.6	$^{+6.6}_{-5.6}$	14.0	1.02
100 : 158	0.020 : 0.350	80	10.6	$^{+7.6}_{-4.2}$	5.8	1.1
	0.350 : 0.700	45	16.2	$^{+7.6}_{-7.8}$	5.0	0.99
158 : 251	0.020 : 0.300	50	14.4	$^{+4.8}_{-6.3}$	3.5	1.16
	0.300 : 0.700	37	17.2	$^{+6.6}_{-4.9}$	4.3	1.04
251 : 1000	0.020 : 0.275	28	24.4	$^{+8.2}_{-10.0}$	2.4	1.26
	0.275 : 0.700	50	20.6	$^{+8.7}_{-5.1}$	6.9	1.07

Table 7.7: Visible cross sections of the $D^{*\pm}$ production in bins of Q^2 and y. The second last column reports the contribution from beauty decays, based on the RAPGAP MC rescaled to ZEUS data. See Table 7.5 for details.

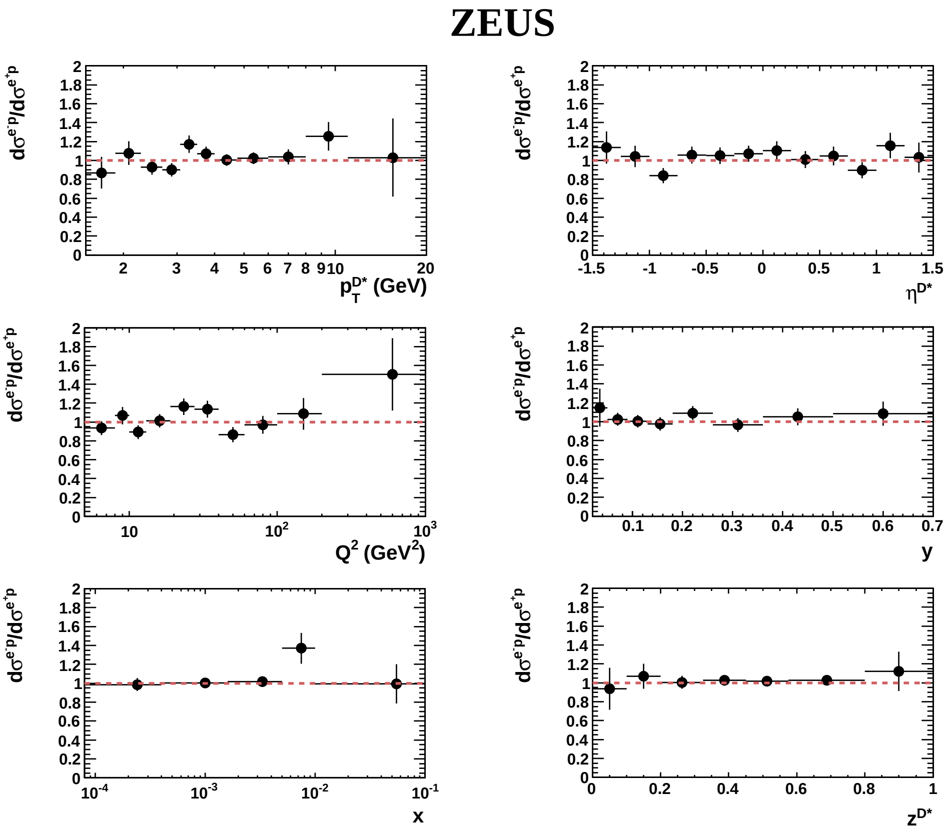

Figure 7.25: The ratio of $\sigma^{e^-p}/\sigma^{e^+p}$ as a function of $p_T^{D^{*\pm}}$, $\eta^{D^{*\pm}}$, Q^2, y, x and $z^{D^{*\pm}}$. The vertical lines represent the statistical uncertainties of the measurement, while the horizontal bars show the bin width and the dashed line is the unity line.

preted as a statistical fluctuation. The current measurement of D^* production in DIS is based on almost four times higher statistics, 187 pb^{-1} of the e^+p sample and 174 pb^{-1} of the e^-p sample. Therefore, the new measurement is able to check the result of HERA I.

The behaviour of the ratio $\sigma^{e^-p}/\sigma^{e^+p}$ was measured as functions of $p_T^{D^{*\pm}}$, $\eta^{D^{*\pm}}$, $z^{D^{*\pm}}$, Q^2, y and x in the same binning and kinematic range as in Section 7.11.2. The results are shown in Figure 7.25. Only statistical uncertainties are given. The systematic uncertainties partially cancel in the ratio and no dedicated studies were performed for this purpose. The current measurement shows that the ratio $\sigma^{e^-p}/\sigma^{e^+p}$ is consistent with unity within the quoted statistical uncertainties, confirming that the observation at HERA I was due to a statistical fluctuation.

7.12 Summary

Measurements of $D^{*\pm}$ production in deep inelastic scattering based on the full HERA II statistics of $363\,\text{pb}^{-1}$ are presented. The measurements were performed by reconstructing D^* mesons from the decay mode $D^{*\pm} \rightarrow D^0(\bar{D}^0)\,\pi_s^{\pm}$. The kinematic region covered by the measurements is $5 < Q^2 < 1000\,\text{GeV}^2$ and $0.02 < y < 0.7$ with $1.5 < p_T^{D^{*\pm}} < 20$ GeV and $|\eta^{D^{*\pm}}| < 1.5$. A new method for the extraction of the D^* yields was developed that allowed to reduce the statistical uncertainty of the combinatorial background with respect to the previous results [61, 74, 125]. The understanding of the systematic effects was also significantly improved, for example through corrections to the D^* peak tail. Inefficiencies of the track reconstruction related to the hadronic interactions as well as trigger related inefficiencies were implemented in order to obtain the correct acceptance corrections. The diffractive charm production was included in the MC simulation for a better description of the hadronic system by the simulations.

Differential cross sections as functions of $p_T^{D^{*\pm}}$, $\eta^{D^{*\pm}}$, $z^{D^{*\pm}}$, Q^2, y and x were presented as well as double-differential cross sections in bins of Q^2 and y. The theoretical NLO QCD predictions describe the measurements within the quoted uncertainties. The current ZEUS measurements show the same precision as the H1 measurements in the same phase space. As the measurement was performed in the common phase space, agreed by the H1 and ZEUS collaborations, further combinations or comparisons are much simplified. The present measurement shows much smaller statistical uncertainties than any of the previous measurements by ZEUS. Unfortunately, direct comparisons to the previous results is not possible at the level of visible cross sections as they were performed in a different phase space and binning.

Chapter 8

Measurement of $F_2^{c\bar{c}}$

Measurements of charm production can be performed with different experimental methods as well as with different analysis techniques and in different parts of phase space [61, 108, 130, 137, 149, 150]. Thus, any comparisons or combinations of results are only possible once the measurements are extrapolated to the full or a common phase space.

In this chapter the extraction of the charm contribution to the proton structure,F_2, see Chapter 2, is presented. The results are based on the double-differential cross section measurements of $D^{*\pm}$ production in DIS, presented in Chapter 7. The double-differential cross sections in Q^2 and x of $c\bar{c}$ pair production can be written as:

$$\frac{d^2\sigma^{c\bar{c}}}{dx\,dQ^2} = \frac{2\pi\alpha_{em}^2}{xQ^4}\,(1+(1-y)^2)\left[F_2^{c\bar{c}}(x,Q^2) - \frac{y^2}{1+(1-y)^2}F_L^{c\bar{c}}(x,Q^2)\right], \tag{8.1}$$

where $F_2^{c\bar{c}}$ is the charm contribution to the inclusive structure function F_2 and $F_L^{c\bar{c}}$ is the charm contribution to the longitudinal structure function F_L originating from the exchange of longitudinally polarised photons. The latter is only relevant at high-y and its contribution is small in the kinematic range of this analysis of the order of a few percent [152].

8.1 Extraction techniques

The charm contribution to the proton structure function, $F_2^{c\bar{c}}$, can be expressed in terms of reduced cross sections as

$$\sigma_{\rm red}^{c\bar{c}}(x,Q^2) = F_2^{c\bar{c}}(x,Q^2) - \frac{y^2}{1+(1-y)^2}F_L^{c\bar{c}}(x,Q^2). \tag{8.2}$$

The reduced cross sections of charm production can be obtained by the extrapolation of the double-differential cross sections to the full phase space using theoretical predictions. In the present measurement the extrapolation from the visible $D^{*\pm}$ production cross section in the phase space $1.5 < p_T^{D^{*\pm}} < 20\,\mathrm{GeV}$ and $|\eta^{D^{*\pm}}| < 1.5$ to the full D^* kinematic range was done using the HVQDIS predictions described in Chapter 7. The beauty contribution to D^* production, σ_{beauty}, was subtracted from the visible D^* cross section, σ_{vis}, by using the predictions from the RAPGAP MC generator scaled up by $k_F^b = 1.6$, see Chapter 7. Thus, the extrapolation procedure was done according to the formula

$$\sigma_{\mathrm{red}}^{c\bar{c}}(x,Q^2) = \left(\sigma_{\mathrm{vis}} - \sigma_{\mathrm{vis}}^{\mathrm{beauty}}\right)\left(\frac{\sigma_{\mathrm{red}}^{c\bar{c}}(x,Q^2)}{\sigma_{\mathrm{vis}}}\right)_{\mathrm{Hvqdis}}. \tag{8.3}$$

The reference x, Q^2 points at which the σ_{red} were extracted, are chosen to be close to the average x and Q^2 inside each measured bin. The extrapolation factor is defined as

$$\epsilon = \frac{1}{A}, \tag{8.4}$$

where the A is the kinematic acceptance calculated as

$$A = \frac{\sigma_{\mathrm{vis}}}{\sigma^{c\bar{c}}}. \tag{8.5}$$

The resulting ϵ ranges from up to 40 % at low y, low Q^2, to 15 % at high y and high Q^2.

The uncertainty of the extrapolation was obtained by varying the parameters of the NLO QCD predictions used for the extrapolation. The variation was obtained according to the prescription of [146] with the exception that the experimental uncertainties of the PDFs were neglected. The theoretical uncertainty evaluation in [146] differs from the one used for the comparisons to the single- and double-differential cross sections. An additional uncertainty was obtained from the uncertainty on the subtracted beauty component that was varied by ±50%. The treatment of the scale uncertainties, factorisation and renormalization, differs from the one used to compare to the double-differential cross sections. In this case the scales were varied simultaneously. Those two uncertainties, the scale uncertainty from the NLO calculation for the comparisons and the scale uncertainty of the extrapolation, refer to different aspects. For the former one, the description of the absolute cross section values is necessary, while for the latter only the description of the shape is important.

8.2 Combined measurements of $F_2^{c\bar{c}}$

Before discussing the result of the present measurement of $F_2^{c\bar{c}}$ it is worthwhile to cover previous measurements that will be compared to the currents ones. Recently the H1 and ZEUS collaborations made a combination of the published measurements of charm production in DIS, see Chapter 3, from the HERA I and HERA II periods [146]. Measured reduced cross sections for charm production were obtained in the kinematic range of $2.5 \leqslant Q^2 \leqslant 2000$ GeV^2 and $3 \cdot 10^{-5} \leqslant x \leqslant 5 \cdot 10^{-2}$. The combination yielded a twice better precision than any of the individual input data sets.

The combined measurements were used to perform a QCD analysis, yielding a measurement of the running charm quark mass in the $\overline{MS}$ scheme using the FFNS fit

$$m_c(m_c) = 1.26 \ \pm \ 0.05(\mathrm{exp}) \ \pm \ 0.03(\mathrm{mod})\,\mathrm{GeV}, \tag{8.6}$$

where only experimental and model uncertainties are listed. Also a fit was performed to determine the optimal value of the charm mass parameter, M_c, for a number of heavy flavour treatment schemes. The inclusion of the charm data into parton distribution function fits introduced further constraints on the PDFs. Thus, the uncertainty on the gluon distribution function was reduced, mostly due to a reduction in the parametrisation uncertainty coming from the constraints that the charm data put on the gluon through the $\gamma\, g \to cc$ process. The uncertainty of the charm sea distribution, $x\bar{c}$, was reduced because of reduction of the variation of M_c. The uncertainty on the $x\bar{u}$ and $x\bar{d}$ sea distributions also decreased through the constraints on $x\bar{U}$ and $x\bar{D}$ coming from the inclusive data.

8.3 Theoretical predictions

For the purpose of global comparisons, the theoretical calculation of $\sigma_{c\bar{c}}$ were performed in the generalised-mass variable-flavour-number scheme (GM-VFNS), explained in Chapter 3. The transition region between massive, $Q^2 \leq m_c^2$, and massless, $Q^2 \gg m_c^2$, calculations, was interpolated using the RT "standard" [153, 59] variant of the GM-VFNS at NLO, corresponding to $O(\alpha_s^2)$ for the massive part and $O(\alpha_s)$ for the massless part. The HERAPDF 1.5 [154] parton density fit to inclusive DIS HERA data was used for the PDFs. For the central prediction a special set with $m_c = 1.5\,\mathrm{GeV}$ was used [155, 136], which is more symmetric with respect to the charm mass variation than the default value of $m_c = 1.4$ GeV that was released with HERAPDF 1.5. Note that HERAPDF 1.5 does not include any of the charm measurements.

The uncertainty of the predictions was estimated as the sum of the experimental, parametrisation and model uncertainties used in the PDF fit added in quadrature. The largest uncertainty comes from the variation of the charm mass parameter by $\pm 0.15\,\mathrm{GeV}$ around the value of $m_c = 1.5\,\mathrm{GeV}$. It was treated as a model uncertainty. However, this is correlated with the variation of the parameter $Q_0^2 = 2.0$ GeV^2 at which the PDF is parametrised. When the parameter was varied upwards, $Q_0^2 = 2.5\,\mathrm{GeV}^2$, the mass of charm quark was increased to $m_c = 1.6\,\mathrm{GeV}$ due to threshold effects of the heavy flavour treatment scheme.

8.4 Results

Results of the measurement of the charm contribution to the proton structure by reconstructing the full kinematic decay mode of $D^{*\pm}$ mesons are presented in Table 8.1 in terms of reduced cross sections, $\sigma_{\mathrm{red}}^{c\bar{c}}$.

Figure 8.1 shows the measurement as a function of x for a given value of Q^2. The predictions from HERAPDF 1.5 presented in Section 8.3 are compared to the current measurements and found to be in agreement. It is worth to notice that the HERAPDF 1.5 was extracted from HERA measurements that do not contain any of the charm data.

Also, the combined previous measurements from HERA (see Section 8.2) are compared to the present ones. Two measurements are in very good agreement. The D^* results from ZEUS show a similar precision in some of the points as the combined measurements. Therefore, further constraints on the PDFs and further improvement of the uncertainty of the charm measurement can be obtained by including the present measurement to the final combination from HERA.

Figure 8.2 shows the current D^* results compared to the recent ZEUS measurement of charm production with reconstruction of $D^{\pm}$ mesons [108, 156]. The two measurements are in good agreement. The D^* measurement has a better signal to background ratio, and is therefore more precise.

8.5 Summary

The extrapolation of measurement of charm production of this thesis to the full phase space was presented. The measurement is in agreement with recent combined results from the H1 and ZEUS experiments and with the latest ZEUS results from $D^{\pm}$. The D^* results alone have similar precision as the combined ones.

The HERAPDF 1.5 predictions for reduced charm cross sections describe the results. The measurement will serve as a valuable input for future HERA combined charm measurements and can further improve the gluon PDF and the measurement of the charm quark mass parameter.

Q^2 (GeV^2)	x	$\sigma_{\text{red}}^{c\bar{c}}$	$\delta_{\text{stat.}}$ (%)	$\delta_{\text{syst.}}$ (%)	$\delta_{\text{theo.}}$ (%)
7	0.00160	0.057	23.1	$^{+17.0}_{-18.0}$	$^{+18.1}_{-9.7}$
	0.00080	0.124	10.0	$^{+9.3}_{-9.1}$	$^{+10.0}_{-5.4}$
	0.00050	0.166	6.1	$^{+6.7}_{-7.1}$	$^{+8.7}_{-4.7}$
	0.00030	0.191	5.4	$^{+5.5}_{-4.7}$	$^{+7.3}_{-5.2}$
	0.00013	0.258	7.1	$^{+6.0}_{-5.1}$	$^{+10.8}_{-9.0}$
12	0.00300	0.098	13.9	$^{+16.4}_{-12.3}$	$^{+19.2}_{-9.7}$
	0.00150	0.153	6.6	$^{+6.7}_{-5.6}$	$^{+9.4}_{-6.5}$
	0.00080	0.177	5.9	$^{+4.4}_{-4.3}$	$^{+8.1}_{-4.7}$
	0.00050	0.244	5.2	$^{+4.5}_{-3.6}$	$^{+6.0}_{-4.9}$
	0.00022	0.350	7.5	$^{+6.6}_{-5.0}$	$^{+8.1}_{-7.1}$
18	0.00450	0.081	14.9	$^{+16.1}_{-12.2}$	$^{+16.9}_{-9.5}$
	0.00250	0.169	6.5	$^{+6.2}_{-7.3}$	$^{+8.0}_{-6.7}$
	0.00135	0.202	5.7	$^{+4.7}_{-4.7}$	$^{+7.9}_{-5.1}$
	0.00080	0.224	6.1	$^{+4.9}_{-4.4}$	$^{+5.9}_{-5.0}$
	0.00035	0.343	7.8	$^{+5.7}_{-6.7}$	$^{+6.5}_{-6.8}$
32	0.00800	0.068	29.2	$^{+17.6}_{-18.5}$	$^{+14.6}_{-10.8}$
	0.00550	0.160	7.0	$^{+7.5}_{-8.1}$	$^{+9.1}_{-6.2}$
	0.00240	0.238	5.5	$^{+4.4}_{-4.3}$	$^{+7.6}_{-4.1}$
	0.00140	0.277	5.3	$^{+4.1}_{-3.4}$	$^{+6.5}_{-4.4}$
	0.00080	0.412	6.4	$^{+6.4}_{-4.5}$	$^{+5.6}_{-5.4}$
60	0.01500	0.068	37.9	$^{+35.4}_{-17.9}$	$^{+15.1}_{-8.6}$
	0.00800	0.176	9.7	$^{+8.0}_{-7.3}$	$^{+6.6}_{-5.6}$
	0.00500	0.169	8.8	$^{+4.9}_{-4.6}$	$^{+6.4}_{-4.7}$
	0.00320	0.273	6.0	$^{+5.3}_{-3.9}$	$^{+6.5}_{-5.0}$
	0.00140	0.359	8.2	$^{+6.6}_{-5.6}$	$^{+5.7}_{-5.7}$
120	0.01000	0.141	11.5	$^{+7.6}_{-4.2}$	$^{+7.0}_{-6.2}$
	0.00200	0.329	18.2	$^{+7.6}_{-7.8}$	$^{+7.1}_{-6.9}$
200	0.01300	0.191	15.5	$^{+4.8}_{-6.3}$	$^{+5.6}_{-5.4}$
	0.00500	0.275	19.4	$^{+6.6}_{-4.9}$	$^{+7.8}_{-8.0}$
350	0.02500	0.113	26.6	$^{+8.2}_{-10.0}$	$^{+5.8}_{-6.0}$
	0.01000	0.234	24.2	$^{+8.7}_{-5.1}$	$^{+9.6}_{-9.2}$

Table 8.1: The reduced cross sections, $\sigma_{\text{red}}^{c\bar{c}}(x, Q^2, s)$, with statistical, systematic and theoretical uncertainties.

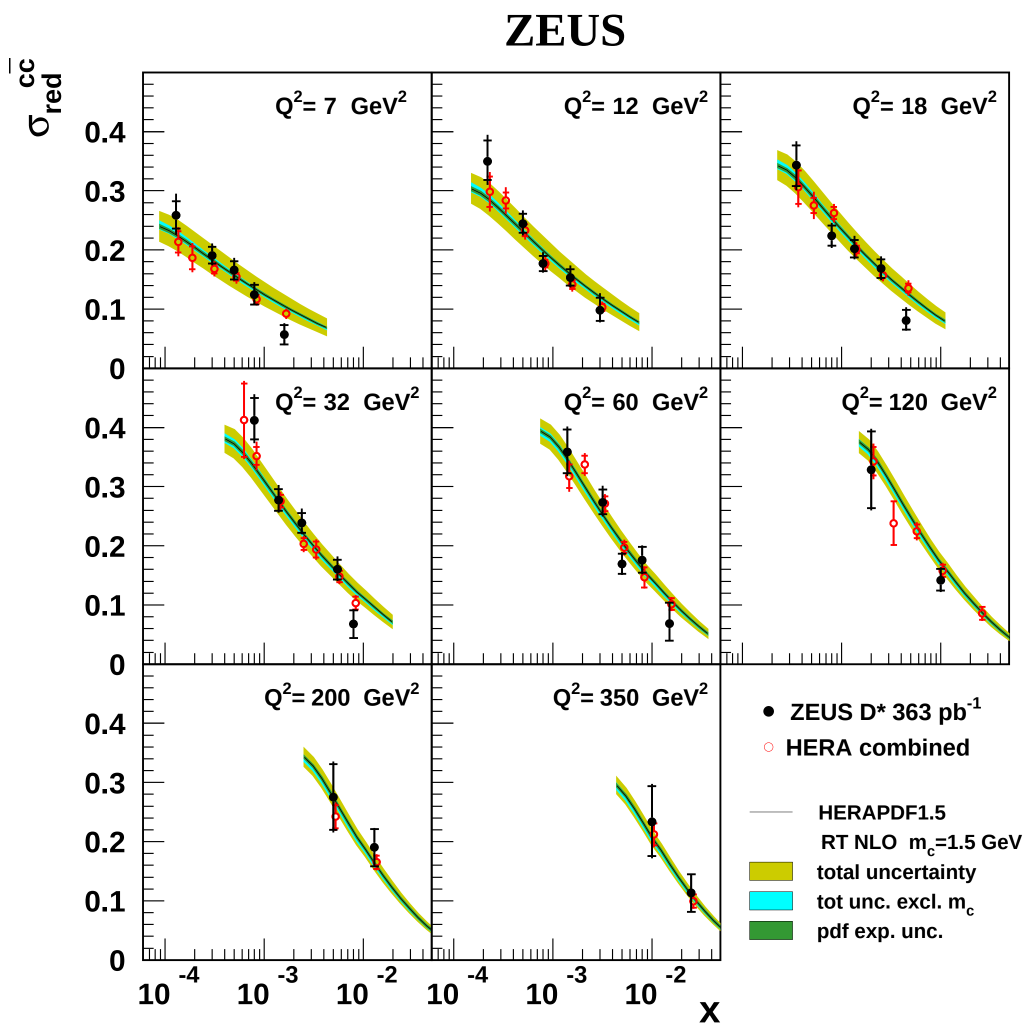

Figure 8.1: Reduced cross sections of charm production, $\sigma_{\mathrm{red}}^{c\bar{c}}$, as functions of x for given value of Q^2. The measurement of this thesis is marked with black filled points. The inner error bars represent the full experimental uncertainty, while the outer line includes the extrapolation uncertainty. The red open points are the HERA combined measurements with inner error bars corresponding to the uncorrelated part of the uncertainty. Theoretical predictions from HERAPDF 1.5 are shown as black solid line for the central values, with colour bands corresponding to different parts of the prediction uncertainties. The largest band on the HERAPDF 1.5 prediction represents the total uncertainty which includes the experimental, parametrisation and the model uncertainty of the PDF fit, including the charm mass variations. Also shown is the sum in quadratures of all uncertainties excluding those involving the charm mass variations, and the experimental uncertainty on the PDFs.

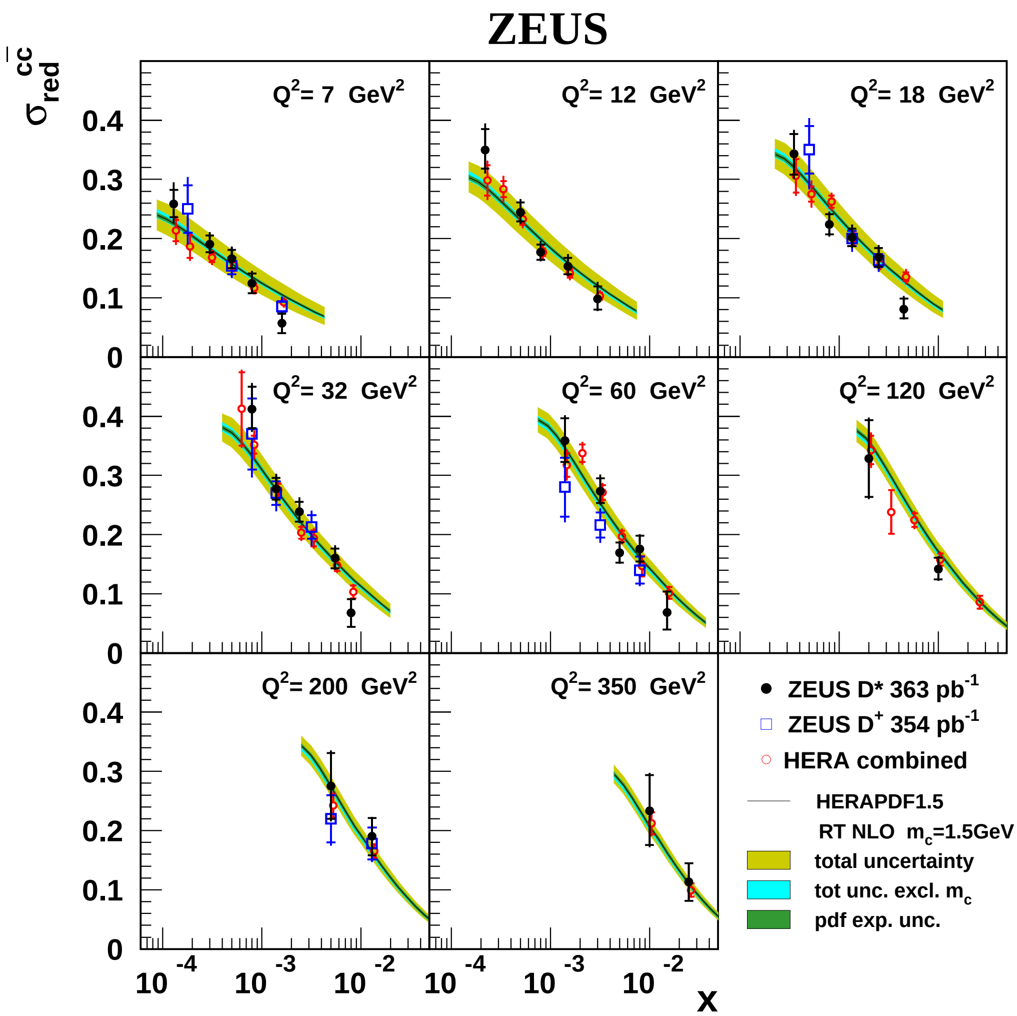

Figure 8.2: Reduced cross sections of charm production, $\sigma_{\rm red}^{c\bar{c}}$, as functions of x for given values of Q^2. The measurement of this thesis is marked with black filled points, the HERA combination results are shown as red open points. The latest ZEUS measurement with $D^{\pm}$ mesons are shown as blue open squares. The predictions from HERAPDF 1.5 are shown as colour bands as in Figure 8.1.

Chapter 9

Conclusions

In this thesis measurement of the production of charm quarks in deep-inelastic scattering at HERA at the centre-of-mass energy of 318 GeV is presented. The analysis was performed on data collected with the ZEUS detector during 2004-2007 with an integrated luminosity of $363\,\mathrm{pb}^{-1}$. Charm quarks were tagged by the presence of $D^{*\pm}$ mesons. The latter were measured from the full kinematic reconstruction of the decay channel $D^{*\pm} \to D^0/\bar{D}^0\,\pi^\pm$ with the subsequent decay of D^0 (or $\bar{D}^0$) to $K^\mp\,\pi^\pm$. The visible phase space of the measurement was $5 < Q^2 < 1000\,\mathrm{GeV}^2$ $0.02 < y < 0.7$ with Q^2 being the exchanged photon virtuality and y being the inelasticity. The visible $D^{*\pm}$ kinematic phase space was determined by the transverse momentum $1.5 < p_T^{D^{*\pm}} < 20\,\mathrm{GeV}$ and by the pseudorapidity $|\eta^{D^{*\pm}}| < 1.5$. This corresponds to the common phase space agreed upon between the H1 and ZEUS collaborations. A new method to extract $D^{*\pm}$ signal was used which resulted in a reduction of the statistical uncertainty with respect to previous analyses of this kind in addition from the reduction from the higher luminosity. In line with the improved precision, systematics effects that were previously not considered were investigated.

The full visible cross section of $D^{*\pm}$ production was measured to be

$$\sigma^{\mathrm{vis}}(D^*) = 5.31\ \pm\ 0.08\,(\mathrm{stat.})\ {}^{+0.27}_{-0.22}(\mathrm{syst.})\ \mathrm{nb}.$$

Single-differential cross sections of $D^{*\pm}$ production were measured as a function of Q^2, y and x and also as a function of $p_T^{D^{*\pm}}$, $\eta^{D^{*\pm}}$ and $z^{D^{*\pm}}$. The results were compared to theoretical predictions at next-to-leading order of α_s by HVQDIS. The theory describes the $p_T^{D^{*\pm}}$ and $\eta^{D^{*\pm}}$ differential cross sections within the quoted uncertainties, while for the $z^{D^{*\pm}}$ distribution, the prediction does not fully describe the shape of the distribution. This may indicate some imperfection of the treatment of fragmentation in theory.

Double-differential cross sections in 31 bins of Q^2 and y were measured and compared to the $D^{*\pm}$ measurements published by the H1 collaboration in the same phase space. The two measurements are in good agreement and have similar precision. Theoretical NLO QCD predictions describe the measured ZEUS results within the uncertainties.

The double-differential cross sections were used to extract the charm contribution to the proton structure function F_2, $F_2^{c\bar{c}}$ expressed in terms of the reduced charm production cross sections, $\sigma_{\mathrm{red}}^{c\bar{c}}$. The reduced cross sections were extracted from the visible charm cross sections by extrapolation to the full $D^{*\pm}$ phase space. The results were compared to the predictions from HERAPDF 1.5. The predictions describe the data. Also, the results were compared to the recent HERA combination measurement which does not contain the ZEUS $D^{*\pm}$ results presented here. The two results are in good agreement and have a similar precision. Recently, also new measurements of charm production tagged by D^+ mesons with ZEUS were performed. Those results are in agreement with the one presented here. The $D^{*\pm}$ measurements are significantly more precise. The current ZEUS results will improve future combination of the HERA charm measurements.

Appendix A

Power pulsing studies for the PLUME project

In this chapter power pulsing studies in the context of a vertex detector for a future Linear Collider (LC) are summarised. The studies for this report were performed with a single silicon pixel sensor chip called MIMOSA26. The basic concepts of CMOS technology, the MIMOSA26 chip and different methods of power pulsing are discussed. Investigation of the different methods was performed with a ^{55}Fe radioactive source.

A.1 The PLUME project

In this studies the main focus was put on future tracking detectors within the framework of detectors at the International Linear Collider (ILC) [157]. A linear electron-positron collider will be one of the possible accelerator machines in the post-LHC era. It will be dedicated to study physics phenomena with high precision. At the ILC a precise reconstruction of secondary vertices is one of the key issues. An excellent single hit resolution of about 2 μm for a track momentum of $p = 1$ GeV and the impact parameter resolution of $\sqrt{(5\ \mu\mathrm{m})^2 + (\frac{10\ \mu\mathrm{m}}{\mathrm{p}\sin(\theta^{2/3})})^2)}$ [157] is required.

Another very important milestone is the reconstruction of particles with short life times, like B and D mesons. They have to be precisely detected within the innermost layers of the tracker that enclose the beam pipe, the vertex detector. Thus, the amount of material in the tracker should be low enough not to influence the track reconstruction performance with multiple hadronic interactions. Therefore, the material budget for the vertex detector is proposed to be $\sim 0.1\%$ of the radiation length, X_0, per layer. This limitation is really significant with respect to e.g. present ATLAS inner tracker, where it is up to 30 % of X_0 in the central tracking region [158]. The physical prospects are challenging on the detector side and has triggered many

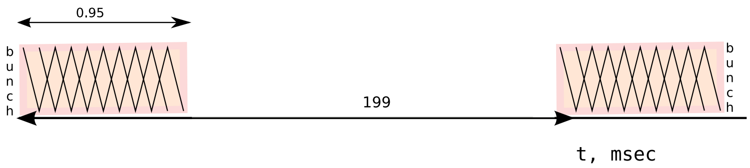

Figure A.1: ILC machine time structure at 5 Hz repetition rate. Every 199 ms a bunch train comes. The bunch train consists of ~ 3000 bunches and has a duration of 0.95 ms.

continuing research and development groups around the globe.

Due to high power dissipation, silicon detectors are heating up and typically active cooling with cooling pipes are used to transport the heat away from the detector. Such cooling pipes introduce a lot of material into a vertex detector and are not an option for a vertex detector at the ILC and other means of cooling or power reduction have to be investigated.

According to the ILC machine time structure, there will be a bunch train every 200 ms, giving a repetition rate of 5 Hz, see Figure A.1. Between the bunch trains are non-bunch periods of a 199 ms length. That rises the possibility to use the non-bunch periods to cool down the detectors by turning them off for a certain time. Such a power cycling method is called Power Pulsing (PP). There is no commonly approved scheme to do power pulsing yet and thus the technical realisation need to be defined.

Pixel Ladder with Ultra-low Material budget (PLUME) is a dedicated R&D project aiming to produce a demonstrator ladder for the vertex detector for the International Linear Detector (ILD) by the end of 2012 [159]. A goal of this project is to study the power pulsing possibilities of MIMOSA26 implemented in such a ladder. In the scope of the presented research, three types of possible PP methods for a single detector chip are discussed.

The ladder concept for PLUME is shown in Figure A.2. There are two modules, each equipped with six MIMOSA26 sensors thinned down to 50 μm and glued onto the supportive silicon carbide foam forming a sandwich-type structure. More details about the pixel sensors will be given as follows. The sensitive length of the ladder is 12.5 cm with a thickness of 2 mm and the achieved material budget is 0.3 % of X_0 (for the two layers) of the radiation length. Several studies [160] for the ladder validation such as ladder design, test of the detector performance under the particle test beam conditions, investigation of the thermal dissipation along the ladder are ongoing. Also mechanical stability of the ladder under operation in magnetic field and simulations of the ladder geometry are also subjects of the research. Finally, the investigation of a MIMOSA26 chip behaviour under power pulsing conditions is

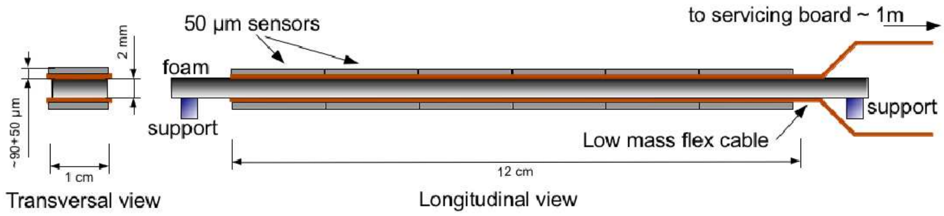

Figure A.2: PLUME double-sided ladder design.

the subject of the present studies.

A.2 MIMOSA26

A MIMOSA26 chip is a Monolithic Active Pixel Sensor (MAPS) [161] where the sensitive area and the readout electrons are grown together on one substrate. The chip is based on the CMOS technology substrate with p- and n-tubes, implanted in lightly doped p-epitaxial silicon, grown on a highly-doped p-substrate. A logic element of CMOS-type contains both n- and p-type MOS transistors [162], called nMOS and pMOS respectively. The nMOS has negative free charge carriers, while pMOS has positive ones.

Each MOS element has a sandwich-like structure made by conducting and insulating materials as shown in Figure A.3(a). It consists of the conducting gate, built up from polysilicon, the silicon bulk (body) and the glass insulator. The gate serves as a control input. Two transistor types, nMOS and pMOS, operate with different logic, described in the following. The body of nMOS is grounded ($V_{GND} \sim 0\,V$), thus the p-n junctions between the source and the body and between the drain and

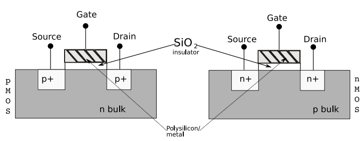

(a)

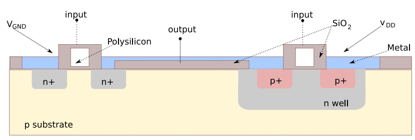

(b)

Figure A.3: (a) Structure of a single MOS element. (b) Structure of a single CMOS element.

the body make a reverse-bias diode [163]. When there is a rising voltage on the gate the nMOS element is open, and if the gate is at ground voltage, the element is closed or OFF. For the pMOS the bulk is at high potential, V_{DD}, and if the voltage on the gate is also high, the transistor goes OFF and gets ON when the gate voltage starts to drop.

The combined CMOS element, see Figure A.3(b), takes an advantage of using both MOS transistor types, thus providing a stable logic zero if pMOS is OFF, and a stable logic one, when nMOS is OFF. CMOS-type transistors have low power consumption, thus, elements operate at low voltages and show low level of noise.

A MIMOSA26 chip is only one type in the MIMOSAs series. Its sensitive layer is made of a junction between the n-well and the p-type epitaxial layer. The principle of detection of charged particles is illustrated in Figure A.4(a). An incoming particle produces electron-hole pairs in the epitaxial layer. The electrons diffuse thermally inside the layer which lies between the two highly-doped zones, the substrate and the p-wells. The concentration of dopants in the latter is three orders of magnitude higher than in the epitaxial layer. That translates into a potential barrier at the region boundaries. As a consequence, electrons remain inside the epitaxial layer. N-wells collect the electrons passing in their neighbourhood. The density of the n-wells is the leading parameter for the sensor spatial resolution.

A MIMOSA26 consists of 576×1152 pixels with a pitch size of a $18.4\,\mu$m. The active area is $(10.6 \times 21.2)\,\text{mm}^2$. Each pixel of MIMOSA26 includes amplification and correlated double sampling (CDS). Each column of pixels ends with a discriminator performing the analogue to digital conversion. The information from the pixels with zero signal is suppressed in order to increase the readout frequency [164]. It is built in the bottom of the sensitive matrix and the corresponding algorithm of the zero-suppression is invoked after the analogue-to-digital conversion. An embedded JTAG

(a) (b)

Figure A.4: (a) Illustration to the particle detection principle with MIMOSA. (b) A photo of a MIMOSA26 chip with a schematic layout drawn on top.

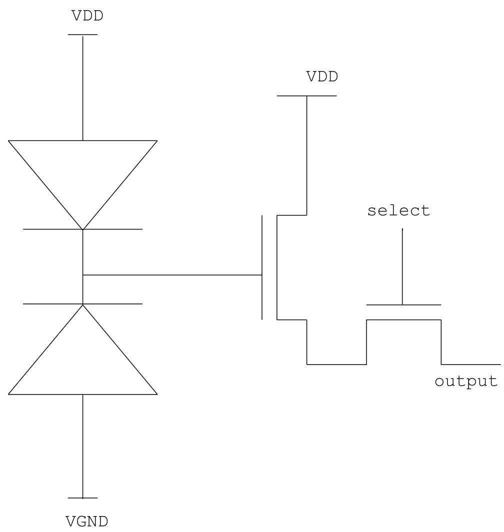

Figure A.5: Pixel circuit of MIMOSA26 analogue readout part. The forward-biased diode is shown on the top of the Figure and the n-well diode is shown in the bottom of the Figure.

controller allows for a communication between the chip and a computer for synchronisation and proper programming. MIMOSA26 operates with nominal frequency of 80 MHz. A typical MIMOSA26's single-point resolution is 3.2 μm [165].

In addition, the MIMOSA26 chip was equipped with analogue readout mounted in the most left part of the chip. In this readout mode, each pixel is read out by a simple circuit, shown in Figure A.5. The charge is collected via the n-well diode and loaded into the parasitic capacity of the pixel. Two voltages drops are being measured, the one on the capacitor and the one on the forward-biased diode. The latter is used to reset the pixel signal to compensate for leakage current. Since the reset procedure is much slower than the readout frequency, the generated signal charge remains in the pixel for several readout cycles. The optimal readout frequency is 20 MHz for the analogue readout mode. In case of analogue readout no zero suppression and on-chip correlated double-sampling is performed. The output data contain the raw signal from each pixel.

The internal registers [166] of the MIMOSA26 chip, e.g. the bias and other registers can be accessed and are fully adjustable via the control interface using JTAG [167]. Such registers include the so-called BIAS_DAC register. It simultaneously sets the 19 DAC registers which control the voltage and current bias on the digital-to-analog converters (DAC) and discriminators. One of those registers is called IAnaBUF. It controls the current bias at the analogue buffer. Another set of registers, called RO_MODE1, control the analogue part of the chip by asserting amplifiers voltages. The set of registers called SEQENCER_PIX_REG control the pixel readout and discriminators sequence.

A.3 Experimental setup

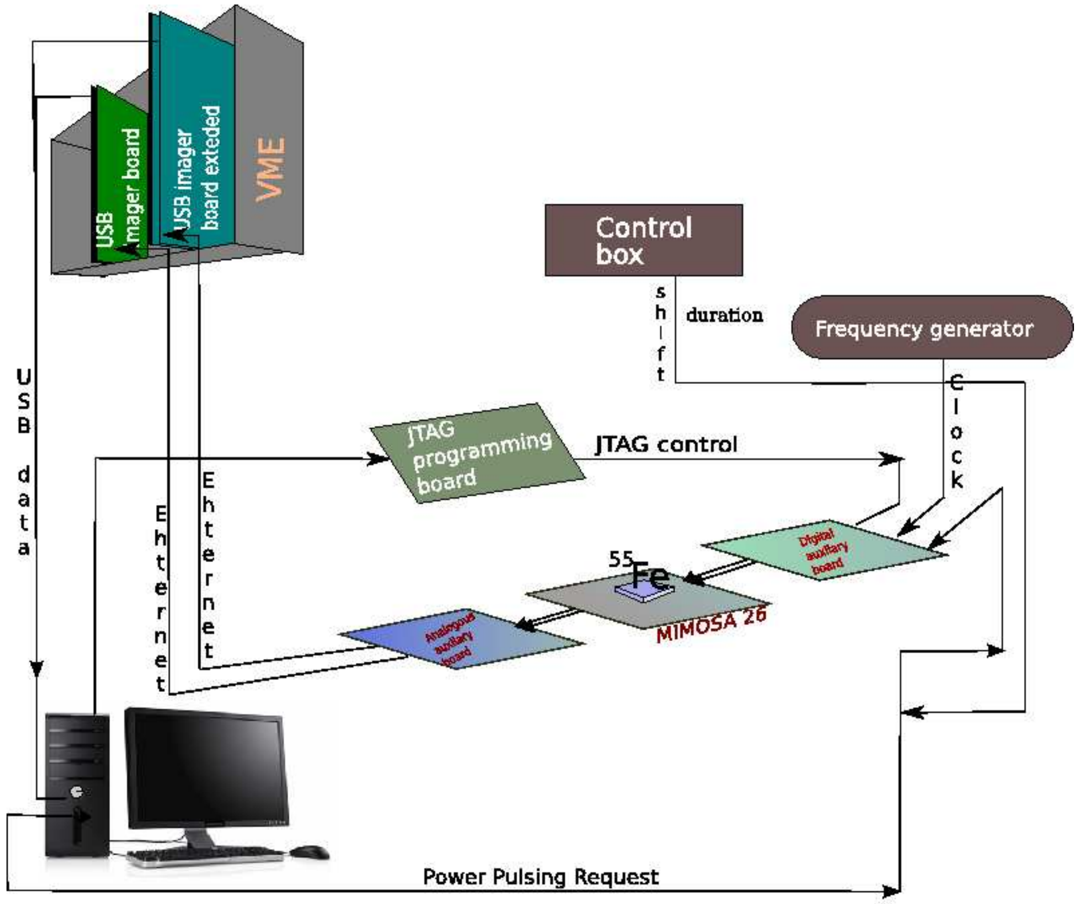

Figure A.6: Schematic drawing of the experimental setup for the power pulsing studies at DESY.

For the very first steps of power pulsing studies the analogue readout was chosen in order to have a good understanding of the effect of power pulsing on the raw signal itself.

The Data Acquisition System (DAQ) used for the presented studies is shown in Figure A.6. The full DAQ consists of:

- Two USB Imager Boards [168] (one with an additional built up board). Each board has four ADC with a 256 Kb memory buffer. The data from those boards are sent to the PC via USB2.0 ports;

- MIMOSA26 chip thinned down to 50 μm;

- Digital auxiliary board, through which the digital part of the chip was powered, programmed and controlled.
- Analogue auxiliary board, which was used to send the data from the analogue part of the chip to the Imager boards. The powering of the analogue line was also sent via this board;
- JTAG programming board, which provided a communication between the computer and the registers of the chip through the JTAG protocol. Its interface is used to setup the discriminator thresholds and other configuration settings, and initialise the chip for power pulsing. The sensor is programmed when the clock is active;
- Personal computer under the WINDOWS XP operating system. The DAQ and JTAG software were run on this PC. The data transmitted from the DAQ boards were stored on the local PC hard drive;
- Analogue power control box;
- VME crate for powering the Imager Boards.
- Frequency generator to provide a 20 MHz clock for the chip.

The synchronisation was performed by the Imager Boards though via an Ethernet interface.

There are two possibilities for the chip readout, one is to read the full sensor (an array of 576×1152 pixels) and the second is to read only the last eight lines (an array of 576×8 pixels). Technically it is not possible to select eight particular lines. The basic idea of the current power pulsing studies is to determine the chip response with time. That is why only the second readout possibility is feasible due to a memory lack in Imager Board ADCs. Therefore, with eight-channel readout mode (one line per channel) it is possible to monitor a chip with 455 time frames, i.e. $\frac{256 \cdot 1024 \ bytes}{576 \ rows} = 455$.

The MIMOSA26's internal clock cycle translates to 209.7 ms (ILC readout cycle is 200 ms) with 1 readout frame corresponding to 0.46 ms. Later on the frame itself will be used as an observable for the time characterisation.

A so-called "speak" signal is provided by the DAQ to indicate that the data from the chip should be processed by the DAQ. The chip provides the data only while the DAQ system tells it to do so by asserting the speak signal. The speak system is provided by the DAQ to initiate the readout of the data. So the frame end is defined by the DAQ system. The frame is completed when the speak rising edge has arrived.

In the present studies the speak signal was also used to generate a power pulsing request input (PPRI), see Figure A.7. The duration and the shift of the PPRI with

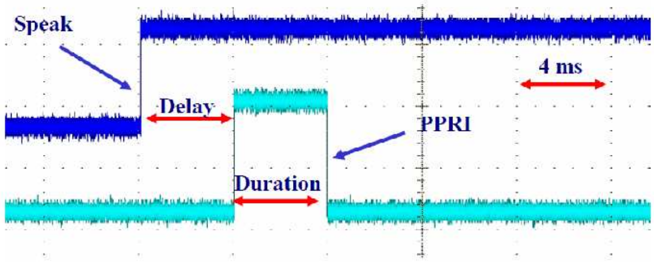

Figure A.7: Illustration of the power pulsing request (PPRI) synchronisation with the DAQ signal (Speak). The start of the power pulsing is delayed with respect to the Speak signal. The duration of the PPRI signal corresponds to the power off time.

respect to the speak signal can be controlled with the analogue power control box and monitored with an oscilloscope.

There are two possible data taking modes with this analogue readout. One of them is the power pulsing scan, where only eight last lines of the chip are read out. The second is the so-called full-chip-scan, in which an array of 1152×576 is read out step by step by eight ADCs. The latter one is used for test purposes and can not be used for the power pulsing studies due to a memory deficit.

Raw data from the chip are not zero-suppressed in the case of the analogue readout. It contains all available information from the discriminators. There is also a possibility to store the PPRI signal by replacing the output of one of the readout channels. Usually, the last channel was used for these purposes. More details about the used data format in the output can be found in Appendix I.

A.4 Data analysis

The analysis procedure was inherited from the previous studies with the previous type of a MIMOSA chip [169]. In the case of the analogue readout, the signal from a single MIMOSA26 chip consists of two components. The first one is READ component that corresponds to the charge collected on a capacitor[1]. The second one is the CALIB component; it corresponds to the output signal in a pixel right before a special reset signal, which sets the a diode capacitance to zero. The difference of those two components defines raw signal. This techniques is called Correlated Double Sampling (CDS). More details can be found in [170].

The analysis procedure of a raw data contains the following steps:

[1]caused by an ionising particle or any noise that is higher than the discriminator threshold

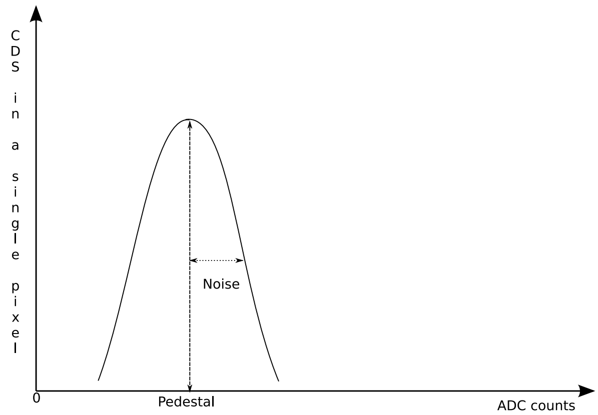

Figure A.8: Illustration of the pedestal distribution and the level of noise.

- **Offset estimation**. In the case when electronics has no leakage current, the output of a detector will always be zero if no ionising particle passes through it. In reality there is an offset from zero, which is called the pedestal, shown in Figure A.8. The full width at half maximum of the pedestal distribution is assigned to the noise level. To estimate the pedestal and noise, it is necessary to take non-physical events, e.g data with no radioactive source or no light exposure (MIMOSA26 is sensitive to photons) and than do the calculation on pixel-by-pixel basis. The pedestal is defined as $p_i = \frac{\sum_{k=1}^{N}(r_k^i)}{N}$, where N is the number of idle events, r_k^i is the raw signal in pixel i in event k. The noise is defined as the standard deviation of the pedestal, $n_i = \sqrt{\frac{N}{N-1}}\sqrt{\frac{1}{N}\sum_{k=1}^{N}(r_i^k)^2 - (p_i)^2}$.

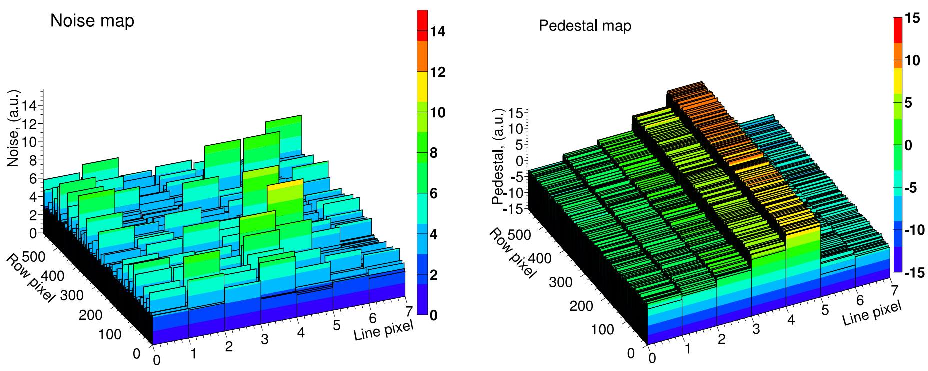

(a) (b)

Figure A.9: (a) The noise and (b) the pedestal maps for a eight-line readout mode. The last column was used to store the PPRI signal, therefore is not shown.

Figure A.9 demonstrates the pedestal and noise maps for the case of the readout of the eight last columns. The noise is almost homogeneously distributed in the pixels, while the pedestal strongly differs from ADC to ADC of the DAQ boards.

- **Clusters formation**. For searches of an indication of an ionising particle, the pedestals need to be subtracted from the raw signal pixel-by-pixel. Afterwards, the search for a seed pixel needs to be performed. The seed pixel is the one in which the signal-to-noise ratio is above a certain value: $S/N = \frac{r_{seed}}{n_{seed}} > V_{thr.}$ where r is a pedestal-free output from the pixel and n is a pixel noise. The search for the seed pixel starts from the one with the highest S/N. Afterwards, a cluster of 3x3 pixels is formed around the seed pixel.

- **Physical signal extraction**. The distribution of r in seed pixels represents the spectra of an ionising source.

A.5 ^{55}Fe γ-source studies

There are several ways to test detector performance. The first one is to irradiate it with a radioactive source. The second way is to irradiate the detector with beam of particles of known energy and position. The present studies were performed with a ^{55}Fe γ-source. It has two emission lines, K_α with $E = 5.89\,\text{keV}$, emission probability is $P = 24.4\%$, and K_β with $E = 6.49\,\text{keV}$ and $P = 3.4\%$. An example of the raw detector signal is demonstrated in Figure A.10. Most sizable spikes correspond to hits produced by a γ- photons.

As mentioned before, for the power pulsing studies only 1/144 of the sensitive chip area was used. Therefore, the number of events with real hits was significantly reduced. The event reconstruction was performed as discussed in the previous section. Figure A.11 shows the spectrum of a ^{55}Fe source taken with the MIMOSA26 chip. This spectrum represents the charge accumulated in a seed pixel over 3000 of events. The spectrum was fitted with a Double-Gauss function. The fit parameters provide all the necessary information to perform the chip calibration (ADC-to-charge conversion). In silicon, the energy required to produced an electron-hole pair is 3.6 eV. Therefore, K_α (K_β) photon can produce about 1640 (1830) electron-hole pairs.

As for the power pulsing studies only the analogue part of the chip was used, the chip calibration was not performed and all the working units are given in counts of ADC (a.u.). The conversion can always be done using parameters extracted from the fit.

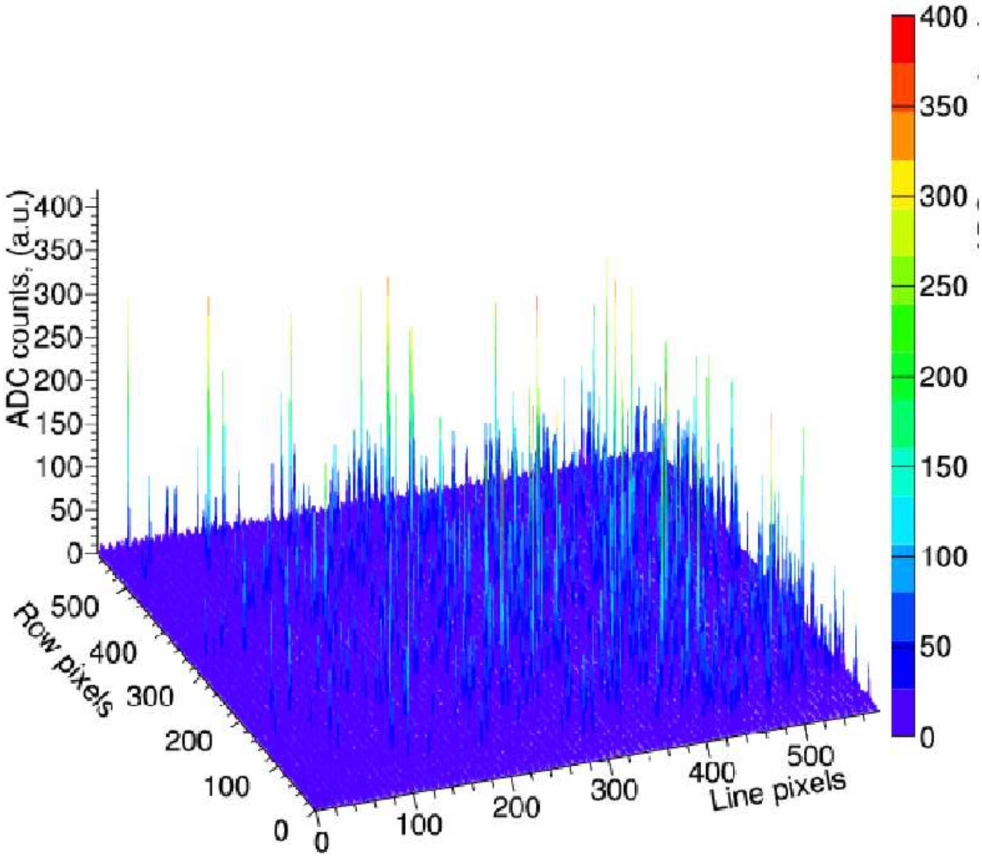

Figure A.10: An example of a ^{55}Fe event for the scan readout mode. Only the CDS information without any analysis steps is depicted. Only half of the pixel array is shown. The spikes show the possible reconstructed hits in the detector caused by ^{55}Fe γ-rays.

A.6 Power Pulsing Studies

MIMOSA26 chip was not designed for an optimal operation under power pulsing conditions. Nevertheless, the chip has certain programmable registers that can be used to perform and study the power pulsing. At this stage of studies, the chip response is the subject of interest.

Once a chip is completely powered off, about 100 ms are needed to re-configure the chip via the JTAG control. This would not be very effective compared to the 199 ms between the bunch trains of the ILC time structure. Thus, a different way of reducing the power consumption needs to be introduced. Three different methods of power pulsing were developed by the CMOS group at Strasbourg for a single chip detector with the analogue readout.

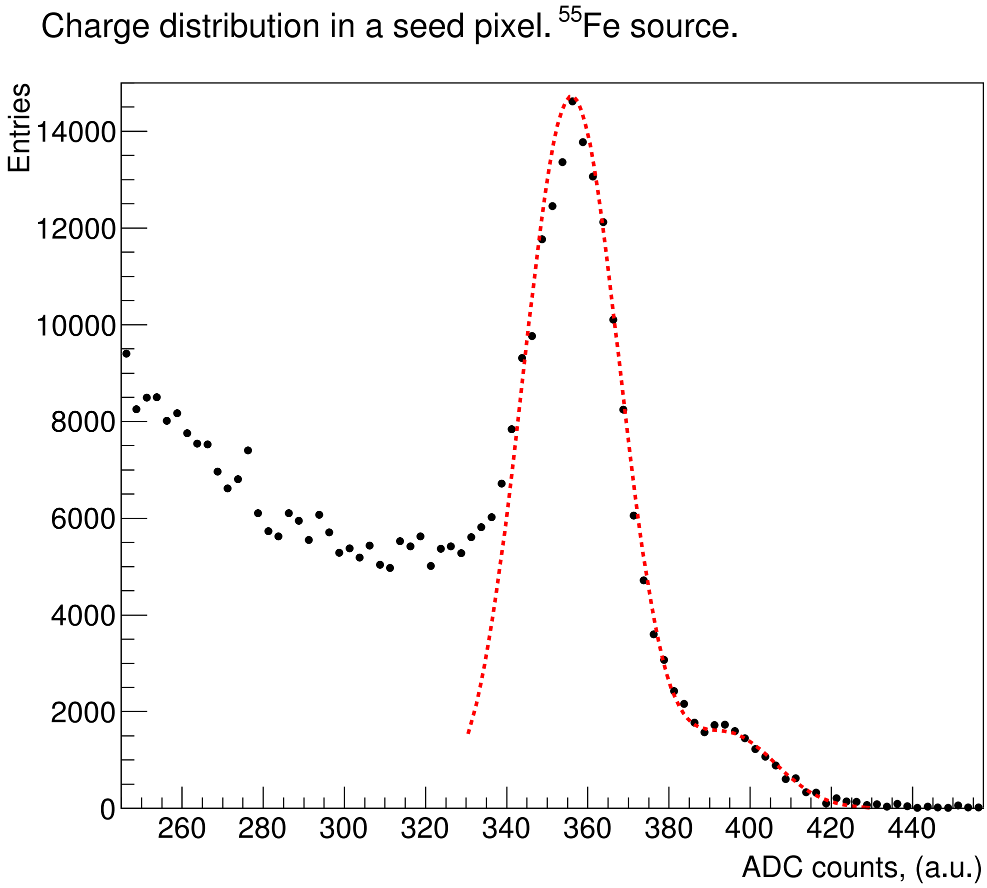

Figure A.11: The spectrum of ^{55}Fe source. Dashed line corresponds to a fit with a double-Gaussian function. The first peak corresponds to the K_α line and the second to K_β.

A.6.1 Power Pulsing I

It is possible to introduce a bias to the MIMOSA26 registers [166]. In this way, the value of the InaBUF register was set to 0. That did not result in a visible power pulsing. Another possibility is to switch some of the amplifiers and discriminators to the stand-by mode for some moment by changing the other register values. Therefore, the power pulsing was performed by decreasing the voltage of the discriminators, thus powering off the pixel amplifiers. In this case, all discriminators are set to the so-called "stand-by" mode. This was done by setting the EnDiscriPwrSave and EnDiscriAOP registers from the RO_MODE1 controls to zero. This method is referred as PPI. The results of the noise and pedestal evolution with time (frame number) are shown in Figure A.12. This does not result in a significant power consumption reduction, but gives at least a visual representation of the studies. The chip is not really off (and is not supposed to). There are four frames of the off-time indicated with splashes in the pedestal and noise distributions.

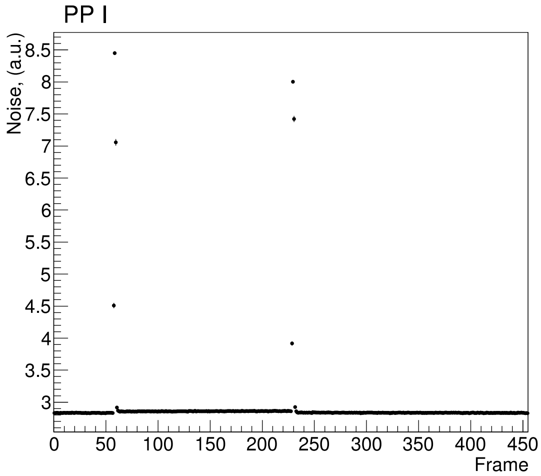

(a)

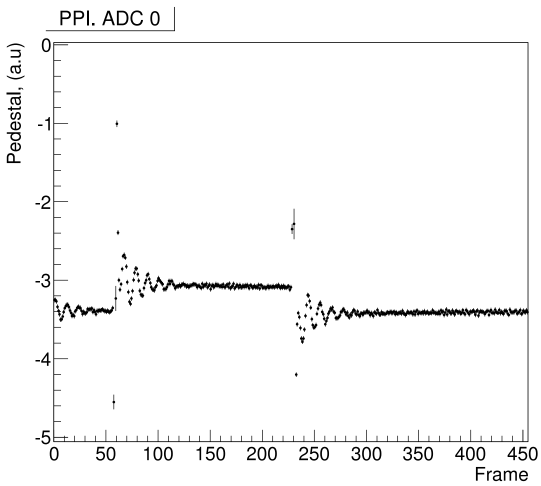

(b)

Figure A.12: Evolution of the chip characteristics with time under power pulsing conditions of type I: (a) noise time line, (b) pedestal time line. One frame corresponds to 1μs.

The peak position of the K_α line of the ^{55}Fe source together with the peak width were reconstructed on a frame-by-frame basis. The result is shown in Figure A.13. Due to time consuming calculations, the frames between dashed lines were not taken into account.

After an introduction of a small bias to the chip registers, the chip comes to the

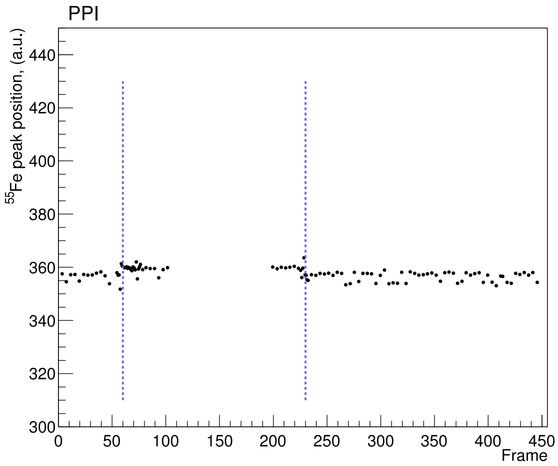

(a)

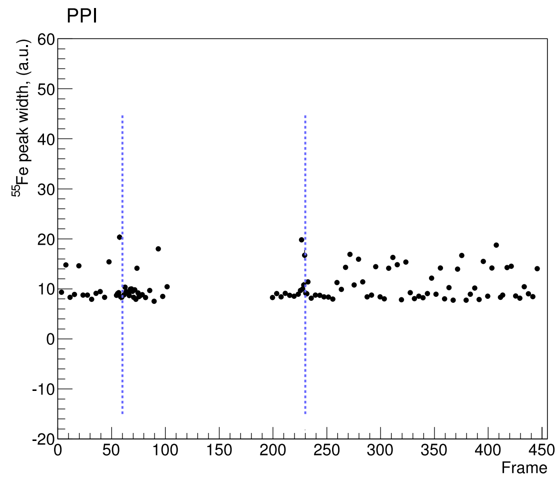

(b)

Figure A.13: Evolution of the of the ^{55}Fe spectrum characteristics with time under power pulsing conditions of type I: (a) position of the peak, (b) width of the peak. One frame corresponds to 1μs. The dashed lines show the beginning and the end of the power pulsing.

nominal operation within five frames. The dissipative structure of the pedestal time line is presented before and after the power pulsing cycle. That may indicate an inappropriate chip configuration.

A.6.2 Power Pulsing II

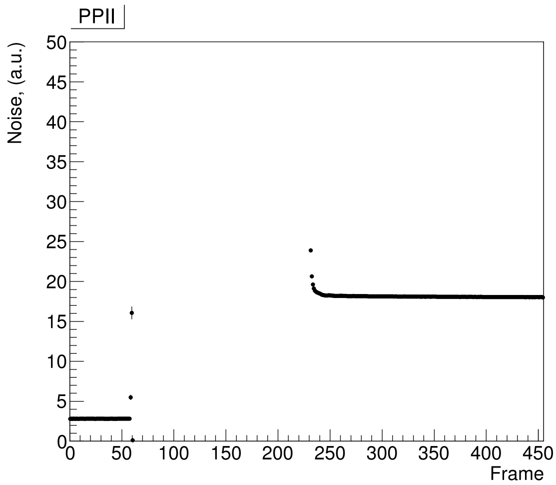

(a)

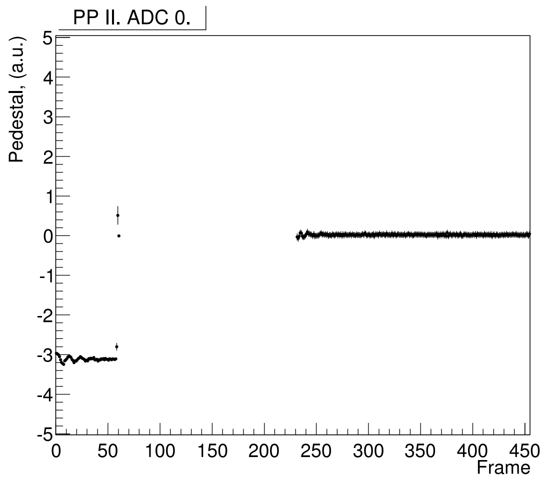

(b)

Figure A.14: Evolution of the chip characteristics with time under power pulsing conditions of type II: (a) noise time line, (b) pedestal time line. One frame corresponds to 1μs.

The second power pulsing method is performed by changing the sequence of the signal sampling by setting the SEQENCER_PIX_REG registers, POWERON1 and POWERON2, to 0. This disables some part of the internal pixel readout logic. As part of the process, the reset signal in the pixel is shifted in time with respect to the nominal readout mode. The pedestal and noise time evolution is shown in Figure A.14. After the power pulsing stop was reached, the offset characteristics do not recover to their nominal values independently of the ADC. Figure A.14(a) shows the results for ADC0. During the analysis of data taken with a radioactive source, the following was discovered. Only one out of five events was useful. The rest events had extremely high values of either noise or pedestal.

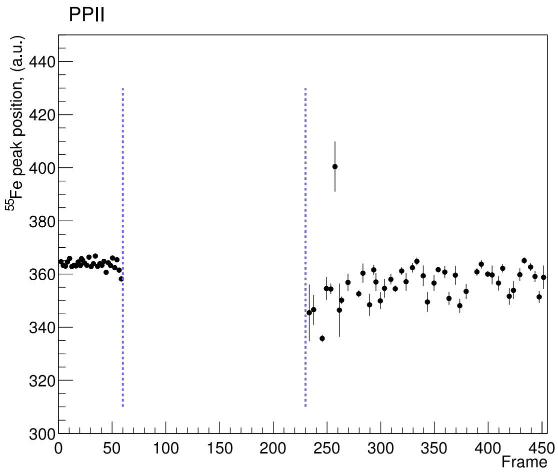

(a)

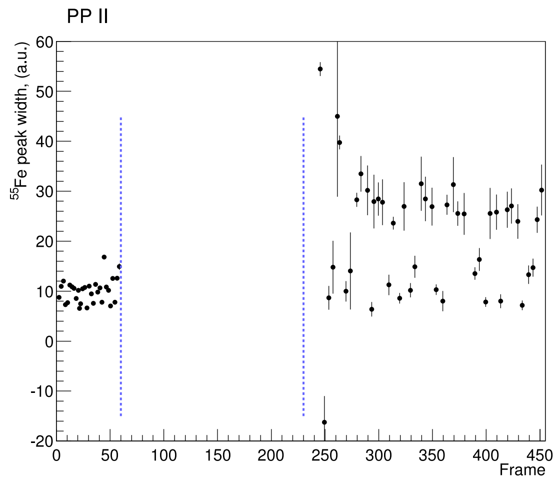

(b)

Figure A.15: Evolution of the ^{55}Fe spectrum characteristics with time under power pulsing conditions of type II: (a) position of the peak, (b) width of the peak. One frame corresponds to 1μs. The dashed lines show the beginning and the end of the power pulsing.

This explains why the statistical uncertainties, as well as the fluctuations shown in Figure A.15, are larger after the PP stops. It is not clear why the chip shows such a kind of response. Additional tests proved that it is not due to the analysis procedure. The measurements taken with an on-line monitor of the DAQ system clearly showed the saturation of the chip response.

A.6.3 Power Pulsing III

For the first two power pulsing methods discussed above, the chip configuration was changed in order to provide a power pulsing possibility. Here, the third method of power pulsing is presented. It is performed via the analogue power control box. The pulsing of the power is performed by switching on and off the analogue power supply. The digital part of the chip stays powered on without any changes to the registers. This method is the most efficient in terms of the reduction of power consumption among the others described above.

Figure A.16 shows the time evolution of the pedestal and the noise. From the figure it is seen that the power drops with some delay with respect to the PP start. The delay is $\sim 20\,\mu$s. The same delay is present for the power up. The pedestal recovery takes 35 frames, i.e. $\sim 35\,\mu$s, with a faster recovering of the noise.

Another aspect of the chip validation under the PP conditions is the peak width and the charge collecting factor demonstrated as the peak position. Figure A.17 shows that the chip recovery is finished at frame 250 within the statistical uncertainties. This agrees with the value of $35\,\mu$s from the pedestal evolution. Thus, the chip fulfils the requirements of the ILC time structure within PPIII.

A.7 Summary and outlook

The studies of the MIMOSA26 chip response under different power pulsing possibilities were presented within the framework of the PLUME project. The measurements were based on the analogue readout of the chip. Three different power pulsing methods were considered. Even though the MIMOSA26 was not optimised for the operation under power pulsing conditions, it showed a sufficiently stable behaviour under PPPIII, thus fulfilling the requirements from the ILC. The studies presented here give only the first glimpse towards the final validation of the possibility to operate the PLUME ladder under power pulsing conditions. Further studies are necessary. For example, the response of a single chip with the digital readout could be one of the next steps. Beside that, a new sufficient power pulsing method for the full ladder equipped with six chips should also be introduced.

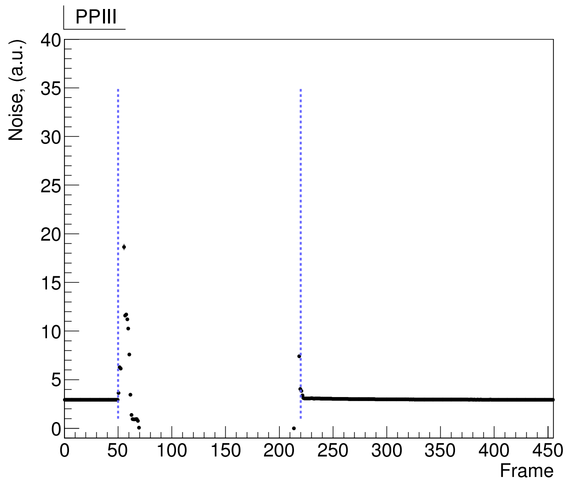

(a)

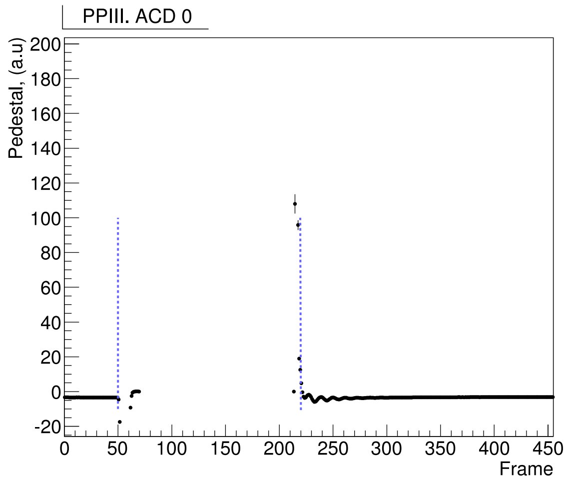

(b)

Figure A.16: Evolution of a chip characteristics with time under power pulsing conditions of type III: (a) noise time line, (b) pedestal time line. One frame corresponds to 1μs.

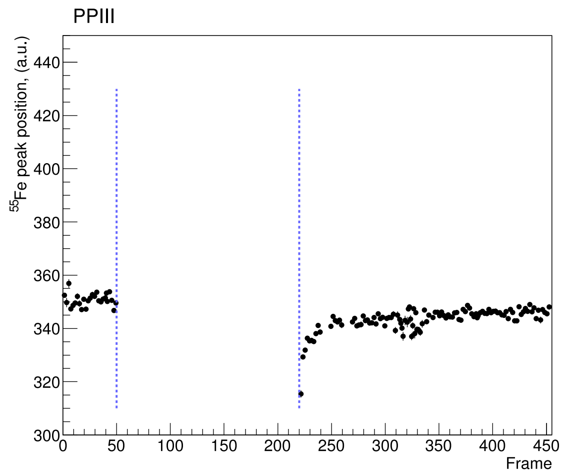

(a)

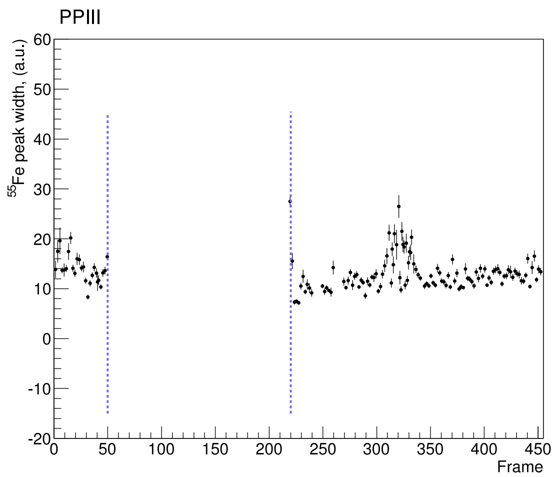

(b)

Figure A.17: Characteristics of the ^{55}Fe spectrum evolution with time under power pulsing conditions of type III: (a) position of the peak, (b) width of the peak. One frame corresponds to 1μs. The dashed lines show the beginning and the end of the power pulsing.

Appendix B

Inclusive DIS control distributions

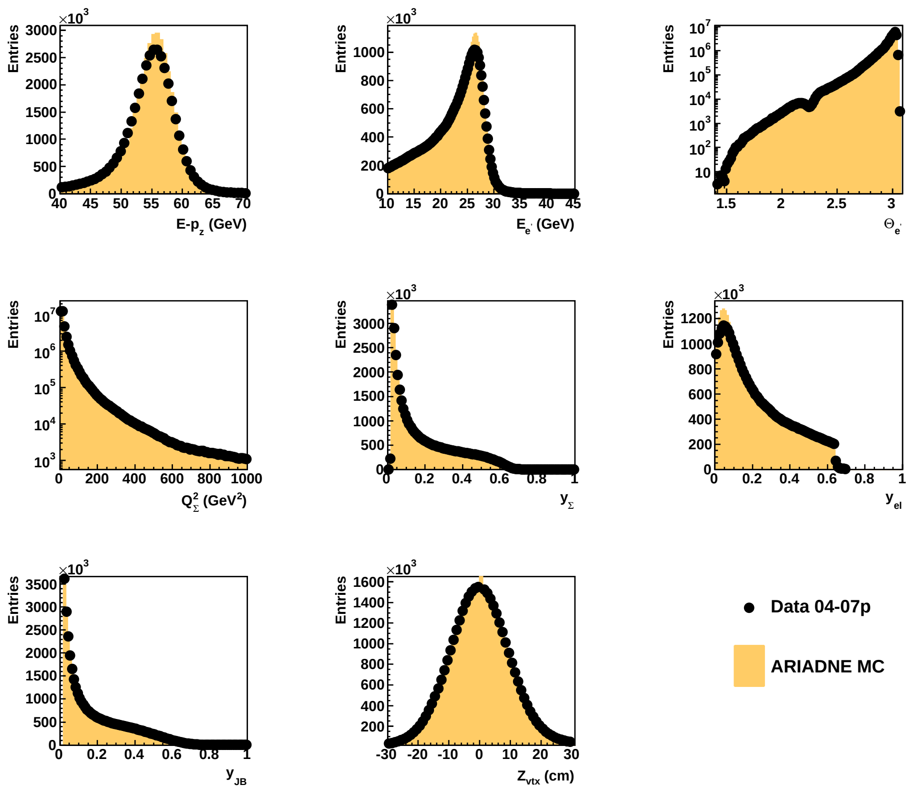

Figure B.1: Comparison of the MC (yellow shaded area) distribution of $E - p_z$ of the event, measured energy of the scattered electron, $E_{e'}$, the scattered electron angle, $\Theta_{e'}$, and DIS kinematic variables, Q^2 and y, with data (filled point) after the DIS selection (see Chapter 7.2). For the MC the inclusive NC ARIADNE simulations were taken. No D^* selection was applied.

Appendix C

D^* and D^0 spectra

The D^* signal extraction procedure did not include any fit of the D^* peak. Therefore in this appendix the basic characteristics of the mass spectra are given for D^* and it's decay product D^0 . Figure C.1(a) shows the ΔM spectrum in data of D^* fitted with a modified Gaussian convoluted with the Granet function $G'(x)$, defined in Section 7.3:

$$\text{Gauss}^{\text{mod}}(x) = A \cdot e^{-0.5\cdot|\frac{x-B}{C}|^{1+\frac{1}{1+0.5|\frac{x-B}{C}|}}}, \tag{C.1}$$

where $x = |\Delta M - m_\pi|$. The choice of the Modified Gaussian is somewhat historical. It was heavily used in the ZEUS experiment in order to describe peak tails with respect to the standard Gaussian. A, B, C are the free parameters of the χ^2 fit, where A stands for the amplitude, B for the peak position and C is the width of the modified Gaussian.

Figure C.1(b) shows the mass spectrum in the data of the D^* decay product D^0 fitted also with the modified Gaussian convoluted with a second order polynomial for the combinatorial background description. The excess of the correct-sign candidates over the combinatorial background, WS, in the mass region below the D^0 mass is due to partly reconstructed decays, mostly $D^0 \to K^+\pi^-\pi^0$.

Table C.1 shows the mass and width parameters of the D^* and D^0 spectra obtained from the fit. The μ parameter is compared to the PDG2012 mass fit

	σ^{mod}, MeV	μ, MeV	μ(PDG2012), MeV
D^*	0.46 ± 0.01	145.42 ± 0.01	145.421 ± 0.010
D^0	12.75 ± 0.23	1862.71 ± 0.23	1864.86 ± 0.13

Table C.1: Summary table of D^* and D^0 spectra (statistical uncertainty only) in data obtained from the fit compared to the PDG2012.

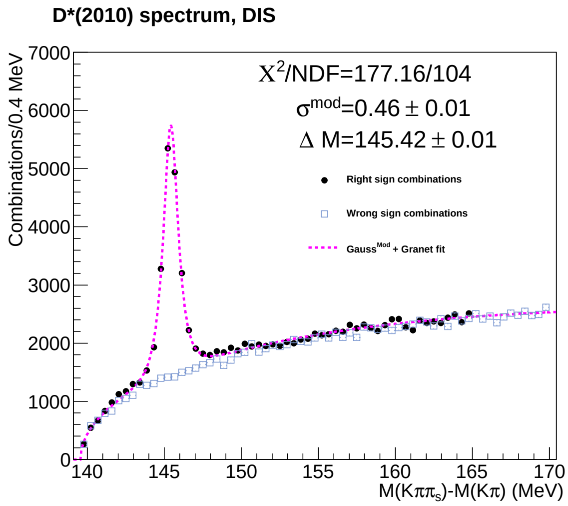

(a)

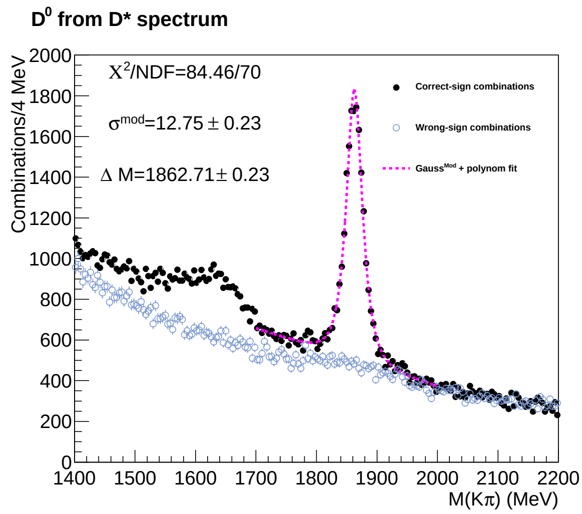

(b)

Figure C.1: (a) D^* spectrum shown for the D^0 mass range $1.80 < M^{D^0} < 1.92\,\mathrm{GeV}$. (b) D^0 spectrum shown for the ΔM D^* mass window $143.2 < \Delta M < 147.7\,\mathrm{MeV}$. The dashed pink lines represent the values of the fit at the bin centres.

values. The mass of the D^* agrees with PDG2012, where the D^0 is slightly lower, but compatible within systematic uncertainty.

Appendix D

ISOe correction

The correction, $I_{<,>}(y_{el})$, was assigned as a weight to the detector level events only in the MC as a function of event inelasticity, y_{el}, reconstructed with the Electron method.
For $RunNr <$ 60400 the correction reads as:

$$I_{<}(y_{el}) = 0.996 + 0.02753 \cdot y_{el} - 0.311 \cdot y_{el}^2 + 1.453 \cdot y_{el}^3 - 3.41 \cdot y_{el}^4 + 2.736 \cdot y_{el}^5.$$

For $RunNr >$ 60400 the correction reads as

$$I_{>}(y_{el}) = 0.998 + 0.02644 \cdot y_{el} - 0.196 \cdot y_{el}^2 + 0.835 \cdot y_{el}^3 - 2.04 \cdot y_{el}^4 + 1.706 \cdot y_{el}^5.$$

The effect on the double-differential cross sections in Q^2 and y is given in Figure D.1.

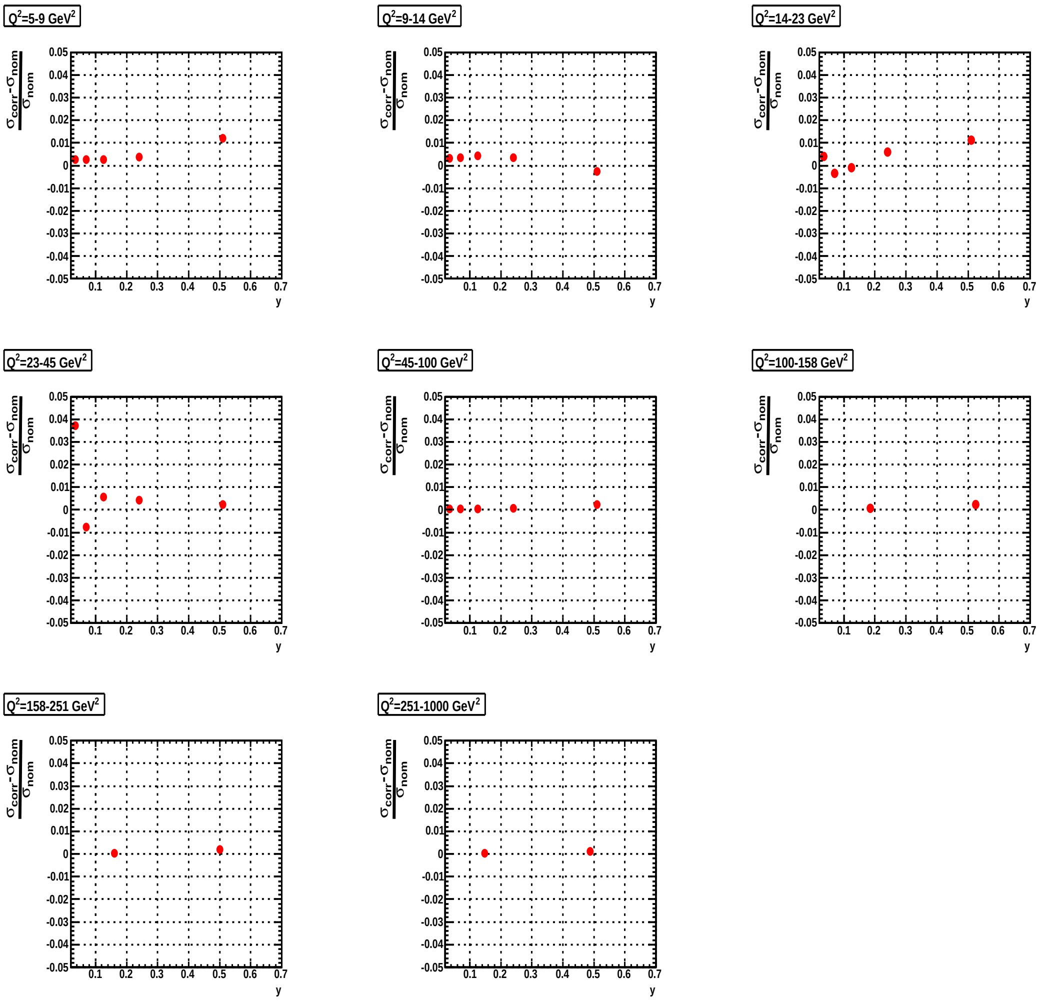

Figure D.1: Effect of the ISOe correction on double-differential cross sections in bins of Q^2, y, defined as $\frac{\sigma_{\mathrm{corr}}-\sigma_{\mathrm{norm}}}{\sigma_{\mathrm{norm}}}$.

Appendix E

Photoproduction event selection

The production of charm quarks in high energy ep collisions at HERA is dominated by photoproduction events, where the electron or positron is scattered at a small angle and not registered in the detector. The kinematic region of photoproduction events usually defined as $Q^2 < 1$ GeV^2. The main production process as in the case of DIS events is photon gluon fusion where the photon interacts directly with the gluon from the proton producing a $c\bar{c}$ pair, $\gamma g \to c\bar{c}$. In the photoproduction regime, apart from the contribution from the direct processes with a point-like photon, resolved photoproduction also gives a significant contribution to the heavy flavour production. In resolved processes, the incoming photon fluctuates in a hadronic state and behaves as a source of partons. Those partons interact with the partons in the proton, $g\,g \to c\bar{c}$.

To study photoproduction processes the same data as described it Section 7 were used with additional data coming from 03p period. The full luminosity of the PHP data sample is 372 pb^{-1}. For the Monte Carlo simulation the Pythia generator was used. It includes direct and resolved photon processes in equal proportions both for charm and beauty flavour production. The MC was generated in the full Q^2 range, but only events with $Q^2 < 1.5$ GeV^2 were considered in the analysis. As in the DIS case, only eight selected D-meson decays were stored in the MC in order to simplify and speed up the analysis procedure.

The following criteria were used to select photoproduction events:

- The energy of the centre-of-mass of the photon boson system, $W = \sqrt{2 \cdot \mathrm{E}_p \cdot (E - p_z)}$, was reconstructed using the information from EFOs, $130 < W < 300\,\mathrm{GeV}$;
- No SINSTRA electron with $E > 5$ GeV and probability, $P > 0.9$;
- $|Z_{vtx}| < 30$cm.

For the D^* reconstruction the same algorithm as in the case of DIS events was used. The D^* candidates were required to have:

- The transverse momentum of the D^* candidate $1.9 < p_T^{D^{*\pm}} < 20$ GeV. The lower edge is dictated by the trigger threshold and the upper edge by available statistics;
- The pseudorapidity of the D^* candidate should be $|\eta^{D^{*\pm}}| < 1.6$ in order to cover the barrel region of the detector;
- The invariant mass of the D^* decay product, D^0 candidate, should be in the region from 1.8 GeV to 1.92 GeV;
- The transverse momenta of D^0 decay products, $K^\pm$ and $\pi^\pm$, should be $p_T^K > 0.4$ GeV and $p_T^\pi > 0.4$ GeV respectively.
- The transverse momentum of the slow pion $p_T^{\pi_s} > 0.12$ GeV;
- $p_T^{D^*}/E_T > 0.12$, where $p_T^{D^*}$ is the transverse momentum of the D^* candidate and the E_T is the transverse energy of the hadronic system measured by the CAL excluding the cone of ten degrees around the beam pipe; This cut was introduced in order to increase signal-to-background ratio the cut on $p_T^{D^*}/E_T > 0.12$ was introduced;
- All three tracks that form a D^* candidate should pass at least three CTD super-layers and at least one MVD layer.

The reconstruction of PHP events strongly relies on the measurement of the hadronic system, while in the DIS case event reconstruction relies of the reconstruction of the scattered electron. Thus, the efficiency of the PHP trigger slots is lower with respect to the DIS ones. For the PHP events selection the following trigger slots were used as logical OR:

- HFL01. Logical OR of all available D-meson related triggers in PHP;
- HFL05. Photoproduction events with two jets with transverse energy of $E_T >$ 4.5 GeV and $E - p_z < 100$ GeV and $p_z/E < 0.95$;
- HFL21. Two jets and at least one of the D mesons from HFL01. The both jets were required to have $E_T > 3.5$ GeV.

Appendix F

Double-differential control plots

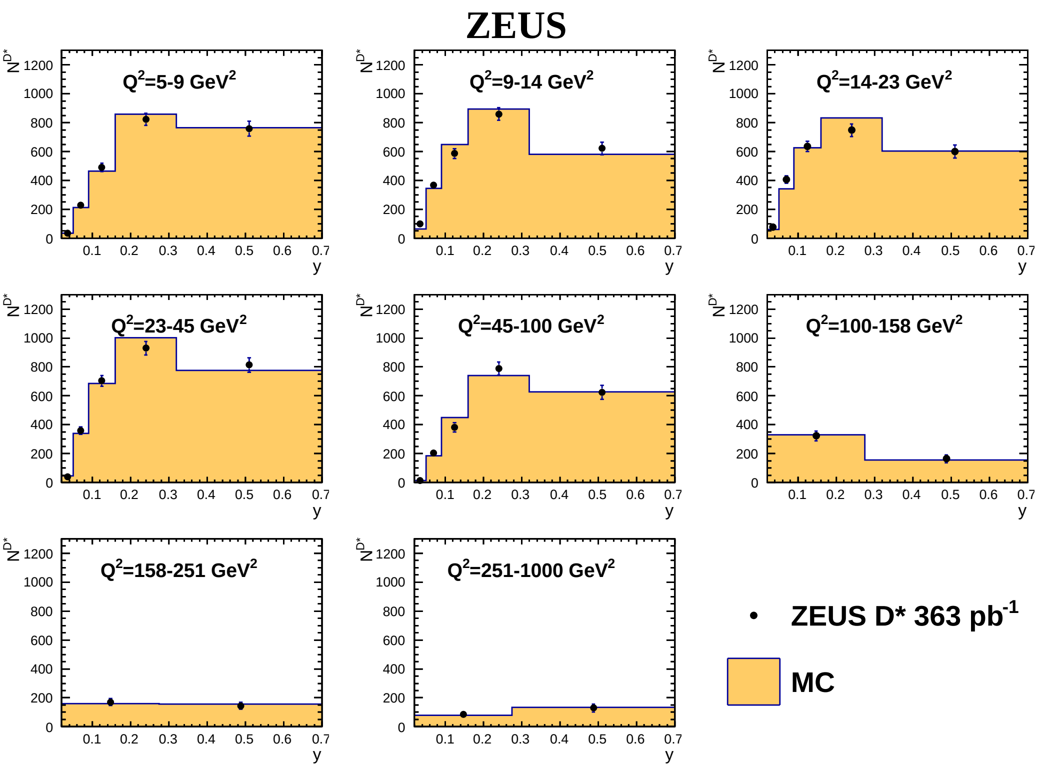

Figure F.1: Comparisons of the D^* yields, ΔN, in MC with respect to the data in Q^2, y double differential bins. The MC contains the same sub-components as in Figure 7.18(a).

Appendix G

Tails correction

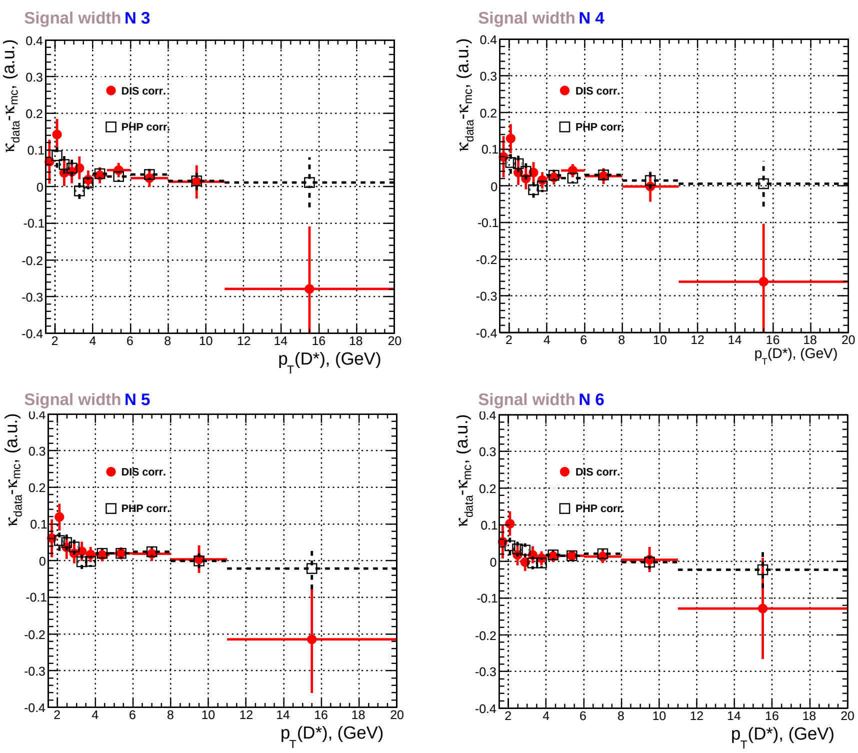

Figure G.1: Tails correction, expressed as a difference between the fraction of missed events outside the selection window in data and in Monte Carlo simulations, as a function of $p_T^{D^*}$ for DIS sample (filled red points) and photoproduction sample (open squares). Each plot represents different width of D^* ΔM selection window. The lower edge of the window is $145.42 - \mathrm{N} \cdot 0.46\,\mathrm{MeV}$ and the upper edge is $145.42 + \mathrm{N} \cdot 0.46\,\mathrm{MeV}$, where N is given in the title.

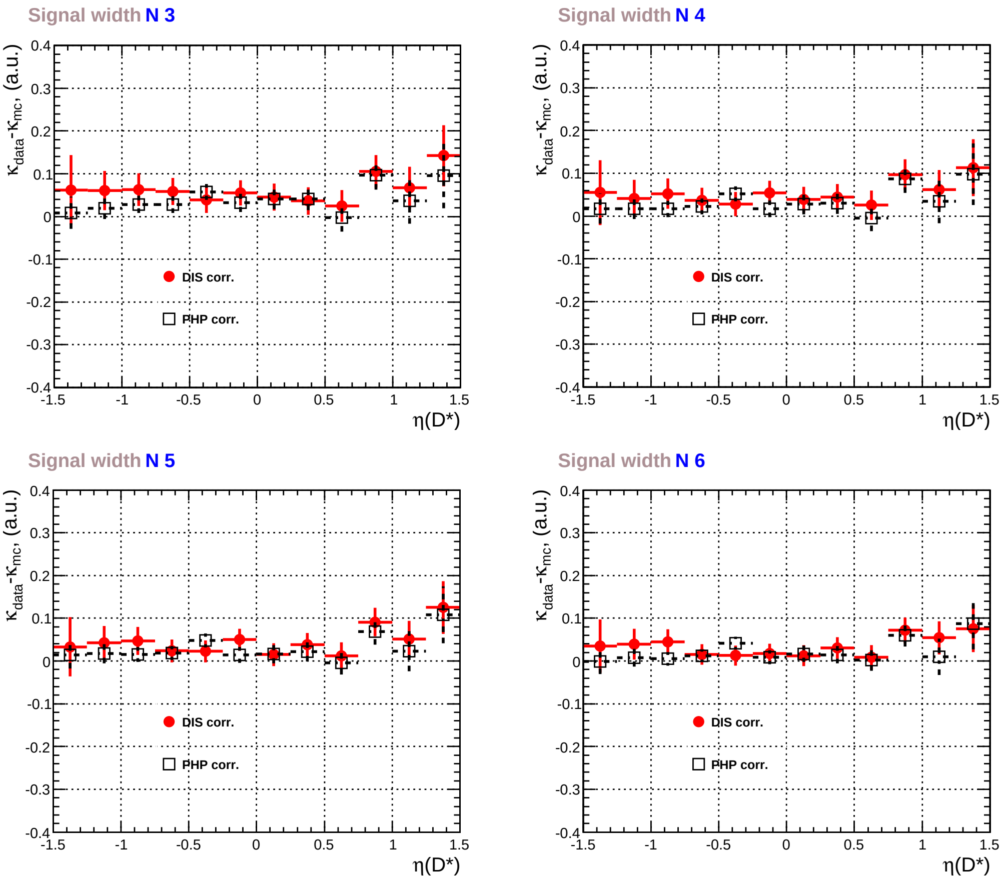

Figure G.2: Tails correction as in Figure G as a function of η^{D^*} for DIS sample (filled red points) and photoproduction sample (open squares) for different width of D^* ΔM selection window. The lower edge of the window is $145.42 - \mathrm{N} \cdot 0.46\,\mathrm{MeV}$ and the upper edge is $145.42 + \mathrm{N} \cdot 0.46\,\mathrm{MeV}$.

Appendix H

Breakdown of systematics

This Appendix lists all systematic uncertainties discussed in Chapter 7. All uncertainties are presented in percent, the sign of each uncertainty is also preserved. Luminosity and branching ratio uncertainties are not listed in tables as they did not enter the final systematic uncertainty. Uncertainty of $+2\,\%$ of D^0 tails was also not included in the tables below, but was accounted for in the final numbers. The effect of the η re-weighting variation, δ_{12}, and effect of ISOe corrections were not taken into account and therefore not listed due to their negligible effect.

$p_T^{D^*}$, GeV	δ_1	δ_2	δ_3	δ_4	δ_5	δ_7	δ_8	δ_9	δ_{10}	δ_{11}	δ_{13}	δ_{14}	δ_{15}	δ_{16}	δ_{18-19}
1.50 : 1.88	$^{+0.2}_{-0.2}$	$^{+0.9}_{-0.7}$	$^{+0.4}_{-0.0}$	$^{+2.3}_{-2.3}$	$^{+3.0}_{-3.0}$	$^{+0.3}_{-0.3}$	$^{+0.6}_{-1.2}$	$^{+0.6}_{-0.7}$	$^{+0.4}_{-0.0}$	$^{+0.9}_{-0.8}$	$^{+1.4}_{-0.0}$	$^{+2.4}_{-0.0}$	$^{+2.6}_{-0.0}$	$^{+3.4}_{-3.2}$	$^{+1.5}_{-1.5}$
1.88 : 2.28	$^{+0.2}_{-0.2}$	$^{+0.5}_{-0.6}$	$^{+0.5}_{-0.0}$	$^{+1.5}_{-1.5}$	$^{+3.0}_{-3.0}$	$^{+0.4}_{-0.4}$	$^{+0.4}_{-0.8}$	$^{+0.2}_{-0.3}$	$^{+0.0}_{-0.3}$	$^{+1.0}_{-0.9}$	$^{+1.3}_{-0.0}$	$^{+0.0}_{-2.2}$	$^{+0.0}_{-2.4}$	$^{+2.9}_{-2.7}$	$^{+1.3}_{-1.3}$
2.28 : 2.68	$^{+0.2}_{-0.2}$	$^{+0.5}_{-0.5}$	$^{+0.4}_{-0.0}$	$^{+1.3}_{-1.3}$	$^{+3.0}_{-3.0}$	$^{+0.1}_{-0.1}$	$^{+0.3}_{-0.7}$	$^{+0.2}_{-0.2}$	$^{+0.0}_{-0.0}$	$^{+0.7}_{-0.6}$	$^{+1.4}_{-0.0}$	$^{+0.0}_{-0.5}$	$^{+0.0}_{-0.1}$	$^{+2.4}_{-2.3}$	$^{+1.1}_{-1.1}$
2.68 : 3.08	$^{+0.0}_{-0.1}$	$^{+0.4}_{-0.3}$	$^{+0.3}_{-0.1}$	$^{+0.1}_{-0.1}$	$^{+3.0}_{-3.0}$	$^{+0.3}_{-0.3}$	$^{+0.2}_{-0.5}$	$^{+0.2}_{-0.2}$	$^{+0.0}_{-0.2}$	$^{+1.1}_{-1.1}$	$^{+1.5}_{-0.0}$	$^{+0.3}_{-0.0}$	$^{+0.0}_{-0.3}$	$^{+2.0}_{-1.9}$	$^{+1.1}_{-1.1}$
3.08 : 3.50	$^{+0.1}_{-0.1}$	$^{+0.2}_{-0.3}$	$^{+0.2}_{-0.0}$	$^{+1.9}_{-1.9}$	$^{+3.0}_{-3.0}$	$^{+0.1}_{-0.1}$	$^{+0.3}_{-0.5}$	$^{+0.1}_{-0.2}$	$^{+0.0}_{-0.0}$	$^{+1.0}_{-1.0}$	$^{+1.4}_{-0.0}$	$^{+0.7}_{-0.0}$	$^{+0.3}_{-0.0}$	$^{+1.6}_{-1.6}$	$^{+1.1}_{-1.1}$
3.50 : 4.00	$^{+0.0}_{-0.1}$	$^{+0.3}_{-0.3}$	$^{+0.3}_{-0.3}$	$^{+0.2}_{-0.2}$	$^{+2.9}_{-2.9}$	$^{+0.1}_{-0.1}$	$^{+0.2}_{-0.3}$	$^{+0.1}_{-0.2}$	$^{+0.0}_{-0.6}$	$^{+0.9}_{-1.0}$	$^{+1.2}_{-0.0}$	$^{+0.2}_{-0.0}$	$^{+0.8}_{-0.0}$	$^{+1.4}_{-1.4}$	$^{+1.1}_{-1.1}$
4.00 : 4.75	$^{+0.0}_{-0.1}$	$^{+0.3}_{-0.4}$	$^{+0.3}_{-0.1}$	$^{+0.1}_{-0.1}$	$^{+2.9}_{-2.9}$	$^{+0.0}_{-0.1}$	$^{+0.3}_{-0.6}$	$^{+0.0}_{-0.0}$	$^{+0.0}_{-0.1}$	$^{+0.8}_{-0.9}$	$^{+1.1}_{-0.0}$	$^{+0.2}_{-0.0}$	$^{+0.3}_{-0.0}$	$^{+1.3}_{-1.2}$	$^{+1.0}_{-1.0}$
4.75 : 6.00	$^{+0.1}_{-0.1}$	$^{+0.4}_{-0.4}$	$^{+0.1}_{-0.1}$	$^{+1.3}_{-1.3}$	$^{+2.8}_{-2.8}$	$^{+0.2}_{-0.2}$	$^{+0.2}_{-0.3}$	$^{+0.1}_{-0.1}$	$^{+0.5}_{-0.0}$	$^{+0.8}_{-0.8}$	$^{+1.2}_{-0.0}$	$^{+0.0}_{-0.1}$	$^{+0.0}_{-0.5}$	$^{+1.1}_{-1.1}$	$^{+1.0}_{-1.0}$
6.00 : 8.00	$^{+0.2}_{-0.0}$	$^{+0.3}_{-0.3}$	$^{+0.0}_{-0.0}$	$^{+0.2}_{-0.2}$	$^{+2.7}_{-2.7}$	$^{+0.3}_{-0.4}$	$^{+0.2}_{-0.4}$	$^{+0.1}_{-0.1}$	$^{+0.6}_{-0.0}$	$^{+0.6}_{-0.6}$	$^{+1.3}_{-0.0}$	$^{+0.0}_{-1.5}$	$^{+0.0}_{-1.2}$	$^{+1.1}_{-1.0}$	$^{+1.2}_{-1.2}$
8.00 : 11.00	$^{+0.1}_{-0.1}$	$^{+0.3}_{-0.3}$	$^{+0.0}_{-0.0}$	$^{+0.6}_{-0.6}$	$^{+2.7}_{-2.7}$	$^{+0.2}_{-0.2}$	$^{+0.3}_{-0.5}$	$^{+0.5}_{-0.7}$	$^{+1.3}_{-0.0}$	$^{+0.2}_{-0.2}$	$^{+0.7}_{-0.0}$	$^{+0.0}_{-0.1}$	$^{+0.0}_{-0.7}$	$^{+1.0}_{-1.0}$	$^{+1.9}_{-1.9}$
11.00 : 20.00	$^{+0.1}_{-0.1}$	$^{+0.3}_{-0.2}$	$^{+0.0}_{-0.0}$	$^{+0.3}_{-0.3}$	$^{+2.6}_{-2.6}$	$^{+0.2}_{-0.1}$	$^{+0.1}_{-0.3}$	$^{+0.8}_{-1.4}$	$^{+0.8}_{-0.0}$	$^{+0.1}_{-0.1}$	$^{+0.4}_{-0.0}$	$^{+0.0}_{-2.5}$	$^{+0.0}_{-2.5}$	$^{+1.0}_{-1.0}$	$^{+3.6}_{-3.6}$

η^{D^*}	δ_1	δ_2	δ_3	δ_4	δ_5	δ_7	δ_8	δ_9	δ_{10}	δ_{11}	δ_{13}	δ_{14}	δ_{15}	δ_{16}	δ_{18-19}
-1.50 : -1.25	$^{+0.0}_{-0.2}$	$^{+1.1}_{-1.4}$	$^{+0.3}_{-0.3}$	$^{+0.0}_{-0.0}$	$^{+4.8}_{-4.8}$	$^{+0.0}_{-0.0}$	$^{+0.6}_{-1.3}$	$^{+0.7}_{-1.0}$	$^{+0.7}_{-0.0}$	$^{+0.6}_{-0.6}$	$^{+2.5}_{-0.0}$	$^{+0.0}_{-0.0}$	$^{+0.0}_{-2.4}$	$^{+2.1}_{-2.1}$	$^{+2.4}_{-2.4}$
-1.25 : -1.00	$^{+0.3}_{-0.1}$	$^{+0.8}_{-0.9}$	$^{+0.0}_{-0.3}$	$^{+1.6}_{-1.6}$	$^{+3.8}_{-3.8}$	$^{+0.1}_{-0.2}$	$^{+0.5}_{-1.0}$	$^{+0.0}_{-0.1}$	$^{+0.8}_{-0.0}$	$^{+0.8}_{-0.8}$	$^{+1.2}_{-0.0}$	$^{+0.0}_{-0.4}$	$^{+0.0}_{-1.1}$	$^{+2.0}_{-1.9}$	$^{+1.7}_{-1.7}$
-1.00 : -0.75	$^{+0.3}_{-0.2}$	$^{+0.7}_{-0.7}$	$^{+0.2}_{-0.0}$	$^{+1.3}_{-1.3}$	$^{+3.2}_{-3.2}$	$^{+0.0}_{-0.0}$	$^{+0.5}_{-1.0}$	$^{+0.2}_{-0.3}$	$^{+3.1}_{-0.0}$	$^{+1.1}_{-1.1}$	$^{+0.6}_{-0.0}$	$^{+0.8}_{-0.0}$	$^{+1.7}_{-0.0}$	$^{+1.9}_{-1.8}$	$^{+1.3}_{-1.3}$
-0.75 : -0.50	$^{+0.1}_{-0.3}$	$^{+0.5}_{-0.6}$	$^{+0.3}_{-0.0}$	$^{+0.7}_{-0.7}$	$^{+2.7}_{-2.7}$	$^{+0.0}_{-0.0}$	$^{+0.4}_{-0.7}$	$^{+0.3}_{-0.4}$	$^{+1.6}_{-0.0}$	$^{+0.7}_{-0.7}$	$^{+0.7}_{-0.0}$	$^{+0.1}_{-0.0}$	$^{+0.1}_{-0.0}$	$^{+1.9}_{-1.8}$	$^{+1.2}_{-1.2}$
-0.50 : -0.25	$^{+0.1}_{-0.1}$	$^{+0.3}_{-0.5}$	$^{+0.2}_{-0.2}$	$^{+0.6}_{-0.6}$	$^{+2.4}_{-2.4}$	$^{+0.2}_{-0.2}$	$^{+0.3}_{-0.6}$	$^{+0.5}_{-0.6}$	$^{+1.4}_{-0.0}$	$^{+0.7}_{-0.7}$	$^{+0.7}_{-0.0}$	$^{+0.0}_{-0.0}$	$^{+0.2}_{-0.0}$	$^{+1.8}_{-1.7}$	$^{+1.2}_{-1.2}$
-0.25 : 0.00	$^{+0.1}_{-0.0}$	$^{+0.3}_{-0.2}$	$^{+0.3}_{-0.1}$	$^{+1.7}_{-1.7}$	$^{+2.3}_{-2.3}$	$^{+0.3}_{-0.3}$	$^{+0.3}_{-0.6}$	$^{+0.4}_{-0.5}$	$^{+0.5}_{-0.0}$	$^{+0.5}_{-0.5}$	$^{+1.1}_{-0.0}$	$^{+0.0}_{-0.4}$	$^{+0.0}_{-0.5}$	$^{+1.8}_{-1.7}$	$^{+1.1}_{-1.1}$
0.00 : 0.25	$^{+0.2}_{-0.1}$	$^{+0.4}_{-0.3}$	$^{+0.6}_{-0.0}$	$^{+0.2}_{-0.2}$	$^{+2.2}_{-2.2}$	$^{+0.0}_{-0.1}$	$^{+0.2}_{-0.5}$	$^{+0.3}_{-0.4}$	$^{+1.5}_{-0.0}$	$^{+0.6}_{-0.6}$	$^{+1.1}_{-0.0}$	$^{+0.0}_{-0.3}$	$^{+0.0}_{-1.1}$	$^{+1.8}_{-1.7}$	$^{+1.1}_{-1.1}$
0.25 : 0.50	$^{+0.1}_{-0.1}$	$^{+0.3}_{-0.3}$	$^{+0.2}_{-0.1}$	$^{+0.4}_{-0.4}$	$^{+2.4}_{-2.4}$	$^{+0.2}_{-0.2}$	$^{+0.2}_{-0.4}$	$^{+0.1}_{-0.1}$	$^{+1.3}_{-0.0}$	$^{+0.5}_{-0.5}$	$^{+1.0}_{-0.0}$	$^{+0.1}_{-0.0}$	$^{+0.9}_{-0.0}$	$^{+1.8}_{-1.7}$	$^{+1.1}_{-1.1}$
0.50 : 0.75	$^{+0.0}_{-0.1}$	$^{+0.3}_{-0.2}$	$^{+0.5}_{-0.2}$	$^{+0.3}_{-0.3}$	$^{+2.7}_{-2.7}$	$^{+0.1}_{-0.1}$	$^{+0.2}_{-0.4}$	$^{+0.4}_{-0.5}$	$^{+1.5}_{-0.0}$	$^{+0.7}_{-0.7}$	$^{+0.5}_{-0.0}$	$^{+0.5}_{-0.0}$	$^{+0.7}_{-0.0}$	$^{+1.8}_{-1.7}$	$^{+1.2}_{-1.2}$
0.75 : 1.00	$^{+0.0}_{-0.1}$	$^{+0.2}_{-0.2}$	$^{+0.1}_{-0.1}$	$^{+0.4}_{-0.4}$	$^{+3.2}_{-3.2}$	$^{+0.5}_{-0.5}$	$^{+0.2}_{-0.3}$	$^{+0.3}_{-0.4}$	$^{+1.5}_{-0.0}$	$^{+0.8}_{-0.8}$	$^{+0.6}_{-0.0}$	$^{+0.0}_{-0.0}$	$^{+0.0}_{-1.2}$	$^{+1.8}_{-1.8}$	$^{+1.2}_{-1.2}$
1.00 : 1.25	$^{+0.1}_{-0.1}$	$^{+0.5}_{-0.2}$	$^{+0.3}_{-0.0}$	$^{+1.3}_{-1.3}$	$^{+3.8}_{-3.8}$	$^{+0.1}_{-0.1}$	$^{+0.2}_{-0.4}$	$^{+0.4}_{-0.5}$	$^{+1.2}_{-0.0}$	$^{+0.6}_{-0.6}$	$^{+0.3}_{-0.0}$	$^{+0.0}_{-0.6}$	$^{+0.0}_{-1.6}$	$^{+1.8}_{-1.8}$	$^{+1.5}_{-1.5}$
1.25 : 1.50	$^{+0.0}_{-0.0}$	$^{+0.0}_{-0.1}$	$^{+0.3}_{-0.1}$	$^{+1.2}_{-1.2}$	$^{+4.7}_{-4.7}$	$^{+0.5}_{-0.6}$	$^{+0.2}_{-0.4}$	$^{+0.7}_{-0.8}$	$^{+1.6}_{-0.0}$	$^{+0.3}_{-0.3}$	$^{+0.1}_{-0.0}$	$^{+1.1}_{-0.0}$	$^{+3.8}_{-0.0}$	$^{+1.9}_{-1.9}$	$^{+1.9}_{-1.9}$

z^{D^*}	δ_1	δ_2	δ_3	δ_4	δ_5	δ_7	δ_8	δ_9	δ_{10}	δ_{11}	δ_{13}	δ_{14}	δ_{15}	δ_{16}	δ_{18-19}
0.00 : 0.10	$^{+2.8}_{-4.7}$	$^{+1.4}_{-0.7}$	$^{+0.0}_{-0.3}$	$^{+0.0}_{-0.0}$	$^{+3.4}_{-3.4}$	$^{+0.0}_{-0.2}$	$^{+0.9}_{-1.8}$	$^{+1.5}_{-1.9}$	$^{+5.0}_{-0.0}$	$^{+0.3}_{-0.3}$	$^{+2.4}_{-0.0}$	$^{+1.5}_{-0.0}$	$^{+1.6}_{-0.0}$	$^{+2.4}_{-2.3}$	$^{+2.1}_{-2.1}$
0.10 : 0.20	$^{+3.5}_{-2.8}$	$^{+0.6}_{-0.8}$	$^{+0.3}_{-0.0}$	$^{+0.1}_{-0.1}$	$^{+2.9}_{-2.9}$	$^{+0.2}_{-0.2}$	$^{+0.6}_{-1.2}$	$^{+0.8}_{-1.0}$	$^{+2.0}_{-0.0}$	$^{+0.6}_{-0.7}$	$^{+1.3}_{-0.0}$	$^{+0.0}_{-0.3}$	$^{+0.1}_{-0.0}$	$^{+2.2}_{-2.1}$	$^{+1.2}_{-1.2}$
0.20 : 0.32	$^{+2.2}_{-2.2}$	$^{+0.5}_{-0.5}$	$^{+0.1}_{-0.0}$	$^{+1.5}_{-1.5}$	$^{+2.9}_{-2.9}$	$^{+0.1}_{-0.1}$	$^{+0.4}_{-0.9}$	$^{+0.9}_{-1.1}$	$^{+1.4}_{-0.0}$	$^{+1.0}_{-1.1}$	$^{+0.9}_{-0.0}$	$^{+0.1}_{-0.0}$	$^{+0.0}_{-0.4}$	$^{+2.0}_{-2.0}$	$^{+0.8}_{-0.8}$
0.32 : 0.45	$^{+0.6}_{-0.1}$	$^{+0.4}_{-0.3}$	$^{+0.3}_{-0.0}$	$^{+0.0}_{-0.0}$	$^{+2.9}_{-2.9}$	$^{+0.1}_{-0.1}$	$^{+0.2}_{-0.4}$	$^{+0.5}_{-0.6}$	$^{+1.2}_{-0.0}$	$^{+1.2}_{-1.2}$	$^{+0.8}_{-0.0}$	$^{+0.0}_{-0.3}$	$^{+0.4}_{-0.0}$	$^{+1.8}_{-1.8}$	$^{+0.7}_{-0.7}$
0.45 : 0.57	$^{+1.1}_{-1.5}$	$^{+0.3}_{-0.3}$	$^{+0.2}_{-0.1}$	$^{+0.6}_{-0.6}$	$^{+2.9}_{-2.9}$	$^{+0.1}_{-0.0}$	$^{+0.1}_{-0.1}$	$^{+0.2}_{-0.2}$	$^{+0.5}_{-0.0}$	$^{+1.0}_{-1.0}$	$^{+1.5}_{-0.0}$	$^{+0.3}_{-0.0}$	$^{+0.0}_{-0.4}$	$^{+1.7}_{-1.6}$	$^{+0.8}_{-0.8}$
0.57 : 0.80	$^{+4.0}_{-3.5}$	$^{+0.2}_{-0.3}$	$^{+0.2}_{-0.0}$	$^{+0.1}_{-0.1}$	$^{+2.9}_{-2.9}$	$^{+0.1}_{-0.1}$	$^{+0.1}_{-0.2}$	$^{+1.2}_{-1.0}$	$^{+1.8}_{-0.0}$	$^{+0.1}_{-0.1}$	$^{+2.5}_{-0.0}$	$^{+0.1}_{-0.0}$	$^{+0.0}_{-0.5}$	$^{+1.5}_{-1.5}$	$^{+1.0}_{-1.0}$
0.80 : 1.00	$^{+4.8}_{-5.6}$	$^{+0.2}_{-0.2}$	$^{+0.0}_{-0.1}$	$^{+1.3}_{-1.3}$	$^{+3.1}_{-3.1}$	$^{+0.1}_{-0.3}$	$^{+0.0}_{-0.0}$	$^{+4.2}_{-3.4}$	$^{+3.7}_{-0.0}$	$^{+1.2}_{-1.3}$	$^{+2.7}_{-0.0}$	$^{+1.8}_{-0.0}$	$^{+0.0}_{-0.1}$	$^{+1.4}_{-1.4}$	$^{+3.7}_{-3.7}$

Table H.1: Systematic uncertainties given in % for the differential cross-sections in bins of $p_T^{D^*}$, η^{D^*}, z^{D^*}. δ_6, δ_{12}, δ_{17} and δ_{20} were skipped intentionally. They are $\pm 1.9\%$, $\pm 0.5\%$, $+2.0\%$ and 1.5%, respectively (independently of the kinematic range).

Q^2, GeV^2	δ_1	δ_2	δ_3	δ_4	δ_5	δ_7	δ_8	δ_9	δ_{10}	δ_{11}	δ_{13}	δ_{14}	δ_{15}	δ_{16}	δ_{18-19}
5.00 : 8.00	$^{+0.5}_{-0.9}$	$^{+3.2}_{-3.2}$	$^{+1.5}_{-1.1}$	$^{+2.7}_{-2.7}$	$^{+3.0}_{-3.0}$	$^{+0.1}_{-0.1}$	$^{+0.6}_{-1.2}$	$^{+0.3}_{-0.3}$	$^{+0.2}_{-0.0}$	$^{+1.6}_{-1.5}$	$^{+1.6}_{-0.0}$	$^{+0.4}_{-0.0}$	$^{+0.0}_{-0.6}$	$^{+2.1}_{-2.1}$	$^{+1.2}_{-1.2}$
8.00 : 10.00	$^{+0.2}_{-0.4}$	$^{+1.0}_{-1.1}$	$^{+0.3}_{-0.4}$	$^{+2.7}_{-2.7}$	$^{+3.0}_{-3.0}$	$^{+0.1}_{-0.1}$	$^{+0.3}_{-0.6}$	$^{+0.6}_{-0.7}$	$^{+1.5}_{-0.0}$	$^{+1.8}_{-1.6}$	$^{+1.2}_{-0.0}$	$^{+0.5}_{-0.0}$	$^{+0.9}_{-0.0}$	$^{+2.1}_{-2.0}$	$^{+1.3}_{-1.3}$
10.00 : 13.00	$^{+0.4}_{-0.2}$	$^{+0.3}_{-0.7}$	$^{+0.0}_{-0.8}$	$^{+0.3}_{-0.3}$	$^{+3.0}_{-3.0}$	$^{+0.1}_{-0.1}$	$^{+0.2}_{-0.5}$	$^{+0.0}_{-0.0}$	$^{+1.5}_{-0.0}$	$^{+1.1}_{-1.0}$	$^{+1.1}_{-0.0}$	$^{+0.5}_{-0.0}$	$^{+0.0}_{-0.6}$	$^{+2.1}_{-2.0}$	$^{+1.2}_{-1.2}$
13.00 : 19.00	$^{+0.1}_{-0.1}$	$^{+0.9}_{-0.1}$	$^{+0.0}_{-0.2}$	$^{+0.4}_{-0.4}$	$^{+3.0}_{-3.0}$	$^{+0.0}_{-0.1}$	$^{+0.3}_{-0.5}$	$^{+0.0}_{-0.0}$	$^{+0.6}_{-0.0}$	$^{+3.2}_{-3.2}$	$^{+1.1}_{-0.0}$	$^{+0.0}_{-0.3}$	$^{+0.0}_{-0.7}$	$^{+2.0}_{-1.9}$	$^{+1.0}_{-1.0}$
19.00 : 27.50	$^{+0.1}_{-0.0}$	$^{+0.6}_{-0.7}$	$^{+0.0}_{-0.0}$	$^{+0.0}_{-0.0}$	$^{+2.9}_{-2.9}$	$^{+0.1}_{-0.1}$	$^{+0.3}_{-0.5}$	$^{+0.1}_{-0.1}$	$^{+1.6}_{-0.0}$	$^{+1.6}_{-1.5}$	$^{+1.0}_{-0.0}$	$^{+0.2}_{-0.0}$	$^{+0.1}_{-0.0}$	$^{+1.9}_{-1.8}$	$^{+1.0}_{-1.0}$
27.50 : 40.00	$^{+0.0}_{-0.1}$	$^{+1.2}_{-1.0}$	$^{+0.0}_{-0.0}$	$^{+0.0}_{-0.0}$	$^{+2.9}_{-2.9}$	$^{+0.1}_{-0.1}$	$^{+0.2}_{-0.5}$	$^{+0.1}_{-0.1}$	$^{+1.5}_{-0.0}$	$^{+0.9}_{-0.8}$	$^{+1.1}_{-0.0}$	$^{+0.3}_{-0.0}$	$^{+0.0}_{-0.2}$	$^{+1.7}_{-1.7}$	$^{+1.0}_{-1.0}$
40.00 : 60.00	$^{+0.3}_{-0.3}$	$^{+1.2}_{-1.4}$	$^{+0.0}_{-0.0}$	$^{+0.0}_{-0.0}$	$^{+2.9}_{-2.9}$	$^{+0.4}_{-0.4}$	$^{+0.2}_{-0.4}$	$^{+0.2}_{-0.2}$	$^{+0.8}_{-0.0}$	$^{+3.4}_{-3.6}$	$^{+1.0}_{-0.0}$	$^{+0.0}_{-0.3}$	$^{+0.0}_{-1.8}$	$^{+1.6}_{-1.5}$	$^{+1.1}_{-1.1}$
60.00 : 100.00	$^{+1.1}_{-0.8}$	$^{+2.2}_{-2.8}$	$^{+0.0}_{-0.0}$	$^{+0.0}_{-0.0}$	$^{+2.9}_{-2.9}$	$^{+0.4}_{-0.5}$	$^{+0.1}_{-0.2}$	$^{+0.7}_{-0.6}$	$^{+4.6}_{-0.0}$	$^{+1.9}_{-2.1}$	$^{+1.4}_{-0.0}$	$^{+0.0}_{-0.5}$	$^{+1.0}_{-0.0}$	$^{+1.5}_{-1.4}$	$^{+1.2}_{-1.2}$
100.00 : 200.00	$^{+0.4}_{-0.6}$	$^{+3.0}_{-1.7}$	$^{+0.0}_{-0.0}$	$^{+0.0}_{-0.0}$	$^{+2.9}_{-2.9}$	$^{+1.3}_{-1.5}$	$^{+0.3}_{-0.5}$	$^{+0.0}_{-0.0}$	$^{+2.6}_{-0.0}$	$^{+1.1}_{-1.2}$	$^{+1.4}_{-0.0}$	$^{+0.0}_{-0.6}$	$^{+2.7}_{-0.0}$	$^{+1.3}_{-1.3}$	$^{+1.4}_{-1.4}$
200.00 : 1000.00	$^{+1.1}_{-1.2}$	$^{+1.9}_{-3.0}$	$^{+0.0}_{-0.0}$	$^{+0.0}_{-0.0}$	$^{+2.8}_{-2.8}$	$^{+0.9}_{-1.0}$	$^{+0.3}_{-0.6}$	$^{+0.2}_{-0.3}$	$^{+0.2}_{-0.0}$	$^{+0.5}_{-0.6}$	$^{+0.7}_{-0.0}$	$^{+0.0}_{-0.0}$	$^{+3.5}_{-0.0}$	$^{+1.3}_{-1.2}$	$^{+2.2}_{-2.2}$

y	δ_1	δ_2	δ_3	δ_4	δ_5	δ_7	δ_8	δ_9	δ_{10}	δ_{11}	δ_{13}	δ_{14}	δ_{15}	δ_{16}	δ_{18-19}
0.02 : 0.05	$^{+10.8}_{-8.4}$	$^{+7.1}_{-4.5}$	$^{+0.4}_{-0.0}$	$^{+0.9}_{-0.9}$	$^{+4.2}_{-4.2}$	$^{+0.0}_{-0.0}$	$^{+0.3}_{-0.6}$	$^{+4.3}_{-3.4}$	$^{+3.8}_{-0.0}$	$^{+0.0}_{-0.0}$	$^{+1.9}_{-0.0}$	$^{+0.5}_{-0.0}$	$^{+0.0}_{-1.7}$	$^{+2.1}_{-2.0}$	$^{+3.3}_{-3.3}$
0.05 : 0.09	$^{+3.4}_{-3.9}$	$^{+1.6}_{-2.2}$	$^{+0.4}_{-0.2}$	$^{+1.6}_{-1.6}$	$^{+3.4}_{-3.4}$	$^{+0.0}_{-0.0}$	$^{+0.0}_{-0.0}$	$^{+0.8}_{-0.7}$	$^{+2.4}_{-0.0}$	$^{+0.6}_{-0.6}$	$^{+0.0}_{-1.4}$	$^{+0.0}_{-0.1}$	$^{+0.0}_{-0.9}$	$^{+2.0}_{-1.9}$	$^{+1.2}_{-1.2}$
0.09 : 0.13	$^{+1.0}_{-1.4}$	$^{+0.7}_{-0.7}$	$^{+0.3}_{-0.0}$	$^{+0.4}_{-0.4}$	$^{+2.9}_{-2.9}$	$^{+0.0}_{-0.0}$	$^{+0.0}_{-0.0}$	$^{+0.3}_{-0.4}$	$^{+0.9}_{-0.0}$	$^{+0.9}_{-0.9}$	$^{+0.0}_{-0.5}$	$^{+0.0}_{-0.0}$	$^{+0.0}_{-0.3}$	$^{+1.9}_{-1.8}$	$^{+1.0}_{-1.0}$
0.13 : 0.18	$^{+0.7}_{-0.2}$	$^{+0.4}_{-0.4}$	$^{+0.3}_{-0.1}$	$^{+0.6}_{-0.6}$	$^{+2.6}_{-2.6}$	$^{+0.0}_{-0.0}$	$^{+0.0}_{-0.0}$	$^{+0.6}_{-0.8}$	$^{+1.6}_{-0.0}$	$^{+0.7}_{-0.7}$	$^{+0.0}_{-3.2}$	$^{+0.1}_{-0.0}$	$^{+0.9}_{-0.0}$	$^{+1.9}_{-1.8}$	$^{+0.9}_{-0.9}$
0.18 : 0.26	$^{+0.5}_{-0.2}$	$^{+0.2}_{-0.0}$	$^{+0.2}_{-0.0}$	$^{+1.0}_{-1.0}$	$^{+2.7}_{-2.7}$	$^{+0.1}_{-0.1}$	$^{+0.1}_{-0.1}$	$^{+0.5}_{-0.6}$	$^{+1.9}_{-0.0}$	$^{+0.8}_{-0.8}$	$^{+1.3}_{-0.0}$	$^{+0.0}_{-0.0}$	$^{+0.1}_{-0.0}$	$^{+1.8}_{-1.8}$	$^{+0.9}_{-0.9}$
0.26 : 0.36	$^{+0.6}_{-1.1}$	$^{+0.4}_{-0.5}$	$^{+0.3}_{-0.0}$	$^{+0.0}_{-0.0}$	$^{+2.8}_{-2.8}$	$^{+0.0}_{-0.1}$	$^{+0.3}_{-0.5}$	$^{+0.9}_{-1.0}$	$^{+1.7}_{-0.0}$	$^{+1.0}_{-1.0}$	$^{+0.4}_{-0.0}$	$^{+0.1}_{-0.0}$	$^{+1.1}_{-0.0}$	$^{+1.8}_{-1.7}$	$^{+0.9}_{-0.9}$
0.36 : 0.50	$^{+2.1}_{-1.4}$	$^{+0.9}_{-0.3}$	$^{+0.1}_{-0.2}$	$^{+0.1}_{-0.1}$	$^{+3.1}_{-3.1}$	$^{+0.1}_{-0.2}$	$^{+0.8}_{-1.6}$	$^{+0.4}_{-0.5}$	$^{+1.2}_{-0.0}$	$^{+0.9}_{-0.9}$	$^{+0.9}_{-0.0}$	$^{+0.0}_{-0.7}$	$^{+0.0}_{-0.8}$	$^{+1.8}_{-1.7}$	$^{+1.0}_{-1.0}$
0.50 : 0.70	$^{+5.2}_{-5.1}$	$^{+0.0}_{-0.8}$	$^{+0.1}_{-0.1}$	$^{+0.2}_{-0.2}$	$^{+3.2}_{-3.2}$	$^{+0.5}_{-0.6}$	$^{+1.2}_{-2.5}$	$^{+0.0}_{-0.1}$	$^{+1.7}_{-0.0}$	$^{+0.6}_{-0.6}$	$^{+5.8}_{-0.0}$	$^{+1.5}_{-0.0}$	$^{+0.0}_{-1.4}$	$^{+1.7}_{-1.7}$	$^{+1.4}_{-1.4}$

x	δ_1	δ_2	δ_3	δ_4	δ_5	δ_7	δ_8	δ_9	δ_{10}	δ_{11}	δ_{13}	δ_{14}	δ_{15}	δ_{16}	δ_{18-19}
0.000080 : 0.000400	$^{+1.6}_{-1.3}$	$^{+1.7}_{-1.8}$	$^{+0.6}_{-0.0}$	$^{+1.2}_{-1.2}$	$^{+3.1}_{-3.1}$	$^{+0.1}_{-0.1}$	$^{+0.8}_{-1.7}$	$^{+0.8}_{-1.0}$	$^{+1.6}_{-0.0}$	$^{+1.8}_{-1.6}$	$^{+1.8}_{-0.0}$	$^{+0.4}_{-0.0}$	$^{+0.0}_{-0.9}$	$^{+2.0}_{-1.9}$	$^{+0.9}_{-0.9}$
0.000400 : 0.001600	$^{+0.4}_{-0.6}$	$^{+0.3}_{-0.2}$	$^{+0.3}_{-0.0}$	$^{+0.5}_{-0.5}$	$^{+2.9}_{-2.9}$	$^{+0.1}_{-0.1}$	$^{+0.2}_{-0.5}$	$^{+0.4}_{-0.5}$	$^{+1.8}_{-0.0}$	$^{+1.4}_{-1.3}$	$^{+0.8}_{-0.0}$	$^{+0.1}_{-0.0}$	$^{+0.0}_{-0.2}$	$^{+2.0}_{-1.9}$	$^{+0.6}_{-0.6}$
0.001600 : 0.005000	$^{+0.8}_{-0.6}$	$^{+1.5}_{-1.5}$	$^{+0.0}_{-0.1}$	$^{+0.0}_{-0.0}$	$^{+2.9}_{-2.9}$	$^{+0.1}_{-0.1}$	$^{+0.1}_{-0.1}$	$^{+0.4}_{-0.3}$	$^{+0.9}_{-0.0}$	$^{+0.7}_{-0.7}$	$^{+1.8}_{-0.0}$	$^{+0.0}_{-0.0}$	$^{+0.3}_{-0.0}$	$^{+1.7}_{-1.6}$	$^{+0.7}_{-0.7}$
0.005000 : 0.010000	$^{+1.4}_{-1.2}$	$^{+3.7}_{-3.2}$	$^{+0.0}_{-0.1}$	$^{+0.1}_{-0.1}$	$^{+3.1}_{-3.1}$	$^{+0.2}_{-0.3}$	$^{+0.0}_{-0.1}$	$^{+0.1}_{-0.1}$	$^{+0.7}_{-0.0}$	$^{+0.2}_{-0.2}$	$^{+1.9}_{-0.0}$	$^{+0.0}_{-0.9}$	$^{+1.4}_{-0.0}$	$^{+1.4}_{-1.4}$	$^{+1.3}_{-1.3}$
0.010000 : 0.100000	$^{+3.6}_{-3.9}$	$^{+6.6}_{-5.9}$	$^{+0.0}_{-0.1}$	$^{+0.3}_{-0.3}$	$^{+3.3}_{-3.3}$	$^{+0.1}_{-0.2}$	$^{+0.2}_{-0.3}$	$^{+0.8}_{-0.8}$	$^{+0.4}_{-0.0}$	$^{+0.7}_{-0.8}$	$^{+1.1}_{-0.0}$	$^{+0.0}_{-0.9}$	$^{+1.8}_{-0.0}$	$^{+1.3}_{-1.2}$	$^{+2.3}_{-2.3}$

Table H.2: Systematic uncertainties given in % for the differential cross-sections in bins of Q^2, y, x. δ_6, δ_{12}, δ_{17} and δ_{20} were skipped intentionally. They are $\pm 1.9\%, \pm 0.5\%, +2.0\%$ and 1.5%, respectively (independently of the kinematic range).

Q^2	y	δ_1	δ_2	δ_3	δ_4	δ_5	δ_7	δ_8	δ_9	δ_{10}	δ_{11}	δ_{13}	δ_{14}	δ_{15}	δ_{16}	δ_{18-19}
5 : 9	0.020 : 0.050	$^{+10.5}_{-12.3}$	$^{+1.8}_{-0.0}$	$^{+2.6}_{-2.9}$	$^{+9.0}_{-9.0}$	$^{+2.5}_{-2.5}$	$^{+0.0}_{-0.0}$	$^{+0.0}_{-0.0}$	$^{+4.2}_{-4.2}$	$^{+1.8}_{-0.0}$	$^{+0.1}_{-0.1}$	$^{+2.2}_{-0.0}$	$^{+0.0}_{-7.0}$	$^{+0.0}_{-3.4}$	$^{+2.5}_{-2.4}$	$^{+8.8}_{-8.8}$
	0.05 : 0.09	$^{+3.5}_{-4.0}$	$^{+5.1}_{-4.8}$	$^{+2.0}_{-4.3}$	$^{+6.6}_{-6.6}$	$^{+2.1}_{-2.1}$	$^{+0.1}_{-0.1}$	$^{+0.0}_{-0.0}$	$^{+2.3}_{-1.9}$	$^{+3.0}_{-0.0}$	$^{+0.8}_{-0.7}$	$^{+0.0}_{-1.6}$	$^{+0.7}_{-0.0}$	$^{+0.0}_{-1.9}$	$^{+2.4}_{-2.2}$	$^{+3.5}_{-3.5}$
	0.09 : 0.16	$^{+1.5}_{-3.4}$	$^{+3.3}_{-4.0}$	$^{+1.9}_{-1.6}$	$^{+1.1}_{-1.1}$	$^{+1.8}_{-1.8}$	$^{+0.1}_{-0.1}$	$^{+0.0}_{-0.0}$	$^{+0.6}_{-0.8}$	$^{+1.8}_{-0.0}$	$^{+1.5}_{-1.4}$	$^{+0.0}_{-2.0}$	$^{+1.0}_{-0.0}$	$^{+0.5}_{-0.0}$	$^{+2.3}_{-2.2}$	$^{+2.3}_{-2.3}$
	0.16 : 0.32	$^{+0.9}_{-0.0}$	$^{+2.9}_{-2.7}$	$^{+1.2}_{-0.4}$	$^{+3.5}_{-3.5}$	$^{+1.8}_{-1.8}$	$^{+0.0}_{-0.0}$	$^{+0.3}_{-0.5}$	$^{+0.7}_{-0.9}$	$^{+0.0}_{-0.5}$	$^{+1.8}_{-1.7}$	$^{+0.7}_{-0.0}$	$^{+0.6}_{-0.0}$	$^{+0.3}_{-0.0}$	$^{+2.2}_{-2.1}$	$^{+1.7}_{-1.7}$
	0.32 : 0.70	$^{+1.7}_{-1.5}$	$^{+1.9}_{-0.7}$	$^{+0.4}_{-0.5}$	$^{+1.9}_{-1.9}$	$^{+1.9}_{-1.9}$	$^{+0.0}_{-0.0}$	$^{+1.4}_{-2.8}$	$^{+0.3}_{-0.4}$	$^{+0.0}_{-0.6}$	$^{+1.5}_{-1.4}$	$^{+3.1}_{-0.0}$	$^{+0.2}_{-0.0}$	$^{+0.0}_{-1.5}$	$^{+2.0}_{-1.9}$	$^{+1.7}_{-1.7}$
9 : 14	0.020 : 0.050	$^{+11.0}_{-6.9}$	$^{+7.3}_{-4.8}$	$^{+0.5}_{-1.5}$	$^{+2.5}_{-2.5}$	$^{+2.4}_{-2.4}$	$^{+0.1}_{-0.1}$	$^{+0.0}_{-0.0}$	$^{+4.7}_{-4.5}$	$^{+3.0}_{-0.0}$	$^{+0.7}_{-0.7}$	$^{+1.4}_{-0.0}$	$^{+0.0}_{-0.1}$	$^{+0.0}_{-2.1}$	$^{+2.2}_{-2.1}$	$^{+6.1}_{-6.1}$
	0.05 : 0.09	$^{+3.1}_{-3.2}$	$^{+1.9}_{-0.0}$	$^{+0.3}_{-1.4}$	$^{+2.1}_{-2.1}$	$^{+2.0}_{-2.0}$	$^{+0.0}_{-0.0}$	$^{+0.0}_{-0.0}$	$^{+1.5}_{-1.2}$	$^{+2.7}_{-0.0}$	$^{+1.2}_{-1.2}$	$^{+0.0}_{-1.6}$	$^{+0.6}_{-0.0}$	$^{+0.1}_{-0.0}$	$^{+2.2}_{-2.1}$	$^{+2.5}_{-2.5}$
	0.09 : 0.16	$^{+0.5}_{-0.6}$	$^{+0.3}_{-0.1}$	$^{+0.6}_{-1.6}$	$^{+1.6}_{-1.6}$	$^{+1.7}_{-1.7}$	$^{+0.2}_{-0.2}$	$^{+0.0}_{-0.0}$	$^{+0.1}_{-0.1}$	$^{+0.8}_{-0.0}$	$^{+1.7}_{-1.6}$	$^{+0.0}_{-2.0}$	$^{+0.5}_{-0.0}$	$^{+0.0}_{-0.3}$	$^{+2.1}_{-2.0}$	$^{+1.8}_{-1.8}$
	0.16 : 0.32	$^{+0.5}_{-0.0}$	$^{+0.5}_{-0.0}$	$^{+0.0}_{-0.4}$	$^{+0.5}_{-0.5}$	$^{+1.8}_{-1.8}$	$^{+0.1}_{-0.1}$	$^{+0.1}_{-0.1}$	$^{+0.6}_{-0.7}$	$^{+1.1}_{-0.0}$	$^{+1.9}_{-1.8}$	$^{+0.4}_{-0.0}$	$^{+0.3}_{-0.0}$	$^{+0.5}_{-0.0}$	$^{+2.1}_{-2.0}$	$^{+1.5}_{-1.5}$
	0.32 : 0.70	$^{+3.8}_{-2.8}$	$^{+1.1}_{-0.7}$	$^{+0.0}_{-0.1}$	$^{+0.4}_{-0.4}$	$^{+1.8}_{-1.8}$	$^{+0.2}_{-0.3}$	$^{+0.8}_{-1.6}$	$^{+0.4}_{-0.5}$	$^{+0.2}_{-0.0}$	$^{+2.0}_{-1.8}$	$^{+2.8}_{-0.0}$	$^{+0.4}_{-0.0}$	$^{+0.0}_{-0.2}$	$^{+1.9}_{-1.9}$	$^{+1.9}_{-1.9}$
14 : 23	0.020 : 0.050	$^{+11.5}_{-8.8}$	$^{+6.4}_{-3.8}$	$^{+0.0}_{-0.2}$	$^{+0.0}_{-0.0}$	$^{+2.4}_{-2.4}$	$^{+0.2}_{-0.2}$	$^{+0.0}_{-0.0}$	$^{+2.4}_{-2.7}$	$^{+4.1}_{-0.0}$	$^{+0.8}_{-0.8}$	$^{+1.7}_{-0.0}$	$^{+0.3}_{-0.0}$	$^{+2.5}_{-0.0}$	$^{+2.1}_{-2.0}$	$^{+6.0}_{-6.0}$
	0.05 : 0.09	$^{+2.5}_{-3.9}$	$^{+1.5}_{-3.8}$	$^{+0.1}_{-0.5}$	$^{+0.9}_{-0.9}$	$^{+2.0}_{-2.0}$	$^{+0.1}_{-0.1}$	$^{+0.0}_{-0.0}$	$^{+1.1}_{-0.9}$	$^{+2.3}_{-0.0}$	$^{+1.8}_{-1.9}$	$^{+0.0}_{-1.7}$	$^{+0.2}_{-0.0}$	$^{+1.0}_{-0.0}$	$^{+2.1}_{-2.0}$	$^{+2.4}_{-2.4}$
	0.09 : 0.16	$^{+1.3}_{-0.0}$	$^{+0.8}_{-0.4}$	$^{+0.0}_{-0.3}$	$^{+0.3}_{-0.3}$	$^{+1.7}_{-1.7}$	$^{+0.1}_{-0.1}$	$^{+0.0}_{-0.0}$	$^{+0.3}_{-0.4}$	$^{+0.7}_{-0.0}$	$^{+2.2}_{-2.3}$	$^{+0.0}_{-2.0}$	$^{+0.0}_{-1.0}$	$^{+0.0}_{-1.6}$	$^{+2.0}_{-1.9}$	$^{+1.7}_{-1.7}$
	0.16 : 0.32	$^{+0.5}_{-0.9}$	$^{+0.0}_{-0.6}$	$^{+0.0}_{-0.0}$	$^{+0.6}_{-0.6}$	$^{+1.7}_{-1.7}$	$^{+0.1}_{-0.2}$	$^{+0.2}_{-0.3}$	$^{+1.0}_{-1.3}$	$^{+0.4}_{-0.0}$	$^{+2.6}_{-2.6}$	$^{+0.4}_{-0.0}$	$^{+0.0}_{-0.9}$	$^{+1.7}_{-0.0}$	$^{+1.9}_{-1.9}$	$^{+1.5}_{-1.5}$
	0.32 : 0.70	$^{+1.3}_{-2.9}$	$^{+0.0}_{-1.7}$	$^{+0.0}_{-0.0}$	$^{+0.1}_{-0.1}$	$^{+1.8}_{-1.8}$	$^{+0.2}_{-0.3}$	$^{+1.0}_{-1.9}$	$^{+0.3}_{-0.4}$	$^{+0.0}_{-1.5}$	$^{+2.7}_{-2.7}$	$^{+2.9}_{-0.0}$	$^{+0.0}_{-0.3}$	$^{+0.0}_{-3.1}$	$^{+1.9}_{-1.8}$	$^{+1.8}_{-1.8}$
23 : 45	0.020 : 0.050	$^{+9.5}_{-8.4}$	$^{+11.5}_{-6.7}$	$^{+0.0}_{-0.0}$	$^{+0.0}_{-0.0}$	$^{+2.2}_{-2.2}$	$^{+0.3}_{-0.3}$	$^{+0.0}_{-0.0}$	$^{+2.4}_{-2.3}$	$^{+3.7}_{-0.0}$	$^{+0.6}_{-0.6}$	$^{+1.7}_{-0.0}$	$^{+1.3}_{-0.0}$	$^{+0.0}_{-12.7}$	$^{+1.9}_{-1.8}$	$^{+7.0}_{-7.0}$
	0.05 : 0.09	$^{+4.3}_{-4.6}$	$^{+4.3}_{-4.8}$	$^{+0.0}_{-0.0}$	$^{+0.0}_{-0.0}$	$^{+1.9}_{-1.9}$	$^{+0.0}_{-0.0}$	$^{+0.0}_{-0.0}$	$^{+0.5}_{-0.4}$	$^{+0.1}_{-0.0}$	$^{+1.6}_{-1.5}$	$^{+0.0}_{-1.4}$	$^{+0.0}_{-0.3}$	$^{+0.0}_{-0.2}$	$^{+1.8}_{-1.7}$	$^{+2.4}_{-2.4}$
	0.09 : 0.16	$^{+0.9}_{-1.1}$	$^{+1.8}_{-1.4}$	$^{+0.0}_{-0.0}$	$^{+0.0}_{-0.0}$	$^{+1.6}_{-1.6}$	$^{+0.2}_{-0.3}$	$^{+0.0}_{-0.0}$	$^{+0.3}_{-0.3}$	$^{+0.0}_{-0.0}$	$^{+1.7}_{-1.7}$	$^{+0.0}_{-2.1}$	$^{+0.3}_{-0.0}$	$^{+0.0}_{-0.1}$	$^{+1.8}_{-1.7}$	$^{+1.6}_{-1.6}$
	0.16 : 0.32	$^{+1.2}_{-1.0}$	$^{+0.0}_{-0.4}$	$^{+0.0}_{-0.0}$	$^{+0.0}_{-0.0}$	$^{+1.6}_{-1.6}$	$^{+0.1}_{-0.2}$	$^{+0.1}_{-0.2}$	$^{+0.0}_{-0.1}$	$^{+0.7}_{-0.0}$	$^{+1.8}_{-1.8}$	$^{+0.4}_{-0.0}$	$^{+0.2}_{-0.0}$	$^{+0.1}_{-0.0}$	$^{+1.8}_{-1.7}$	$^{+1.3}_{-1.3}$
	0.32 : 0.70	$^{+3.5}_{-2.6}$	$^{+1.1}_{-0.0}$	$^{+0.0}_{-0.0}$	$^{+0.0}_{-0.0}$	$^{+1.8}_{-1.8}$	$^{+0.1}_{-0.2}$	$^{+0.6}_{-1.3}$	$^{+0.2}_{-0.2}$	$^{+2.1}_{-0.0}$	$^{+1.7}_{-1.7}$	$^{+2.4}_{-0.0}$	$^{+1.0}_{-0.0}$	$^{+0.0}_{-0.0}$	$^{+1.8}_{-1.7}$	$^{+1.6}_{-1.6}$
45 : 100	0.020 : 0.050	$^{+26.2}_{-6.4}$	$^{+18.2}_{-9.7}$	$^{+0.0}_{-0.0}$	$^{+0.0}_{-0.0}$	$^{+2.0}_{-2.0}$	$^{+0.0}_{-0.0}$	$^{+0.0}_{-0.0}$	$^{+3.4}_{-2.6}$	$^{+5.0}_{-0.0}$	$^{+2.0}_{-2.2}$	$^{+3.5}_{-0.0}$	$^{+0.0}_{-0.1}$	$^{+2.3}_{-0.0}$	$^{+1.5}_{-1.4}$	$^{+12.8}_{-12.8}$
	0.05 : 0.09	$^{+4.2}_{-3.5}$	$^{+3.7}_{-4.0}$	$^{+0.0}_{-0.0}$	$^{+0.0}_{-0.0}$	$^{+1.8}_{-1.8}$	$^{+0.1}_{-0.1}$	$^{+0.0}_{-0.0}$	$^{+0.0}_{-0.2}$	$^{+3.3}_{-0.0}$	$^{+1.3}_{-1.4}$	$^{+0.0}_{-1.6}$	$^{+0.0}_{-2.0}$	$^{+0.0}_{-0.1}$	$^{+1.5}_{-1.5}$	$^{+3.2}_{-3.2}$
	0.09 : 0.16	$^{+1.1}_{-0.7}$	$^{+2.4}_{-2.0}$	$^{+0.0}_{-0.0}$	$^{+0.0}_{-0.0}$	$^{+1.5}_{-1.5}$	$^{+0.3}_{-0.4}$	$^{+0.0}_{-0.0}$	$^{+0.0}_{-0.0}$	$^{+1.5}_{-0.0}$	$^{+1.7}_{-1.9}$	$^{+0.0}_{-2.1}$	$^{+0.0}_{-0.8}$	$^{+0.0}_{-0.3}$	$^{+1.5}_{-1.4}$	$^{+1.9}_{-1.9}$
	0.16 : 0.32	$^{+0.0}_{-0.7}$	$^{+1.9}_{-1.5}$	$^{+0.0}_{-0.0}$	$^{+0.0}_{-0.0}$	$^{+1.5}_{-1.5}$	$^{+0.6}_{-0.7}$	$^{+0.0}_{-0.0}$	$^{+0.0}_{-0.0}$	$^{+3.0}_{-0.0}$	$^{+2.1}_{-2.3}$	$^{+0.2}_{-0.0}$	$^{+0.3}_{-0.0}$	$^{+0.5}_{-0.0}$	$^{+1.6}_{-1.5}$	$^{+1.5}_{-1.5}$
	0.32 : 0.70	$^{+3.2}_{-2.8}$	$^{+0.0}_{-0.8}$	$^{+0.0}_{-0.0}$	$^{+0.0}_{-0.0}$	$^{+1.6}_{-1.6}$	$^{+0.5}_{-0.7}$	$^{+0.4}_{-0.9}$	$^{+0.7}_{-0.6}$	$^{+2.4}_{-0.0}$	$^{+2.5}_{-2.7}$	$^{+2.9}_{-0.0}$	$^{+0.0}_{-0.6}$	$^{+0.0}_{-2.4}$	$^{+1.7}_{-1.6}$	$^{+1.7}_{-1.7}$
100 : 158	0.020 : 0.350	$^{+1.7}_{-0.6}$	$^{+4.4}_{-1.3}$	$^{+0.0}_{-0.0}$	$^{+0.0}_{-0.0}$	$^{+1.4}_{-1.4}$	$^{+0.9}_{-1.1}$	$^{+0.0}_{-0.0}$	$^{+0.2}_{-0.2}$	$^{+1.3}_{-0.0}$	$^{+1.2}_{-1.3}$	$^{+0.0}_{-0.2}$	$^{+0.0}_{-2.2}$	$^{+4.4}_{-0.0}$	$^{+1.3}_{-1.3}$	$^{+2.0}_{-2.0}$
	0.35 : 0.70	$^{+0.8}_{-5.3}$	$^{+0.0}_{-2.5}$	$^{+0.0}_{-0.0}$	$^{+0.0}_{-0.0}$	$^{+1.5}_{-1.5}$	$^{+2.6}_{-3.2}$	$^{+0.5}_{-1.1}$	$^{+0.1}_{-0.4}$	$^{+0.0}_{-0.2}$	$^{+1.1}_{-1.3}$	$^{+2.9}_{-0.0}$	$^{+1.8}_{-0.0}$	$^{+4.4}_{-0.0}$	$^{+1.4}_{-1.4}$	$^{+3.1}_{-3.1}$
158 : 251	0.020 : 0.300	$^{+0.3}_{-0.8}$	$^{+2.0}_{-4.3}$	$^{+0.0}_{-0.0}$	$^{+0.0}_{-0.0}$	$^{+1.3}_{-1.3}$	$^{+0.8}_{-1.0}$	$^{+0.1}_{-0.1}$	$^{+0.4}_{-0.6}$	$^{+0.0}_{-1.3}$	$^{+0.8}_{-0.9}$	$^{+0.1}_{-0.0}$	$^{+0.0}_{-1.9}$	$^{+0.0}_{-0.3}$	$^{+1.2}_{-1.2}$	$^{+3.2}_{-3.2}$
	0.30 : 0.70	$^{+2.6}_{-2.6}$	$^{+0.6}_{-0.2}$	$^{+0.0}_{-0.0}$	$^{+0.0}_{-0.0}$	$^{+1.4}_{-1.4}$	$^{+0.1}_{-0.7}$	$^{+0.5}_{-1.0}$	$^{+0.3}_{-0.5}$	$^{+1.1}_{-0.0}$	$^{+0.9}_{-1.0}$	$^{+3.0}_{-0.0}$	$^{+1.8}_{-0.0}$	$^{+1.7}_{-0.0}$	$^{+1.4}_{-1.3}$	$^{+3.2}_{-3.2}$
251 : 1000	0.020 : 0.275	$^{+0.0}_{-2.2}$	$^{+5.9}_{-5.8}$	$^{+0.0}_{-0.0}$	$^{+0.0}_{-0.0}$	$^{+1.3}_{-1.3}$	$^{+0.8}_{-1.3}$	$^{+0.0}_{-0.0}$	$^{+0.9}_{-1.0}$	$^{+0.0}_{-3.3}$	$^{+0.1}_{-0.1}$	$^{+0.0}_{-0.3}$	$^{+0.0}_{-4.6}$	$^{+0.0}_{-0.0}$	$^{+1.2}_{-1.2}$	$^{+4.8}_{-4.8}$
	0.28 : 0.70	$^{+4.3}_{-0.8}$	$^{+3.8}_{-1.7}$	$^{+0.0}_{-0.0}$	$^{+0.0}_{-0.0}$	$^{+1.4}_{-1.4}$	$^{+0.0}_{-0.1}$	$^{+0.7}_{-1.4}$	$^{+0.4}_{-0.5}$	$^{+0.0}_{-1.4}$	$^{+0.9}_{-1.0}$	$^{+0.9}_{-0.0}$	$^{+2.5}_{-0.0}$	$^{+3.5}_{-0.0}$	$^{+1.4}_{-1.3}$	$^{+3.8}_{-3.8}$

Table H.3: Systematic uncertainties given in % for the double differential cross-sections in bins of Q^2, y. δ_6, δ_{12}, δ_{17} and δ_{20} were skipped intentionally. They are $\pm1.9\%, \pm0.5\%, +2.0\%$ and 1.5%, respectively (independently of the kinematic range).

Appendix I

Data format explanation

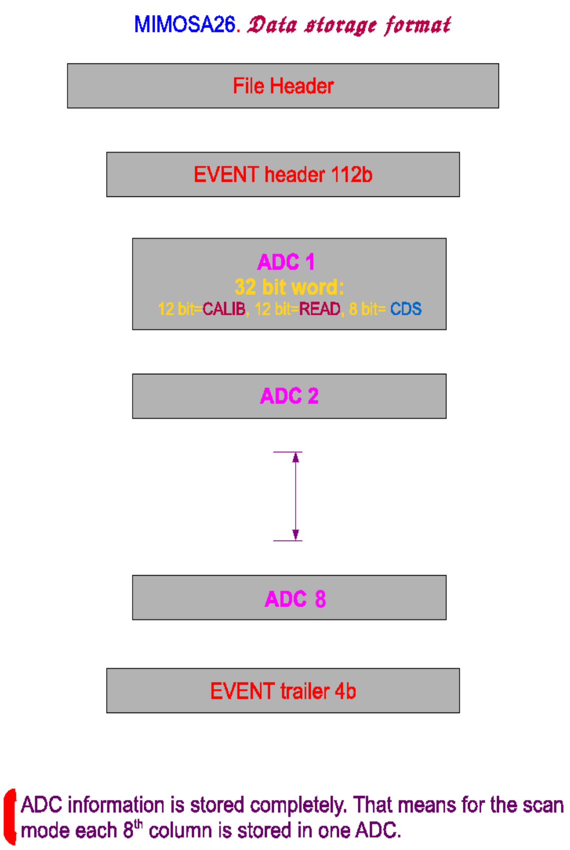

Figure I.1: Data format at analogue readout of MIMOSA26 chip. Eight ADCs read information in parallel. The DAQ stores the data from each ADC consequently, ADC by ADC. First 112 bits are reserved for the event header and the last eight bits for the event trailer. Beside the ADC counts, primary CDS information is also available in 8 bits only. The CDS information was omitted.

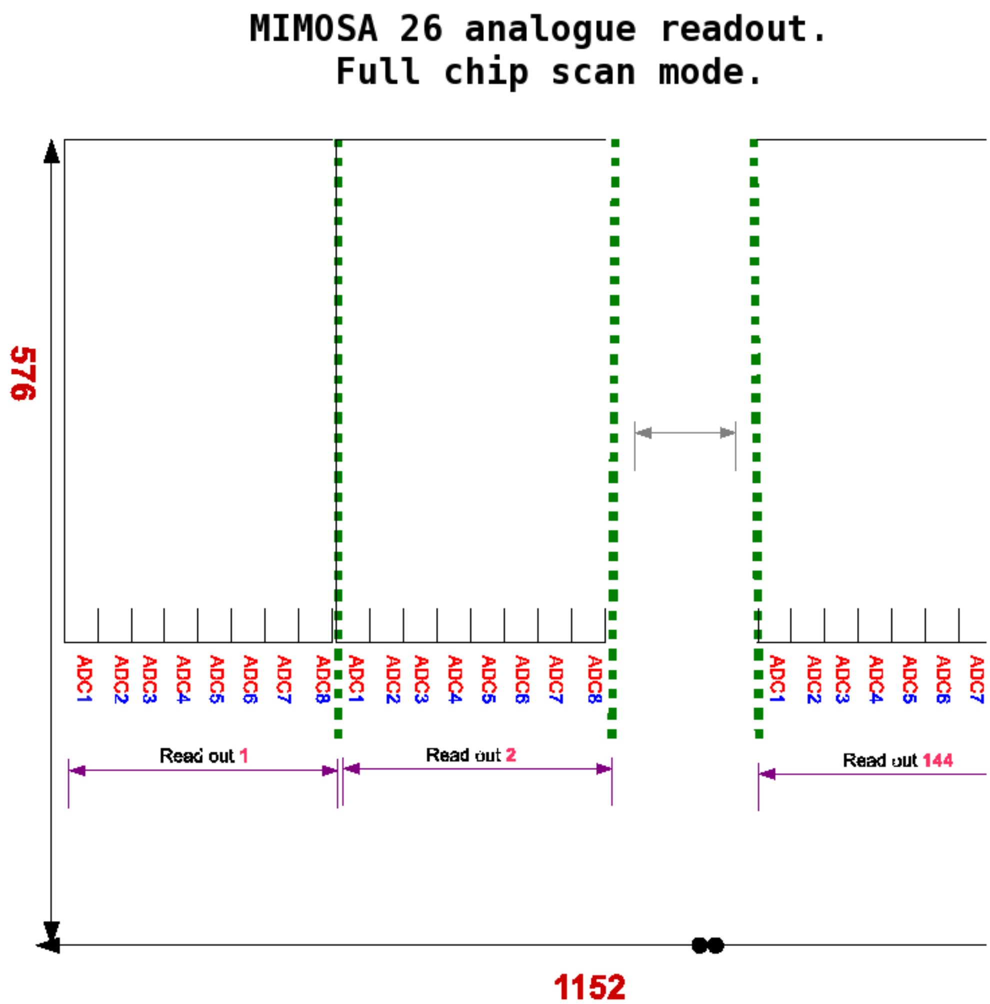

Figure I.2: Illustration to the full chip scan mode data format with eight ADCs. Thus 1152 lines of MIMOSA26 chip with 576 pixels in each line are read out by a consequence of eight channels. Each channel reads 576 pixels.

Bibliography

[1] B. H. Wiik, "*Weak interaction physics at HERA*", Nucl. Phys. B (*Proc. Suppl.*) **19** (1991) 461.

[2] W. N. Cottingham, D. A. Greenwood, "*An Introduction to the Standard Model of Particle Physics*", 2nd edn., (Cambridge University Press, Cambridge, 2007), 292 pages.

[3] S. L. Glashow, "*Partial-symmetries of weak interactions*", Nucl. Phys. **22** (1961) 579-588.

[4] S. Weinberg, "*A Model of Leptons*", Phys. Rev. Lett. B **19** (1967) 1264.

[5] H. Fritzsch, M. Gell-Mann, P. Minkowski, "*Vectorlike weak currents and new elementary fermions*", Phys. Lett. B **59** (1975) 256.

[6] E. C. G. Sudarshan and R. E. Marshak, "*Chirality Invariance and the Universal Fermi Interaction*", Phys. Rev. **109** (1958) 1860.

[7] P. W. Higgs, "*Broken Symmetries and the Masses of Gauge Bosons*", Phys. Rev. Lett. **13** (1964) 508.

[8] CMS Collaboration, S. Chatrchyan *et al.*, "*Observation of a new boson at a mass of 125 GeV with the CMS experiment at the LHC*", Phys. Lett. B **716** (2012) 30.

[9] ATLAS Collaboration, G. Aad *et al.*, "*Observation of a new particle in the search for the Standard Model Higgs boson with the ATLAS detector at the LHC*", Phys. Lett. B **716** (2012) 1.

[10] J. Beringer *et al.* (Particle Data Group), "*Review of Particle Physics*", Phys. Rev. D **86**, (2012) 010001.

[11] Ch. Kraus *et al.*, "*Final results from phase II of the Mainz neutrino mass searching for tritium β decay*", Eur. Phys. J. C **40** (2003) 447.

[12] K. Assamagan *et al.*, "*Upper limit of the muon-neutrino mass and charged pion mass from momentum analysis of a surface muon beam*", Phys. Rev. D **53** (1996) 6065.

[13] R. McNulty, "*A review of (MeV range) tau neutrino masses*", Nucl. Phys. B(*Proc. Suppl.*) **76** (1999) 409.

[14] I. C. Brock, T. Schoerner-Sadenius, "*Physics at the Terascale*", (Wiley-VCH, Berlin, 2011), 476 pages.

[15] F. Schleck, "*Electroweak and Strong interactions. Phenomenology, Concepts, Models*", 3rd edn., (Springer-Verlag, Berlin Heidelberg, 2012), 441 pages.

[16] R. K. Ellis, W. J. Stirling, B. R. Webber, "*QCD and collider physics*", Cambridge Monographs on Particle Physics, Nuclear Physics and Cosmology (No. 8), (Cambridge University Press, Cambridge, 1996), 435 pages.

[17] D. J. Gross, "*The discovery of asymptotic freedom and the emergence of QCD*", Proc. Natl. Acad. Sci. U.S.A. **102** (2005) 9099.

[18] G. 't Hooft, M. Veltmann, "*Regularization and renormalization of gauge fields*", Nucl. Phys. B **44** (1972) 189.

[19] M. Böhm, H. Spiesberger, W. Hollik, "*On the 1-Loop Renormalization of the Electroweak Standard Model and its Application to Leptonic Processes*", Fortschr. Phys. **34** (1986) 687.

[20] S. Narison, "*QCD as a Theory of Hadrons. From Partons to Confinement*", (Cambridge University Press, Cambridge, 2004), 812 pages.

[21] R. Tarrach, "*The polemass in perturbative QCD*", Nucl. Phys. B **183** (1981) 384;

I. I. Bigi, M. A. Shifman, N. G. Uraltsev, A. I. Vainshtein, "*Pole mass of the heavy quark: Perturbation theory and beyond*", Phys. Rev. D **50** (1994) 2234.

[22] S. Alekhin, S. Moch, "*Heavy-quark deep-inelastic scattering with a running mass*", Phys. Lett. B **699** (2011) 345.

[23] J. A. M. Vermaseren, S. A. Larin, T. van Ritbergen, "*The 4-loop quark mass anomalous dimension and the invariant quark mass*", Phys. Lett. B **405** (1997) 327.

[24] K. Melnikov, T. van Ritbergen, "*The three-loop relation between the $\overline{MS}$ and the pole quark masses*", Phys. Lett. B **482** (2000) 99.

[25] M. D. Scadron, F. Kleefeld, G. Rupp, "*Constituent and current quark masses at low chiral energies*", Europhys. Lett. **80** (2007) 51001, pre-print arXiv:0710.2273 [hep-ph].

[26] E. D. Bloom *et al.*, "*High-Energy Inelastic e-p Scattering at 6° and 10°*", Phys. Rev. Lett. **23** (1969) 930.

[27] L. W. Whitlow, E. M. Riordan, S. Dasu, "*Precise measurements of the proton and deuteron structure functions from a global analysis of the SLAC deep inelastic electron scattering cross sections*", Phys. Lett. B **282** (1992) 475.

[28] H1 and ZEUS Collaborations, F. D. Aaron *et al.*, "*Combined measurement and QCD analysis of the inclusive $e^{+-}p$ scattering cross sections at HERA*", JHEP **01** (2010) 109.

[29] J. D. Bjorken, "*Inequality for Backward Electron- and Muon-Nucleon Scattering at High Momentum Transfer*", Phys. Rev. **163** (1967) 1767.

[30] R. P. Feynman, "*Very High-Energy Collisions of Hadrons*", Phys. Rev. Lett. **23** (1969) 1415.

[31] T. Eichten *et al.*, "*Measurement of the neutrino-nucleon and antineutrino-nucleon total cross sections*", Phys. Lett. B **46** (1973) 274.

[32] A. M. Cooper-Sarkar, R. C. E. Devenish, A. De Roeck, "*Structure Functions of the Nucleon and their Interpretation*", DESY Note No. DESY-97-226, 1997, Int. J. Mod. Phys. A **13**, (1998) 3385.

[33] F. D. Aaron *et al.*, "*Measurement of the Inclusive $ep^{\pm}$ Scattering Cross Section at High Inelasticity y and of the Structure Function F_L* " Eur. Phys. J. C **71** (2011) 1579.

[34] F. Januschek, "*Measurement of e^+p neutral current deep-inelastic scattering with a longitudinally polarised positron beam and x-ray radiation damage for silicon sensors*", PhD thesis, Hamburg University (2011), DESY-THESIS-2012-012, http://www-library.desy.de/preparch/desy/thesis/desy-thesis-12-012.pdf.

[35] S. Z. Habib, "*Unpolarized Neutral Current $e^{\pm}p$ Cross Section Measurements at the H1 Experiment, HERA*", PhD thesis, Hamburg University (2009), DESY-THESIS-2009-039, http://www-library.desy.de/preparch/desy/thesis/desy-thesis-09-039.pdf.

[36] C. G. Callan, Jr. and D. J. Gross, "*High-energy Electroproduction and the Constitution of the Electric Current*", Phys. Rev. Lett. **22** (1969) 156.

[37] V. N. Gribov, L. N. Lipatov, "*Deep inelastic ep scattering in perturbation theory*", Sov. J. Nucl. Phys. **15** (1972) 438;

L. N. Lipatov, "*The parton model and perturbation theory*", Sov. J. Nucl. Phys. **20** (1975) 94;

G. Altarelli, G. Parisi, "*Asymptotic freedom in parton language*", Nucl. Phys. B **126** (1977) 298;

Y. Dokshitzer, "*Calculation of the structure functions for deep inelastic scattering and e^+e^- annihilation by perturbation theory in Quantum Chromodynamics*", Sov. Phys. JETP **46** (1977) 641.

[38] E. A. Kuraev, L. N. Lipatov, V. S. Fadin, "*Multi-Reggeon processes in the Yang-Mills theory*", Sov. Phys. JETP **44** (1976) 443;

E. A. Kuraev, L. N. Lipatov, V. S. Fadin, "*The Pomeranchuk singularity in nonabelian gauge theories*", Sov. Phys. JETP **45** (1977) 199;

I. I. Balitsky, L. N. Lipatov, "*The Pomeranchuk Singularity in Quantum Chromodynamics*", Sov. J. Nucl. Phys. **28** (1978) 822.

[39] M. Ciafaloni, "*Coherence effects in the initial jets at small Q^2*", Nucl. Phys. B **296** (1998) 49;

S. Catani, F. Fiorani, G. Marchesini, "*QCD coherence in initial state radiation*", Phys. Lett. B **234** (1990) 339;

M. Catani, F. Fiorani, G. Marchesini, "*Small-x behaviour of initial state radiation in perturbative QCD*", Nucl. Phys. B **336** (1990) 18.

[40] J. C. Collins, D. E. Soper, "*Parton distribution and decay functions*", Nucl. Phys. B **194** (1982) 445.

[41] G. Sterman, "*Partons, Factorization and Resummation*", Lectures at the Theoretical Advanced Study Institute (TASI95), pre-print arXiv:hep-ph/9606312.

[42] H1 Collaboration, F. D. Aaron *et al.*, "*Inclusive Deep Inelastic Scattering at High Q^2 with Longitudinally Polarised Lepton Beams at HERA*", DESY Note No. DESY-12-107, 2012, JHEP **09** (2012) 061.

[43] ZEUS Collaboration, H. Abramowicz *et al.*, "*Measurement of high-Q^2 neutral current deep inelastic e^+p scattering cross sections with a longitudinally polarised positron beam at HERA*", submitted to Eur. Phys. J. C, manuscript ID EPJC-12-08-066, pre-print arXiv:1208.6138 [hep-ex];

ZEUS Collaboration, H. Abramowicz *et al.*, "*Measurement of high-Q^2 charged current deep inelastic scattering cross sections with a longitudinally polarised positron beam at HERA*", Eur. Phys. J. C **70** (2010) 945.

[44] CMS Collaboration, S. Chatrchyan *et al.*, "*Measurement of the Electron Charge Asymmetry in Inclusive W Production in pp Collisions at $\sqrt{s} = 7$ TeV*", Phys. Rev. Lett. **109** (2012) 111806;

M. Vesterinen, "*Single W and Z boson production properties and asymmetries*", to appear in proceedings of Rencontres de Moriond 2011, pre-print arXiv:1105.5783 [hep-ex].

[45] CDF Collaboration, T. Affolder *et al.*, "*Measurement of the Strong Coupling Constant from Inclusive Jet Production at the Tevatron $\bar{p}p$ Collider*", Phys. Rev. Lett. **88** (2002) 042001;

ZEUS Collaboration, H. Abramowicz *et al.*, "*Inclusive-jet photoproduction at HERA and determination of α_s*", Nucl. Phys. B **864** (2012) 1.

[46] S. Alekhin, J. Blümlein, S. Klein, S. Moch, "*3-, 4-, and 5-flavor next-to-next-to-leading order parton distribution functions from deep-inelastic-scattering data and at hadron colliders*", Phys. Rev. D **81** (2010) 014032.

[47] J. Pumplin, A. Belyaev, J. Huston, D. Stump, W.-K. Tung, "*Parton distributions and the strong coupling: CTEQ6AB PDFs*", JHEP, **02** (2006) 032.

[48] A. D. Martin, W. J. Stirling, R. S. Thorne, G. Watt, "*Parton distributions for the LHC*", Eur. Phys. J. C **63** (2009) 189.

[49] NNPDF Collaboration, R. D. Ball, *et al.*, "*A first unbiased global NLO determination of parton distributions and their uncertainties*", Nucl. Phys. B **838** (2010) 136.

[50] H1 Collaboration, F. D. Aaron *et al.*, ZEUS Collaboration, I. Abt *et al.*, "*Combined Measurement of Neutral and Charged Current Cross Sections at HERA*", preliminary results, H1prelim-10-142, ZEUS-prel-10-018; H1prelim-11-042, ZEUS-prel-11-002.

[51] ZEUS Collaboration, J. Breitweg *et al.*, "*Measurement of $D^{*\pm}$ production and the charm contribution to F_2 in deep inelastic scattering at HERA*", Eur. Phys. J. C **12** (2000) 35.

[52] L. E. Gordon, J. K. Storrow, "*The parton distribution functions of the photon and the structure function $F_2^\gamma(x, Q^2)$*", Z. Phys. C **56** (1992) 307.

[53] ZEUS Collaboration, S. Chekanov *et al.*, "*Measurement of the charm fragmentation function in D^* photoproduction at HERA*", JHEP **04** (2009) 082.

[54] C. Peterson, D. Schlatter, I. Schmitt, P. M. Zerwas, "*Scaling violations in inclusive e^+e^- annihilation spectra*", Phys. Rev. D **27** (1983) 105.

[55] M. G. Bowler, "*e^+e^- production of heavy quarks in the string model*", Z. Phys. C **11** (1981) 169.

[56] V. G. Kartvelishvili, A. K. Likhoded, V. A. Petrov, "*On the fragmentation functions of heavy quarks into hadrons*", Phys. Lett. B **78** (1978) 615.

[57] M. Glück,E. Reya,M. Stratmann, "*Heavy quarks at high energy colliders*", Nucl. Phys. B **422** (1994) 37;

M. Glück, E. Reya, A. Vogt, "*Dynamical parton distributions of the proton and small-x physics*", Z. Phys. C **67** (1995) 433;

H. L. Lai, W. K. Tung, "*Charm production and parton distributions*", Z. Phys. C **74** (1997) 463.

[58] J. C. Collins, W. K. Tung, "*Calculating heavy quark distributions*", Nucl. Phys. B **278** (1986) 934;

R. S. Thorne, "*Variable-flavor number scheme for next-to-next-to-leading order*", Phys. Rev. D **73** (2006) 054019.

[59] R. S. Thorne, R. G. Roberts, "*Ordered analysis of heavy flavor production in deep-inelastic scattering*", Phys. Rev. D **57** (1998) 6871.

[60] M. Krämer, F. I. Olness, D. E. Soper, "*Treatment of heavy quarks in deeply inelastic scattering*", Phys. Rev. D **62** (2000) 096007.

[61] ZEUS Collaboration, S. Chekanov *et al.*, "*Measurement of $D^{*\pm}$ production in deep inelastic $e^{\pm}p$ scattering at HERA*", Phys. Rev. D **69** (2004) 012004.

[62] B. H. Wiik, "*HERA: The accelerator and the physics*", Acta Phys. Polon. B **16** (1985) 127.

[63] B. Parker *et al.*, "*HERA Luminosity upgrade superconducting magnet production at BNL*", IEEE Trans. Appl. Supercond. **11** (2001) 1518, Brookhaven National Laboratory Report No. BNL-68284, 2000.

[64] G.-A. Voss and B. H. Wiik, "*The Electron-Proton Collider HERA*", Annu. Rev. Nucl. Part. Sci **44** (1994) 413.

[65] U. Schneekloth, "*HERA luminosity upgrade*", DESY internal report, unpublished.

[66] ZEUS collaboration, "*ZEUS blue book*", DESY, unpublished, available at http://www-zeus.desy.de/bluebook/bluebook.html.

[67] E. Acerbi *et al.*, "*Thin and compensating solenoids for ZEUS detector*", IEEE Trans. Magn. **24** (1988) 1354.

[68] G. Abbiendi *et al.*, "*The ZEUS barrel and rear muon detector*", Nucl. Instrum. Meth. A **333** (1993) 342.

[69] R. Szwed, "*The VETO WALL detectors for ZEUS*", ZEUS Internal Note No. ZEUS-89-098, 1989, unpublished.

[70] W. Schott, "*The C5 Counter*", ZEUS Internal Note No. ZEUS-95-039, 1995, unpublished.

[71] J. A. Crittenden, W. Hain, U. Schneekloth, U. Wollmer and C. Youngman, "*The C5 upgrade*", ZEUS Internal Note No. ZEUS-01-002, 2001, unpublished.

[72] V. Chiochia, "*The ZEUS micro-vertex detector*", Nucl. Instrum. Meth. A **501** (2003) 60.

[73] E. N. Koffeman, "*A silicon micro vertex detector for the ZEUS experiment*", Nucl. Instrum. Meth. A **453** (2000) 89.

[74] P. D. Allfrey, "*Measurement of charmed hadron production in $e^{\pm}p$ deep inelastic scattering with the ZEUS detector*", PhD thesis, University of Oxford (2007), http://ora.ox.ac.uk/objects/uuid:5ab29a9c-75b2-46df-872b-399b834cb5e6.

[75] D. Dannheim, "*The silicon strip detectors of the ZEUS microvertex detector*", Diploma thesis, Hamburg University (1999), DESY-THESIS-99-027, http://www-library.desy.de/preparch/desy/thesis/desy-thesis-99-027.ps.gz.

[76] C. B. Brooks *et al.*, "*Development of the the ZEUS central tracking detector*", Nucl. Instrum. Meth. A **283** (1989) 477.

[77] D. Bailey, R. Hall-Wilton, "*Experience with the ZEUS central tracking detector*", Nucl. Instrum. Meth. A **515** (2003) 37.

[78] B. Foster *et al.*, "*The performance of the ZEUS central tracking detector z-by-timing electronics in a transputer based data acquisition system*", Nucl. Phys. B (*Proc. Suppl.*) **32** (1993) 181.

[79] R. H. Wilthon *et al.*, "*The CTD resolution*", ZEUS Internal Note No. ZEUS-99-024, 1999, unpublished.

[80] A. Spiridonov, "*RTFIT news: track resolution*", Internal ZEUS collaboration meeting presentation on Feb. 11, 2011, unpublished, available at https://www-zeus.desy.de/zems/ZEUS_ONLY/display_from_link.php?fid=12065.

[81] S. Fourletov, "*Straw tube tracking detector (STT) for ZEUS*", Nucl. Instrum. Meth. A **535** (2004) 191.

[82] E. Hilger, "*The ZEUS uranium-scintillator calorimeter for HERA*", Nucl. Instrum. Meth. A **257** (1987) 488.

[83] P. de Jong, "*The measurement of the hadronic energy flow and jet production with the ZEUS calorimeter in deep inelastic scattering events at HERA*", PhD thesis, University of Amsterdam (1993).

[84] A. Andersen *et al.*, "*Response of a uranium-scintillator calorimeter to electrons, π and protons in the momentum range* $0.5 - 10$ *GeV/c*", Nucl. Instrum. Meth. A **290** (1990) 95.

[85] A. Andresen *et al.*, "*Construction and beam test of the ZEUS forward and rear calorimeter*", Nucl. Instrum. Meth. A **309** (1991) 101.

[86] M. Derrick *et al.*, "*Design and construction of the ZEUS barrel calorimeter*", Nucl. Instrum. Meth. A **309** (1991) 77.

[87] ZEUS Collaboration, M. Derrick *et al.*, "*Measurement of elastic Omega photoproduction at HERA*", Z. Phys. C **73** (1996) 73, DESY Note No. DESY-96-159, 1996, pre-print arXiv:hep-ex/9608010.

[88] A. Bamberger *et al.*, "*The small angle rear tracking detector of ZEUS*", Nucl. Instrum. Meth. A **401** (1997) 63.

[89] H. Bethe, W. Heitler, "*On the Stopping of Fast Particles and on the Creation of Positive Electrons*", Proc. R. Soc. Lond. A **146** (1934) 83.

[90] M. Helbich, "*The spectrometer system for measuring ZEUS luminosity at HERA*", Nucl. Instrum. Meth. A **565** (2006) 572.

[91] J. Chwastowski, "*Aerogel Cherenkov detectors for the luminosity measurement at HERA*", Nucl. Instrum. Meth. A **504** (2003) 222.

[92] R. Carlin, "*The trigger of ZEUS, a flexible system for a high bunch crossing rate collider*", Nucl. Instrum. Meth. A **379** (1996) 542.

[93] S. Silverstein *et al.*, "*The ZEUS calorimeter first level trigger*", Nucl. Instrum. Meth. A **360** (1995) 322.

[94] P. D. Allfrey, "*The design and performance of the ZEUS global tracking trigger*", Nucl. Instrum. Meth. A **580** (2007) 1257.

[95] H. Uijterwaal, "*Global Second Level Trigger for ZEUS*", PhD thesis, University of Amsterdam (1992).

[96] U. Behrens, L. Hagge, Th. Schlichting, W. Vogel, "*The eventbuilder of the ZEUS detector*", Nucl. Phys. B (*Proc. Suppl.*) **32** (1993) 346.

[97] S. Bharda *et al.*, "*The ZEUS third-level trigger system*", Comput. Phys. Commun. **57** (1989) 321.

[98] G. Hartner, "*VCTRAK Briefing, Program and Math*", ZEUS Internal Note No. ZEUS-98-058, 1998, unpublished.

[99] A. Spiridonov, "*Mathematical Framework for Fast and Rigorous Track Fit for the ZEUS Detector*", DESY Note No. DESY-08-182, 2008, pre-print arXiv:0812.1245.

[100] R. E. Kalman, "*A new approach to linear filtering and prediction problems*", Trans. ASME J. Basic Eng. D **82** (1960) 35, available at http://www.cs.unc.edu/ welch/kalman/media/pdf/Kalman1960.pdf.

[101] N. Tuning, "*ZUFOs: Hadronic Final State Reconstruction with Calorimeter, Tracking and Backsplash Correction*", ZEUS Internal Note No. ZEUS-01-021, 2001, unpublished, available at http://www-zeus.desy.de/ sunil/slana_docs/zufos_tuning_2001.ps.gz.

[102] B. Reisert, "*CAL Energy Scale Calibration*", Internal ZEUS FL group presentation on Jan. 22, 2008, unpublished, available at https://www-zeus.desy.de/zems/ZEUS_ONLY/display_from_link.php?fid=9870.

[103] H. Abramowicz, A. Caldwell, R. Sinkus, "*Neural network based electron identification in the ZEUS calorimeter*", Nucl. Instrum. Meth. A **365** (1995) 508.

[104] A. López-Dúran Viani, S. Schlenstedt, "*Electron finder efficiencies and impurities. A comparison between SINISTRA95, EM and EMNET*", ZEUS Internal Note No. ZEUS-99-077, 1999, unpublished.

[105] T. Doeker, A. Fray, M. Nakao, "*Electron position reconstruction - update of the ELECPO routines*", ZEUS Internal Note No. ZEUS-94-123, 1994, unpublished.

[106] S. Weinzierl, "*Introduction to Monte Carlo methods*", NIKHEF Report No. 00-012, pre-print arXiv:hep-ph/0006269.

[107] "*GEANT Detector Description and Simulation Tool*", GEANT3 description, CERN, Geneva (1993).

[108] M. Lisovyi, "*Measurement of Charm Production in Deep Inelastic Scattering using Lifetime Tagging for $D^{\pm}$ Meson Decays with the ZEUS Detector at HERA*", PhD thesis, Hamburg University (2011), DESY-THESIS-2011-033, http://www-library.desy.de/preparch/desy/thesis/desy-thesis-11-033.pdf.

[109] T. Sjöstrand, L. Lönnblad, S. Mrenna, "*Pythia 6.2 Physics and Manual*", pre-print arXiv:hep-ph/0108264.

[110] H. Jung, "*Hard diffractive scattering in high energy ep collisions and the Monte Carlo Generator RAPGAP*", Comput. Phys. Commun. **86** (1995) 147.

[111] CTEQ Collaboration, H. L. Lai *et al.*, "*Global QCD analysis of parton structure of the nucleon: CTEQ5 parton distributions*", Eur. Phys. J. C **12** (2000) 375.

[112] M. Glück, E. Reya, A. Vogt, "*Parton structure of the photon beyond the leading order*", Phys. Rev. D **45** (1992) 3986.

[113] ZEUS Collaboration, S. Chekanov *et al.*, "*Measurement of the open-charm contribution to the diffractive proton structure function*", Nucl. Phys. B **672** (2003) 3.

[114] H1 Collaboration, C. Adloff *et al.*, "*Inclusive Measurement of Diffractive Deep Inelastic ep Scattering*", Z. Phys. C **76** (1997) 613.

[115] DELPHI Collaboration, P. Abreu *et al.*, "*Tuning and Test of Fragmentation Models Based on Identified Particles and Precision Event Shape Data*", Z. Phys. C **73** (1996) 11.

[116] L. Lönnblad, "*Ariadne version 4 — A program for simulation of QDC cascades implementing the colour dipole model*", Comput. Phys. Commun. **71** (1992) 15.

[117] G. Gustafson, U. Pettersson, "*Dipole formulation of QCD cascades*", Nucl. Phys. B **306** (1988) 746.

[118] V. Drugakov, "*Luminosity Measurement*", Internal ZEUS collaboration presentation on Feb. 10, 2010, unpublished, available at https://www-zeus.desy.de/zems/ZEUS_ONLY/display_from_link.php?fid=11450.

[119] L. K. Gladilin, *Private communication*, DESY.

[120] J. Grebenyuk, P. Kaur Devgun, "*FL extension from the shifted vertex*", paper in preparation, presentation on Oct. 10, 2012, unpublished, available at https://www-zeus.desy.de/zems/ZEUS_ONLY/display_from_link.php?fid=12842.

[121] P. Roloff, "*Measurement of charm and beauty production in deep inelastic scattering at HERA*", PhD thesis, Hamburg University (2011), DESY-THESIS-2011-049, http://www-library.desy.de/preparch/desy/thesis/desy-thesis-11-049.pdf.

[122] ZEUS Collaboration, S. Chekanov *et al.*, "*Measurement of $D^{\pm}$ and D^{0} Production in Deep Inelastic Scattering Using a Lifetime Tag at HERA*", Eur. Phys. J. C **63** (2009) 171.

[123] A. Geiser, *Private communication*, DESY.

[124] L3 Collaboration, M. Acciarri *et al.*, "*Measurement of inclusive $D^{*\pm}$ production in two-photon collisions at LEP*", Phys. Lett. B **467** (1999) 137;

ATLAS Collaboration, "*Measurement of D^{*} meson production cross sections in pp collisions at $\sqrt{s} = 7\,TeV$ with the ATLAS detector*", ATLAS Internal Note No. ATLAS-CONF-2011-017, 2011, available at http://cdsweb.cern.ch/record/1336746/files/ATLAS-CONF-2011-017.pdf?version=1.

[125] W. Dunne, "*Measurements of D^{*} Production in Deep Inelastic Scattering at HERA*", PhD thesis, University of Glasgow (2007), http://ppewww.physics.gla.ac.uk/ bdunne/thesis/thesis.pdf.

[126] A. Savin, "*CFLT RCAL Isoe during 2004-2005 running period*", Internal ZEUS trigger group presentation on Dec. 14, 2005, unpublished, available at https://www-zeus.desy.de/zems/ZEUS_ONLY/display_from_link.php?fid=6137;

A. Savin, "*CFLT/CFLTp Status Report*", Internal ZEUS collaboration meeting presentation on Oct. 16-21, 2006, unpublished, available at https://www-zeus.desy.de/zems/ZEUS_ONLY/display_from_link.php?fid=7960.

[127] O. Bachynska, "*D* in DIS: systematic effects*" Internal ZEUS Heavy Flavour group meeting presentation on June 16, 2012, unpublished, available at https://www-zeus.desy.de/zems/ZEUS_ONLY/display_from_link.php?fid=12759.

[128] O. Behnke, "*Track efficiency tests with K_s^0 decays*", Internal ZEUS heavy flavor group presentation on Mar. 25, 2010, unpublished, available at https://www-zeus.desy.de/zems/ZEUS_ONLY/display_from_link.php?fid=11566.

[129] W. Erdmann, "*Untersuchung der Photoproduktion von D^{*}-Mesonen am ep- Speicherring HERA*", PhD thesis, ETH Zurich (1996), http://dx.doi.org/10.3929/ethz-a-001609482.

[130] V. Libov, "*Measurement of charm and beauty production in DIS at HERA*", PhD thesis in preparation, Hamburg University, DESY.

[131] M. Corradi, "*Check of material and hadronic interactions with secondary vertices*", Internal ZEUS heavy flavor group presentation on Jun. 27, 2012, unpublished, available at https://www-zeus.desy.de/zems/ZEUS_ONLY/display_from_link.php?fid=12760.

[132] A. Spiridonov, "*Mapping of tracking efficiency with VMCU utility*", Internal ZEUS heavy flavor group presentation on Apr. 4, 2012, unpublished, available at https://www-zeus.desy.de/zems/ZEUS_ONLY/display_from_link.php?fid=12691.

[133] G. Molière, "*Theorie der Streuung schneller geladener Teilchen II. Mehrfach- und Vielfachstreuung*", Z. Naturforsch. **3a** (1950) 78;

C. T. Case, E. L. Battle, "*Molière's Theory of Multiple Scattering*", Phys. Rev. **169** (1968) 201.

[134] A. Salii, "*D^* in photoproduction. Tails of peak*", Internal ZEUS heavy flavor group presentation on Dec. 15, 2010, unpublished, available at https://www-zeus.desy.de/zems/ZEUS_ONLY/display_from_link.php?fid=11999.

[135] O. Bachynska, "*Measurement of the $D^{*\pm}$ protoproduction with ZEUS detector at HERA*", Master thesis, Taras Shevchenko National University of Kyiv (2009) (in Ukrainian), unpublished.

[136] M. Corradi, *Private communication*, DESY.

[137] ZEUS Collaboration, S. Chekanov *et al.*, "*Measurement of charm and beauty production in deep inelastic ep scattering from decays into muons at HERA*", Eur. Phys. J. C **65** (2010) 65, pre-print arXiv:0904.3487 [hep-ex].

[138] ZEUS Collaboration, H. Abramowicz *et al.*, "*Measurement of beauty production in deep inelastic scattering at HERA using decays into electrons*", Eur. Phys. J. C **71** (2011) 1573, pre-print arXiv:1101.3692 [hep-ex].

[139] ZEUS Collaboration, S. Chekanov *et al.*, "*Measurement of beauty production in deep inelastic scattering at HERA*", Phys. Lett. B **599** (2004) 173, pre-print arXiv:hep-ex/0405069.

[140] V. Sola, "*Inclusive diffractive cross sections in deep inelastic ep scattering at HERA*", PhD thesis, University of Torino (2012), DESY-THESIS-2012-008, http://www-library.desy.de/preparch/desy/thesis/desy-thesis-12-008.pdf.

[141] ZEUS Collaboration, S. Chekanov *et al.*, "*Differential cross sections of $D^{*\pm}$ photoproduction in ep collisions at HERA*", Phys. Lett. B **401** (1997) 192, pre-print arXiv:hep-ex/9704011.

[142] ZEUS Collaboration, H. Abramowicz *et al.*, "*Measurement of high-Q2 neutral current deep inelastic e+p scattering cross sections with a longitudinally polarised positron beam at HERA*", DESY Note No. DESY-12-145, 2012, pre-print arXiv:1208.6138 [hep-ex].

[143] S. Shimizu, "*Measurement of the Longitudinal Structure Function FL at HERA*", PhD thesis, University of Tokyo (2009), http://www-zeus.desy.de/physics/sfe/theses/shimaFL.pdf.

[144] M. Paterno, "*Calculating Efficiencies and Their Uncertainties*", Fermilab Internal Note No. FERMILAB-TM-2286-CD, 2003, available at http://home.fnal.gov/ paterno/images/effic.pdf.

[145] B. W. Harris, J. Smith, "*Heavy-quark correlations in deep-inelastic electroproduction*", Nucl. Phys. B **452** (1995) 109;

B. W. Harris, J. Smith, "*Invariant mass distribution for heavy quark-anti-quark pairs in deep inelastic electroproduction*",
Phys. Lett. B **353** (1995) 535,
Phys. Lett. B **359** (1995) 423 (erratum).

[146] H1 and ZEUS Collaborations, F. D. Aaron *et al.*, "*Combination and QCD analysis of charm production cross section measurements in deep-inelastic ep scattering at HERA*", DESY Note No. DESY-12-172, submitted to Eur. Phys. J. C.

[147] H1 and ZEUS Collaborations, F. D. Aaron *et al.*, "*Combined measurement and QCD analysis of the inclusive $e^{\pm}p$ cross sections at HERA*", JHEP **1** (2010) 109.

[148] E. Lohrmann "*A Summary of Charm Hadron Production Fractions*", pre-print arXiv:1112.3757 [hep-ex].

[149] O. Bachynska, M. Corradi, A. Gizhko, "*Measurement of $D^{*\pm}$ production in deep inelastic scattering at HERA*", paper in preparation, internal No. ZEUS-prel-11-012.

[150] H1 Collaboration, F. D. Aaron *et al.*, "*Measurement of $D^{*\pm}$ Meson Production and Determination of $F_2^{c\bar{c}}$ at low Q^2 in Deep-Inelastic Scattering at HERA*", Eur. Phys. J. C **71** (2011) 1769.

[151] H1 Collaboration, F. D. Aaron *et al.*, "*Measurement of the D^* meson production cross section and $F_2^{c\bar{c}}$, at high Q^2, in ep scattering at HERA*", Phys. Lett. B **686** (2010) 91.

[152] A. V. Kotikov, A. V. Lipatov and N. P. Zotov, "*The contribution of off-shell gluons to the longitudinal structure function F_L*", Eur. Phys. J. C **27** (2003), 219;

K. Daum *et al.*, *Proceedings of the workshop on "Future physics at HERA"*, eds. G. Ingelmann, A. De Roeck and R. Klanner, pre-print arXiv:hep-ph/9609478.

[153] R. S. Thorne, R. G. Roberts, "*A practical procedure for evolving heavy flavour structure functions*", Phys. Lett. B **421** (1998) 303.

[154] V. Radescu, "*HERA Precision Measurements and Impact for LHC Predictions*", Moriond QCD 2011 conference, La Thuile, Italy, 2011,
pre-print arXiv:1107.4193 [hep-ex];

K. Lipka, "*Recent results from HERA and their impact for LHC*", 2011 Hadron Collider Physics symposium (HCP-2011), Paris, France, 2011, pre-print arXiv:1201.4486[hep-ex].

[155] A. Cooper-Sarkar, *Private communication*, DESY.

[156] M. Lisovyi, O. Zenaiev, "*Measurement of $D^{\pm}$ production in deep inelastic ep scattering with the ZEUS detector at HERA*", paper in preparation.

[157] "*International Linear Collider Reference Design Report*", available at http://www.linearcollider.org/about/Publications/Reference-Design-Report.

[158] "*The material budget of the ATLAS inner detector*", Report No. LHCC 98-18, INDET-NO-207, 1998.

[159] A. Nomerotski *et al.*, "*PLUME collaboration: Ultra-light ladders for linear collider vertex detector*", Nucl. Instrum. Meth. A **650** (2011) 208, URL http://www.iphc.cnrs.fr/plume.html.

[160] J. Baudot *et al.*, "*Development of Single- and Double-sided Ladders for the ILD Vertex Detectors*", pre-print arXiv:1203.3689 [physics.ins-det].

[161] R. Turchetta *et al.*, "*A monolithic active pixel sensor for charged particle tracking and imaging using standard VLSI CMOS technology*", Nucl. Instrum. Meth. A **458** (2001) 677.

[162] N. H. E. Weste, D. Harris, "*CMOS VLSI design. A Circuits and System Perspective*", 3rd edn., (Addison Wesley Publishing Company, 2004). 800 p.

[163] J. Sparkes, "*Semiconductor Devices*", 2nd edn., (CRC Press, 1994), 240 pages.

[164] A. Himmi, G. Dozire, O. Torheim, C. Hu-Guo, M. Winter, "*A Zero Suppression Micro-Circuit for Binary Readout CMOS Monolithic Sensors*", TWEPP-09: Topical Workshop on Electronics for Particle Physics, available at http://cdsweb.cern.ch/record/1235850/files/p426.pdf?version=1.

[165] C. Hu-Guo *et al.*, "*First reticule size MAPS with digital output and integrated zero suppression for the EUDET-JRA1 beam telescope*", Nucl. Instrum. Meth. A **623** (2010) 480.

[166] "*MIMOSA 26 User Manual*", available at http://www.iphc.cnrs.fr/IMG/pdf/M26_UserManual_light.pdf.

[167] "*IEEE Standard Test Access Port and Boundary-Scan Architecture*", IEEE Standard No. 1149.1-1999 (2000), URL 10.1109/IEEESTD.2001.92950.

[168] K. Jaaskelainen, "*IMAGER 12-bit digitizer-controller card with USB 2.0 connection*", Internal Note, IPHC Strasbourg, 2009.

[169] D. Contarato, "*Silicon Detectors for Particle Tracking at Future High-Energy Physics Experiments*", PhD thesis, Hamburg University (2005), http://www-library.desy.de/preparch/desy/thesis/desy-thesis-05-044.pdf.

[170] M. Tabet, "*Double Sampling Techniques for CMOS Image Sensors*", PhD thesis, University of Waterloo (2002), http://www.cse.yorku.ca/visor/pdf/Tabet_PhD_thesis.pdf.

Acknowledgments

The way through this thesis was not an easy one. It was full of interesting adventures in the physics world. This thesis would not been completed without great support from the people I was working with.

First of all, I would like to express my gratitude to Dr. Achim Geiser for the possibility to do research within the ZEUS collaboration and for guiding me through the research. Thank you for reading the text of this thesis from the very beginning. Your "First convince yourself, then you will convince the others" will stay with me forever.

Great Thanks goes to Dr. Massimo Corradi for sharing with me the work on the D^* analysis. Your guidance and support were constantly giving me inspiration. I learnt a lot during the time of our cooperation.

Another huge Thank You goes to Dr. Iris Abt. Dear Iris, you were there for me when I desperately needed an advice or a cheer up. Thank you for all the support with the analysis and with this thesis.

I want to address my Thank You to Prof. Ewald Paul for the proof-reading of the thesis.

I would also like to thank Prof. Erika Garutti and Dr. Achim Geiser for agreeing to refer the dissertation, and Prof. Brian Foster and Dr. Thomas Schörner-Sadenius for agreeing to refer the disputation.

Also, I would like to express my gratitude to Olaf Behnke and Misha Lisovyi for nice and fruitful discussions. I have learnt a lot from you. Misha, thank you for making all your comments to the analysis and for noticing things that I was not aware of. Additional Thanks goes to Jörg Behr for the help with my German. I would also like to thank Andrii Gizhko for the second analysis and for sharing with me those harsh times during the release of the preliminary results.

Dear Uli, Dear Artem, thank you for all the nice time in the lab. That was amusing.

Also, I want to thank Dr. Volodymyr Aushev who opened for me a window to the world of particle physics.

The time I spent in the ZEUS collaboration would not be that fun without my friends. Dear Inna and Denis, thank you for listening all my complaints and whining, you really helped me to keep going. Dear Anastasia and Julia, thank you for all the nice chats, tea drinking time and friendship. Dear Friederike, thank you for being the best office-mate. Dear Slava, thank you for being my bro in the charm physics analysis. Dear Maxim, thank you being my old good friend and for the funny skype chats accompanied with the guitar play.

My dear mother, thank you for your indefectible understanding and for the support. You understand me more than anyone on the Earth. Forgive me, that I was not always around. My dear father, I wished you could see me now...

My dear Sanya, thank you for being patient, supportive and helpful at ever stage of this thesis. And thank you for sitting next to me till after midnight and for our long debugging sessions. Thank you for pushing me to keep going and for all the nice and warm surprises which were melting my heart.